Yellow Matters

Laanen, M.L.

2007

document version
Publisher's PDF, also known as Version of record

citation for published version (APA)
Laanen, M. L. (2007). *Yellow Matters: Improving the remote sensing of Coloured Dissolved Organic Matter in inland freshwaters*. [PhD-Thesis - Research and graduation internal, Vrije Universiteit Amsterdam]. Water Insight BV.

Yellow Matters

Improving the remote sensing of Coloured Dissolved Organic Matter in inland freshwaters

Marnix Laanen

Yellow Matters – Improving the remote sensing of Coloured Dissolved Organic Matter in inland freshwaters

(Ph.D. dissertation Vrije Universiteit Amsterdam)

Gekleurde stoffen opgelost – Verbeteringen van de teledetectie van gekleurde opgeloste organische stoffen in zoete binnenwateren

(Academisch proefschrift Vrije Universiteit Amsterdam)

This research is part of the Netherlands Research School for the Socio-Economic and Natural Sciences of the Environment programme

This research is part of the Wetlands in the Randstad programme funded by the Vrije Universiteit Amsterdam

This publication is supported by Water Insight BV

ISBN: 978-90-9021921-9

VRIJE UNIVERSITEIT

Yellow Matters

Improving the remote sensing of Coloured Dissolved Organic Matter in inland freshwaters

ACADEMISCH PROEFSCHRIFT

ter verkrijging van de graad Doctor aan

de Vrije Universiteit Amsterdam,

op gezag van de rector magnificus

prof.dr. L.M. Bouter,

in het openbaar te verdedigen

ten overstaan van de promotiecommissie

van de faculteit de Aard- en Levenswetenschappen

op dinsdag 12 juni 2007 om 10.45 uur

in de aula van de universiteit,

De Boelelaan 1105

door

Marnix Leo Laanen

geboren te Vlissingen

promotoren: prof.dr.ir. P. Vellinga

prof.dr. W. Salomons

copromotoren: dr. S.W.M. Peters

dr. A.G. Dekker

Symbols, definitions and abbreviations

Symbols list

Energy

Symbol	Description	Unit
ε	Energy	J
h	Planck's constant ($6.63*10^{-34}$)	Js
c	Speed of light ($2.998*10^{8}$)	ms^{-1}
λ	Wavelength	nm

Apparent optical properties

Radiance (wavelength dependency omitted)

Symbol	Description	Unit
L	Radiance	W m^{-2} sr^{-1}
L_{wu}	Upwelling subsurface radiance	W m^{-2} sr^{-1}
L_{au}	Upward radiance above the water at nadir angle (42º)	W m^{-2} sr^{-1}
L_{water}	Radiance measured by a spectrometer pointed towards the water surface	W m^{-2} sr^{-1}
L_{sky}	Radiance of skylight at zenith angle (42º)	W m^{-2} sr^{-1}
L_{s}	Incident sky radiance reflected by the water surface	W m^{-2} sr^{-1}
L_{rs}	Direct component of L_{ad}	W m^{-2} sr^{-1}
L_{dif}	Diffuse component of L_{ad}	W m^{-2} sr^{-1}

Irradiance (wavelength dependency omitted)

Symbol	Description	Unit
E	Irradiance	W m^{-2}
E_{u}	Upwelling irradiance	W m^{-2}
E_{d}	Downwelling irradiance	W m^{-2}
E_{wu}	Upwelling irradiance just below the water surface	W m^{-2}
E_{ad}	Downward irradiance just above the water surface	W m^{-2}
E_{wd}	Downwelling irradiance just below the water surface	W m^{-2}

F	Fraction diffuse light of E_{ad}	-
E_{sun}	Direct downwelling irradiance or solar constant	W m^{-2}
E_{dif}	Diffuse downwelling irradiance or sky light	W m^{-2}

Miscellaneous

Symbol	Description	Unit
θ	Zenith angle	-
ϕ	Azimuth angle	-
Φ	Radiant flux	W
S	Apparent unit area	m^2
ω	Solid angle	sr
R	Irradiance reflectance	-
I	Radiant intensity	W sr^{-1}
$\bar{\beta}$	Volume scattering function	$m^{-1}sr^{-1}$
μ	Average cosine of the zenith angle	-
Ξ	Unit sphere	-
z	Depth	m
K_d	Vertical attenuation coefficient	m^{-1}
ζ	Optical depth	-
SD	Secchi Disk depth	m
z_0	Reference depth	m
Φ_a	Radiant flux absorbed	W
Φ_b	Radiant flux scattered	W
$R(0-)$	Subsurface irradiance reflectance	-
Q	Conversion coefficient for L_{wu} to E_{wu}	-
μ_{ad}	Average cosine of light just above the water surface	-
n	Refractive index of water	-
r^0	Fresnel coefficient (0° angle of incidence)	-
g	Conversion constant of L_{au} to L_{wu}	-
ρ_{sky}	Fresnel reflectance coefficient of sky radiance at the water surface at zenith angle (42º)	-
ρ_{Θ}	Fresnel reflectance coefficient for sunlight	-
r_{dif}	Average reflectance coefficient for diffuse light	-
ρ_w	Downward reflectance of the diffuse upwelling irradiance	-
f	Anisotropy of downwelling irradiance correction factor	-
r_d	Shape factor for upward scattering	-
r_u	Shape factor for downward scattering	-

Inherent optical properties

Beam attenuation (wavelength dependency omitted)

Symbol	Description	Unit
C	Attenuance	-
c	Beam attenuation coefficient	m^{-1}
c_d	Diffuse attenuation function for downwelling irradiance	m^{-1}
c_u	Diffuse attenuation function for upwelling irradiance	m^{-1}
c_{dd}	Local transmittance functions for downwelling irradiance	m^{-1}
c_{uu}	Local transmittance function for upwelling irradiance	m^{-1}

Absorption (wavelength dependency omitted)

Symbol	Description	Unit
A	Absorbance	-
a	Absorption coefficient	m^{-1}
a_d	Diffuse absorption function for downwelling irradiance	m^{-1}
a_u	Diffuse absorption function for upwelling irradiance	m^{-1}
a_w	Absorption coefficient of pure water	m^{-1}
a_{tr}	Absorption coefficient of tripton	m^{-1}
a_{ph}	Absorption coefficient of phytoplankton	m^{-1}
a_{CDOM}	Absorption coefficient of CDOM	m^{-1}
a^*_{tr}	Specific absorption coefficient of tripton at 550 nm	$m^2\ mg^{-1}$
a^*_{ph}	Specific absorption coefficient of phytoplankton at 676 nm	$m^2\ \mu g^{-1}$
$\bar{a}_{CDOM}$	Normalised absorption coefficient of CDOM at 440 nm	m^{-1}
a_{HA}	Humic acid absorption	m^{-1}
a_{FA}	Fulvic acid absorption	m^{-1}

Scattering (wavelength dependency omitted)

Symbol	Description	Unit
B	Scatterance	-
b	Scattering coefficient	m^{-1}
b_{dd}	Diffuse downward scattering function for downwelling	m^{-1}
b_{uu}	Diffuse upward scattering function for upwelling irradiance	m^{-1}
b_{du}	Diffuse downward scattering function for upwelling	m^{-1}
b_{ud}	Diffuse upward scattering function for downwelling	m^{-1}
b_f	Forward scattering coefficient	m^{-1}
b_b	Backscattering coefficient	m^{-1}
B_w	Forward- to backscatter ratio of pure water	-

b_w	Scattering coefficient of pure water	m^{-1}
B	Forward- to backscatter ratio	-
b_{ses}	Scattering coefficient of seston	m^{-1}
b_{tr}	Scattering coefficient of tripton	m^{-1}
b_{ph}	Scattering coefficient of phytoplankton	m^{-1}
b_b^*	Total specific backscattering coefficient at 550 nm	$m^2\ mg^{-1}$

Concentrations

Symbol	Description	Unit
C_{TCHL}	Concentration of Total Chlorophyll (chlorophyll α + phaeopigments)	$\mu g\ l^{-1}$
C_{TCHL}	Concentration of chlorophyll α	$\mu g\ l^{-1}$
C_{PHAEO}	Concentration of phaeopigments	$\mu g\ l^{-1}$
C_{TSM}	Concentration of Total Suspended Matter	$mg\ l^{-1}$
C_{CDOM}	Concentration of CDOM (estimated by the absorption value at 440 nm)	-

Spectrometer and PSICAM symbols (wavelength dependency omitted)

Symbol	Description	Unit
SNR	Signal to noise ratio	-
DN_{dark}	Recorded digital numbers of dark measurement	-
$DN_{reference}$	Recorded digital numbers of reference measurement	-
DN_{sample}	Recorded digital numbers of sample measurement	-
l	Path length	m
P_s	Probability of photon survival in transit across the cavity	-
C_f	Average number of photon collisions with the wall	-
l_f	Average photon path length (in the PSICAM)	m
r	The cavity radius	m
ρ	The reflectivity of the cavity wall	-
T	Transmittance	-
F_0	Outwardly directed irradiance at the surface of the cavity	$W\ m^{-2}$
$F_0^{\ w}$	Outwardly directed irradiance at the surface of the cavity	$W\ m^{-2}$
P	Power	W
V	Volume (of the PSICAM cavity)	m^3
SA	The surface area of the cavity wall	m^2
T_{AB}	The relative transmittance of A to B	-
κ	Relative spectral absorption coefficient	$l\ mol^{-1}\ cm^{-1}$

CDOM exponential fit symbols (wavelength dependency omitted)

Symbol	Description	Unit
S	slope parameter in exponential CDOM or tripton	nm^{-1}
S_{HA}	humic acid slope parameter in exponential CDOM	nm^{-1}
S_{FA}	fulvic acid slope parameter in exponential CDOM	nm^{-1}
$Offset$	Offset parameter in exponential CDOM absorption model	m^{-1}

Statistical and mathematical symbols

Symbol	Description	Unit
σ	Standard deviation	-
R^2	Correlation coefficient	-
N	Number of samples	-
χ^2	Squared difference between observed and expected values	-
M	Matrix of optical properties of the sample	-
x	Matrix of unknown concentrations	-
y	Matrix of optical properties of pure water	-
∂	Partial differential	-
Δ	Relative error	-

Abbreviations

CAESAR	CCD Airborne Experimental Scanner for Application in Remote
CASI	Compact Airborne Spectrographic Imager
CCD	Charge-Coupled Device
CDOM	Coloured Dissolved Organic matter
CSIRO	Commonwealth Scientific and Industrial Research Organisation (Canberra, Australia)
DAIS	Digital Airborne Imaging Spectrometer
DLR	Deutsches Luft- und Raumfahrtzentrum (Oberpfaffenhofen, Germany)
EPSA	Environmental Probe System A
FWHM	Full Width Half Maximum
GPS	Global Positioning System

GRG2	Generalised Reduced Gradient non linear optimisation technique (Microsoft Excel©)
GWA	Gemeentelijk Waterleidingbedrijf Amsterdam (City of Amsterdam drinking water company) currently WLB
ICAM	Integrating-Cavity Absorption Meter
LSQNONLIN	Least Squares Non-Linear optimisation technique (Matlab©)
PAR	Photosynthetically Available Radiation
PSICAM	Point-Source Integrating-Cavity Absorption Meter
PTFE	Polytetrafluorethylene
ROSIS	Reflective Optics System Imaging Spectrometer
RTE	Radiative Transfer Equation
WLB	Waterleidingbedrijf (City of Amsterdam drinking water company) formerly GWA

Yellow Matters – Improving the remote sensing of Coloured Dissolved Organic Matter in inland freshwaters

1. Introduction 7
  1.1 Scope of research 7
  1.2 The Vecht Wetlands study area 8
    1.2.1 Geographical location and general description 9
    1.2.2 Hydrology and ecology of the Vecht Wetlands 10
    1.2.3 Criteria for choosing the Vecht Wetlands as the study area 14
  1.3 The colour of water 14
  1.4 Improving the accuracy of optically retrieved Coloured Dissolved Organic Matter 17
  1.5 Research goals and questions 18
  1.6 Dissertation outline 18

Part A: Background on Coloured Dissolved Organic Matter 21

2. Coloured Dissolved Organic Matter in the Vecht Wetlands 23
  2.1 Introduction 23
  2.2 Organic Matter in natural waters 23
    2.2.1 Definitions of organic matter 23
    2.2.2 Estimation of DOM 24
  2.3 Characteristics of Coloured Dissolved Organic Matter 25
    2.3.1 CDOM and humic substances 25
    2.3.2 Biochemical pathways for the formation of CDOM 26
    2.3.3 Molecular structures of CDOM 27
    2.3.4 Optical differences between humic and fulvic acids 29
    2.3.5 Relationships between CDOM and DOC 31
  2.4 Sources and sinks of Coloured Dissolved Organic Matter 32
    2.4.1 Coloured Dissolved Organic Matter sources 32
    2.4.2 Coloured Dissolved Organic Matter sinks 36
  2.5 Dynamics of aquatic CDOM 37
    2.5.1 CDOM as a buffer 37
    2.5.2 Spatial distribution of CDOM 38
    2.5.3 Seasonal fluctuations of CDOM 40
  2.6 CDOM in the Vecht Wetlands 41
    2.6.1 Spatial variation of CDOM in the Vecht Wetlands 41
    2.6.2 Seasonal fluctuations of CDOM in the Vecht Wetlands 41
  2.7 Discussion and conclusions 43

Part B: Optical modelling theory 45

3. An introduction to remote sensing methodologies for water quality assessments 47
  3.1 Introduction to water quality retrieval algorithms types 47
    3.1.1 Empirical algorithms 48
    3.1.2 Analytical and Semi-analytical algorithms: underlying bio-optical models 49
  3.2 Analytical Algorithm development based on complex bio-optical models 50
    3.2.1 Semi-analytical algorithm development based on simplified bio-optical models. 51
    3.2.2 Essential algorithm choices for the present study 52
  3.3 Choice of the underlying optical model for this study 53

4. Theoretical aspects of analytical water quality modelling 55
  4.1 Introduction 55
  4.2 Principles of light and radiometry 57
    4.2.1 Light as electromagnetic energy 57
    4.2.2 The principles of radiometry 58

- 4.3 From analytical to Semi-analytical optical modelling 58
  - 4.3.1 The Radiative Transfer Equation 59
  - 4.3.2 Two-flow modelling 60
  - 4.3.3 A generic (semi-)analytical model for the subsurface irradiance reflectance 63
  - 4.3.4 The Gordon-Walker optical model 65
- 4.4 Parameterisation of the optical model 65
  - 4.4.1 Inherent Optical Properties 66
  - 4.4.2 Apparent Optical Properties 68
- 4.5 Inverse optical modelling methods 69
  - 4.5.1 Matrix Inversion Method 70
  - 4.5.2 Levenberg-Marquardt (LM) 71
- 4.6 Discussion and conclusions 71

5. Measurement of Inherent Optical Properties 73
- 5.1 Introduction 73
- 5.2 Optically active water constituents 73
- 5.3 The SIOP of natural water constituents required for optical modelling 75
  - 5.3.1 An SIOP model suitable for this study 75
  - 5.3.2 Pure water absorption and scattering 76
  - 5.3.3 Coloured Dissolved Organic Matter absorption and concentration 77
  - 5.3.4 Seston scattering 78
  - 5.3.5 Tripton absorption 79
  - 5.3.6 Phytoplankton pigment absorption and concentration 80
- 5.4 Discussion and conclusions 82

6. The above water measurement of the subsurface irradiance reflectance 83
- 6.1 Introduction 83
- 6.2 Measuring the subsurface irradiance reflectance 84
  - 6.2.1 Correcting the remotely sensed signal 84
  - 6.2.2 Principles of above-water reflection measurements 85
- 6.3 Above-water reflection measurements using a hand-held spectrometer 89
  - 6.3.1 Measurement protocol 89
  - 6.3.2 Examples of measured radiance spectra 92
  - 6.3.3 The subsurface irradiance reflectance 95
- 6.4 Discussion and conclusions 96

7. Sensitivity analysis of inversion of the bio-optical model using a simulated dataset 97
- 7.1 Introduction 97
- 7.2 Inherent errors of parameters 98
- 7.3 Examples of forward and inverse modelling 99
- 7.4 The sensitivity of the Gordon-Walker model and its parameterisation 100
  - 7.4.1 Description of the simulated dataset using random concentrations 101
  - 7.4.2 Concentration distribution characteristics 101
  - 7.4.3 Construction of the simulated dataset 103
  - 7.4.4 Inversion techniques 103
  - 7.4.5 Measured reflectance sensitivity analysis 105
  - 7.4.6 SIOP sensitivity analysis 110
- 7.5 Discussion and conclusions 112

Part C: Improving CDOM retrieval accuracy analyses 115

8. Improving retrieved CDOM concentrations by state-of-art inversion of quality controlled measurement data 117
  8.1 Introduction 117
  8.2 Discussion of and selection of suitable measurement stations 117
    8.2.1 Comparison of measured to literature concentration ranges 118
    8.2.2 Comparison of measured SIOP to literature SIOP ranges 118
  8.3 Forward modelling based on all-observed parameters per station in order to optimise B per station: analysis of the similarity between observed and modelled $R(0-)$ per station 119
    8.3.1 The stray light effect in $R(0-)$ measurements 119
    8.3.2 Optimisation of B per station from selected observations 120
    8.3.3 Results of the forward modelling using optimized B-values: comparison between measured and modelled $R(0-)$. 122
    8.3.4 Selection of sample locations based on normalised χ^2 differences between measured and forward modelled $R(0-)$ spectra 128
    8.3.5 CDOM masking by high total chlorophyll concentrations 130
    8.3.6 Summary of data selection results 130
  8.4 Construction of an median SIOP set from selected stations to be used for inversion 130
  8.5 Retrieved CDOM concentrations from measured reflectance spectra 133
    8.5.1 Retrieved CDOM concentrations using measured spectra and the per-sample SIOP sets 133
    8.5.2 Retrieved CDOM concentrations using measured spectra and the median SIOP set 136
  8.6 CDOM retrieval discussion and conclusions 139

9. Improving CDOM absorption measurements by using a Point-Source Integrating-Cavity Absorption Meter 143
  9.1 Introduction 143
  9.2 PSICAM Theory 146
    9.2.1 PSICAM concept and specifications 146
    9.2.2 Absorption measurements: the cuvette method and the PSICAM method 149
  9.3 Calibration of the PSICAM 152
    9.3.1 Introduction 152
    9.3.2 The calibration reference absorption measurements 156
    9.3.3 Results of the PSICAM calibration of all four methods 162
    9.3.4 Selection of the best PSICAM calibration method 166
    9.3.5 Calibration discussion and conclusion 169
  9.4 Case study: PSICAM and cuvette measurements 171
    9.4.1 Introduction 171
    9.4.2 Data collection 172
    9.4.3 Results 173
    9.4.4 Case study discussion and conclusions 178
  9.5 CDOM retrieval improvement by using PSICAM instead of cuvette reference measurements 179
  9.6 PSICAM Discussion and conclusions 182
    9.6.1 Applicability of the PSICAM 182
    9.6.2 PSICAM recommendations 182
    9.6.3 Conclusions 184

10. Improving CDOM concentration retrieval by using two-component CDOM absorption spectrum modelling 187
  10.1 Introduction 187

- 10.2 Theory of CDOM absorption modelling 188
  - 10.2.1 Single component CDOM absorption models 190
  - 10.2.2 Correcting for baseline shifts: the offset 191
  - 10.2.3 Proposed two-component CDOM absorption model for this study 193
- 10.3 Linear and non-linear CDOM decomposition techniques 194
  - 10.3.1 Linear least squares regression and its end-member slopes 194
  - 10.3.2 Non-linear least squares optimisation 195
- 10.4 Case study: Decomposing measured CDOM absorption spectra of inland waters 196
  - 10.4.1 Introduction 196
  - 10.4.2 Methods 197
  - 10.4.3 Results 198
  - 10.4.4 Case study discussion and conclusions 201
- 10.5 Improvement of CDOM retrieval by using the two-component model for the normalised CDOM absorption spectrum SIOP 202
- 10.6 Two component CDOM modelling discussion and conclusion 204

Part D Synthesis 207

11. Synthesis 209
- 11.1 Summary and conclusions 209
  - 11.1.1 Part A: Background on Coloured Dissolved Organic Matter 209
  - 11.1.2 Part B: Optical modelling theory 210
  - 11.1.3 Part C: Improving CDOM retrieval accuracy analyses 211
- 11.2 Recommendations 214
  - 11.2.1 Recommendations for optical model development 214
  - 11.2.2 Recommendations for Specific Inherent Optical Property measurements 214
  - 11.2.3 Recommendations for Apparent Optical Property measurements 215
- 11.3 Outlook to the future 216
  - 11.3.1 Retrieving CDOM from remote sensing images 216
  - 11.3.2 PSICAM total absorption 224
  - 11.3.3 Water quality information provided by humic and fulvic acid absorption data 224

12. References 227

Appendix I: Map of the sample locations 241

Appendix II: Description of the field campaigns 242

Appendix III: Measurement protocols 245

Samenvatting 251

Acknowledgements 256

Curriculum Vitae Marnix L. Laanen 257

1. Introduction

1.1 Scope of research

The amount and type of dissolved organic matter (DOM) that is present in natural waters is regarded as an important measure of physico-chemical water quality. This DOM has been identified as a source of organic pollution, as an energy source for microbe-based aquatic food webs, as a factor in the cycling of trace elements and also as a factor in the biological activity of phytoplankton and bacteria (Imai, Fukushima, Matsushige, and Kim 2001). Because of its large organic complexes DOM usually acts as a buffer, thereby regulating the phyto- and zooplankton ecosystem and immobilising xenobiotic compounds such as heavy metals (Klavins and Apsite 2002; Kramer, Jak, Stroomberg, Hooftman, and Mayer 2002). By binding contaminants, their bioavailability is reduced (Chin 2002). Being the most important biochemical buffer, DOM can interact with some 50 different elements. At the same time, the oceanic DOM pool is identified as a major reservoir of organic carbon for the global carbon cycle (Aiken, McKnight, Wershaw, and MacCarthy 1985). The latter has resulted in a surge in oceanic DOM research in the past decade, aiming to provide the data required for completing climate models (Hansell and Carlson 2002).

As DOM cannot be measured directly, the determination of the dissolved organic carbon (DOC) concentration is therefore included in many Dutch and international water monitoring programmes (CIW 2001; Anonymus 2000). DOC measurements involve point sampling and laboratory analysis. The coloured fraction of DOM, called Coloured Dissolved Organic Matter (CDOM), is proposed as an alternative proxy for DOM (Steinberg 2003). It has been postulated that CDOM may be accurately determined from remotely sensed data. In that case it would be more cost-effective than traditional in-situ methods in most cases (Hansell and Carlson 2002) and the remote sensing method would, in addition, provide a wealth of spatial and temporal information.

The use of remote sensing data for water quality assessment, originally for oceanic waters, dates back to the late 1970s, when the first capable multispectral satellites were launched. The proof-of-concept was the Coastal Zone Colour Scanner (CZCS, 1978-1986), which was built specifically to determine the feasibility of remote sensing to monitor oceanic biological productivity and optical seawater clarity. Despite its name, the CZCS was not suited for near-shore coastal waters due to the relatively low spatial resolution (1 km^2 pixel size) of the instrument and near-shore atmospheric correction problems. During the project, optical remote sensing quickly proved to be a feasible technique for obtaining information on phytoplankton concentrations (Total Chlorophyll or TCHL) in oceanic waters – and in effect the only alternative when regional and global patterns are under study, due to the sheer size of the oceans.

Over the last 15 years, as instrument capabilities gradually allowed, research has increasingly focussed on optically complex water systems, such as coastal and inland waters. In these shallow waters, the water colour as observed by the remote sensing instrument is not dominated by the phytoplankton but also influenced by the suspended sediments (Total Suspended Matter or TSM), CDOM, the water bottom (when visible), water plants and by stratification of the water column. Dekker *et al.* give a good overview of coastal and inland water remote sensing in their book chapter (Dekker, Brando, Anstee, Pinnel, Kutser, Hoogenboom, Peters, Pasterkamp, Vos, Olbert, and Malthus 2001). Other literature on this subject includes the dissertations by (Dekker 1993; Dekker and Peters 1993; Hakvoort 1994; Krijgsman 1994) and the book by (Kirk 1994a).

As knowledge about the optical characteristics of TCHL and TSM has accumulated to a satisfactory level the attention now gradually shifts to CDOM, which was previously ignored as a parameter. An issue here is that the influence of CDOM is mainly in the UV and blue region where the signal to noise ratio of most instruments is weak due to atmospheric effects. Sathyendranath *et al.* found that a three-component model based on TCHL, TSM and CDOM was required to successfully simulate ocean colour (Sathyendranath, Prieur, and Morel 1989). Until today, this three-component model is applied in most optical modelling studies. In inland waters, where CDOM concentrations are much more variable than in oceanic waters, the three-component model improves the quality of the modelling results. This is because TCHL, TSM and CDOM are related in the optical model, so it is expected that an improvement in the way CDOM is parameterised in the model will also result in better TCHL ad TSM retrieval accuracies (as also suggested e.g. by (Darecki and Stramski 2004)).

The present combinations of sensors, models and parameterisations have not been successful to retrieve CDOM concentrations in inland waters in other than in isolated cases (Dekker, Brando, Anstee, Pinnel, Kutser, Hoogenboom, Peters, Pasterkamp, Vos, Olbert, and Malthus 2001; Peters, Dekker, and Keller 1998; Dekker, Moen, Kootwijk, van Rossum, Hoogenboom, Belfroid, and Claassen 1999), indicating the need for research to determine under which conditions CDOM can be retrieved from remote sensing observations.

Only a handful of studies have been found that use the semi-analytical optical modelling technique to retrieve water quality parameters from remote sensing data. Studies that focus on inland water or those include algorithms to retrieve CDOM are even scarcer. The frequent use of simulated datasets in literature also masks information on true retrieval accuracies.

In order to make a relevant contribution to this field this study will attempt to use semi-analytical optical models to their full potential by improving the parameterisation and calibration for CDOM and to analyse the inverse performance in the simultaneous retrieval of TCHL, TSM and CDOM concentrations focussing on Dutch shallow eutrophic inland waters. Special attention will be given to the determination of the normalised CDOM absorption.

As mentioned above, remote sensing can provide spatial information, which is a considerable advantage over *in situ* sampling. Almost all spaceborne and airborne instruments are imaging spectrometers. The original research methodology also called for the use of remote sensing images. Because the spatial resolution of hyperspectral satellite imagery was too low for the Vecht Wetland study area, the focus was on airborne imagery. Several (experimental) airborne remote sensing images were acquired during this research but none of the resulting images was of sufficient quality to successfully retrieve CDOM. This was due to a combination of limited infrastructure, operational restrictions and cloudy weather conditions, and experience showed that these problems were more the rule rather than the exception. As a consequence only remote sensing data collected with a hand held spectrophotometer was used for the analyses in this research.

1.2 The Vecht Wetlands study area

In this section first the general location of the study area and the investigated lakes will be given. Subsequently the hydrological and ecological characteristics of the area will be described leading to arguments and criteria why this area is suitable as study area for the present study.

1.2.1 Geographical location and general description

The Vecht Wetlands are located in the heart of the Netherlands, in the provinces of Utrecht and Noord-Holland (figure 1.1). It is a wetland region, comprised of a number of lakes, the River Vecht, the Amsterdam-Rijnkanaal and some reclaimed polders that are protected by dykes.

The Amsterdam-Rijnkanaal is the Western border of the Vecht Area, a 60 km long and 100 m wide canal connecting the River Rhine with the city of Amsterdam. The Eastern border of the Vecht area is formed by the Utrechtse Heuvelrug, a large body of sand stretching from the IJsselmeer in the North to the river Waal in the South. Formed in the Saalien ice age, the Utrechtse Heuvelrug is the main supplier of groundwater to the Vecht Wetlands as it lies several meters above mean sea level (and the Vecht Wetlands).

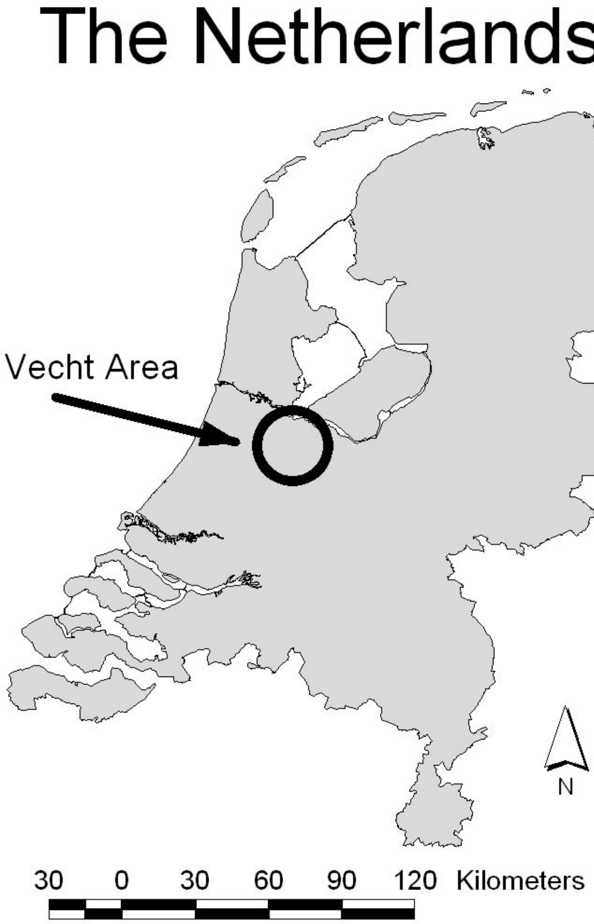

Figure 1.1: Map of the Netherlands showing the Vecht Area (© Topografische Dienst, Emmen)

To the North lies the IJmeer while the city of Utrecht and its surrounding villages form the Southern border of the Vecht Area. The River Vecht, once a branch of the Rhine, flows from the South of the city of Utrecht to the IJmeer, and is connected to the Amsterdam-Rijnkanaal at several locations.

In the Vecht wetlands area 18 water bodies were identified for this study; their location is indicated on figure 1.2. They are mostly lakes, with the exception of two canals and the river Vecht. Since the environmental conditions of the water bodies in the Vecht Area wetlands vary widely, a broad range in water types and water quality can be found (with for instance Secchi disk depths ranging from 40 cm to about 5 meters). Here we find Lakes with almost any combination from shallow to deep, oligotrophic to hypertrophic and disturbed to relatively natural.

The shallow lakes have a bottom of peaty soil while the deeper ones are situated on top of Pleistocene sand. All lakes, except the Naardermeer, are artificial, being the result of peat mining. More information on the process and results of peat mining can be found in e.g. van Wirdum (Wirdum 1993) or Gulati *et al.* (Gulati, van Liere, and Siewertsen 1991). Some original water bodies have been reclaimed as polders by pumping them dry (e.g. the round-shaped Bethunepolder in the middle of the Vecht Wetlands). More recently sand excavation led to the formation of the deeper lakes (10-20 m deep). The Naardermeer is, despite two reclamation efforts that left their marks, a natural lake created by a flooding of the IJsselmeer at the time the latter still had an open connection to the North Sea.

The Vecht Wetlands are used for recreational purposes (boating, sailing and swimming); some parts are nature reserves (e.g. the Naardermeer and the Kortenhoefsche Plassen). The city of Amsterdam also operates a drinking water treatment facility and storage basin in the area. In the Vecht Wetlands in general, but especially in the largest polder (the Bethunepolder), dairy farms are the dominant type of farming. Crop farming is not feasible in the polders as the groundwater level is just centimetres below the ground level. For most water bodies in the Vecht Wetlands recreational, nature and other functions are combined. Together with the hydrological demands of the surrounding meadows, friction between the different stakeholders often occurs (Bergh, Barendregt, Gilbert, Herwijnen, Horssen, Kandelaars, Lorenz, and Rabeling 1999).

1.2.2 Hydrology and ecology of the Vecht Wetlands

The hydrology, ecology and backgrounds and results of lake restoration projects of the region are discussed at length in for instance (Gulati, van Liere, and Siewertsen 1991; Liere and Gulati 1991; Gulati and Donk 2002). Most hydrological and ecological data available of the area was collected during the ten-year study carried out by the multi-disciplinary WQL working group (Water Quality research Loosdrecht lakes) in the 1980’s (Breebaart, Ebert, and van Liere 1989). Since then, no large-scale research has been carried out in the area because of the vast resources required. This absence of recent measurements can serve as a drive to advocate the use of remote sensing. Relatively inexpensive remote sensing images could for instance be acquired each year, providing valuable time series.

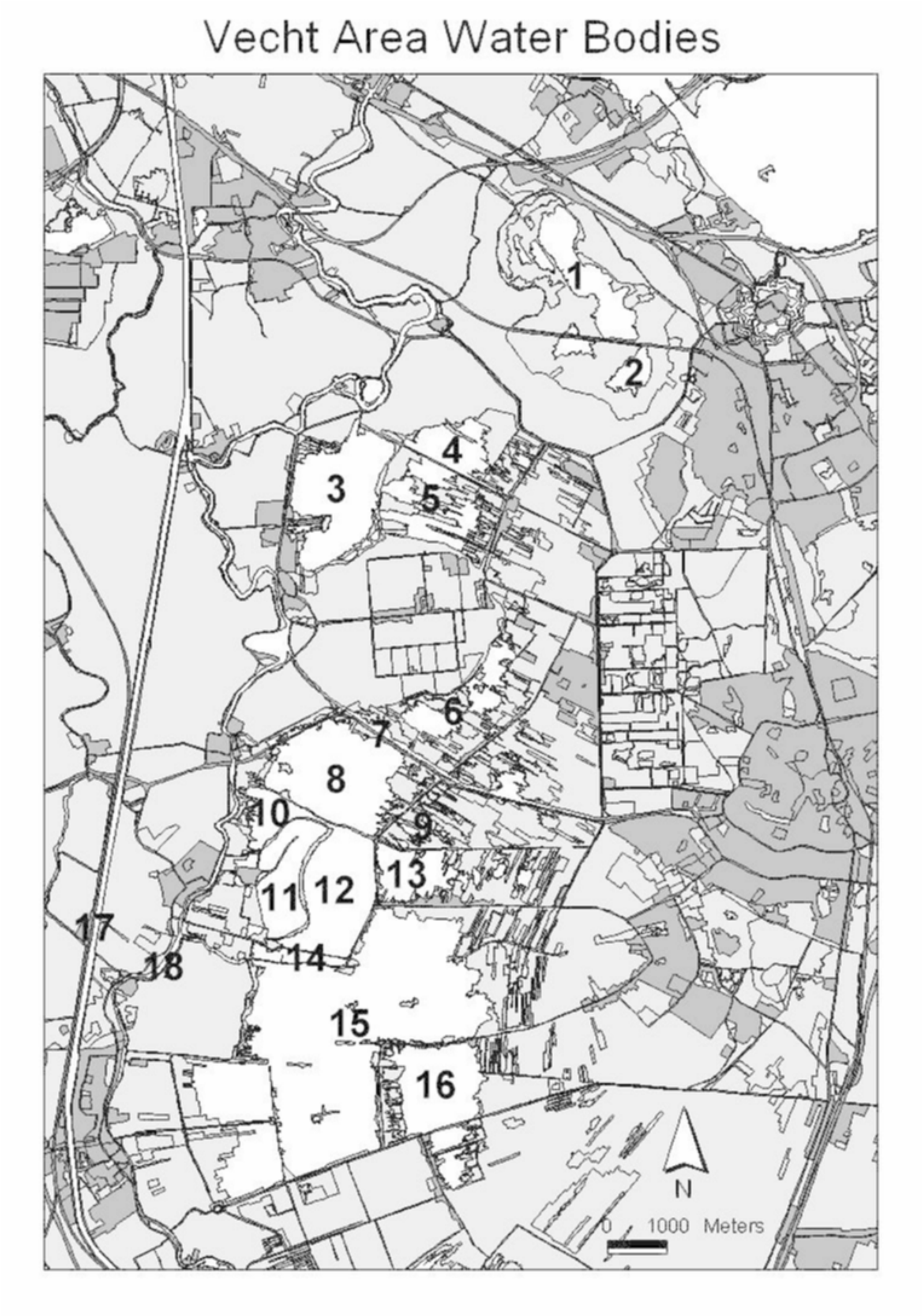

Figure 1.2: Map of the Vecht Wetlands water bodies (numbers correspond to lake names in table 1.1) (© Topografische Dienst, Emmen)

Because of constant seepage into the adjacent polders (which are up to several meters below mean sea level), most of the Vecht Wetlands lakes need an extra input of water. Although water can be pumped back from the polders, this is not enough to maintain the desired water level. Furthermore, this discharge water is often of poor ecological quality and will cause severe eutrophication when returned into the lakes. For the majority of the lakes water was taken in first from the river Vecht and later from the Amsterdam-Rijnkanaal canal (through a pipeline system).

Due to the influx of large amounts of fertilizer and sewage, the river water was polluted with high concentrations of nutrients, adding to the eutrophication of the lakes. Eutrophication also occurs through mineralisation of peat layers due to the lowering of the groundwater table. A future eutrophication hazard is the nitrate-contaminated groundwater travelling from the Utrechtse Heuvelrug (Liere and Gulati 1991).

At first eutrophication was countered by decreasing the anthropogenous nutrient influx. This was done by connecting every household in the vicinity to the sewage system, followed by more strict rules for manuring and finally by placing a number of dephosphorising plants. On a more local scale by dredging and creating silt sink pits the turbidity accompanying eutrophication was also treated, for instance in the Loosdrecht lakes (Gulati, van Liere, and Siewertsen 1991). Turbidity can be high in the Vecht Wetland lakes as a result of the combination shallow water, peaty substrate and wave action. In some cases successful biomanipulation experiments have been undertaken (Terra Nova, pers. comm. G. ter Heerdt Msc.).

The present water management policy is aimed at reducing the intake of allochthonous water by raising the water level in the adjacent polders and thus decreasing seepage from the lakes. The lake sediments however are still rich in nutrients and their release alone can maintain eutrophic conditions in many lakes for years to come (Søndergaard, Jensen, and Jeppesen 1999; van der Molen and Boers 1994).

Oligo- to mesotrophic water quality is found in the Spiegelplas, which is not connected to the Vecht, Lake Stichts Ankeveen, which is replenished mainly by groundwater flow and water from the Spiegelplas, Lake ‘t Hol and the Naardermeer, which receives purified water since a number of years. The water treatment facility of the city of Amsterdam operates a drinking water reservoir, the Lake Waterleidingplas. For obvious reasons only pre-treated water is let in into this hydrologically isolated lake resulting in oligo- to mesotrophic water quality.

Table 1.1 lists the names of the Vecht Wetlands water bodies and the reference numbers used in figure 1.2, the average depth, the average Secchi Disk Depth and the trophic state. As a consequence of the lack of recent publications, the sources used in table 1.1 are over ten years old. In terms of trophic state however, no significant changes have taken place since.

Table 1.1 Water Bodies in the Vecht Wetlands with average bottom depth, Secchi Disk Depth and trophic state indication (from Dekker, 1993 and Liere and Gulati, 1991). Data marked with † originates from Dekker, 1993.

Lake name	Reference number	Average bottom depth	Secchi Disk Depth (min – max [cm])	Trophic state
North Naardermeer	1	Shallow (<2.5 m)	80 – 120†	oligo- to mesotrophic
South Naardermeer	2	shallow	25 – 30†	mesotrophic
Spiegelplas	3	deep (4 – 20 m)	320	oligotrophic
Hollands Ankeveen	4	shallow	40	meso-eutrophic
Stichts Ankeveen	5	shallow	140	oligo- to mesotrophic
Kortenhoefse Plassen	6	shallow	40	Meso-eutrophic
Hilversums Kanaal	7	shallow	60	eutrophic
Wijde Blik	8	very deep (20 - 40 m)	230	oligo- to mesotrophic
‘t Hol	9	shallow	150†	mesotrophic†
Vuntus	10	shallow	35 – 40†	hypertrophic†
Terra Nova	11	shallow	n/a	n/a
Waterleidingplas	12	deep	360 - 400	oligotrophic
Loenderveen	13	shallow	70	n/a
Nieuwe Polder	14	shallow	60	n/a
Loosdrecht	15	shallow	40	n/a
Breukelerveen	16	shallow	30 – 40†	hypertrophic†
Amsterdam-Rijnkanaal	17	shallow	60 – 90†	eutrophic†
Vecht River	18	shallow	110	eutrophic

According to Dekker (Dekker 1993), the dominant algae species in the Vecht Wetlands are cryptophyceae flagellates in the shallow oligo-mesotrophic waters and the filamentous cyanobacteria *Oscillatoria spp* and *Prochlorothrix hollandica* in the shallow eutrophic lakes. In the deep lakes the most abundant species are cryptophyceae in the Waterleidingplas, diatoms in the Spiegelplas and the cyanobacteria *Microcystis* in Wijde Blik. Diatoms are most abundant in the Amsterdam-Rijnkanaal and the Vecht River. No major change in algal species abundance has been reported since.

1.2.3 Criteria for choosing the Vecht Wetlands as the study area

The Vecht Wetlands were selected as the study area for a variety of reasons:

- ➔ The different water bodies of the Vecht area display a broad range of water qualities (from oligotrophic and clear to hypertrophic and turbid). The inter-lake variability in water quality parameters is one to two orders of magnitude greater than the intra-lake variability. Because the Vecht Wetland water bodies are relatively small, the applicability of the remote sensing algorithm can be determined for various water qualities simultaneously (i.e., within a single image).
- ➔ More specifically, there is also a broad range in types and concentrations of organic matter present in the Vecht Wetlands.
- ➔ Because of its variability, the Vecht area already has already been the subject of a great number of studies, both involving remote sensing (for instance Dekker and Seyhan 1988; Dekker, Malthus, Peters, and Seyhan 1990; Dekker 1993 and Dekker, Zamurovic-Nenad, Hoogenboom, and Peters 1996), ecology (Malthus, Best, and Dekker 1990; Gulati, van Liere, and Siewertsen 1991; van Liere, Roijackers, and Verstraelen 1989) and even an integrated analysis study combining ecology and economy (Bergh, Barendregt, Gilbert, Herwijnen, Horssen, Kandelaars, Lorenz, and Rabeling 1999). A head start can be made in new research by using the results and findings of these earlier studies. For instance, Dekker already demonstrated that the semi-analytical optical modelling approach is feasible in the Vecht Wetlands (Dekker and Peters 1993).
- ➔ This research is part of the research programme "Wetlands in the Randstad" initiated by the Vrije Universiteit Amsterdam. Within this programme, the interactions between natural and societal processes are investigated in the Vecht Wetlands. Key issue in the "Wetlands in the Randstad" research is a proposed raise in the water level in the Vecht Wetlands. This raise is deemed necessary by the water management and nature preservation organisations, but opposed by local residents and farmers. The determination of water quality was deemed necessary for the "Wetlands in the Randstad" project.

1.3 The colour of water

In this section first an introduction is given on the relationship between the water colour ands water composition. An example is given of some characteristic spectra as measured in the study area illustrating the underlying concept.

The colour of natural surface water is determined by the spectral characteristics and the concentrations of coloured compounds inside, either in solution or in suspension. Qualitative and quantitative relationships between the water colour and the concentrations of coloured compounds are expressed in bio-optical simulation models and inverse relationships (usually called algorithms). As mentioned earlier, three such water compounds usually dominate the water colour: Total Chlorophyll (TCHL), Total Suspended Matter (TSM) and Coloured Dissolved Organic Matter (CDOM). Spectral observations also allow the determination of the vertical extinction coefficient K_D, a measure of the transparency of the water. The K_D is related to the Secchi Disk depth SD, a simple transparency measurement performed routinely by water managers all over the world as a quick indicator of general water quality.

In order to illustrate the concept of water remote sensing and bio-optical modelling a number of example spectra is given in this section. Using Bio-Opti, a tool developed by E. Hoogenboom at the IVM, a number of spectra is simulated.

First, the effect of the individual water quality parameters is demonstrated, starting with TCHL. The effect of the concentration of chlorophyll on the reflectance spectrum is shown in figure 1.3A. At the lowest concentration (top line) of the series, the reflectance peaks at over 5%. Because of the light absorbing properties of chlorophyll, the reflectance peak decreases with increasing chlorophyll concentration. Another notable feature is the ratio between the dip at 676 nm (chlorophyll pigment absorption maximum) and the peak at 704 nm. At low TCHL concentrations the dip and peak are almost at the same level, but the 676 nm dip lowers with increasing TCHL concentrations.

The effect of TSM on the subsurface reflectance is demonstrated in figure 1.3B. The increase in TSM concentration results in an increase in reflectance at all wavelengths, which is caused by the fact that TSM particles are mostly scattering rather than an absorbing light.

Finally, an increase in the CDOM concentration has an effect mostly on the reflectance values in the blue and green light region of the spectrum (figure 1.3C). With increasing CDOM concentrations, the peak at 550 nm also increases. Beyond 650 nm the influence of CDOM decreases but remains significant as will be demonstrated in this research.

In order to discriminate between TCHL, TSM and CDOM, information is thus required of the total reflection in the green wavelength area (550-600 nm), of the TCHL absorption peak around 676 nm, of the reflection paek at 706 nm where only TSM is opticvally active and in the blue area (400-450 nm) where only CDOM is optically active.

Now that the individual effects of TCHL, TSM and CDOM have been shown (figure 1.3), also the combined effect of all three parameters together will be demonstrated. For instance, it has been found that at high concentrations chlorophyll is completely dominating the spectrum, inhibiting a successful retrieval of the CDOM concentration. The influence of the increasing (doubling) CDOM concentrations at high TCHL concentrations (100 µg l^{-1}) on the resulting spectra in figure 1.4 is small (<0.5%). This illustrates the problems at accurately retrieving CDOM concentrations from remote sensing spectra.

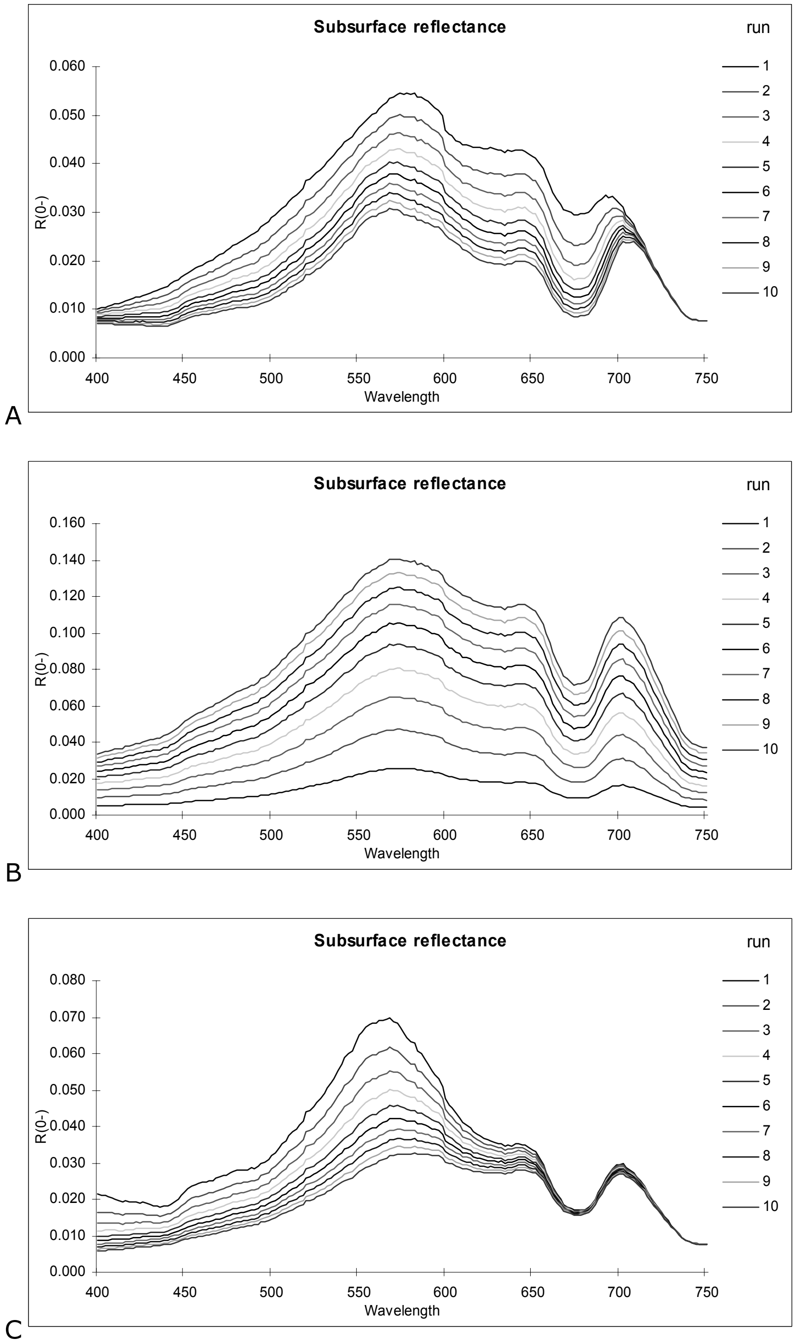

Figure 1.3 Simulated subsurface reflectance showing the effect of increasing concentrations (using Bio-Opti): A) increasing TCHL (10 – 100 µg l^{-1}) at fixed TSM (9 mg l^{-1}) and CDOM (2,4 m^{-1}) concentrations (top line is series 1) B) increasing TSM (5 – 50 mg l^{-1}) at fixed TCHL (40 µg l^{-1}) and CDOM (2,4 m^{-1}) concentrations (top line is series 10) and C) increasing CDOM (0.5 – 4 m^{-1}) at fixed TSM (9 mg l^{-1}) and TCHL (40 µg l^{-1}) concentrations (top line is series 1)

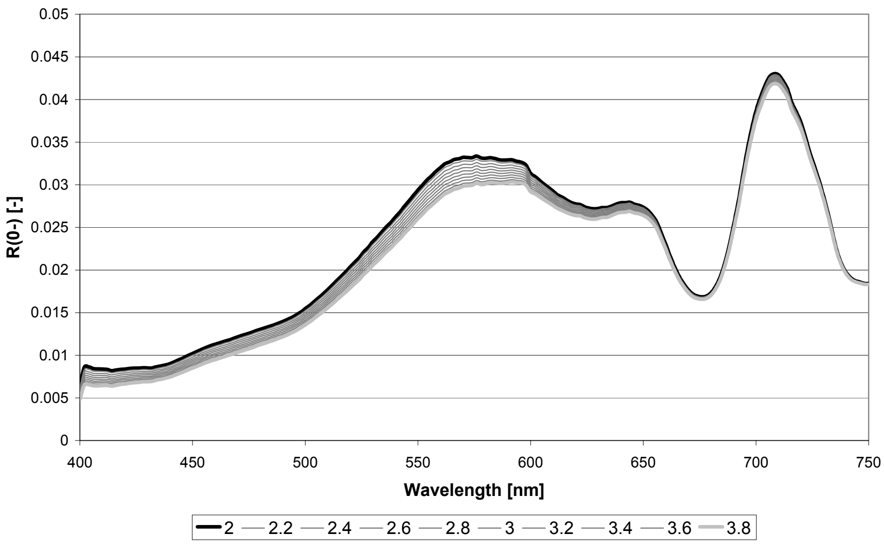

Figure 1.4: Forward simulated subsurface reflectance spectra showing the effect of an increasing CDOM concentration (10 series from 2.0 to 3. 8 m^{-1}) with a constant TCHL concentration 100 μg l^{-1} and TSM concentration of 24 mg l^{-1}.

1.4 Improving the accuracy of optically retrieved Coloured Dissolved Organic Matter

In order to achieve a satisfactory degree of CDOM concentration retrieval accuracy, three possible improvements are pursued in this research. Two of these are designed to improve the parameterisation of the optical model. Because optical properties of the water quality compounds are used in the optical model, the accuracy of these properties is crucial for the model performance. In this thesis therefore enhancements of the laboratory protocols for CDOM concentration measurements (e.g. the REVAMP (Tilstone, Moore, Sørensen, Doerffer, Pasterkamp, and Jørgensen 2002) and SEAWifs (Mueller and Austin 2000) protocols) are investigated. The third CDOM retrieval accuracy improvement pursued is the use of promising recently published algorithms. The details of the possible improvements are given below:

- ➔ More accurate laboratory CDOM concentration measurements. Vos *et al.* (Vos, Peters, and Rijkeboer 1999) found that the measured CDOM absorptions used as input for the bio-optical modelling were often a source of error, indicating that model accuracy could be increased by improving lab and in situ measurement techniques. For this research an alternative device for absorption measurements, a so-called Point-Source Integrating-Cavity Absorption Meter (PSICAM), has been studied (Kirk 1995; Kirk 1997; Leathers, Downes, and Davis 2000; Lerebourg, Pilgrim, Ludbrook, and Neal 2003; Dekker, Brando, Daniel, Anstee, and Clementson 2002).
- ➔ The main advantage of using a PSICAM is that it is insensitive to scattering effects in the sample. These scattering effects do occur in a cuvette, and most protocols therefore call for a removal of a size group of particles in order to minimise the effect, introducing a gap in the total absorption coefficient. The PSICAM measurement technique was made operational and its performance compared to a classic bench spectrometer, again based on field measurements.
- ➔ More accurate input CDOM absorption spectra (optical properties). Measured CDOM absorption spectra need to be corrected (for systematic errors and

random noise) by means of modelling (Green and Blough 1994;Stedmon, Markager, and Kaas 2000). Currently CDOM absorption spectra are fitted to a single exponential function, but it has been argued that a two-component exponential function may provide better results (Carder, Steward, Harvey, and Ortner 1989). This is attributed to the fact that CDOM in fact comprises of two groups of compounds, humic and fulvic acids, with differing properties. The two-component exponential modelling approach was first pursued by Carder (Carder, Steward, Harvey, and Ortner 1989) and also by Krijgsman (Krijgsman 1994).

➔ High performance recently developed algorithms such as Matrix Inversion Methods and Levenberg-Marquardt optimisation. Also the performance of Ratio Levenberg-Marquardt optimisation will be tested, comparable to Peters *et al.* (Peters, Pasterkamp, and van der Woerd 2002).

In contrast with many remote sensing studies, actual measured data rather than simulated data will be used to validate the analyses performed in this research. The accuracies of retrieved concentrations (and the possible improvements thereof) thus demonstrate the real world performance of water quality remote sensing.

1.5 Research goals and questions

The goal of this research is to improve the accuracy of the concentration of coloured dissolved organic matter retrieved from remote sensing spectra in shallow eutrophic inland waters. This is pursued in three complementary ways: by deriving a more accurate CDOM algorithm using new techniques in optical modelling, by using a Point-Source Integrating-Cavity Absorption Meter (PSICAM) device for more accurate CDOM absorption measurements in the laboratory and by decomposing CDOM into its major groups of humic and fulvic acids and modelling the measured absorption spectra separately. In addition the specifications (spectral bands and sensitivity) required for a remote sensing instrument that can accurately detect CDOM concentrations are determined.

Based on the considerations in this chapter three specifically targeted research questions were formulated, namely:

1. Which forward and inverse semi-analytical optical modelling techniques lead to obtain a sufficiently accurate CDOM retrieval algorithm?
2. Is a Point-Source Integrating-Cavity Absorption Meter better suited to measure the absorption spectrum of CDOM of natural Dutch inland waters than a laboratory bench spectrophotometer?
3. Is the absorption spectrum of CDOM more accurately described by separating it into two spectra of its major groups humic and fulvic acid and modelling both groups separately prior to input in the optical model?

1.6 Dissertation outline

The remaining chapters of this dissertation can be grouped into four parts:

A.	Background on CDOM properties	(chapter 2)
B.	Optical modelling theory	(ch. 3 – 7)
C.	Improving CDOM retrieval accuracy analyses	(ch. 8 – 10)
D.	Synthesis, recommendations and outlook to the future	(ch. 11)

Part A: Background on CDOM properties

In order to gain insight in the subject compound of this research, CDOM, the molecular characteristics, sinks and sources and the role in the lake ecosystem of CDOM - wherever possible focussed on the Vecht Wetland research area - are explained in chapter 2, based on extensive literature study. While it is not strictly required to know why CDOM has certain properties when understanding the analyses in later chapters, the background provided by this chapter helps the reader to put CDOM in a broader perspective.

Part B: Optical modelling theory

The theoretical part comprises of chapters 3 - 7. This part is meant to provide a theoretical background for people outside the field of water remote sensing, again based on extensive literature study. First the choice for the analytical optical modelling approach for this study is explained in chapter 3. In chapter 4 the radiative transfer theory is discussed, describing the interaction between light and water. The semi-analytical optical model that is used in this research is also derived from the radiative transfer theory in chapter 4. The crucial parameterisation of the selected optical model is performed in chapters 5 and 6. The Specific Inherent Optical Properties (SIOP - optical characteristics of water constituents that are independent of the light field) are identified and discussed in chapter 5. In chapter 6 the Apparent Optical Properties (AOP) are derived from (corrected) above-water irradiance measurements. As a check on the model parameterisation and to identify possible areas of improvement with respect to CDOM retrieval, the sensitivity of the optical model to errors in the measured spectra and in the necessary SIOP dataset is determined in chapter 7.

Part C: Improving CDOM retrieval accuracy analyses

The research and analysis part is made up of the chapters 8 – 10. First the SIOP and AOP data collected at various sample locations in the study area for this research is described in chapter 8, where they are quality controlled prior to the construction of a median SIOP dataset that can be used for the optical model. With the parameterisation complete, the optical model is also applied in chapter 8. Here the water quality parameter concentration retrieval performance of three selected inversion methods is tested. Next, CDOM absorption coefficient measurements collected using a PSICAM and a cuvette system are compared in chapter 9, investigating the expected advantages of the PSICAM. In chapter 10 the improvement in CDOM absorption spectra measurements by using a two-component exponential absorption fit model instead of a single exponential model is investigated.

Part D: Synthesis, recommendations and outlook to the future

The synthesis of this research is given in chapter 11. The conclusions from the separate chapters are integrated here, leading to several recommendations for water quality retrieval of eutrophic inland waters using semi-analytical optical modelling, especially with respect to CDOM.

Part A: Background on Coloured Dissolved Organic Matter

2. Coloured Dissolved Organic Matter in the Vecht Wetlands

2.1 Introduction

Before commencing with the investigation of the proposed improvements for CDOM optical modelling, CDOM properties will be discussed in this chapter, which will help to understand the optical properties of CDOM, the relationships between CDOM and other water quality parameters and the spatial and temporal variation of CDOM that can be observed from remote sensing data.

The focus of this research is on CDOM in shallow eutrophic inland waters, the Dutch Vecht Wetlands in particular. As a consequence, the role of CDOM in the aquatic environment is discussed mainly from an inland water point of view, although also coastal water CDOM literature is cited due to the limited number of publications in this field. In this chapter an overview is given of the relevant inland water CDOM literature.

The basic framework of organic matter in natural freshwaters is outlined in the first section. The biochemical characteristics of CDOM and other types of organic matter are given in §2.3, with the emphasis on the molecular structure of CDOM. After all, it is the interaction of light and the organic molecules that is of interest in this research. The formation and degradation processes of DOM are treated in §2.4. The role of DOM in aquatic ecosystems and background knowledge of the spatial and temporal distribution of CDOM in inland and coastal waters is discussed in section 2.5. In §2.6 the focus is on the spatial and seasonal distribution of CDOM in the Vecht Wetlands research area. Finally a discussion and conclusions of this chapter is presented section 2.7.

2.2 Organic Matter in natural waters

2.2.1 Definitions of organic matter

Organic matter consists of any compound with a basis of carbon atoms. The only aquatic compounds that contain carbon atoms but that are not considered organic matter are carbonates (HCO_3^-, which is CO_2 dissolved in water) or cyanides (CN^- groups). Inorganic matter consists mostly of suspended matter (sand, silt and clay minerals). In some cases, such as deep oceanic waters, the aquatic environment is made up almost exclusively of organic matter in low absolute concentrations, while in other cases, for instance inside sediment plumes of discharging rivers into sea, the inorganic matter is dominant (possibly in very high absolute concentrations). In the Vecht Wetlands study area large absolute concentrations of both organic and inorganic matter are present but the organic matter is dominant.

Two main groups of aquatic organic matter are distinguished: particulate and dissolved organic matter. Dissolved Organic Matter (DOM) is operationally defined as the fraction which passes though a filter with a 0.45 μm pore size (Steinberg 2003) while the particulate organic matter remains on the same filter as residue. This operational definition of DOM is given in figure 2.1. Relatively large breakdown products of cell material make up Particulate Organic Matter (POM). POM is comprised of the organic part of tripton. The latter is sometimes misleadingly called detritus, as detritus in fact spans all breakdown products and not just the organic matter. The POM is discussed in the tripton analysis (see chapter 5 about the IOP of natural waters). The DOM and POM combined give the Total Organic Matter (TOM).

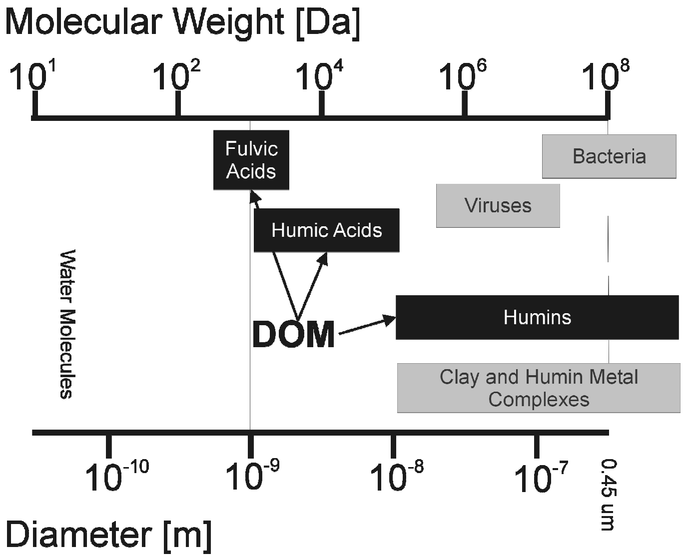

Figure 2.1: A graphical representation of DOM. The main components of DOM (shown in black) are Humic and Fulvic acids and Humin (after Steinberg 2003)

2.2.2 Estimation of DOM

The concentration of each type of organic matter is cumbersome to determine directly because it involves the determination of numerous different compounds. Instead, the dissolved organic carbon (DOC) is commonly used as a substitute value for DOM (Stumm and Morgan 1981; Hansell and Carlson 2002; Steinberg 2003). The organic matter incorporates the mass of all the atoms of the carbon complexes, whereas the organic carbon is defined as the mass of just the carbon atoms. The estimation of DOM from DOC is based on the finding that some 60% of DOM consists of carbon, resulting in a positive linear relationship between DOM and DOC. Relationships between DOC and other water quality variables are thus considered similar to those of DOM and other water quality variables.

The Total Organic Carbon TOC of a water sample is determined by the amount of carbon dioxide that is produced after combustion or strong oxidation (while removing inorganic carbonates) of a water sample. The DOC is determined in the same way as the TOC but the water sample is filtered first over a 0.45 µm filter. Similar to TOM, POM and DOM, the organic carbon is thus expressed as TOC, POC and DOC.

Another method to estimate the DOM concentration is based on a characteristic that is shared by the majority of the compounds that make up DOM: colour. Some 60-80% of freshwater DOM consists of coloured molecules (Steinberg 2003); this group is called Coloured Dissolved Organic Matter (CDOM). As with DOC, a positive linear relationship between DOM and CDOM is assumed. In this research concentration of CDOM will be determined by optical measurements, for instance with a laboratory spectrometer but also from remote sensing data. The characteristics of CDOM are discussed in the next sections.

2.3 Characteristics of Coloured Dissolved Organic Matter

2.3.1 CDOM and humic substances

The colour characteristic is reflected in the many names given to CDOM in literature, of which a number are shown in table 2.1. In this dissertation however the term CDOM is adopted, as it is the most commonly used name in recent inland water studies (Kirk 1994a, Stedmon, Markager, and Kaas 2000, Dekker, Brando, Anstee, Pinnel, Kutser, Hoogenboom, Peters, Pasterkamp, Vos, Olbert, and Malthus 2001).

Table 2.1: CDOM Synonyms and their usage

Name	Literature
Gelbstoff	Kalle 1966
Yellow substance	Carder, Steward, Harvey, and Ortner 1989, Lindell, Pierson, Premazzi, Zillioli, and et.al. 1999
Humic substances	De Haan, De Boer, Kramer, and Voerman 1982, Stumm and Morgan 1981, Pfeifer, Klaus, Hoffman, and Spiteller 2001, Lehtonen, Hänninen, and Ketola 2001
Gilvin	Kirk 1983
Aquatic Humus	Dekker 1993, Krijgsman 1994
Chromophoric Dissolved Organic Matter	Hoge, Vodacek, Swift, Yungel, and Blough 1995, Ferrari, Dowell, Grossi, and Targa 1996 Hansell and Carlson 2002

The term CDOM stems from remote sensing studies. In limnology and soil science the same chemicals in natural waters are commonly referred to as humic substances (HS). Humic substances are heterogeneous organic compounds that constitute the major organic matrix in surface water, soil and other environmental compartments. They are negatively charged and tend to bind to heavy metals and various organic compounds (Pfeifer, Klaus, Hoffman, and Spiteller 2001). The composition of humic substances is usually expressed in terms of its three major fractions (Aiken, McKnight, Wershaw, and MacCarthy 1985):

1. Humin: The fraction of humic substances that is not soluble in water at any pH value. Although insoluble it is still present in natural waters in suspension, so its absorption behaviour contributes to the tripton absorption spectrum. A brown to black colour of the filter residue for the total suspended matter measurements indicate a high humin concentration.
2. Humic acid: The fraction of humic substances that is not soluble in water under acid conditions (below pH 2), but becomes soluble at greater pH.
3. Fulvic acid: The fraction of humic substances that is soluble under all pH conditions.

All these three fractions share the characteristics of being heterogeneous biomolecules that are yellow to brown or black in colour and moderate to high molecular weight (see figure 2.2). Because humin is insoluble in water, it is not considered part of CDOM. CDOM thus is comprised of only two major fractions: humic and fulvic acids. Although the names humic and fulvic acids are considered obsolete and confusing or unsuited for aquatic or oceanic use by many, it was decided to continue using them in this dissertation to make this work compatible with the prior work of others.

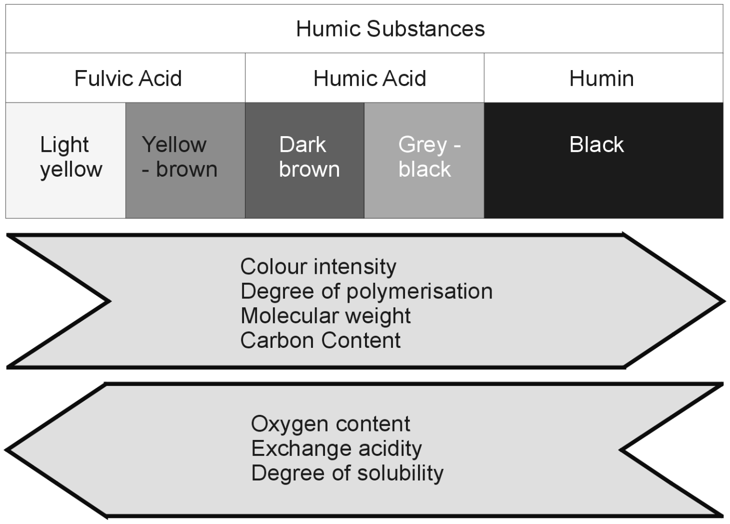

Figure 2.2: Colour and chemical characteristics of humic substances (after Stevenson 1982)

The spectral and other characteristics (shown in figure 2.2) of CDOM are determined by the molecular structures of humic and fulvic acids. The absorption spectrum of CDOM can be described by an exponentially decreasing function, with high absorption in the UV and blue wavelengths and almost no absorption in the red and infrared region (discussed in detail in chapter 10).

2.3.2 Biochemical pathways for the formation of CDOM

Direct or indirect processes of photosynthesis produce living organic matter (such as algae), while degradation processes result in non-living organic matter (such as DOM). The degradated plant matter which makes up CDOM mainly consists of (poly)phenols. Phenols are a class of weakly acidic organic compounds where the molecule contains one or more hydroxyl groups (OH group). Polyphenol compounds are capable of binding to proteins and to some complex carbohydrates (such as cellulose and starch). Lignins and tannins are the most common types of polyphenols. A lignin is a complex polymer that forms an extensive network within the cell walls of certain plants giving strength and rigidity to the cell wall. Tannins are a group of simple and complex phenol, polyphenol, and flavonoid compounds that can bind to starches. Produced by plants, tannins are generally protective substances found in the outer and inner tissues of cells. Tannins in general are relatively resistant to digestion or fermentation by bacteria or fungi. The biochemical range of other DOM components includes free amino acids, sugars, fatty acids (lipids), urea, hydrocarbons and vitamins (Stumm and Morgan 1981).

Traditionally two different pathways by which CDOM can form are discriminated: The degradative and the condensation polymerisation pathway (Steinberg 2003). In the degradative pathway CDOM is simply formed by the partial degradation of macromolecules. The condensation polymerisation pathway is more complex as it spans three different models for abiotic condensation processes: The polyphenol model, the melanoidin model and the polyunsaturated structure model.

With the degradative pathway the source of CDOM are plant polymers such as lignin. The lignin theory, popularised by Waksman (Waksman 1932), assumes that lignin is incompletely utilized by micro-organisms and the residual becomes part of the soil humic substances. The degradation of lignin includes the loss of methoxyl (OCH_3) groups, the generation of hydroxyphenols and oxidation of aliphatic side chains to form COOH groups. The modified material, together with amino acids formed by the breakdown of proteins, is subject to further unknown changes to yield first humic acids and then fulvic acids. The formation of CDOM by this pathway occurs primarily in vegetated catchments or in littoral zones with macrophytes. This kind of CDOM production is generally called autochthonous.

The most important model of the condensation polymerisation pathway, the polyphenol model by Flaig (Flaig 1968), involves the formation of quinones (a yellowish compound). In this case the lignin undergoes enzymatic conversion to quinones during microbiological attack, which in turn polymerise in the presence or absence of amino compounds to form humic macromolecules. Next to lignin, possible sources of phenols for humus synthesis include micro-organisms, uncombined phenols in plants and tannins. Little is known of the formation of humic substances from tannins. Flaig's concept of humus formation from lignin is (Flaig 1968):

1. Lignin, freed of its linkage with cellulose during decomposition of plant residues, is subjected to oxidative splitting with the formation of primary structural units (derivatives of phenylpropane).
2. The side-chains of the lignin-building units are oxidized, demethylation occurs, and the resulting polyphenols are converted to quinones by polyphenoloxidase enzymes.
3. Quinones arising from the lignin (and from other sources) react with N-containing compounds to form dark-coloured polymers (humic substances).

In the melanoidin model CDOM is formed from sugars and amino acids, while in the polyunsaturated structure model CDOM is formed from polyunsaturated compounds such as fatty acids and carotenoids. The melanoidin and polyunsaturated structure model however are still subject to discussion and will not be explained further. The condensation polymerisation pathway is generally considered autochthonous, as it is observed in extreme lakes and catchments without higher plant cover (i.e. a lignin-poor environment) (Steinberg 2003).

CDOM formation by both pathways will occur in most freshwaters. Depending on factors such as the ratio of the lake surface area to the catchment area, the type and amount of vegetation and human pressure present, the primary production of the lake and hydrological inputs either the degradative (allochthonous) or condensation polymerisation pathway (autochthonous) is dominant. For the Vecht Wetlands, with relatively small and shallow lakes, it is likely that the allochthonous input (peat resuspension and surface runoff) exceeds the autochthonous CDOM production (algae).

2.3.3 Molecular structures of CDOM

The molecular structures of CDOM range from simple, with a basis of just a few carbon atoms, to extremely complex, with 100,000s of carbon atoms and functional groups (Stumm and Morgan 1981). As the DOM molecules are also constantly interacting (on the scale of days) there is also no 'standard' molecular structure. The organic acidic structural elements of DOM molecules are predominantly hydroxyl (-OH) and carboxyl groups (-COOH), added to large biomolecules. Other important functional groups are composed of hydroxyl (-OH), amines (-NH^2), esters, and ethers (Kracht 2001). Buscail *et al.* made an analysis of the average relative abundance of elements found in DOM samples collected at the Mediterranean coast between Perpignan and Marseille (France): 55% carbon (C), 34% oxygen (O), 6% hydrogen (H), 4% nitrogen (N) and 1% sulphur (S) (Buscail, Pocklington, and Germain 1995).

Two proposed general structures of the main groups of CDOM, humic and fulvic acids, are given in figure 2.3 (Stevenson 1982) and figure 2.4 (McKnight and Aiken 1998), both of which adequately represent the heterogeneous composition and the multitude of functional groups included. However, the determination of the structure of humic and fulvic acids is still under debate and the question remains if there is any common structure at all (Kracht 2001). The examples show the difference in mean molecular weight; the humic acid molecule is clearly larger than its fulvic counterpart. Other proposed structures are given by Harvey *et al.*(Harvey, Boran, Chesal, and Tokar 1983) and in the textbook by Kirk (Kirk 1994a).

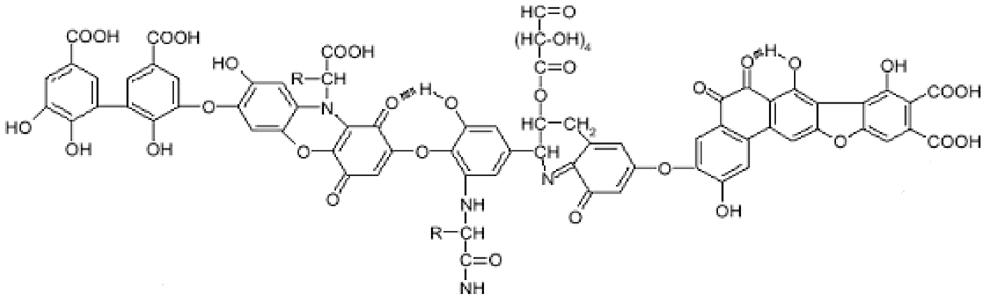

Figure 2.3: Model structure of humic acid, showing possible types of bonds and groups (after Stevenson 1982)

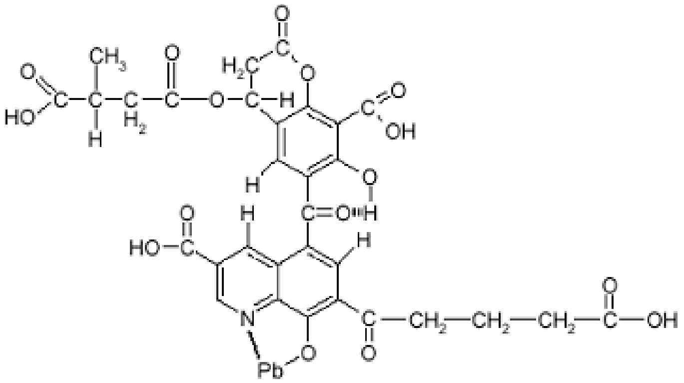

Figure 2.4: Model structure of fulvic acid showing possible types of bonds and groups (after McKnight and Aiken 1998)

Molecular weight and size of CDOM

The molecular weight *MW* of a compound is equal to the average mass of its molecules (Atkins 1989). The *MW* of CDOM ranges from 100 Da for fulvic acids to more than 100,000 Da for humic acids (McKnight and Aiken 1998) and (Aikenhead-Peterson, McDowell, and Neff 2002). A Dalton is equivalent to the weight of a single atom (hydrogen H). Schnitzer and Kahn (Schnitzer and Kahn 1972) found a mean CDOM MW of 10000 Da. Visser found a range of 5,000 – 22,000 Da for fulvic acids and 20,000 – 75,000 Da for humic acids in North American boreal lakes (Visser 1984). Please note that there is some overlap in the MW of humic and fulvic acids. Although the MW of humic acids is generally larger, the difference between humic and fulvic acids is solely based on their solubility.

Laboratory size distribution measurements of CDOM by Kracht showed a size range of approximately 0.5 nm to 0.1 µm (Kracht 2001). This range is well below the threshold value for dissolved material (0.45 µm) and the 0.22 µm filter pore size used for CDOM measurements in some Ocean Colour protocols.

The structure of coloured molecules

The electromagnetic energy of a photon colliding with a molecule can change the electron distributions of that molecule. In some cases the relocations of electrons can be severe enough to break a bond and dissociate a molecule. This occurs for instance at the process of photodegradation, which is discussed in §2.4.2. The energy can also be released by radiative decay, when the molecule discards the received energy by excitation of a photon. However, a more common way for molecules to release energy is thermal degradation, when the energy is converted to rotational and vibrational energy. Because the energy levels of the electrons are discrete (quantised), molecules can only absorb and emit light of certain wavelengths.

The wavelengths that can be absorbed are determined by the number of electrons present in the molecule. By only absorbing part of the spectrum and transmitting the rest, molecules appear coloured. Some molecules only absorb very weakly and are therefore regarded colourless. In the visible light region, strong absorbing molecules have aromatic carbon rings or conjugated systems with many electrons. In other words: the carbon atoms in the molecule are bound by intermittently a single (C-C) and a double bond (C=C). The electrons in the double bond require less excitation energy than electrons in a single bond, resulting in a higher (light) absorption capability. Pigments for instance consist of these kinds of molecules with intermittently double- and single bound atoms.

The difference between DOM and its coloured fraction CDOM is therefore the abundance of double bonds and attached oxygen and nitrogen in the latter. The colour of CDOM is largely due to the presence of multiple (carbon) bounds and unshared electron pairs in the molecular structure (Orlov, 1972 and Atherton *et al.*, 1967 *in* Visser, 1984). This is reflected in the proposed structures of CDOM molecules that are shown in figure 2.3 and figure 2.4. By comparing the molecular structures of humic and fulvic acids shown in both figures it is expected that humic acids are more optically active because their molecules have a relatively higher amount of double bonds than the fulvic acid molecules. This supposition has actually been observed by Visser (Visser 1984), who found that the humic acids are more intensely coloured than fulvic acids as they contribute 35% percent of the colour of natural waters (based on absorption measurements) while they only account for 15% of the concentration of CDOM in North American boreal lakes.

2.3.4 Optical differences between humic and fulvic acids

In section 2.3.1 it was already mentioned that the chemical separation of humic substances is based on their solubility in water. Next to this, a number of relative differences between humic and fulvic acids that stem from their molecular structures is given in figure 2.2. In this section we will focus on the differences that are of importance on the spectral properties of Humic and Fulvic acids. These are given in table 2.2 below.

Table 2.2: Optical differences between humic and fulvic acids

Humic acid	Fulvic acid
More recalcitrant/refractory	More labile
Higher specific absorption	Lower specific absorption
Higher MW (20.000 - 100.000 Da)	Lower MW (100 – 22.000 Da)
Higher aromaticity	Lower aromaticity
Flatter absorption slope S	Steeper absorption slope S

In limnology and ecology another subdivision of DOM is made, based on the average time between formation and subsequent degradation of DOM components (called turn-over time). Two classes of DOM are identified (Wetzel 2002):

1. Labile DOM (LDOM), which has a turn-over time of hours to days
2. Recalcitrant or refractory DOM (RDOM), which has a turn-over time of weeks to months, although a fraction of RDOM has a turn-over time of years because it is very resistant to micro-organisms and is mainly broken down under the influence of photobleaching.

The humic and fulvic acids are both part of RDOM, with the humic acids being generally more resistant to degradation. Humic acids therefore remain optically active for longer periods than fulvic acids.

In the previous section it was explained that humic acids are generally more intensively coloured because humic acid molecules contain relatively more double bonds. Furthermore, humic acid molecules are relatively larger than fulvic acids, and also contain relatively more aromatic carbon rings.

The slope S of the exponential function that describes the CDOM absorption curve (discussed in detail in chapter 10) can be regarded as an indicator for the molecular properties of the humic substances present in a water sample. A number of relationships have been identified (Green and Blough 1994 and De Haan, De Boer, Kramer, and Voerman 1982):

- ➔ S is larger for fulvic acids than for humic acids
- ➔ S increases with decreasing molecular weight
- ➔ S increases with decreasing aromatic content (carbon rings)
- ➔ S increases with decreasing pH

A number of humic and fulvic acid absorption slope values found in literature are given in table 2.3. All of the slopes are probably modelled without the use of an offset (see chapter 10), resulting in higher values compared to Aldrich humic acid slope determined using an offset in this study.

Table 2.3: Overview of humic and fulvic acid specific absorptions and slopes. †) Recalculated to 440 nm from other reference wavelength using the exponential model.

Type	Source	a^* [$m^2 g^{-1}$]	S [nm^{-1}]
Aldrich humic acid, CAS 68131-04-4	This study	1.14 ± 0.23	0.0089 ± 0.005
Suwannee River Humic Acid † (IHSS)	Hansell and Carlson 2002	0.67	0.0137
Aldrich humic acid † (pH 6)	Zepp and Schlotzhauer 1981	2.46	0.0104
Gulf loop intrusion Humic †	Carder, Steward, Harvey, and Ortner 1989	0.15	0.0111
Suwannee River Fulvic Acid † (IHSS)	Hansell and Carlson 2002	0.24	0.0172
Gulf loop intrusion Fulvic †	Carder, Steward, Harvey, and Ortner 1989	0.01	0.0189
Sedimentary Fulvic Acid †	Hayase and Tsubota 1985	0.21	0.0163
Contech Fulvic Acid † (pH 6)	Zepp and Schlotzhauer 1981	0.70	0.0128

2.3.5 Relationships between CDOM and DOC

In section 2.2.2 it was mentioned that both DOC and CDOM are used to approximate DOM. A number of CDOM – DOC relationships found in literature for coastal and inland studies are given in Table 2.4. The goodness-of-fit of the CDOM-DOC relationships ranges from 0.54 to a 0.96. The relationship found by Dekker in the Vecht Wetlands is based on averaged CDOM and DOC values over a summer campaign at 13 sample locations in the Vecht Wetlands and Friesland (Netherlands), possibly explaining the high correlation. The large number of samples taken by Ferrari *et al.* possibly also contributed to a high correlation.

Ferrari *et al.* assumed that the absorption of the relatively uncoloured DOM components was given by the intercept value in the plot of CDOM absorption versus DOC (Ferrari, Dowell, Grossi, and Targa 1996).

Table 2.4: The various relationships between CDOM and DOC found in literature (please note that Stedmon *et al.* used TOC instead of DOC). †) Regression values recalculated from µM C, range values from a_{355} to a_{440} using S =0.014. ‡) Recalculated a_{375} to a_{440} using S =0.014.

Author	CDOM - DOC [mg l^{-1}] relation	R^2	Number of samples	DOC range [mg l^{-1}]
Dekker and Peters 1993 (Vecht Wetlands)	CDOM = -2.042 + 0.423 * DOC	0.96	13 (bulk)	7.3 – 14.5
Ferrari, Dowell, Grossi, and Targa 1996†	CDOM = -1.5 + 1.2 * DOC	0.84	214	0.4 – 1
Stedmon, Markager, and Kaas 2000‡	CDOM = -0.72 + 0.30 * TOC	0.63	89	0.7 – 3.1
Kramer, Jak, Stroomberg, Hooftman, and Mayer 2002	CDOM = 0.22 + 0.27 * DOC	0.76	12	3.2 – 18.9
This study	CDOM = 0.98 + 0.147 * DOC	0.54	27	4.8 – 19.1

2.4 Sources and sinks of Coloured Dissolved Organic Matter

2.4.1 Coloured Dissolved Organic Matter sources

Allochthonous versus autochthonous CDOM

With respect to the origin of CDOM in the Vecht Area surface waters two major pools are discriminated (see §2.3.2):

1. Autochthonous CDOM, which is formed in the aquatic environment by micro-organisms (mostly algae) and macrophytes through secretions and autolysis of cellular contents.
2. Allochthonous CDOM, which is composed largely of humic substances of terrestrial plant origin by means of humification. Due to surface runoff processes, groundwater flows and peat degradation this terrestrial CDOM finds its way into the aquatic environment.

The autochthonous and allochthonous sources of CDOM are shown in Figure 2.5. The average molecular structures of these two pools are slightly different. Quantification of DOM is therefore likely to result in information on the origin of DOM and on whether it is autochthonous or allochthonous in the water (Imai, Fukushima, Matsushige, and Kim 2001 and McKnight, Boyer, Westerhof, Doran, Kulbe, and Andersen 2001). The autochthonous or allochthonous origin of CDOM is believed to be related to the ratio between humic and fulvic acids. Although fulvic acids are always far more abundant than humic acids, the concentration of the latter may vary. Because allochthonous CDOM generally comprises of larger and more complex molecules due to the terrestrial background, the mentioned ratio in allochthonous CDOM is relatively in favour of the humic acids. As a result of the relative simpler molecules that are breakdown products of algae, autochthonous CDOM generally comprises of fulvic acids. The ratio between humic and fulvic acids therefore can be regarded as a proxy of the origin of the CDOM material.

The ratio between humic and fulvic acids can be determined in the laboratory by using the DOM-fraction distribution and the UV absorbance to dissolved organic carbon ratio (Imai, Fukushima, Matsushige, and Kim 2001), or by using the Fluorescence Index developed by McKnight *et al.* (McKnight, Boyer, Westerhof, Doran, Kulbe, and Andersen 2001). In chapter 10 of this research it will be investigated whether spectral CDOM information in the visible wavelengths can be used to determine the ratio between humic and fulvic acids, thus indicating an allochthonous or autochthonous CDOM origin. In the next sections the formation of CDOM is discussed; first the allochthonous formation and then the autochthonous CDOM formation.

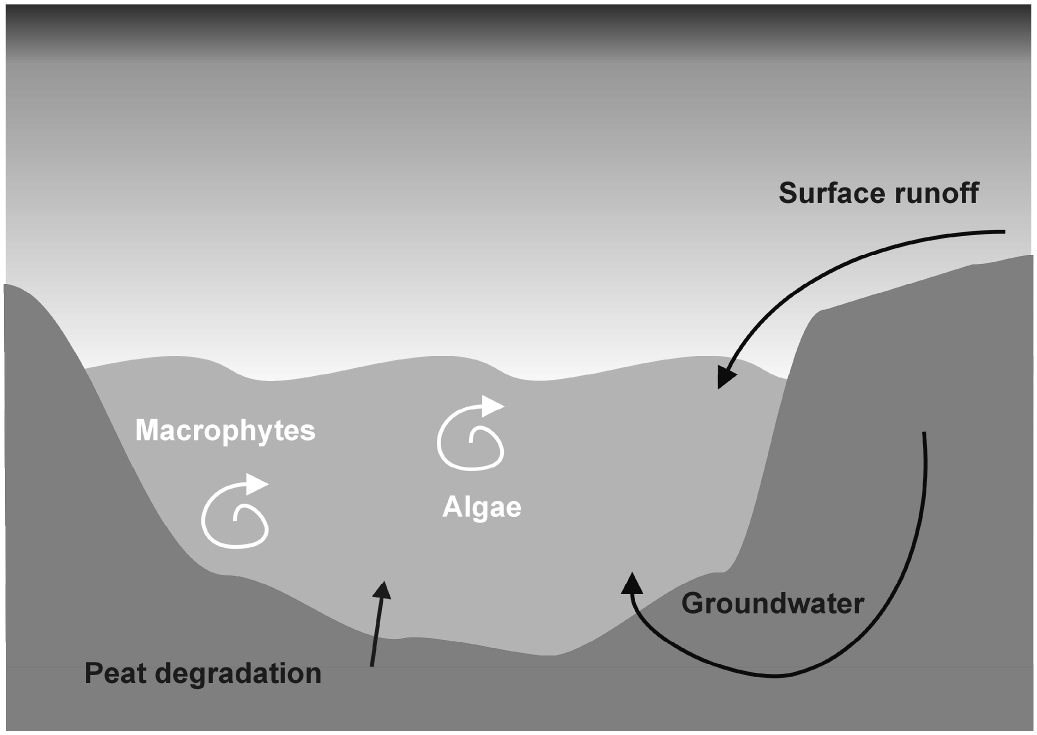

Figure 2.5: Sources of autochthonous (white) and allochthonous (black) CDOM in the Vecht Wetland lakes

Allochthonous CDOM formation

Aquatic humic substances in freshwater ecosystems, such as the Vecht Area, are primarily of terrestrial origin (Aiken, McKnight, Wershaw, and MacCarthy 1985; Wetzel 1983). Allochthonous CDOM is formed mainly by biological degradation of terrestrial plant cell matter. In the topsoil humification of leaf litter takes place by macrofauna, fungi or bacteria, decomposing all plant components, including lignin, into simpler monomers (Kracht and Gleixner 2000; Aiken, McKnight, Wershaw, and MacCarthy 1985). In broad terms, longer and more complex organic compounds are reworked into smaller and simpler compounds. These simpler organic compounds can then be recycled by serving as food for other soil organisms. Groundwater or surface runoff, however, transport a portion of the soil organic matter into the surface water. In the case of groundwater as the agent, the organic matter ending up in the lake is often the more refractory, because the more labile components are filtered out along the route (McKnight and Aiken 1998). In natural inland waters the CDOM comprises mostly of fulvic acids that originate from nearby soils (McKnight and Aiken 1998; De Haan 1986).

Allochthonous CDOM can also be formed from peat: As plant tissues die, a number of processes take place: First the enzymes within the dead cells cause proteolysis and other autolytic degradations. Then the released amino acids, sugars, tannins, phenols and quinines may be oxidised by chemical or enzymatic catalysis to produce humus-like pigments (Aiken, McKnight, Wershaw, and MacCarthy 1985). The availability of oxygen increases the humification rate of peat (Aiken, McKnight, Wershaw, and MacCarthy 1985).

Autochthonous CDOM formation

Most autochthonous CDOM material in the Vecht Area is released as a result of the lysis of phytoplankton. The process of lysis is defined as the breaking down or dissolution of cells (Henderson 1979). The decay of phytoplankton is the main source of autochthonous production of CDOM, and although there are several processes of formation possible, the extent of CDOM production is thus determined by the primary production. The primary production is the fixation of inorganic carbon by living organisms by the use of sunlight, producing organic compounds. A schematic overview of the autochthonous CDOM formation is given in Figure 2.6.

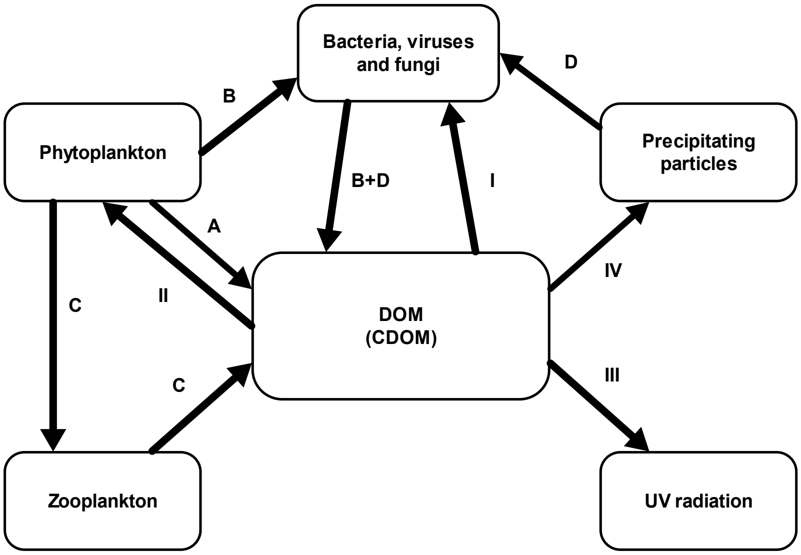

Figure 2.6: Schematic overview of the formation and degradation of autochthonous aquatic CDOM. The processes of CDOM formation (A - D) are discussed in the text, while the processes of CDOM degradation (I – IV) are treated in section 2.4.2.

Figure 2.6 shows that there are 4 CDOM formation processes (A – D):

A. Phytoplankton autolysis and extra-cellular CDOM production
B. Phytoplankton grazing induced CDOM production by zooplankton
C. CDOM production by viral and bacterial induced phytoplankton cell lysis and fungal parasitism
D. Solubilisation of particles by bacteria

Phytoplankton autolysis and extra- cellular CDOM production

Autolysis, the destruction of cells and tissues of an organism by enzymes produced by the cells themselves, occurs when the phytoplankton is under stress, e.g. under nutrient-poor conditions. In other words, autolysis occurs when phytoplankton dies of age or exhaustion.

Extra-cellular phytoplankton production concerns the release of carbohydrates, nitrogenous compounds and organic acids by algae. Bjørnsen (Bjørnsen, G., R.Gimbel, and H.D. Spangenberg 1998) estimated the extra-cellular production to be about 5% of the phytoplankton biomass per day. There are two models circulating in literature that can explain extra-cellular phytoplankton production: The overflow model and the passive diffusion model (Fogg 1966; Hansell and Carlson 2002).

The concept of the overflow model is that when the available radiation for photosynthesis exceeds the availability of nutrients for cell growth, the photosynthate of that cell is released (an 'overflow') (Fogg 1966). Discarding these compounds apparently is less costly in terms of energy than storage because the latter requires additional capsular cell material (Hansell and Carlson 2002).

The passive diffusion model is based on the assumption that low molecular weight compounds pass the cell membrane in order to maintain a concentration gradient. Once outside the cell, diffusion and uptake by bacteria takes place, requiring fresh DOM compounds to restore the gradient. It has been suggested that this release of organic matter is a defence mechanism against viruses. Wetzel also mentions the extra-cellular release of organic compounds by algae that are intended to inhibit or stimulate others (a process called allelopathy). Backed by observations (see Hansell and Carlson 2002), it is thought that both extra cellular phytoplankton production models are correct, depending on the environmental conditions present.

Similar to phytoplankton, macrophytes are also capable of the extra-cellular release of organic matter. The organic matter released by macrophytes is also labile (low molecular weight) material. According to Bertilsson and Jones the release of DOM by macrophytes can be significant for shallow lakes (Bertilsson and Jones 2002).

Phytoplankton grazing by zooplankton

Both micro- and macro-zooplankton (proterozoa and metazoa) graze on phytoplankton, removing up to 60-70% of the phytoplankton production in marine systems. These grazers therefore play a significant role in transforming particulate organic matter (in the form of algae) into dissolved organic matter, by means of sloppy feeding and excretion. Estimates for grazing efficiency in freshwater inland systems are not available but probably similar.

Viral and bacterial lysis and fungal parasitism

The abundance of viral particles in natural waters is very high: typical concentrations observed aquatic environments are in the range of 10^{12} - 10^{15} pp m^{-3} (Bergh, Borsheim, Bratbak, and Heldal 1989). By means of lytic infection, viruses inside a host cell start to produce numerous progeny viruses until the host cell bursts, releasing the progeny viruses, cell fragments and the nucleic acids of the cell. Most of the cell contents then become part of the dissolved organic matter pool.

Bacterial lysis has only recently been observed in experimental cultures and its mechanisms and importance remains subject of research (Hansell and Carlson 2002) and (Simis 2006).

Fungal parasitism can play a significant role in phytoplankton cell lysis. Because the different fungi attack specific algal types, fungal parasitism may be decisive in the algal competition (Wetzel 1983).

Solubilisation of particles

Particulate organic matter can be transformed in to CDOM by a process called ‘enzymatic hydrolysis’. The particulate matter is altered by bacteria as it floats or descends trough the water column. Knowledge of enzymatic hydrolysis is still limited and requires additional research (Hansell and Carlson 2002).

It has been found that bacteria can also produce CDOM without lysis or enzymatic hydrolysis, although the mechanisms for this are poorly understood to date (Hansell and Carlson 2002). Since the resulting biochemical structural units such as simple sugars, amino acids, fatty acids, and lignin building blocks are commonly much smaller than CDOM, several researchers have suggested that DOM ultimately is formed from a re-organization, polymerisation and condensation of these small precursors by microbial activity (Kracht 2001).

2.4.2 Coloured Dissolved Organic Matter sinks

Aiken *et al.* describe the degradation of CDOM as ‘losses of dissolved humic substances from the water column occur via adsorption onto surfaces of minerals, decomposition by microbes and by cleavage upon exposure to UV radiation or ozone‘ (Aiken, McKnight, Wershaw, and MacCarthy 1985). These CDOM degradation processes are also shown in Figure 2.6 as processes I – IV:

I. Consumption of CDOM by bacteria
II. Grazing of CDOM by phytoplankton
III. Adsorption to sinking particles
IV. Photodegradation under influence of UV radiation

Consumption of CDOM by bacteria

Bacterioplankton are regarded as the dominant consumers of DOM (in the oceanic environment) (Hansell and Carlson 2002). These prokaryotes, unicellular organisms lacking a nucleus and consisting of nothing more than a collection of molecules inside a membrane and a cell wall, are capable of taking up DOM. Via the process called permeasis, low molecular weight DOM compounds are transported through their cell membranes. In the Vecht Wetlands a special form of prokaryotes occurs next to cyanobacteria: the Prochlorophyta, who lack the phicobilin pigments but have chlorophyll-α and chlorophyll-β pigments. Only one species of Prochlorophyta exist in the Vecht wetlands, the Prochlorothrix hollandica (see e.g. Burger-Wiersma, Veenhuis, Korthals, Van de Wiel, and Mur 1986; Burger-Wiersma 1991).

Grazing of CDOM by phytoplankton

Some *eukaryotes*, cells or organisms with a membrane-bound, structurally discrete nucleus and other well-developed subcellular compartments, such as phytoplankton and zooplankton, are also capable of the direct uptake of CDOM compounds. Compared with the consumption by bacterioplankton the magnitude of grazing of CDOM by phytoplankton is considered small (Wetzel 1983).

Adsorption to sinking particles

The process of adsorption of relatively old CDOM onto relatively young sinking particles has been proposed to explain the discrepancy between the ^{14}C –age and the precipitation rate of the particles. When dated, lake sediments were namely found to be older than could be expected based on the precipitation rate of particulate matter. The magnitude of CDOM removal by this process in relation to the consumption by bacterioplankton however is thought to be small (Hansell and Carlson 2002).

Photodegradation

High molecular weight CDOM compounds, that usually can withstand bacterial consumption, are transformed to low molecular weight compounds under the influence of UV light. This process is called photodegradation, photobleaching or photooxidation, and is extensively discussed by Gao and Zepp (Gao and Zepp 1998). It has been found in field and laboratory experiments that the CDOM absorption slope parameter S increases after exposure to UV light (Hansell and Carlson 2002; Whitehead, de Mora, Demers, Gosselin, Monfort, and Mostajir 2000; Vodacek, Blough, DeGrandpre, Peltzer, and Nelson 1997). An increase of S was also observed during controlled laboratory photodegradation experiments by Whitehead *et al.* (Whitehead, de Mora, Demers, Gosselin, Monfort, and Mostajir 2000).

On the other hand researchers found that the S values decrease as a result of photodegradation (Gao and Zepp 1998; Morris and Hargreaves 1997). In these latter two studies however the slope parameter was determined by a linear regression on the log-transformed CDOM absorption spectrum rather than a true non-linear regression technique as used in the other studies (and in this research). Therefore, an increase in S as a result of photodegradation is most likely because the calculation method used by Whitehead *et al* is more reliable. Field observations of photodegradation may also be affected by changes in the CDOM composition as a result of the mixing of terrestrial and in situ formed material.

Photodegradation is regarded as the main sink of oceanic DOM (Blough and Del Vechhio *in* Hansell and Carlson 2002). The resulting low molecular weight compounds after photodegradation can easily be reworked by bacteria. By absorbing UV light, CDOM shields the other aquatic life forms from this harmful radiation. At high concentrations however CDOM also absorbs a significant amount of the visible light as well, reducing the amount of photosynthetic energy available to phytoplankton and macrophytes and thus possibly reducing primary production.

2.5 Dynamics of aquatic CDOM

2.5.1 CDOM as a buffer

As already stated in the introduction, CDOM has excellent buffer capacities due to its large organic complexes (Klavins and Apsite 2002; Kramer, Jak, Stroomberg, Hooftman, and Mayer 2002). An example of the buffering capacity of DOM is given by the Mermayde project, a study in the biological availability of Copper in Dutch surface waters by Kramer *et al.* (Kramer, Jak, Stroomberg, Hooftman, and Mayer 2003). The negative biological effect of Cu^{2+} on the algae population has been demonstrated in literature (e.g. Gavis, Guillard, and Woodward 2004 and Lee, Lustigman, and Maccari 1993). Robinson and Brown found that copper could bind to organic matter, thereby reducing the toxicity of the copper for algae

(Robinson and Brown 1991). In the Mermayde project this role of DOC as a buffer was investigated, by measuring the algal toxicity at various concentrations of Cu^{2+} and DOC.

The algal toxicity was determined by using the 48h-EC50 exposure method on the freshwater green algae *Pseudokirchneriella subcapitata* (also known as *Selenastrum capricormutum*)*.* Various concentrations of Cu^{2+} were added to collected water samples, and after 48 hours of exposure the percentage of affected algae was determined. From this measurement range, the Cu^{2+} concentration was determined at which 50% of the algae were affected (the 48h-EC50 value). For their research water samples were taken from six Dutch surface waters (including a peaty lake similar to those found in the Vecht Wetlands) covering a broad range of DOC concentrations in April and September.

A very strong relationship was found between the DOC concentration *and* CDOM concentration at 380 nm at the one hand and the 48h-EC50 algal toxicity at the other hand (R^2 values > 0.95). Kramer *et al.* therefore concluded that the toxicity of copper was reduced significantly by the complexation of copper to DOC (Kramer, Jak, Stroomberg, Hooftman, and Mayer 2003). Finally, Kramer *et al.* argue that the small seasonal differences in the DOC – toxicity relationship are due to a difference in DOC composition between April and September (Kramer, Jak, Stroomberg, Hooftman, and Mayer 2003).

The buffering capacity of CDOM also plays a role in the bio-availability of polychlorinated biphenyls (PCB), a group of man-made compounds that were used in coolants and lubricants in transformers, capacitors, and other electrical equipment because of their good heat resistant and insulating capacities. In the late 70’s it was discovered that PCB’s were also highly toxic and carcinogenic, leading to a halt in production. By this time however PCB’s had found their way into the environment, and because they are resistant to breakdown they will remain in natural waters and sediments for many years.

Studies by Hoogenboom and Leonards and Dekker *et al.* (Hoogenboom and Leonards 1997; Dekker, Moen, Kootwijk, van Rossum, Hoogenboom, Belfroid, and Claassen 1999) have resulted in an algorithm to indirectly retrieve the PCB concentration based on remote sensing data. A dynamic equilibrium simulation model was also established, where the PCB concentration was determined based on the total chlorophyll, the total suspended matter and the CDOM concentration. Because the CDOM concentration could not be determined accurately enough at the time, a constant value for C_{CDOM} was used. The retrieved values by the algorithm could not be validated with actual PCB concentration measurements in the water because there was not enough data available. The contribution of CDOM to the buffering of PCB’s is thus unknown.

2.5.2 Spatial distribution of CDOM

A characterisation of Dutch inland water types with respect to the CDOM concentration and the absorption slope parameter is given by Rijkeboer *et al.* (Rijkeboer, Hoogenboom, and Dekker 1997). Spectral measurements and SIOP data was collected in this Spectral Library project of all Dutch waters in 1995. In Table 2.5 the average C_{CDOM} and S for all types of Dutch inland freshwaters are shown.

Table 2.5: The average CDOM concentration and absorption slope parameter per water type, measured in Dutch inland waters. The number of available sample locations per water type (N) is also given.

Water type	Number of waters N	Average C_{CDOM} [m^{-1}]	Average S [nm^{-1}]
Canals	5	2.39	0.016
Rivers	10	1.02	0.014
Lakes	71	3.82	0.016
Peat cut	12	10.08	0.016
Fens	3	42.44	0.012
Sand or gravel pit	13	1.31	0.020

Comparing inland water CDOM concentration and absorption slope parameters given the Table 2.5 with the values for separated humic and fulvic acids given earlier in Table 2.3, it is probable that relatively high concentration of humic acids are only present in fens, hence the low S values. These waters apparently have the largest input of allochthonous CDOM. In fens this is due to the degradation of peat, also resulting in very high C_{CDOM} values. Surface runoff will deliver substantial quantities of terrestrious plant material to the rivers, where autochthonous production is low due to high turbidity, resulting in low C_{CDOM} values.

Canals and lakes appear to have predominantly autochthonous CDOM production because of the high slope parameters. Sand and gravel pits finally are completely dominated by fulvic acids, probably because the humic molecules that otherwise remain active for long periods are lost to sedimentation here.

Most CDOM studies involving a spatial component are studies that investigate the mixing of CDOM rich flow from rivers and coastal regions into the ocean. Twardowski and Donaghay found a strong inverse linear relationship (R^2 >0.99) between the absorption of CDOM at 412 nm and the salinity in the East Sound, WA, USA (Twardowski and Donaghay 2002). The primary water source in the East Sound was river outflow. No significant relationship was found between the absorption of CDOM at 375 nm and the salinity in the coastal region near Oman, where no discharging rivers occur (Del Castillo and Coble 2000).

Next to the relationship between the CDOM concentration and salinity there are also relations with water temperature and acidity (Twardowski and Donaghay 2002). These relationships however may also be related to the discharging of river water into the sea. No other spatial relationships between the CDOM concentration and other water quality parameters are known.

The spatial variation in the composition of DOM has also been investigated. Imai found that DOM fraction distribution patterns differ depending on their origin in a eutrophic Japanese lake (with conditions roughly comparable to the Vecht Wetlands study area) and its inflowing streams (Imai, Fukushima, Matsushige, and Kim 2001). The DOM contributed by the streams had a higher mean molecular weight than the DOM sampled from the lake.

Similarly, the large spatial variability in CDOM absorption slope parameter *S* can be explained by patchiness in algal and bacterial populations with respect to both region and depth (Stedmon, Markager, and Kaas 2000). The different algal and bacterial populations produce different types of CDOM molecules, causing a variety of slope parameters.

2.5.3 Seasonal fluctuations of CDOM

Research has been conducted to link the CDOM concentration to the eutrophication status of natural waters, but the scientific community is divided here. Bricaud *et al.* (Bricaud, Morel, and Prieur 1981) found such a relation (for Case I waters) while Dekker (Dekker 1993) did not find evidence for this (for Case II waters). This discrepancy can be explained by the fact that in Case I waters only autochthonously produced CDOM is present, ensuring a direct link to the phytoplankton population, while in Case II waters it assumed that the majority of CDOM is of allochthonous production.

Carder *et al.* (Carder, Steward, Harvey, and Ortner 1989) considered marine CDOM as a by-product of primary production and plotted literature values of C_{CDOM} against literature values of primary production at log scale, showing a positive relationship between the two. A complicating factor here is that in oceanic environments CDOM has a very long alteration time in comparison with the algal mass. This principle was also acknowledged by Kopelevich and Burenkov, who proposed to split up CDOM between a relatively old and refractory component that is resistant to biological activity and a component that fluctuates in accordance to the chlorophyll concentrations (Kopelevich and Burenkov in (Twardowski and Donaghay 2001)). The refractory pool is believed to originate from terrestrial plant sources. The portion of CDOM absorption that correlated with salinity (see previous section) can be regarded as the refractory pool from terrestrial origin according to Twardowski and Donaghay (Twardowski and Donaghay 2001). Subsequently they determined the autochthonous CDOM pool, which correlates with the primary production, by subtracting the refractory pool absorption from the total measured absorption spectrum.

A similar idea is presented by Stedmon *et al.* (Stedmon, Markager, and Kaas 2000). In order to better describe the marine CDOM behaviour during the seasons they proposed a two-pool CDOM model consisting of a coloured terrestrial end-member and a relatively uncoloured oceanic end-member. Additionally a third pool might exist: a constant proportion of uncoloured material in the terrestrial end-member. Sasaki noted that after phytoplankton blooms inside Funka Bay, Japan, C_{CDOM} and S values increased. In other words, mainly fulvic acids are produced by phytoplankton (autochthonous production) (Sasaki, Tanaka, Ishizaka, and Saitoh 2002).

The CDOM absorption slope parameter S fluctuates from 0.018 nm^{-1} in late summer and winter to 0.014 nm^{-1} in spring in the Middle Atlantic Bight (Vodacek, Blough, DeGrandpre, Peltzer, and Nelson 1997), indicating a shift in the average molecule size, in other words a change in the humic and fulvic acid ratio. In boreal lakes in the U.S.A. and Canada the fulvic acid concentration remains more or less constant, but humic acid concentration increases during the February - September season by as much as 4 to 13 fold (Visser 1984). The molecular weight of humic acids decreases in winter, while the MW of fulvic acids increased. The MW of all CDOM fractions were found to decrease in the autumn.

As mentioned earlier, the bulk of CDOM material originates from terrestrial sources. It is therefore not surprising that the CDOM concentration varies according to the seasonal variability of freshwater input from surrounding watersheds and new CDOM production from *in situ* biologic activity (Keith, Yoder, and Freeman 2002). This observation is shared by Visser: The increase in spring CDOM concentrations in boreal lakes in the U.S.A. and Canada is caused by resuspension and surface runoff due to the discharge peak of melting water (Visser 1984).

2.6 CDOM in the Vecht Wetlands

2.6.1 Spatial variation of CDOM in the Vecht Wetlands

Most surface water in the study area is artificially replenished by dephosphorised water taken from the Amsterdam-Rijnkanaal canal (see section 1.2.2 on the hydrology of the Vecht Wetlands). Allochthonous CDOM in the Vecht Wetlands is therefore largely originating from the river Rhine.

CDOM concentrations in the study area vary significantly between shallow eutrophic waters and deep clear waters. The shallow eutrophic waters in the dataset have an average CDOM concentration of 2.8 m^{-1}, while the deep clear lakes have an average CDOM concentration of 1.0 m^{-1}. These values are similar to those found by Dekker in his research (Dekker and Peters 1993) and to the findings of the Spectral Library project (Rijkeboer, Hoogenboom, and Dekker 1997).

In deep and clear lakes there is probably less formation of CDOM by algae, less influx of allochthonous CDOM and no resuspension of CDOM by lake sediments, leading to a CDOM concentration that is half of that of shallow eutrophic waters. Within the deep lakes group, the Spiegelplas, Wijde Blik and the Waterleidingplas have very similar C_{CDOM} values (0.9, 1.2 and 1.0 m^{-1} respectively). For more information on these lakes see the map on page 11 and Table 1.1 for additional properties. The shallow eutrophic waters have the lowest CDOM concentrations in the rivers and canals and the highest concentrations are found in Terra Nova Helder, probably due to the abundance of macrophytes.

The spatial variation in the slope parameter S in the study area is also considerable. The lowest slope values were found in the Kortenhoefsche and the Loosdrechtse Plassen (0.013 nm^{-1} and 0.014 nm^{-1} respectively) with relatively high algal concentrations (autochthonous production). The highest values for S were found in Terra Nova Helder and the Spiegelplas (0.017 nm^{-1} and 0.016 nm^{-1} respectively). Dekker found the lowest values (0.011 nm^{-1}) in the river Vecht and the highest in lake Naardermeer (0.018 nm^{-1}).

Because of the inaccuracy of available CDOM maps derived from airborne remote sensing images, no information on the within-lake distribution of CDOM can be given. Based on experiences with chlorophyll and suspended matter however, it is most likely that the inter-lake variability in CDOM will be much larger than the intra-lake variability in the study area.

2.6.2 Seasonal fluctuations of CDOM in the Vecht Wetlands

The seasonal fluctuations of the CDOM concentration in the study area are shown in Figure 2.7. Seasonal data was only available within the GWA dataset, for the lakes Loenderveen, Terra Nova Troebel and Terra Nova Helder. CDOM measurements were performed on April 24th, June 5th, July 29th and September 12, 2002. On June 5th only one location per lake could be sampled, while on the other dates 3 sample locations per lake were measured. For the June 5th values therefore no standard deviation could be calculated. The same seasonal fluctuation of the CDOM concentration is present in lakes Loenderveen and Terra

Nova Helder: high CDOM concentrations in the spring and autumn and low concentrations in the early summer. Note that Terra Nova Helder has a large standard deviation, probably due to the presence of macrophytes. Lake Terra Nova Troebel has the lowest CDOM concentration in spring, increasing in the summer and again significantly decreasing in the autumn.

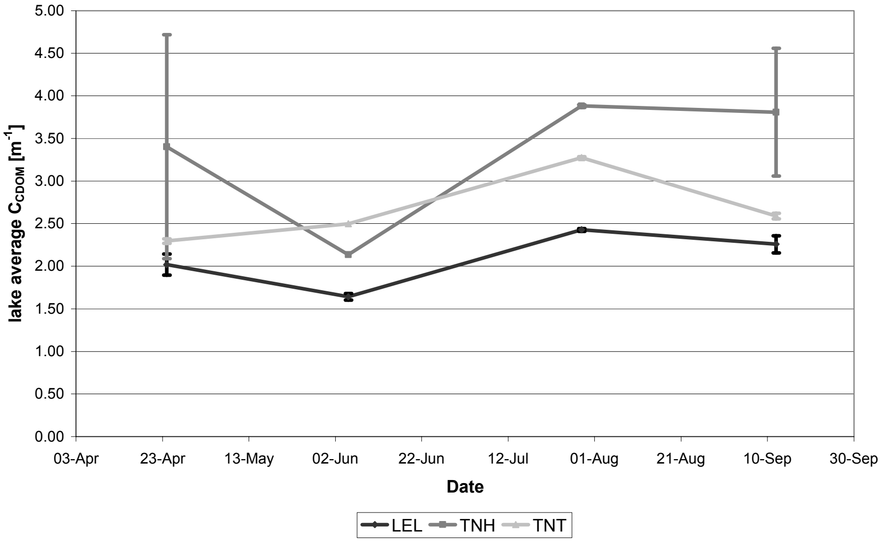

Figure 2.7: The seasonal fluctuation of the average CDOM concentration for lakes Loenderveen, Terra Nova Helder and Terra Nova Troebel (with error bars indicating standard deviation)

Low summer CDOM concentrations may be caused by two processes: 1) the influx of allochthonous organic material decreases in summer as a result of the decrease in precipitation in summer and 2) the CDOM is being consumed by blooming algae populations in spring and autumn, and is released in early summer. A similar seasonal CDOM fluctuation was observed by Vos *et al.* in the IJsselmeer (Vos, Boderie, Gons, Splunder, Hoogenboom, Woerd, Villars, Hoogveld, Rijkeboer, Jordans, and Hakvoort 2002).

The seasonal fluctuation in the average CDOM absorption slope parameter is shown in Figure 2.8. The fluctuation in S is the same for all three lakes: a decrease in S (relative increase of humic acid to fulvic acid) in spring and autumn as fulvic acids are consumed by phytoplanton, while in summer fulvic acid is reeased by algae. These findings are not compatible with the IJsselmeer study by Vos *et al.*, as they found a continuous decrease in S from April to September (Vos, Boderie, Gons, Splunder, Hoogenboom, Woerd, Villars, Hoogveld, Rijkeboer, Jordans, and Hakvoort 2002). Such a relative decrease of fulvic acid can be explained as a result of increased photobleaching of primarily fulvic acids in summer. The discrepancy between the slope parameters found for this study and the work of Vos *et al.* however can be the result of different CDOM absorption modelling techniques (as explained in chapter 10).

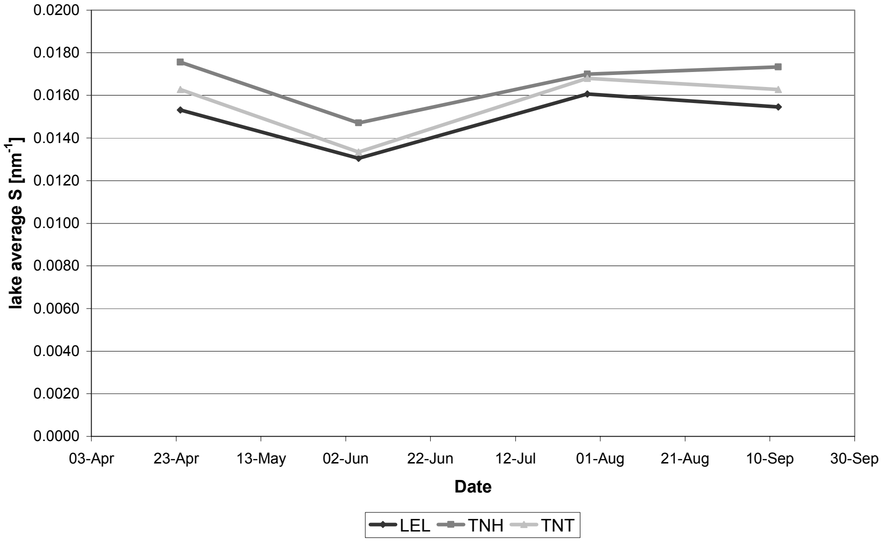

Figure 2.8: The seasonal fluctuation of the average CDOM absorption slope parameter for lakes Loenderveen, Terra Nova Helder and Terra Nova Troebel

2.7 Discussion and conclusions

Coloured Dissolved Organic Matter is the visible portion of the organic matter present in the aquatic environment. The total amount of dissolved organic matter pool, which acts as an important buffer for the aquatic ecosystem, can be estimated from CDOM measurements. As a consequence of the molecular structure of CDOM, UV and blue light are strongly absorbed. The absorption spectrum of CDOM can be described by an exponentially decreasing function.

The CDOM pool itself can be subdivided into two major components: the humic acids that are comprised of relatively large and refractory molecules and the fulvic acids that are composed of relatively smaller and more labile molecules. This subdivision of CDOM into humic and fulvic acids helps to understand the variability in optical characteristics of CDOM. The slope parameter of the exponential CDOM absorption model is influenced by the relative contributions of humic and fulvic acids, which can change over space and time.

The ratio between humic and fulvic acids is determined by the sources of CDOM. In general, a high humic acid content indicates that the CDOM present originates mainly from the remains of terrigenous plant material and entered the water body by surface runoff or groundwater flows (allochthonous CDOM). On the other hand, a high fulvic acid content is found when the CDOM is mostly comprised of the remains of deceased phytoplankton (autochthonous CDOM).

The small case study attached at the end of this chapter showed that there are seasonal fluctuations of CDOM abundance and CDOM composition in the Vecht Wetlands research area. A larger experiment is however required to substantiate these fluctuations. In the Vecht Wetlands study area the CDOM is mostly autochthonous, derived from algal remains (as the high absorption spectrum slope parameter indicates that fulvic acids are dominant). The main removal processes of CDOM in the study area are consumption by bacteria and phytoplankton and photobleaching.

The literature research carried out in the current chapter has a number of implications on the remainder of this study. From the spectral characteristics of CDOM, which differs from the absorption spectra of chlorophyll and suspended matter, it can be concluded that it is at least theoretically possible to retrieve CDOM concentrations from optical measurements. Also the difference in absorption slopes of humic and fulvic acids may play a role in improving CDOM retrieval accuracy (chapter 11). Before commencing with CDOM retrieval improvements some theoretical aspects of optical modelling will be explained first in Part B: Optical modelling theory (chapters 3-7).

Part B: Optical modelling theory

3. An introduction to remote sensing methodologies for water quality assessments

In this chapter the concept of water quality algorithms is outlined and an overview is given of various algorithm types and their applicability to the present study. The underlying principles of bio-optical models will be briefly introduced and a rationale will be given that guided some essential choices in this research regarding the application of models and algorithms.

3.1 Introduction to water quality retrieval algorithms types

For the purpose of this dissertation an algorithm is defined as a calculation method to derive concentrations of optically active water constituents from spectral observations of water leaving light. Since a remote sensing image is a 2 dimensional matrix of spectra, algorithms can be applied to each pixel in an image thus creating 2-dimensional maps of water quality parameters.

With remote sensing the colour of water as observed in the spectrum of water leaving light can be studied. From this spectrum concentrations of optically active constituents in the upper layer of the observed water body can be determined using specific algorithms. Essentially there are two groups of approaches to achieve this goal: empirical algorithms based on statistical relationships and analytical algorithms based on the inversion of a calibrated bio-optical model. An extensive overview of algorithm techniques can be found in the third report of the International Ocean-Colour Coordinating Group (IOCCG 2000).

In the next sections we will discuss what types of algorithms are suitable to support the research in this thesis. In first instance (section 3.1.1) it will be discussed why empirical algorithms have little relevance to the research. Next (semi-) analytical algorithms will be evaluated. Since these algorithms are based on bio-optical models, an overview and general discussion will be provided on types and relevance of these models (section 3.1.2). To conclude this section a general introduction to semi-analytical algorithms will be provided in section 3.2 with a rationale why this type of algorithms is most suitable for the currently presented research. An overview of the different empirical and analytical algorithms is given in figure 3.1.

Figure 3.1 illustrates the links between algorithm development approaches and bio-optical modelling approaches.

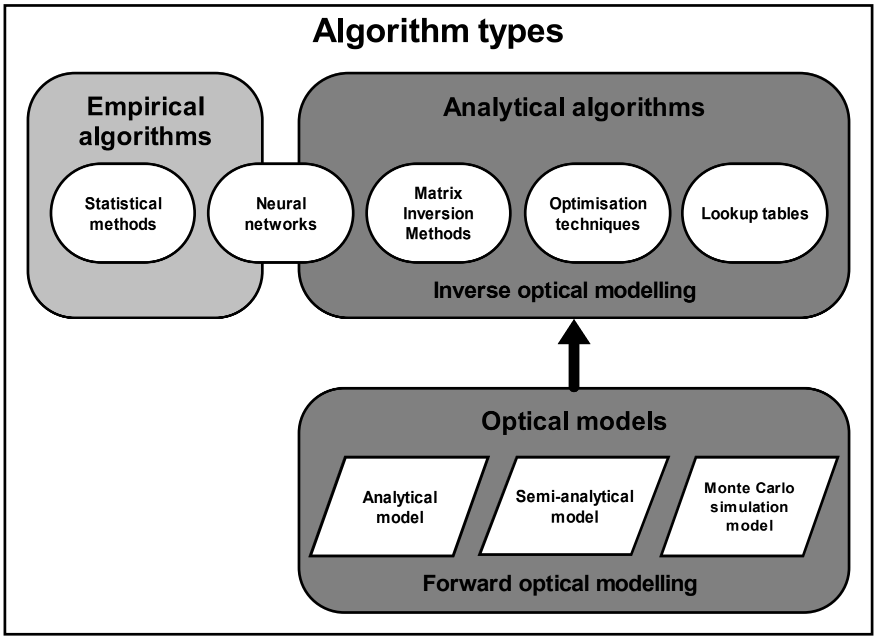

Figure 3.1 Overview of types of algorithms (empirical and analytical) and optical models used in water quality remote sensing

3.1.1 Empirical algorithms

Empirical methods require no *a priori* knowledge of the water system. Statistical relations are determined between parts of the spectrum (e.g. in a linear combination of spectral bands or by using a combination of band-ratios) by means of regression analysis to a set of *in situ* measured concentrations. In global ocean-colour studies empirical algorithms are quite commonplace and give good results because they are based on large datasets (O'Reilly, Maritorena, Mitchell, Siegel, Garver, and Kahru 1998) and because they operate on atmospherically corrected images. Inland waters have a much larger diversity and ranges of concentrations, which causes empirical algorithms to be very site specific. Therefore, for inland waters, the results of empirical modelling are varying but generally inaccurate and the statistical relationships found are not necessarily meaningful. Each image to be processed will need an accompanying ground truth dataset, as the statistical relationships will differ for each occasion, both in space and time.

Although sporadically, empirical methods sometimes have to be used because they have the following advantages:

- ➔ They can operate on raw image data which eliminates the need for atmospheric correction of the image.
- ➔ Statistical regression methods yield simple and fast algorithms.
- ➔ If applied correctly, they resolve the same spatial patterns as complex algorithms, but with less accuracy

When looking at multitemporal observations of the same area it is strongly recommended to apply atmospheric correction on the data and use band ratios if possible.

An example of the use of a true empirical method is given by Doxaran *et al.* (Doxaran, Froidefond, Lavender, and Castaing 2002), who constructed an empirical algorithm for coastal TSM. Although there are also published empirical TCHL retrieval algorithms (O'Reilly, Maritorena, Mitchell, Siegel, Garver, and Kahru 1998), No example of an empirical CDOM algorithm could be found in literature, probably because the form of the CDOM absorption spectrum and the relatively low influence of CDOM on the reflectance spectrum and interference of other water quality parameters at all relevant wavelengths do not allow accurate empirical CDOM algorithms (Dekker, Brando, Anstee, Pinnel, Kutser, Hoogenboom, Peters, Pasterkamp, Vos, Olbert, and Malthus 2001; Peters and Landa 1998; Dekker, Moen, Kootwijk, van Rossum, Hoogenboom, Belfroid, and Claassen 1999). For an empirical approach the CDOM information in the blue wavelengths would be required, but these are usually heavily affected by atmospheric conditions and instrument (in)sensitivity in the shorter wavelength region.

Since one of the main questions of this research is to determine how to accurately determine CDOM in inland lakes from observed spectra (including the optical properties of this substance and its role in the complete optical characterisation of the surface water) empirical algorithms are of less interest and the focus will lie with analytical algorithm development which will be discussed next.

3.1.2 Analytical and Semi-analytical algorithms: underlying bio-optical models

Calibrated bio-optical models can be used to simulate a (part of the) spectrum by varying the concentrations of optical active constituents until sufficient similarity is achieved. In this way concentrations of optical active constituents can be obtained.

Bio-optical models can be complex analytical models or simplified semi-analytical models. There are currently three types of bio-optical modelling approaches that are generally applied in water quality remote sensing studies (see e.g. also Dekker, Vos, and Peters 2001):

4. Stochastic approaches such as Monte Carlo simulation models: Monte Carlo simulation models are stochastic models where, in the case of forward optical modelling, the fate of large numbers of simulated photons is tracked, leading to an average reflectance spectrum (see for instance Mehrtens and Martin 2002 or Kirk 1994b). This type of models is very difficult to invert in a computational efficient way, therefore they are not further discussed and used in this thesis.
5. Complex Analytical models: In analytical models the physics are provided by the radiative transfer equation, describing the propagation of light through water and air (see chapter 4). In current literature the most exact and standard bio-optical model is Hydrolight. Hydrolight is a software program that computes radiance distributions and derived quantities using a numerical radiative transfer model (Sequoia Scientific Inc., USA, http://www.sequoiasci.com/products/Hydrolight.aspx). Input for the Hydrolight software consists of the water absorption and scattering properties, the sky conditions, the bottom boundary conditions and the viewing geometry while the resulting output comprises of the water-leaving radiance and remote sensing reflectance (Mobley 1998). Hydrolight numerically solves the radiative transfer equation (see chapter 4) using the given boundary conditions. An example of the use of Hydrolight to derive a simplified formulation for the shape factors is given by (Albert and Mobley 2003). Parameterisation of Hydrolight for spectral inversion purposes requires the measurement of a number of optical properties. Because of the complexities involved some

parameters are substituted by published standard values (such as the volume scattering function and the scattering phase function.

6. Simplified semi-analytical models: To reduce processing time and arithmetic complexities, simplifications of the radiative transfer equation can be introduced leading to so-called semi-analytical model formulations. An overview of published semi-analytical models relevant to optical detection of inland water quality can be found in (Dekker, Brando, Anstee, Pinnel, Kutser, Hoogenboom, Peters, Pasterkamp, Vos, Olbert, and Malthus 2001).

3.2 Analytical Algorithm development based on complex bio-optical models

Analytical algorithms based on the inversion of models like Hydrolight (Mobley 1998; Mobley 1999f) require settings for a number of parameters (including the volume scattering function (see chapter 4) and surface characteristics). Often it is difficult to enter accurate values for these parameters because sometimes only a few measurements have ever been done. For instance, even today the volume scattering functions by (Petzold 1972) are used for most studies.

The advantage of an analytical algorithm is that, once established, it can be applied to similar images as well, without the need for an extensive new ground truth dataset. Similar images are for instance images taken of adjacent or comparable water bodies, or images taken with another suitable sensor, or images collected at another point in time. The method is relatively insensitive to sensor characteristics and spatial and temporal variation. Since this method is based on physical modelling, it requires full atmospheric correction of the image.

For algorithm development by direct analytical inversion the numerical Hydrolight simulations are mathematically too complex and computationally too time-consuming. Because of the high accuracy of the model, current research is focussing on finding alternative more efficient ways to indirectly invert the model while retaining as much as possible the inversion accuracy. This has very recently lead to some different innovative approaches of which we name:

- ➔ A parameterised and calibrated version of Hydrolight is used to simulate of series of spectra and concentrations. This dataset is used to train a neural network which is subsequently used to rapidly invert a large number of satellite observed spectra. NNs may produce approximately correct results if the spectra fall within the same ranges as the training data. Background information on the operation of NN, especially when applied in remote sensing, is given by (Atkinson and Tatnall 1997). Examples of the neural network approach are the recent studies performed by (Schiller and Doerffer 1997; Buckton, O'Mongain, and Danaher 1999; Baruah, Oki, and Nishimura 2000; Krasnapolski, Gemmil, and Breaker 2000 and by Zhang, Pulliainen, Koponen, and Hallikainen 2002). No example of the application of a NN for retrieving CDOM in inland waters based on measured data could be found.
- ➔ A recent publication by Pasterkamp *et al.* (2005) advocates a different approach where HYDROLIGHT is used to generate a simulated look-up table containing absorption and scattering values using series of input concentrations. This look-up table is subsequently approximated by high order polynomial equations. A Levenberg-Marquard procedure is used next to fit a simulated spectrum (based on the polynomial expressions for absorption and scattering, measured inherent optical properties and concentrations) to an observed spectrum with a reported accuracy (for North Sea Case II waters) better than 98%. The results of this method have been validated for Chlorophyll-a, but not for CDOM, although this is also one of the products of the algorithm (Pasterkamp 2005).

Besides the computational quality, stability and performance of the techniques, for this specific study it was found essential that the applied models were physically based and transparent. This way, the factors that influence the success of the newly developed methods can be analysed as well.

As a direct consequence of these considerations it was concluded that the preferred methods are not empirical (not physically based) nor neural network methods (not transparent) but analytical inversion and inversion of exact models using look-up tables. During the period covering this study, Hydrolight performance increased because of increases in computer performance that allowed, very recently and too late for this study, to implement lookup techniques based on this exact model. The first results are only just emerging (Mobley, Sundman, Davis, Montes, and Paul Bisset 2002). Additionally, this approach would also require a considerable effort to construct due to the large amount of water types in the study area. Therefore it was decided in an early stage to concentrate on semi-analytical approaches as discussed in the next section.

3.2.1 Semi-analytical algorithm development based on simplified bio-optical models.

Dekker *et al.* indicate that a number of authors have already shown that semi-analytical bio-optical models usually sufficiently describe the complex physical relationships between optical properties of water quality parameters and spectral observations of the watercolour (Gordon, Smith, and Zaneveld 1984) and are suitable for inversion (Kirk 1983). A distinctive advantage of semi-analytical algorithms is the decoupling of the algorithm itself and its calibration factors. These algorithms can be adapted easily by changing the specific inherent optical properties that are usually stored in separate look-up files without having to modify or re-run the underlying bio-optical model.

Because of these reasons and the fact that the main controlling physical/optical variables can be measured, studied and controlled in this approach, it was decided that semi-analytical models should form the theoretical foundation for algorithm development for this thesis research.

(Semi-) analytical algorithms can have many formulations depending on the degree of simplification of the underlying bio-optical model and the number and types of parameters to be retrieved and the number of spectral bands of the sensor.

Multispectral / multi parameter algorithms

Multi / hyperspectral observations can be inverted for multiple parameters in the following ways:

- ➔ If the underlying bio-optical model can be linearised (as is the case with some standard semi-analytical models to be discussed further on) matrix inversion techniques can be used to solve the (usually over-determined) system of linear equations. Matrix inversion methods (MIM) are true linear mathematical inversions of the optical model for multiple bands and multiple parameters (Hoge and Lyon 1996)
- ➔ When the underlying bio-optical model is non-linear then optimisation techniques can be used to achieve spectral fitting (e.g. by Levenberg Marquard optimisation).
- ➔ Independent on the specific underlying bio-optical model, lookup table approaches can be used, whereby measured spectra are matched by looking

up the most similar spectrum in a vast database. This database is constructed by stepwise varying concentrations and angular dependencies in an optical model (Mobley, Sundman, Davis, Montes, and Paul Bisset 2002).

To parameterise the bio-optical model for use with multispectral images one requires detailed knowledge of the spectral behaviour of the water quality parameters, such as the specific (per unit measure) absorption and scattering coefficients. (Dekker 1993) and (because of variable viewing and illumination conditions) a parameterisation of the viewing geometry expressed in so called shape factors (see e.g. Walker 1994).

Recent examples of multiband / multiparameter semi-analytical algorithms include studies by Li *et al.* (Li, Budd, and Green 2004), Carder *et al.* (Carder, Chen, Cannizzaro, Campbell, and Mitchell 2004), Darecki & Stramsky (Darecki, Weeks, Sagan, Kowalczuk, and Kaczmarek 2003), Siegel *et al.* (Siegel, Maritorena, Nelson, Hansell, and Lorenzi-Kayser 2002), Peters *et al.* (Peters, Pasterkamp, and van der Woerd 2002), Lee and Carder (Lee and Carder 2004), Dekker *et al.* (Dekker, Brando, Anstee, Pinnel, Kutser, Hoogenboom, Peters, Pasterkamp, Vos, Olbert, and Malthus 2001), Keller (Keller 2001) and Pierson and Strömbeck (Pierson and Strombeck 2001). Of these, only Pierson and Strömbeck retrieved CDOM in inland waters, reporting a considerable overestimation.

An advantage of multiband / multiparameter semi-analytical optical models and algorithms is that they will allow the evaluation of retrieval accuracies of TCHL, TSM, and CDOM.

Low spectral / one parameter algorithms

If only one or a few spectral bands are available, the methods mentioned above can be simplified to one parameter algorithms. These algorithms can be designed based on the solution of e.g. a single band or a band ratio formulation of the bio-optical model and require further assumptions on the concentrations of constant parameters.

A well-known and often-used example of a (one parameter, three spectral bands) semi-analytical band ratio algorithm for chlorophyll *a* was published by (Gons 1999). It was developed based on measurements performed in the IJsselmeer and Vecht Wetlands study area (Gons, Rijkeboer, and Ruddick 2002). Relevant algorithms for inland water studies found in literature include Dekker and Peters (1993) and Gons (1999).

3.2.2 Essential algorithm choices for the present study

Recapitulating it was found that:

- ➔ CDOM has a more overall influence on the spectrum and lacks strong distinguishable spectral features like the absorption peaks and valley of chlorophyll
- ➔ CDOM influence is relatively strong in the blue-UV region but there the in-situ measurement difficulties are large (sensors are rather insensitive in this region and the amount of solar incoming radiation in this region is usually quite low)
- ➔ In all parts of the visible spectrum the optical influence of CDOM is mixed with the influence of water, CHL and TSM (except for very typical waters containing only CDOM)
- ➔ In order to address the problems stated above empirical solutions will not suffice and a physically based approach is needed

- ➔ The international research community has not yet produced any validated CDOM algorithm. CDOM is sometimes calculated as an additional free parameter in multiband / multiparameter (semi-) analytical algorithms
- ➔ Simple one parameter / few spectral bands algorithms for CDOM have not been found in literature
- ➔ A neural network solutions is discarded because it does not provide insight in the relationships between the water quality parameters
- ➔ Inversion of complex analytical algorithms fall outside the scope and possibilities of this study

As a result of these considerations, multiband / multiparameter semi-analytical approaches were selected for this research. Specifically the Matrix Inversion Methods (MIM) and Levenberg-Marquardt (LM) inversion techniques will be tested because they lead to fast and easily adaptable algorithms. MIM has the advantage that it always finds the unique solution to the problem. In theory this linearised solution is the best, but in practice it does not necessarily yield the best results because of its sensitivity to small errors in the spectrum. Optimisation techniques such as the LM method are less sensitive to small spectral errors but they may suffer from local minima and depend on initial estimates and the formulation of the spectral fitting criterion (Peters, Pasterkamp, and van der Woerd 2002). Because of the inherent drawbacks of each method mentioned above, both techniques will be compared.

3.3 Choice of the underlying optical model for this study

After establishing which techniques will be used to improve the CDOM retrieval from observed water leaving spectra by inversion of semi-analytical bio-optical models now a selection must be made of available models.

Dekker *et al.* have identified a number of potentially suitable models (Dekker, Brando, Anstee, Pinnel, Kutser, Hoogenboom, Peters, Pasterkamp, Vos, Olbert, and Malthus 2001). From these the Gordon-Walker semi-analytical optical model was selected for use in this research (Gordon, Brown, Evans, Brown, Smith, Baker, and Clark 1988), to be further explained in chapter 4. This semi-analytical optical model is relatively easy to implement and offers good performance. An important additional factor, which will be elaborated in chapter 8, is the fact that all input parameters can be measured / estimated based on the available *in situ* measurements.

Only a handful of studies have been found that successfully use the semi-analytical optical modelling technique to retrieve water quality parameters from remote sensing data. Darecki & Stramsky (Darecki, Weeks, Sagan, Kowalczuk, and Kaczmarek 2003) are an exception, validating CDOM retrieval from MODIS with in situ data. They found that the semi-analytical approach yielded the best results. Studies that focus on inland water or those include algorithms to retrieve CDOM are even scarcer. The frequent use of simulated datasets in literature also masks information on true retrieval accuracies.

In order to make a relevant contribution to this field this study will attempt to use semi-analytical optical models to their full potential by improving the parameterisation and calibration for CDOM and to analyse the inverse performance in the simultaneous retrieval of TCHL, TSM and CDOM concentrations.

4. Theoretical aspects of analytical water quality modelling

4.1 Introduction

The absorption and scattering characteristics of dissolved and suspended particles determine the under water light climate. The under water light climate is an important factor for the development of aquatic life. High concentrations of strongly absorbing particles for instance result in a decrease of transparency. This hampers e.g. the development of benthic flora and may e.g. have negative consequences for recreational use.

The presence and abundance of optically active natural water constituents is revealed by recording the colour of a water body by remote sensing instruments. The water colour spectrum is an apparent optical property (AOP) of the water. Its value changes with the optical properties and concentrations of the optically active substances in the water (the inherent optical properties or IOPs).

A very high concentration of green pigments such as chlorophyll indicates either the presence of an algal bloom, which is usually the result of eutrophication, or the presence of submerged vegetation (which would be an indicator for very clear water). If the presence of submerged vegetation can be ruled out, the chlorophyll concentration can be regarded as a proxy/indicator for the trophic state of a water body.

Next to chlorophyll (as Total Chlorophyll; Chlorophyll-a plus phaeopigments, abbreviated TCHL), the other optical water quality parameters include suspended particles or Total Suspended Matter (TSM) and the subject of this research: Coloured Dissolved Organic Matter (CDOM).

In the field of water remote sensing the relationships between the concentrations of the mentioned water quality parameters and the resulting water colour are studied by means of bio-optical models. Correct calibration of these relationships/models is a prerequisite for successful inversion and the determination of concentrations of water quality parameters from observed spectral remote sensing data.

A quantitative measurement of the watercolour is the spectrum of water leaving (upwelling) light. (Dekker 1993) found that expressing the upwelling light as the dimensionless subsurface irradiance reflectance $R(0-)$ is convenient. By expressing the output of bio-optical models in the same unit they can be used to simulate $R(0-)$ spectra that match measured spectra.

In order to achieve a successful match, the following issues need to be resolved:

1. What is the correct formulation of the optical model to simulate the subsurface irradiance reflectance?
2. What are the correct sets of IOPs, viewing and illumination geometry parameters to calibrate the model?

This spectral matching for inverse retrieval of concentrations of water quality parameters from measured subsurface irradiance reflectance data can be achieved by various methods such as optimisation techniques or by analytical model inversion techniques. So, an additional third issue has to be addressed, which is:

3. What is the correct method for performing the inversion of the optical model, to retrieve concentrations of water quality parameters, in this case especially CDOM in the presence of particulate matter and algal pigments?

A schematic overview of the detailed optical modelling process flow is shown in figure 4.1. The numbers in Figure 4.1 correspond to the issues raised above. The parameterisation of the optical model concerns two sets of properties: the Inherent Optical Properties (IOP) and the Apparent Optical Properties (AOP). Note that the simulation of $R(0-)$ from measured or assumed concentrations of water constituents is referred to as 'forward modelling' and that the retrieval of concentrations from measured $R(0-)$ spectra is called 'inverse modelling'.

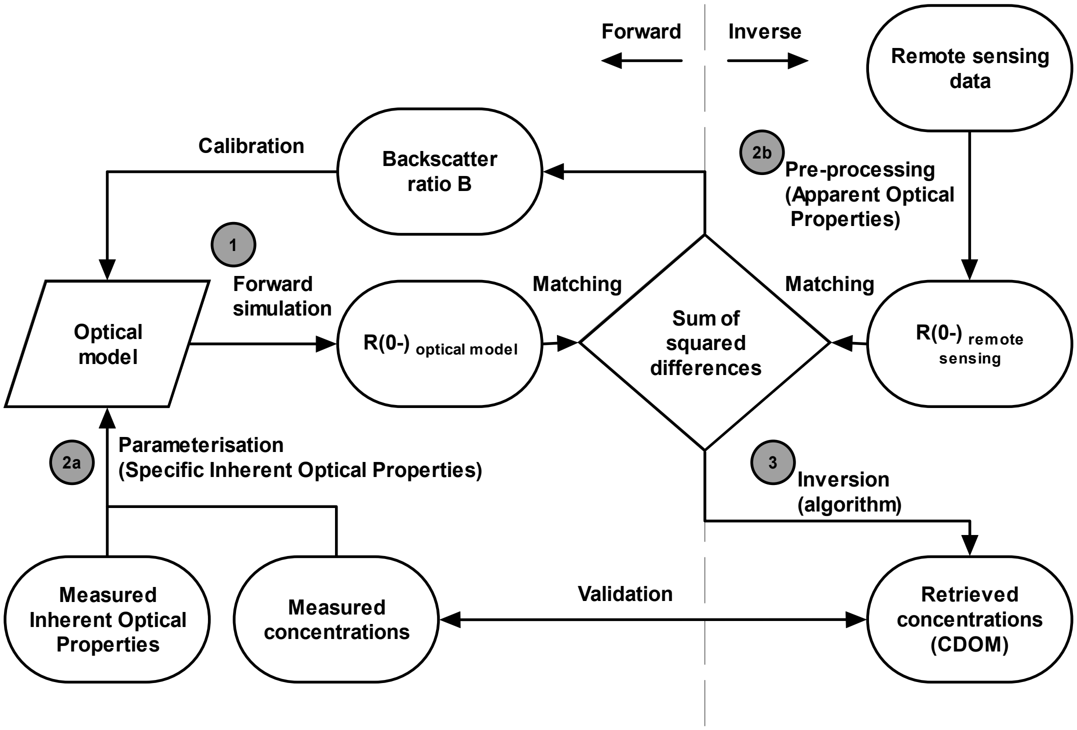

Figure 4.1: Schematic overview of the semi-analytical approach to optical modelling of water quality remote sensing. The shapes depict the different model components, while the arrows represent the different processes. The numbers in grey circles correspond to the research questions 1 – 3 raised in the text above.

In this chapter the theory of analytical optical modelling will be discussed. Some underlying concepts about light itself and radiometry are treated in section 4.2, providing the necessary background for understanding the Radiative Transfer Equation. In the next section (4.3) the first issue raised above is addressed by deriving a practical and adequate optical model from the Radiative Transfer Equation, based on the two-flow model for irradiance and the generic analytical model by Aas (Aas 1987). The parameterisation of the optical model, issue 2, is discussed in §4.4. The last issue raised above (number 3) is treated in section 4.5, explaining the theory of two optical model inversions: Matrix Inversion Method and Levenberg-Marquardt optimisation.

The parameterisation of the optical model will be dealt with in the next chapter, addressing the measurement techniques for obtaining the Inherent and Apparent Optical Properties and discussing the datasets collected for this research.

4.2 Principles of light and radiometry

4.2.1 Light as electromagnetic energy

The underwater light field can be described by opto-physical modelling and therefore the basics of light physics are discussed. Because the focus of water quality remote sensing historically was on photosynthesis by algae, the underwater light field is usually limited to the Photosythetically Active Radiation (PAR) wavelength region (between 400 – 700 nm), which coincides with the wavelength range of visible light. Light or electromagnetic radiation acts in accordance with the principles of basic wave theory. The wave theory describes the electromagnetic energy as travelling in a harmonic and sinusoidal wave, at the speed of light. The distance between two peaks of a sinusoidal wave, called a wavelength, determines the type of electromagnetic energy involved (figure 4.2).

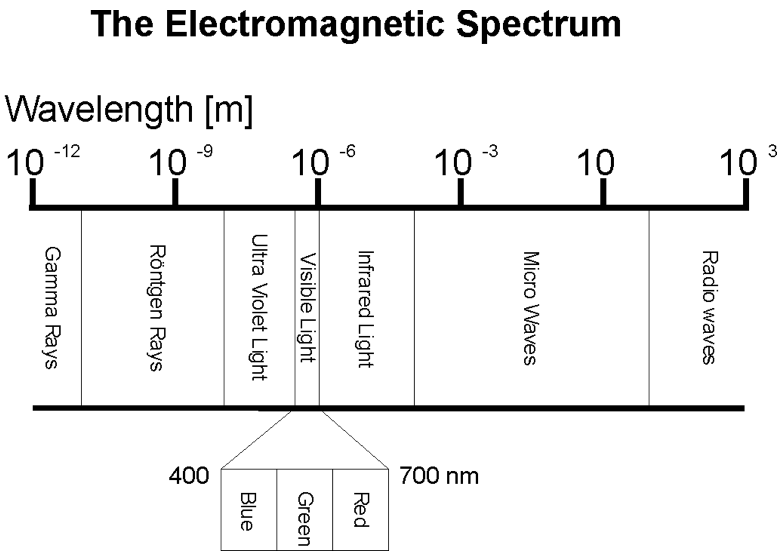

Figure 4.2: Overview of the electromagnetic spectrum, showing that the visible light is just a small portion of all electromagnetic energy. A frequently used subdivision of the visible light is blue (400-500 nm), green (500-600 nm) and red (600-700 nm) light.

The relationship between the wavelength and energy content is given by the particle theory, which states that the electromagnetic radiation is composed of discrete units of energy. This relationship is given by Planck's equation:

$$\varepsilon = \frac{hc}{\lambda} \qquad 4.1$$

In which the energy ε is expressed in Joule, h is Planck's constant [$6.63*10^{-34}$ Js], c is the speed of light [$2.998*10^{8}$ ms^{-1}] and λ the wavelength [nm].

The discrete energy units of the particle theory are called *photons*. Photons are emitted by all matter above absolute zero temperature (0°K or -273°C). Because of its high temperature, the sun is the main light source for passive optical remote sensing as it emits the vast majority of the photons in the Earth's biosphere.

A more detailed treatise of the principles of light and electromagnetic energy can be found in textbooks such as Kirk (Kirk 1983) or Mobley (Mobley 1994).

4.2.2 The principles of radiometry

The science of measuring electromagnetic energy is called radiometry (Mobley 1994). Some fundamental concepts in radiometry, of importance to remote sensing of water quality, are radiance, irradiance and irradiance reflectance, which are discussed below.

Radiance is the amount of radiation as derived from measurements by the remote sensing instrument. Radiance L [W m^{-2} sr^{-1}] is defined as the radiant flux at a point in space in a given direction per unit solid angle per unit area at right angles to the direction of propagation (Kirk 1994a) as expressed by the following equation:

$$L(\theta,\phi) = \frac{d^2\Phi}{dS\cos\theta d\omega} \tag{4.2}$$

with zenith angle θ, azimuth angle ϕ, radiant flux Φ [W], S the apparent unit area [m^2] as seen from the viewing direction and ω the solid angle [sr]. The zenith angle is the angle between a single beam of light and the upward vertical. The azimuth angle is the angle between the vertical plane incorporating the single light beam and the vertical plane of the sun. The radiant flux is the time rate of flow of the radiant energy. The solid angle is the angle of the infinitesimal small cone of the single light beam.

Irradiance is typically the radiation emitted or reflected by the surface of interest in all directions within half a sphere. Irradiance E [W m^{-2}] is defined as the radiant flux per unit area of a surface (Kirk 1994a), given by the following equation:

$$E = \frac{d\Phi}{dS} \tag{4.3}$$

The irradiance reflectance R [-] is the ratio between the upwelling irradiance E_u and downwelling irradiance E_d at a given point:

$$R = \frac{E_u}{E_d} \tag{4.4}$$

The upwelling irradiance is the irradiance facing up on a horizontal surface, while the downwelling irradiance is the irradiance facing down on a horizontal surface. Relative to the water surface the upwelling irradiance is thus directed towards the sky, while the downwelling irradiance is directed towards the lake bottom.

4.3 From analytical to Semi-analytical optical modelling

In this section, the first research question posed in §4.1 is addressed, formulating the optical model to simulate the subsurface irradiance reflectance. This step is depicted in Figure 4.3 (detail of Figure 4.1).

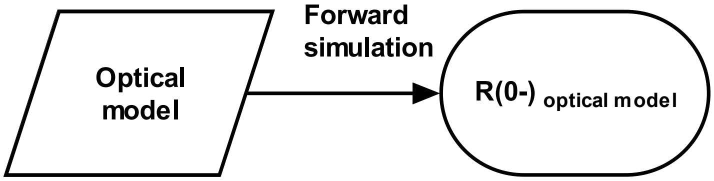

Figure 4.3: The optical model to simulate the subsurface irradiance reflectance (detail of Figure 4.1)

To obtain suitable optical models the Radiative Transfer Equation is simplified analytically.

4.3.1 The Radiative Transfer Equation

The Radiative Transfer Equation (RTE) describes the change in energy of a single beam of radiation along any specified path in a medium (water in this case). Lambert first proposed that the extinction of radiation due to traversing an infinitesimal increment of path must be linearly proportional to the amount of matter along the path. The underlying concept of radiative transfer is that a light beam passing through a medium loses photons by extinction but gains photons by emission. Extinction processes include scattering of photons out of the light path and absorption by matter along the path. Emission processes include thermal emission of photons by matter. For simplicity however, the scattering of photons belonging to another light beam *into* the light path is also regarded as emission.

Photons can only travel in a straight line under vacuum conditions. In other media, like the atmosphere or water, the vast majority of photons will collide with matter after which the photon continues to move in another direction. This process is called scattering. Scattering can occur in a number of ways, depending on the size of the matter with respect to the wavelength. Scattering at particles that have a significantly smaller radius than the wavelength of the incident light is called Rayleigh or density fluctuation scattering, whereas scattering at particles that have a larger radius than the wavelength of incident light is called Mie or particle scattering. Density fluctuation scattering is dominant in only the clearest of natural waters, causing a blue colour. Mie or particle scattering predominates the scattering of most natural waters, including Dutch inland waters (Dekker 1993). Scattering will be explained further in section 5.3.1, examples and measured ranges will be presented in §5.3.4.

At certain energy levels however the photon’s energy is taken up by a molecule or atom of that matter through a process called absorption. In some cases atoms or molecules can release photons when falling back to a lower energy level, this process is called fluorescence. Fluorescence however is not included in this research because the amount of light involved is typically 100 - 200 times smaller than the amount of absorbed light (for phytoplankton under conditions as found in the study area) and can therefore be regarded as insignificant (Gege 1994; Green and Blough 1994). Although there are relatively few studies of the fluorescence by CDOM in the visible light range, it can also be regarded negligible in this research because the fluorescence of CDOM occurs mainly in wavelengths smaller than 450 nm and the fluorescence intensity of CDOM decreases with increasing CDOM absorption (Hayase and Tsubota 1985; Roettgers, Schoenfeld, Kipp, and Doerffer 2005). Absorption will be explained further in section 5.3.1, while examples and measured ranges will be presented in sections §5.3.4.

The RTE is extensively discussed in textbooks by Kirk and by Mobley, as well as in various articles (Kirk 1994a). Here we follow the abbreviated RTE deduction by

Dekker *et al.* (Dekker, Brando, Anstee, Pinnel, Kutser, Hoogenboom, Peters, Pasterkamp, Vos, Olbert, and Malthus 2001) (section 2.2), where the RTE is translated into an analytical expression for the vertical attenuation coefficient using the two-flow model introduced by Aas (Aas 1987). The RTE deduction is extended with an extra step to obtain the subsurface irradiance reflectance, which is the desired analytical (Mobley 1994; Aas 1987) expression to derive water quality parameters from remote sensing observations.

The RTE shows the relationship between radiance and the optical properties of the water. Radiance is a function of the following Inherent Optical Properties: the absorption coefficient a, the scattering coefficient b and the normalised volume scattering function $\bar{\beta}$. Inherent Optical Properties (IOP) are discussed in section 4.4.1. An intermediate step in the analytical model is required, deriving the transfer equations for upwelling and downwelling irradiance from the RTE for radiance. Here it is assumed that the water body is source free, i.e. inelastic scattering and true emission are neglected. Inelastic or Raman scattering is important for water bodies with very low concentrations of chlorophyll and CDOM (Brando and Dekker 2002). As most lakes in the Vecht Wetlands study area are eutrophic, Raman scattering effects can be neglected. In addition, it is assumed that the water body is horizontally homogeneous with a constant index of refraction (Mobley 1994). A final assumption is that the distance between the scattering and absorbing particles is larger (or much smaller) than the wavelengths used for remote sensing. When individual particles are closer together than 0.4 – 0.8 µm, they will act as one larger particle with respect to the scattering, but not with respect to the absorption. In this case the scattering coefficient is no longer independent of the absorption. Although it is possible that such a situation occurs in natural waters, most of the particles present in the water are surrounded by vast quantities of water molecules that are much closer together than the wavelengths of visible light. Furthermore only the bulk properties of the water samples are considered when applying the RTE for water remote sensing studies, and these bulk properties are in accordance with the aforementioned assumption.

Under the assumptions mentioned above, the RTE for unpolarised light is given by:

$$\frac{dL(\theta,\phi)}{dz}\mu = -cL(\theta,\phi) + b\int_{\Xi} L(\theta',\phi')\,\bar{\beta}(\theta,\phi,\theta',\phi')\,d\omega' \qquad 4.5$$

Where Ξ is the unit sphere in directions θ,ϕ, with solid angle ω and the average cosine of the zenith angle μ. For brevity the wavelength and depth dependence is omitted. Equation 4.5 states that the change in radiance over a depth interval dz, corrected for the zenith angle by μ, is equal to that part of the radiance that is not attenuated by absorption or scattering (as $c = a + b$) plus the contribution of the radiance that is scattered from all angles projected onto the initial direction of radiances θ,ϕ.

4.3.2 Two-flow modelling

Beyond a certain depth the radiance distribution becomes diffuse and independent of the radiance distribution incident on the water surface, simplifying the solution of the RTE (see equation 4.5). Depending on the turbidity of the water body this occurs in the order of one to tens of metres below the surface. Near the water surface however, the radiance and irradiance attenuation coefficients are not equal and they depend on depth, providing a more complex situation. Here the RTE can at best be approximated by using one of the following three methods (see (Gordon, Smith, and Zaneveld 1984)):

1. The single scattering method, where photons are allowed to scatter only once in the medium.
2. The quasi single scattering approximation, where the forward part of the volume scattering function is replaced by a delta function but the actual part of the backward volume scattering function is used.
3. The two-flow modelling method, which is actually rewrite of the RTE and not an approximation. As is common practice in the field of radiative transfer, the downwelling and upwelling radiance distributions are assumed to consist of a totally diffuse radiance distribution plus a delta function representing the unscattered solar beam. The term two-flow modelling stems from the fact that both the downwelling and upwelling irradiance can only be solved when regarded simultaneously.

In the days when computing power was limited, the simpler (quasi-)single scattering approximations were preferred in cases where the ratio of the scattering coefficient b to the attenuation coefficient c was small (<0.05 for the single scattering method, < 0.7 for the quasi-single scattering method) (Gordon, Smith, and Zaneveld 1984), i.e. with relatively high absorption levels. The more complicated two-flow model was only used in cases where there was almost no absorption. With today's computers however there is no more reason left not to apply the more comprehensive two-flow model.

Expressions for the downwelling and upwelling irradiance can be derived by integrating equation 4.5 over all angles in the downward and upward hemisphere. With the definitions (Table 4.3.1) for the diffuse Inherent Optical Properties the derivation of the radiative transfer equations for irradiance (downwelling as well as upwelling) can be obtained, by integrating the RTE for radiance over all angles. After several steps of integration and rewriting (see Mobley 1994) the following transfer equation for downwelling irradiance can be derived:

$$\frac{dE_d}{dz} = -\left(a_d + b_{ud}\right)E_d + b_{du}E_u \qquad 4.6$$

Table 4.3.1: The diffuse Inherent Optical Properties descriptions and definitions (Dekker, Vos, and Peters 2001)

Symbol	Description and definition	Units and reference
a_d	diffuse absorption function for downwelling irradiance	m^{-1}
	$a_d \equiv \frac{a}{\bar{\mu}_d}$	Mobley, 1994b
a_u	diffuse absorption function for upwelling irradiance	m^{-1}
	$a_u \equiv \frac{a}{\bar{\mu}_u}$	Mobley, 1994b
b_{dd}	diffuse downward scattering function for downwelling irradiance	m^{-1}

	$b_{\mathrm{dd}} \equiv \frac{b}{E_{\mathrm{d}}} \int_{\Xi_{\mathrm{d}}} \int_{\Xi_{\mathrm{d}}} L(\theta',\phi')\bar{\beta}(\theta,\phi,\theta',\phi')d\omega' d\omega$	Mobley, 1994b
b_{uu}	diffuse upward scattering function for upwelling irradiance	m^{-1}
	$b_{\mathrm{uu}} \equiv \frac{b}{E_{\mathrm{u}}} \int_{\Xi_{\mathrm{u}}} \int_{\Xi_{\mathrm{u}}} L(\theta',\phi')\bar{\beta}(\theta,\phi,\theta',\phi')d\omega' d\omega$	Mobley, 1994b
b_{du}	diffuse downward scattering function for upwelling irradiance	m^{-1}
	$b_{\mathrm{du}} \equiv \frac{b}{E_{\mathrm{u}}} \int_{\Xi_{\mathrm{d}}} \int_{\Xi_{\mathrm{u}}} L(\theta',\phi')\bar{\beta}(\theta,\phi,\theta',\phi')d\omega' d\omega$	Dekker, 2001
b_{ud}	diffuse upward scattering function for downwelling irradiance	m^{-1}
	$b_{\mathrm{ud}} \equiv \frac{b}{E_{\mathrm{d}}} \int_{\Xi_{\mathrm{u}}} \int_{\Xi_{\mathrm{d}}} L(\theta',\phi')\bar{\beta}(\theta,\phi,\theta',\phi')d\omega' d\omega$	Dekker, 2001
c_{d}	diffuse attenuation function for downwelling irradiance	m^{-1}
	$c_{\mathrm{d}} \equiv \frac{c}{\bar{\mu}_{\mathrm{d}}} = a_{\mathrm{d}} + b_{\mathrm{ud}} + b_{\mathrm{dd}}$	Mobley, 1994b
c_{u}	diffuse attenuation function for upwelling irradiance	m^{-1}
	$c_{\mathrm{u}} \equiv \frac{c}{\bar{\mu}_{\mathrm{u}}} = a_{\mathrm{u}} + b_{\mathrm{uu}} + b_{\mathrm{du}}$	Mobley, 1994b
c_{dd}	local transmittance functions for downwelling irradiance	m^{-1}
	$c_{\mathrm{dd}} = a_{\mathrm{d}} + b_{\mathrm{ud}}$	Mobley, 1994b
c_{uu}	local transmittance function for upwelling irradiance	m^{-1}
	$c_{\mathrm{uu}} = a_{\mathrm{u}} + b_{\mathrm{du}}$	Mobley, 1994b
r_{d}	shape factor for upward scattering	-
	$r_{\mathrm{d}} \equiv \frac{b_{\mathrm{ud}}\bar{\mu}_{\mathrm{d}}}{b_{b}}$	Mobley, 1994b
r_{u}	shape factor for downward scattering	-
	$r_{\mathrm{u}} \equiv \frac{b_{\mathrm{du}}\bar{\mu}_{\mathrm{u}}}{b_{b}}$	Mobley, 1994b

In equation 4.6 the change in downwelling irradiance with depth is described, which is equal to the downwelling irradiance that is not diffusely absorbed or diffusely scattered upward plus the diffuse downward scattered part of the upwelling irradiance over that depth interval. Similarly the integration of the RTE over all angles of the upward hemisphere gives the irradiance transfer equation for the upwelling irradiance:

$$-\frac{dE_u}{dz} = -\left(a_u + b_{du}\right)E_u + b_{ud}E_d \qquad 4.7$$

The equations 4.6 and 4.7 form the two-flow model for the source-free case. Note that the downwelling irradiance:

- Decreases with depth because of absorption of E_d
- Decreases because of scattering of E_d into E_u
- Increases because of scattering of E_u into E_d

An analytical solution of the RTE for irradiance

Under certain conditions the two-flow model discussed in the previous section can be solved for the vertical attenuation coefficient K_d. Because the K_d is an Apparent Optical Property, it is discussed in more detail in section 4.4.2. The main assumption here is that the water is optically deep, allowing for bottom effects to be neglected. Furthermore it is assumed that the downwelling irradiance decreases exponentially with depth (in accordance with Beer's Law):

$$E_d\left(z\right) = E_d\left(z_0\right)\exp^{\left(-K_d z\right)} \qquad 4.8$$

where z_0 is the reference depth. Aas (Aas 1987) derives an analytical expression for K_d that includes multiple scattering effects by eliminating E_u in equation 4.6 (by inserting equation 4.7) and by subsequently inserting equation 4.8 into 4.6:

$$K_d \approx c_{dd} - \frac{b_{du}b_{ud}}{c_{uu} + c_{dd}} - \frac{b_{du}^2 b_{ud}^2}{\left(c_{uu} + c_{dd}\right)^3} - \cdots \qquad 4.9$$

In this study only the first and second order scattering are considered for simplicity. Note that by omitting also the second order scattering equation 4.9 reduces to a single-scattering model $\left(K_d \approx c_{dd}\right)$, which is often applied in the case of clear oceanic waters. When rewriting this analytical model (equation 4.9) substituting the used IOP by the easier to obtain absorption and backscattering coefficients (see Table 4.3.1 for definitions) we get:

$$K_d = \frac{a}{\bar{\mu}_d}\left[1 + r_d\frac{b_b}{a}\left(1 - \frac{r_u\bar{\mu}_d}{\bar{\mu}_u + \bar{\mu}_d}\frac{b_b}{a + kb_b}\right)\right], \quad k = \frac{r_d\bar{\mu}_u + r_u\bar{\mu}_d}{\bar{\mu}_u + \bar{\mu}_d} \qquad 4.10$$

Dekker *et al.* (Dekker, Vos, and Peters 2001) consider equation 4.10 as a suitable generic model that relates the total absorption and backscattering coefficient to the vertical attenuation coefficient and that is expected to be valid for both clear and turbid waters.

4.3.3 A generic (semi-)analytical model for the subsurface irradiance reflectance

Numerous authors have discussed the important intermediate role of the subsurface irradiance reflectance in many remote sensing applications on water quality. Various analytical models have been developed for the subsurface reflectance, which can be related to the remote sensing reflectance measured from (far) above the water surface.

The complete derivation of the analytical model for the subsurface irradiance reflectance by Aas (Aas 1987) can act as a reference for understanding all other analytical reflectance models in literature and will therefore be discussed first. In terms of the irradiance reflectance (see equation 4.4) the Aas model for the vertical attenuation coefficient (see equation 4.10) can be written as:

$$R(0-) = \frac{r_d \bar{\mu}_u}{\bar{\mu}_u + \bar{\mu}_d} \frac{b_b}{a + k b_b} \qquad 4.11$$

With k the parameter as given in equation 4.10. Equation 4.11 states that the $R(0-)$ is proportional to the backscattering divided by the sum of the absorption and the second order backscattering. In more detail, equation 4.11 gives that the $R(0-)$ is equal to a factor multiplied by the backscattering divided by the sum of the absorption and the second order backscattering, where the latter is multiplied by another factor. The first multiplication factor accounts for the downwelling shape factor and the average downwelling and upwelling irradiance cosines, while the second multiplication factor also corrects for the upwelling shape factor. Some other reflectance models found in literature are given below in Table 4.3.2:

Table 4.3.2: Analytical and semi-analytical models for the subsurface irradiance reflectance found in literature

Model	Reference
$R(0-) = \sum_{n=0}^{3} f_n \left(\frac{b_b}{a + b_b} \right)^n$	Gordon, Brown, and Jacobs 1975
$R(0-) = \frac{1}{1 + \frac{\bar{\mu}_d}{\bar{\mu}_u}} \frac{b_b}{a + b_b}$	Walker 1994
$R = \frac{r_\mathrm{d} \bar{\mu}_\mathrm{u}}{\bar{\mu}_\mathrm{u} + \bar{\mu}_\mathrm{d}} \frac{b_b}{a + k b_b}, \qquad k = \frac{r_\mathrm{d} \bar{\mu}_\mathrm{u} + r_\mathrm{u} \bar{\mu}_\mathrm{d}}{\bar{\mu}_\mathrm{u} + \bar{\mu}_\mathrm{d}}$	Aas 1987

From the comparison of the models summarised in Table 4.3.2 we see that the model in equation 4.11 is generic in the sense that most of the other models can be obtained by substituting approximate values for the Apparent Optical Properties (see section 4.4.2). For instance, if we set the shape factors to unity, we get the model of Walker (Walker 1994). In case of a diffuse upwelling light field ($\bar{\mu}_u$ = 0.5), the sun zenith is set to 0 and the backscattering term in the denominator is neglected, we get the well-known model by Gordon *et al.* (Gordon, Brown, and Jacobs 1975). Finally, if we assume unit shape factors and $\bar{\mu}_u = \bar{\mu}_d$ the exact solution given in Aas (Aas 1987).

For a more general applicability and because there is little information available yet on the shape factors, the Walker 1994 first model is preferred as it has the least assumptions. Recent publications show the possibility to generate look-up tables for the shape factors from numerous Hydrolight simulations. This would be an interesting option for calculations with large satellite images with strongly varying viewing and illumination conditions, but it is not necessary for the observations used in this dissertation. Other considerations here are the extra efforts and costs associated with using Hydrolight. Because the Walker model is an extension of the well-known model by Gordon *et al.* (Gordon, Brown, and Jacobs 1975) it will be referred to as the Gordon-Walker model from here onwards. The Gordon-Walker is used in this study, and will be discussed in more detail in the next section.

4.3.4 The Gordon-Walker optical model

The general challenge of this study (and similar remote sensing water quality studies) will be to find parameter sets that allow to equate simulated $R(0-)$ using analytical models with measured $R(0-)$. This concept, depicted in equation 4.12, forms the basis of optical modelling of water quality remote sensing.

$$R(0-)_{remote\,sensing} = R(0-)_{optical\,model}\begin{bmatrix} TCHL \\ TSM \\ CDOM \end{bmatrix} + e \qquad 4.12$$

With e a vector containing errors in the measured and modelled $R(0-)$, which are not discussed here and therefore further discarded for brevity. From the reflectance models discussed in the previous section, the Gordon-Walker model, (see equation 4.13), was chosen as the practical analytical approximation for the subsurface irradiance reflectance to be applied in this study.

$$R(0-) = f\frac{b_b}{a + b_b} \qquad 4.13$$

The f in equation 4.13 is a so called pre-factor, and defined as:

$$f = \frac{1}{1 + \frac{\bar{\mu}_d}{\bar{\mu}_u}} \qquad 4.14$$

with the $\bar{\mu}_d$ derived from the solar time using the latitude, date and time metadata that is recorded for every *in situ* reflection measurement and the $\bar{\mu}_u$ a constant with the value of 0.5, assuming a diffuse upwelling light field (Walker 1994).

The choice for the Gordon-Walker model is based on the following grounds:

- ➔ The parameters required by the model correspond with the parameters that could be determined with the available laboratory set up.
- ➔ The Gordon model can be easily linearised for analytical inversion methods.
- ➔ The Gordon model generally provides good performance (Vos, Peters, and Rijkeboer 1999)

Equation 4.13 contains two groups of parameters, 1) the Inherent Optical Properties (the absorption coefficient, the backscattering coefficient and the volume scattering function: to be defined and discussed in the next section, §4.4.1) and 2) the Apparent Optical Properties (the subsurface irradiance reflectance and the vertical attenuation coefficient) in section 4.4.2.

4.4 Parameterisation of the optical model

The parameterisation of the optical model was the second research question posed in the introduction of this chapter. Two types of parameterisation were shown in Figure 4.1: the (Specific) Inherent Optical Properties (in detail given by Figure 4.4) and the Apparent Optical Properties (in detail given by Figure 4.5). Both optical properties will be discussed in this section.

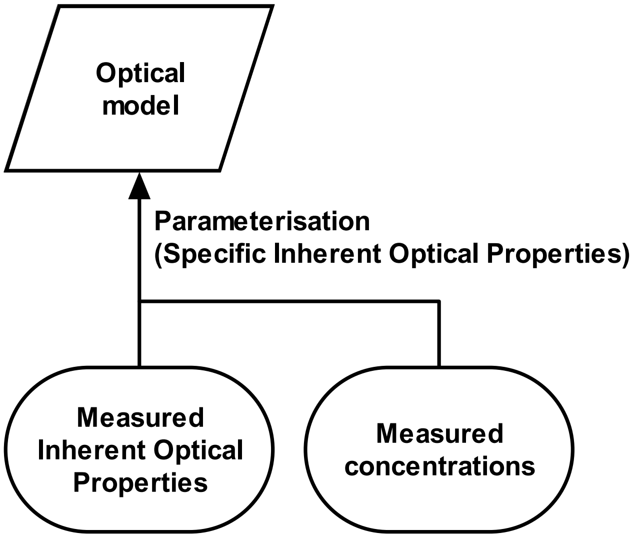

Figure 4.4: The parameterisation of the optical model with the Inherent Optical properties (detail of Figure 4.1)

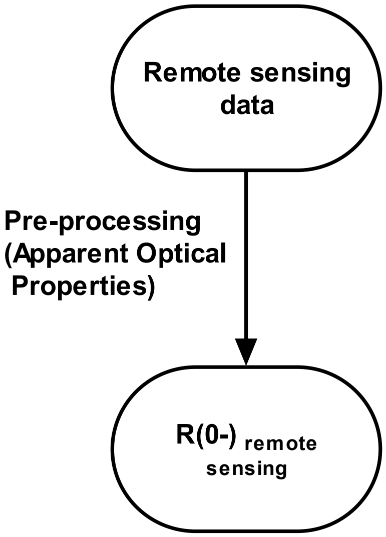

Figure 4.5: The parameterisation of the optical model with the Apparent Optical Properties (detail of Figure 4.1)

4.4.1 Inherent Optical Properties

The optical characteristics of a medium are summarised by its absorption and scattering coefficients and the volume scattering function. These three properties are called the inherent optical properties (IOP), because they are independent of the ambient light field within the medium and solely depend on the characteristics of the medium. In other words, the IOP remain the same regardless of the intensity and direction of the incident light. The inherent optical properties will be discussed in more detail below.

If Φ_0 is the radiant flux incident in the form of a parallel beam on a certain physical system, Φ_a is the radiant flux absorbed and Φ_b is the radiant flux scattered, then

$$A = \frac{\Phi_a}{\Phi_0} \tag{4.15}$$

and

$$B = \frac{\Phi_b}{\Phi_0} \tag{4.16}$$

That is, absorbance and scatterance are the fractions of the radiant flux lost from the incident beam, by absorbing and scattering respectively (Kirk 1994a).

The sum of A and B is referred to as attenuance C:

$$C \equiv A + B \tag{4.17}$$

In the case of an infinitesimally thin layer with thickness Δr, the very small fractions of the incident flux which are lost by absorption and scattering are expressed as the ΔA and ΔB respectively. The absorption coefficient a and the scattering coefficient b are the given by (Kirk 1994a):

$$a = \frac{\Delta A}{\Delta r} \tag{4.18}$$

$$b = \frac{\Delta B}{\Delta r} \tag{4.19}$$

Subsequently the fraction of the incident flux that is lost by absorption and scattering combined is called beam attenuation c and can be defined similarly but also calculated using a combination of equations 4.17, 4.18 and 4.19 (Kirk 1994a):

$$c = \frac{\Delta C}{\Delta r} = a + b \tag{4.20}$$

The scattering properties of the medium determine the angular distribution of the scattered flux. For each medium the angular distribution has a different shape; this characteristic is called the volume scattering function. The volume scattering function $\bar{\beta}(\theta)$ is defined as the radiant intensity I in a given direction θ (the zenith angle) from a volume element, dV, illuminated by a parallel beam of light E, per unit volume [$\mathrm{m}^{-1}\mathrm{sr}^{-1}$] (Kirk 1994a):

$$\bar{\beta}(\theta) = \frac{dI(\theta)}{E\,dV} \tag{4.21}$$

Usually a distinction is made between forward scattering b_f (scattering from the light beam in a forward direction) and backscattering b_b (scattering from the light beam in a backward direction):

$$b = b_f + b_b \tag{4.22}$$

Please note that in water forward scattering is regarded as directed downward and backward scattering is regarded as directed upward. The volume scattering function (see equation 4.21) is needed to calculate the backscattering coefficient b_b:

$$b_b = 2\pi \int_{\pi/2}^{\pi} \beta(\theta) \sin\theta \, d\theta \qquad 4.23$$

The forward scattering coefficient is calculated likewise and is omitted for brevity. For remote sensing water quality modelling purposes the backscattering coefficient b_b [m^{-1}] is of importance since this defines the amount of incident sunlight (mostly directed downward) scattered in an upward (water leaving) direction. Direct measurements of b and b_b *in situ* requires sophisticated instruments such as the ECO-VSF (of Wetlabs Inc., USA) or a HydroRAD (of Hydro-Optics, Biology, & Instrumentation Laboratories Inc., USA). In this thesis research, b is derived from the beam attenuation and absorption measurements. The b_b is calculated using the following equation:

$$b_b = B_w b_w + Bb \qquad 4.24$$

with B_w the forward- to backscatter ratio of pure water [-] usually set equal to 0.5, b_w the scattering coefficient of pure water [m^{-1}] from literature and B the forward- to backscatter ratio of the sample [-]. The B can either be set equal to a constant or it can be optimised in the calibration step in the optical modelling.

The parameters required by the Gordon-Walker model are the total absorption and the total backscattering (see equation 4.13). The total absorption a in this research is defined as the sum of the absorptions of N optically active water constituents:

$$a = a_w + \sum_{i=1}^{N} a^*_{Ci} C_{Ci} \qquad 4.25$$

With a_w the absorption of pure water, and a^*_{Ci} the specific absorption coefficients of water constituent C_i, $C_{C\,i}$ the concentrations of C_i.

The total backscattering b_b in this research is defined likewise as the sum of the identified backscattering water constituents (see equation 4.24)

$$b_b = 0.5 b_w + \sum_{i=1}^{N} B_{Ci} \, b^*_{Ci} C_{Ci} \qquad 4.26$$

With b_w the scattering of pure water, B_{Ci} the forward- to backscattering or Petzold ratio (Petzold 1972) for water constituent C_i, and b^*_{Ci} the specific scattering for C_i.

Specific optical properties

For optical modelling purposes the measured IOP values are divided by accompanying concentration values to yield the absorption and backscattering per unit concentration (the Specific Inherent Optical Properties - SIOP). The measurement protocols for the concentration, absorption and scattering are given in the next chapter.

4.4.2 Apparent Optical Properties

Apparent optical properties (AOP) are those properties that depend both on the medium and the geometric structure of the ambient light field, and that display enough regular features and stability to be useful descriptors of the water body (Mobley 1994). Examples of AOP are for instance the irradiance reflectance *R* and the diffuse attenuation coefficients (so called *K*-functions).

Vertical attenuation coefficients, such as K_d, are strictly spoken properties of the light field. The diffuse attenuation coefficients describe the decrease with depth of the ambient radiances. However in practice, close to the water surface as recorded by remote sensing, they are more dependent of the IOP of the aquatic environment than of the incident light field (because there is usually lots of light) (Kirk 1983), and therefore they are commonly used as optical properties of the water. The K_d is defined as the decrease of downward irradiance with depth [m^{-1}]:

$$K_d = -\frac{1}{E_d}\frac{dE_d}{dz} \qquad 4.27$$

The reflectance used for a solution of the RTE can be any type of reflectance; for this research the reflectance at an infinitesimal distance below the water surface is chosen, called the subsurface irradiance reflectance $R(0-)$. The $R(0-)$ is a very suitable descriptor of the underwater light field as it is independent of the light intensities and only slightly dependent on atmospheric conditions, solar elevation angle and the state of the water surface.

4.5 Inverse optical modelling methods

This section discusses the third and final research question from §4.1, finding correct inversion of the optical model. This is illustrated by Figure 4.6 (detail from Figure 4.1).

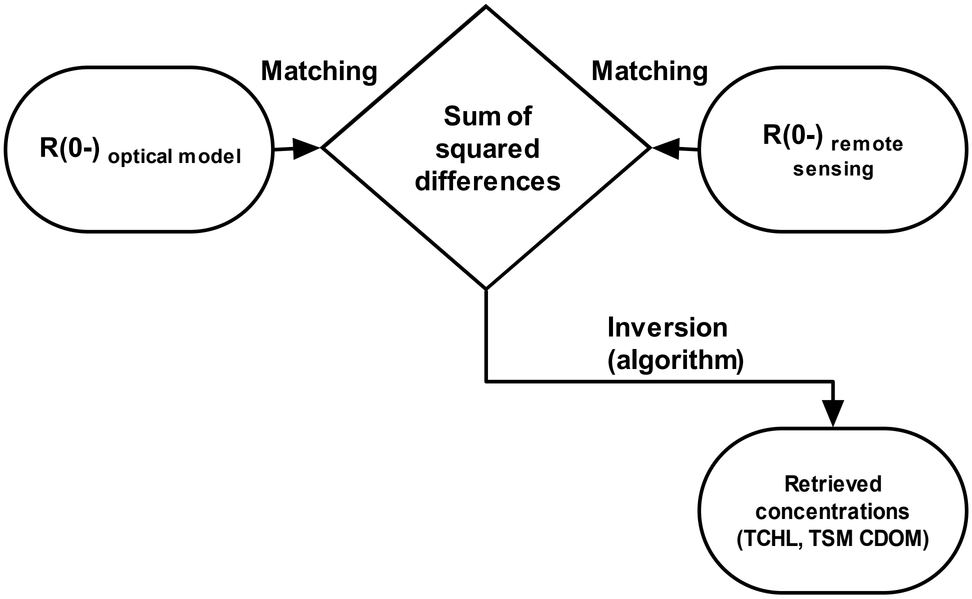

Figure 4.6: The inversion step of the optical (detail from Figure 4.1).

The inversion itself is performed using either a linear technique such as Matrix Inversion Methods or a non-linear optimisation technique such as Levenberg-Marquardt fitting.

Inverse optical modelling involves the retrieval of concentrations from measured AOP. There are several methods available for this of which we mention two, namely the non linear optimisation methods and the analytical inversion methods. In essence both inversion methods use a least squares approach to minimise the difference χ^2 between the measured AOP and the forward simulated reflectance spectra (see equation 8.1 for χ^2).

By means of the optimisation of the concentrations (with a fixed SIOP set) the difference between the measured AOP and the reflectance spectra simulated by forward modelling can be minimised. The concentrations found after optimisation are then the retrieved concentrations, i.e. the concentrations that most probably would have been present at the location where the AOP measurement was taken. With least squares the χ^2 value between the modelled and measured data is minimized by adjusting a vector with the concentrations. The concentrations that yield the lowest χ^2 value are then retained as the retrieved concentrations.

4.5.1 Matrix Inversion Method

There are a number of semi-analytical inversion methods suitable to derive concentrations from the Gordon-Walker model. The most general solution is formed by the Matrix inversion method (Hooge & Lyon 2003, Hakvoort, De Haan, Jordans, Vos, Peters, and Rijkeboer 2000; Hoogenboom, Dekker, and De Haan 1998). With MIM the problem is linearised first and then solved with singular value decomposition.

The Gordon Walker model requires an optically deep medium, i.e. the absence of bottom effects (e.g. bottom sight, submerged macrophytes). It also assumes that there is no stratification in the water column and that inelastic scattering (Raman scattering and fluorescence) does not occur. These conditions are usually fulfilled for Dutch inland waters, mainly because the turbidity is high.

Following the derivations made by Hoogenboom *et al.* (Hoogenboom, Dekker, and De Haan 1998) and substituting equations 4.25 and 4.26 for total absorption and backscattering properties in equation 4.13 gives:

$$R(0-) = \frac{1}{1+\frac{\bar{\mu}_d}{\bar{\mu}_u}} \frac{b_{bw} + \sum_{i=1}^{N} b^*{}_{bCi}}{a_w + b_{bw} + \sum_{i=1}^{N} (a^*{}_{Ci} + b^*{}_{Ci}) C_{Ci}} \qquad 4.28$$

providing an explicit relationship between the subsurface reflectance irradiance, the SIOP and the concentration data. This equation 4.28 can be linearised by rewriting it as a linear system of relationships M, x and y:

$$Mx = y \qquad 4.29$$

$$M = \left(R(0-)\left[1+\frac{\bar{\mu}_d}{\bar{\mu}_u}\right]\left[a^*{}_{Ci} + b^*{}_{bCi}\right] - b^*{}_{bCi}\Big|_{\lambda=1\ldots n} \quad \cdots \right) \qquad 4.30$$

$$y = \left(-R(0-)\left[1+\frac{\bar{\mu}_d}{\bar{\mu}_u}\right]\left[a_w + b_w\right] + b_w\Big|_{\lambda=1\ldots n} \right) \qquad 4.31$$

and the concentration vector:

$$x = \begin{pmatrix} C_{Ci} \\ \vdots \end{pmatrix} \qquad 4.32$$

The linear model given by equation 4.29 can be solved by using a simple least squares approach, retrieving the unknown concentrations x:

$$x = \left[M^T \cdot M\right]^{-1} \cdot M^T y \qquad 4.33$$

with A^T the transpose matrix of A.

Ratio Matrix Inversion

With Ratio Matrix Inversion the ratios between recorded bands are used as input for the inversion, instead of the original bands.

The advantage of using ratios is that they are less sensitive to scaling errors in the original bands. This method is known as the Ratio Matrix Inversion (RMI), and was introduced by Peters (Peters, Pasterkamp, and van der Woerd 2002) who showed that the band-ratio formulation of the Gordon-Walker model can be linearised. As a performance enhancement step, a sensitivity analysis can be carried out to determine if the information presented by a band ratio is significant in relation to the expected concentration range, excluding insignificant band ratios.

4.5.2 Levenberg-Marquardt (LM)

The method by Marquardt (based on by earlier work by Levenberg) is a non-linear optimisation technique. Here, the optimisation is performed iteratively. The iterations end when the similarity criterion chosen as the χ^2 value no longer decreases. The LM method can use two calculation techniques to achieve its goal: the inverse-Hessian and the steepest descent method, both of which are described in detail in Press *et al.* (Press 1989). Depending on the distance to the minimum the LM method can continuously switch between both methods. Firstly, the steepest descent method is used to find the global direction of the minimum. Secondly the inverse-Hessian method uses this information to calculate a more precise solution. These steps are repeated until an acceptable minimum has been reached (within the parameters given). LM usually takes a guessed value as starting point. One of the risks of this method is that a local minimum is found instead of the actual minimum.

4.6 Discussion and conclusions

In this chapter the theoretical background of (semi-)analytical optical modelling of water quality parameters was discussed. The Radiative Transfer Equation serves as the basis of modelling the underwater light climate. Because not all of the parameters of the RTE are known, a simplification is needed. The Two-Flow modelling concept was found to be the most suitable approximation of the RTE for this research. It leads to a solution of the RTE, in the form of the generic (semi-) analytical model for the subsurface irradiance reflectance by Aas (Aas 1987). The Aas model however still requires information on the elusive shape factors. Considering the parameters that could be determined within this research, a further simplification of the optical model was needed as provided by the Gordon-Walker semi-analytical model (Gordon, Brown, and Jacobs 1975; Walker 1994). This GW-model is known for its good performance in general; it has the least assumptions, its parameters could be obtained within this research and it can easily be linearised for inverse modelling. The input parameters: the Specific Inherent Optical Properties and the average cosines of the light field were also identified and discussed in this chapter in general terms. The required IOPs are absorption and scattering and concentrations of the optical water constituents.

The GW-model is parameterised by entering measured SIOP data and the average light field cosines. By comparing simulated $R(0-)$ to selected optimal measurements the parameterisation is verified and the model is further calibrated. Calibration is necessary to determine a representative value for the Backscattering coefficient.

After calibration, the GW-model is ready to be used in inverse mode to retrieve concentrations of CDOM and other water quality parameters from observed $R(0-)$ spectra.

The theoretical concepts of the inversion of the GW-model were explained in the last section of this chapter. Two commonly used inversion techniques are Matrix Inversion Methods (MIM and RMI) and Levenberg-Marquardt optimisation (LM).

In the next chapter the GW-model will be parameterised. The optically natural water constituents that are present in the study area will be identified and their SIOP determined. Also the determination of average cosines and the measurement of $R(0-)$ will be discussed in chapter 6. Finally the sensitivity of the GW-model and its parameterisation to errors in measured spectra and input SIOP set will be analysed in chapter 7.

5. Measurement of Inherent Optical Properties

5.1 Introduction

The IOP measurements required to parameterise the Gordon-Walker model are absorption a and backscattering b_b and the beam attenuation c. Recalling equations 4.25 and 4.26, the total absorption and total scattering can be determined by adding up the partial contributions of each optically active water constituent, including pure water Therefore the absorption and scattering of each optically active constituent present in the natural waters of interest has to be determined, together with the concentration of the constituent to be able to calculate its Specific Inherent Optical Properties or SIOPs.

In this chapter the optically active water constituents are identified in §5.2. The SIOP of the different water constituents are discussed in section 5.3. The measurement protocols for all of the SIOP are given in Appendix III.

5.2 Optically active water constituents

The optical properties of natural waters are determined by the biological, chemical and geological constituents present. Almost all particles are optically active in the sense that they contribute to the scattering properties. Natural waters are composed entirely of particles, ranging from the very small (<0.1 nm) to the very large (>10 m) (Mobley 1994). An overview of particles per size class is given in Table 5.1.

Table 5.1: Size classes and types of particles of natural waters

Size [m]	Particle type
1×10^{-10}	Water molecules
1×10^{-9}	Organic matter
1×10^{-8}	Organic matter, viruses
1×10^{-7}	Organic matter, viruses, bacteria, colloids, clay
1×10^{-6}	Phytoplankton, bacteria, colloids, clay, silt
1×10^{-5}	Zooplankton, phytoplankton, silt, sand
1×10^{-4}	Zooplankton, phytoplankton, sand
1×10^{-3}	Zooplankton, sand
1×10^{-2}	Zooplankton, fish
1×10^{-1}	Fish
1	Fish, man-made objects
1×10^{1}	Whales, man-made objects

The constituents of natural waters are traditionally divided into 'dissolved' and 'particulate' matter, of organic and inorganic origins, living and non-living (Mobley 1994). In this research, the primary division between natural water constituents is made based on size, followed by a grouping in organic or inorganic nature.

The distinction between dissolved and particulate or suspended matter is arbitrary: dissolved matter is defined as everything that passes through a filter with a nominal pore size of 0.45 µm, the residue on the filter is called suspended matter or seston. This threshold value is chosen because it coincides with the shortest wavelength of the visible light: 400 nm. Individual dissolved particles are thus too small to be detected optically as opposed to suspended particles. Oceanic studies even propose to lower the threshold value to 0.2 µm (Mueller and Austin 1992) in order to obtain more accurate dissolved matter absorption measurements.

Particulate organic matter is comprised of zooplankton, phytoplankton and organic detritus. Inorganic particles generally consist of sand, silt and clay minerals or metal oxides (Mobley 1994). Silt and clay are the most abundant in the study area. Clay minerals may be smaller than the 0.45 µm threshold value for particulate matter and thus end up in the dissolved fraction.

The following groups are part of the dissolved matter: Dissolved organic matter, viruses and bacteria. Viruses and bacteria, although present in great numbers 10^{11} - 10^{15} m^{-3}, fall outside the scope of this research. Dissolved Organic Matter (DOM) comprises of a broad range of organic compounds including colloids. A subgroup of DOM is its coloured fraction that can be determined by remote sensing: the Coloured Dissolved Organic Matter (CDOM).

Salt (mainly NaCL) usually dominates the dissolved inorganic matter pool. Dutch inland freshwaters typically have NaCL concentrations below 500 mg l^{-1} (Higler 2000). An average NaCL concentration of about 350 mg l^{-1} was found for the dataset collected for this research. These concentrations are too low to have a significant contribution to the scattering of water (Mobley 1994) and the suspended matter concentration used for optical modelling.

Incorporating all of the water constituents into a unified optical model with its own specific absorption and scattering properties is an unattainable goal because of restrictions of the amount manpower and measurement equipment available. However, Bukata *et al.* (Bukata, Jerome, Pozdnyakov D.V., and Kondratyev 1995) stated that the exclusion of zooplankton, algal fungi, dissolved gases and salts did not significantly deteriorate the applicability of their optical model.

In our study area, phytoplankton, CDOM and suspended matter concentrations are so high that the influence of all other possible optical active water constituents is regarded to be negligible. The IOP of viruses and bacteria, although possibly significant, could not be included in the optical model, for there are no practical methods for separating them physically in natural waters. Their absorption and scattering may influence the measurements of the beam attenuation and the CDOM absorption, but they are ignored in this study. In the next section the SIOP of natural waters based on these three constituents will be constructed.

The IOP of viruses and bacteria, although possibly significant, could not be included in the optical model, for there are no practical methods for separating them physically in natural waters. Their absorption and scattering may influence the measurements of the beam attenuation and the CDOM absorption.

5.3 The SIOP of natural water constituents required for optical modelling

5.3.1 An SIOP model suitable for this study

In the previous chapter it is explained that a SIOP dataset consist of the total absorption and the total scattering coefficients.

The total absorption coefficient a was already given in the previous chapter in a general form (see equation 4.25), and is now parameterised as:

$$a = a_w + a_{CDOM} + a_{ph} + a_{tr} \tag{5.1}$$

With a_w the absorption coefficient of pure water, a_{CDOM} the absorption coefficient of CDOM, a_{ph} the absorption coefficient of phytoplankton pigments and a_{tr} the absorption coefficient of tripton. The total absorption as given by equation 5.1 can also be expressed as SIOP:

$$a = a_w + \bar{a}_{CDOM} C_{CDOM} + a^*_{ph} C_{TCHL} + a^*_{tr} C_{TSM} \tag{5.2}$$

With $\bar{a}_{CDOM}$ the absorption coefficient of CDOM, C_{CDOM} the concentration of CDOM, a^*_{ph} the specific absorption coefficient of phytoplankton pigments, C_{TCHL} the concentration of total chlorophyll, a^*_{tr} as the specific absorption coefficient of tripton and C_{TSM} the concentration of total suspended matter.

The CDOM is only determined optically, and therefore it is not possible to calculate a concentration independent inherent optical property. Although it is possible to measure the concentration of Dissolved Organic Carbon, such measurements are not performed routinely in optical remote sensing studies. Furthermore, the relationship between the concentration of CDOM and the concentration of DOC varies considerably in literature (see chapter 2 on CDOM). As an alternative the modelled CDOM absorption is normalized at 440 nm in order to make it more or less independent of the concentration. The C_{CDOM} in equation 5.2 is thus an optical measure of the concentration of CDOM.

Likewise, the total backscattering b_b in this research is defined as follows (see equation 4.26):

$$b_b = B_w b_w + B\, b^*_{ses} C_{TSM} \tag{5.3}$$

with B_w the forward- to backscatter ratio of pure water [-] set equal to 0.5, b_w the scattering coefficient of pure water [m^{-1}] from literature (Buiteveld, Hakvoort, and Donze 1994) and B the forward- to backscatter ratio of the sample [-], b^*_{ses} the specific seston scattering and C_{TSM} the concentration of total suspended matter.

In conclusion, the IOP collected and used in this research contain the absorption and scattering properties and the concentrations of the following natural freshwater constituents:

1. The absorption and scattering of pure water
2. The absorption and (normalized) concentration of Coloured Dissolved Organic Matter, the only optically active dissolved constituent

3. The absorption and concentration of tripton
4. The scattering and concentration of seston
5. The absorption and concentration of phytoplankton pigments

These IOP are discussed in next sections, providing a general description per IOP, giving an overview of the methods used to determine the IOP and showing examples of the absorption and scattering spectra.

5.3.2 Pure water absorption and scattering

The absorption and scattering coefficients of pure water are considered to depend only on temperature and wavelength. The temperature dependency (a increases with increasing temperature) was avoided by performing all laboratory measurements at room temperature (22° C). The water surface temperature recorded in the field campaigns was around 20° C, allowing the use the same absorption and scattering values of pure water for inverse modelling. It was therefore decided to use absorption and scattering values of pure water from literature. The absorption spectrum of pure water, as determined by Pope & Fry between 350-727 nm and by Buiteveld beyond 727 nm (Pope and Fry 1997; Buiteveld, Hakvoort, and Donze 1994), is shown in Figure 5.1. The absorption of pure water increases with wavelength; at the blue and green wavelengths there is only weak absorption, at around 550 nm it starts to increase and at around 700 nm it increases significantly. Water absorption shoulders are present around 615 nm and 665 nm. It is often assumed that from 700 nm onwards the light absorption of the other water constituents (phytoplankton, tripton and CDOM) is negligible compared to the absorption of pure water.

The density fluctuation scattering of pure water, as determined by Mobley (Mobley 1994), is also shown in Figure 5.1. The scattering of pure water is relatively high in the blue wavelength region where the short wavelengths are of the same order of magnitude as the water molecules. Towards the larger wavelengths the pure water scattering decreases exponentially, approaching zero around 750 nm.

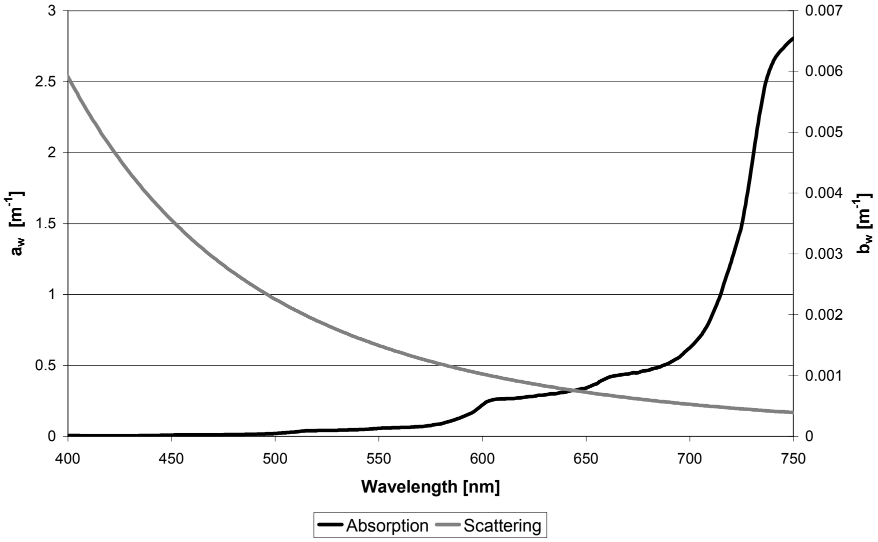

Figure 5.1: Absorption and scattering spectra of pure water (after (Pope and Fry 1997) for values between 400-727 nm and (Buiteveld, Hakvoort, and Donze 1994) for values beyond 727 nm).

Because pure water is the solvent of all natural water constituents, its own 'concentration' in the optical model is equal to 1 at all times.

5.3.3 Coloured Dissolved Organic Matter absorption and concentration

The currently accepted way of estimating the CDOM absorption spectrum is by measuring the absorbance in a dual beam bench spectrometer of the filtered sample against a reference, which is usually distilled water. The absorbance is measured in a standard bench spectrometer, where light passes through a cuvette containing the filtered sample or reference. The difference in attenuation of light between a 10 cm cuvette filled with reference fluid and a cuvette with sample gives the absorbance of the sample, as the influence of the light source, the spectrometer and absorption and scattering by pure water is cancelled out.

In this research another way of determining the absorption of CDOM was tested. Instead of measuring the attenuation of light passing through a cuvette, the attenuation of light in an integrating cavity was measured. Such a device, called the Point-Source Integrating-Cavity Absorption Meter (PSICAM) holds a number of theoretical advantages over the cuvette method (Kirk 1995; Kirk 1997). Detailed protocols for the cuvette and PSICAM CDOM absorption measurement methods are given in Appendix III. The PSICAM is extensively discussed in chapter 9.

CDOM absorption is characterised by a strong absorption in the blue wavelength region, exponentially declining towards longer wavelengths. This exponential shape is thought to be the theoretical form of CDOM absorption and measured CDOM absorption spectra are usually corrected by fitting an exponential function. The resulting exponential function, or modelled CDOM absorption, is then used for optical modelling.

Examples of normalised modelled CDOM absorption spectra are shown in Figure 5.2. Note that the slope of the exponential function varies. This is due to differences in composition of the CDOM material. The effect of the CDOM composition on the slope is discussed at length in chapter 10.

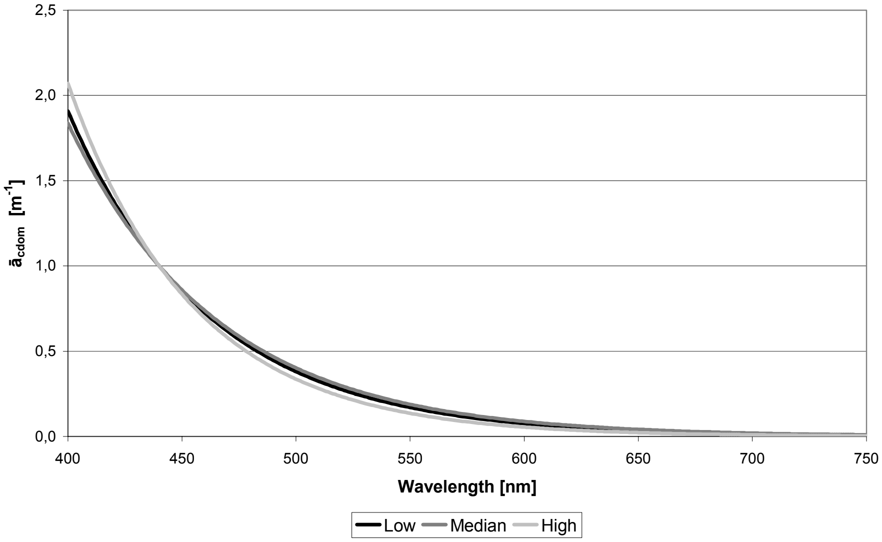

Figure 5.2: Examples of normalised modelled CDOM absorption spectra, based on high (Waterleidingplas), median and low (Terra Nova Troebel) slopes of the dataset collected for this research.

The scattering by CDOM, which may not be negligible contrary to common assumption, is small with respect to the scattering of tripton (see section 5.3.4), and was therefore neglected in the optical model. The validity of this assumption will be discussed in more detail in the chapter concerning the measurements conducted with a PSICAM (chapter 9).

5.3.4 Seston scattering

Other water constituents influencing the subsurface irradiance reflectance are the suspended particles (phytoplankton, inorganic particles and detritus), referred to as seston.

Seston absorption can be separated into phytoplankton pigments absorption and a rest-absorption called the tripton absorption (sometimes also referred to as the bleached seston absorption). Thus defined, the tripton absorption includes the absorption of non-pigmented algal biomass together with the absorption of inorganic particles and detritus.

The seston and tripton and phytoplankton pigments absorption spectra are determined using the filterpad method (see Appendix III). The seston absorption is measured on the filter. Next the seston is bleached and the bleached seston absorption (in this study refer to as tripton absorption) is measured subsequently also on the filter.

Since there was no in-situ measurement instrument for (back)scattering available, the total particle scattering was determined also from the filterpad method. Following this method the total particle scattering is measured as the difference between the measurement of the beam attenuation coefficient c and the measurement of the total absorption a (defined in this case as the sum of the absorptions of water, CDOM and seston).

The diameter of suspended particles (phytoplankton and tripton) is generally much larger than the wavelength of visible light making them efficient scatterers. It is assumed that the seston scattering dominates the total scattering properties of natural inland waters. Furthermore, it is also assumed that most of the seston scattering is contributed by tripton, because the concentration of tripton is typically about 100 times larger than the concentration of the phytoplankton pigments in the study area. Although large particles scatter strongly at small scattering angles, and thus contribute to b, they scatter only weakly at large angles, contributing relatively little to the backscattering.

Figure 5.3 shows examples of specific seston scattering spectra, showing the highest, median and lowest value spectra of the dataset. Please note that the shape of b^*_{ses} in these measurements is variable as a result of differences in particle size distributions. Many other shapes are theoretically possible.

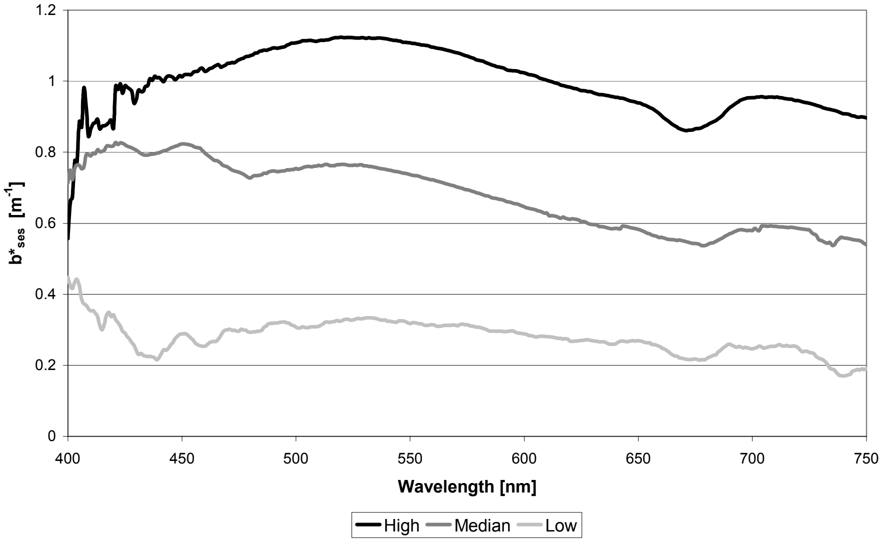

Figure 5.3: Examples of specific seston scattering spectra, showing the highest (Wijde Blik), median and lowest (Vecht River) spectra of the dataset. Note that the lowest value spectra are almost spectrally neutral, while the higher value spectra have relatively higher values in the blue-green area and lower values in the red, indicating that there are relatively smaller particles.

The specific seston scattering is obtained by dividing the seston scattering by the Total Suspended Matter concentration.

5.3.5 Tripton absorption

Tripton consists generally of inorganic particles and large breakdown products of phytoplankton (large enough to remain in suspension). However, in the Vecht Wetlands resuspended (organic) peat particles are also common. By definition, the size of the tripton particles exceeds the filter pore size used, which is 0.7 µm for this research. The phytoplankton cell material, once released, quickly loses its absorption characteristics due to photo-oxidation. The organic part of tripton is sometimes referred to as detritus (Mobley 1994), although strictly speaking the word detritus refers in general to remains of something that has broken up, so it would include both organic and inorganic matter in our case.

The tripton absorption spectra in this study are approximated by the absorption of bleached seston (seston minus pigments, but still including cell material), according to the filterpad method introduced by Trüper and Yentsch (Trüper and Yentsch 1967) and modified by Gilijamse (Gilijamse 1994) and Roesler (Roesler 1998). Therefore the tripton measured in this research also comprises of non-pigmented phytoplankton material.

Tripton has typical absorption properties that are assumed (in phytoplankton dominated waters) to be similar to those of CDOM (Kirk 1980; Davies-Colley 1983; Bricaud and Stramski 1990) and can be expressed with an exponential function, decreasing with increasing wavelength. To avoid measurement noise, an exponential function is fitted to the measured tripton spectra. This fitted function is used for optical modelling. Examples of modelled specific tripton absorption spectra are given in Figure 5.4, showing the highest, median and lowest value spectra.

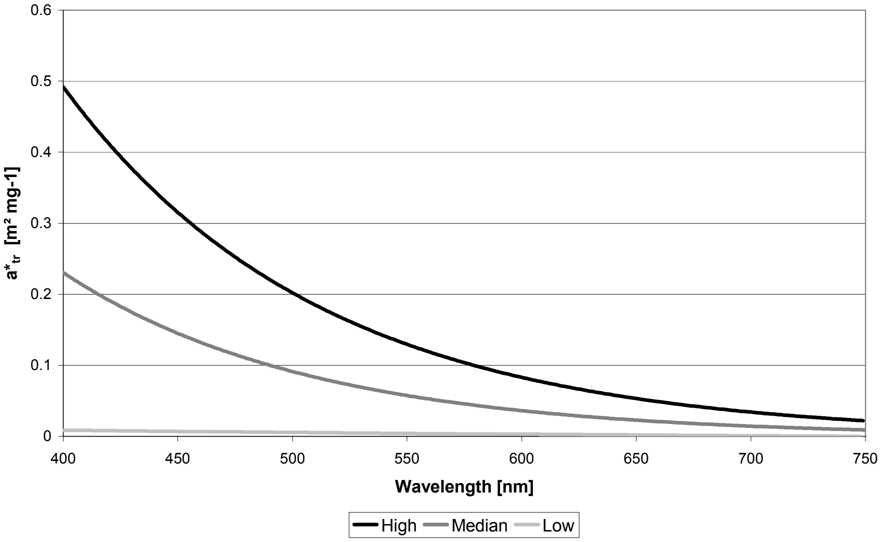

Figure 5.4: The modelled specific tripton absorption of the dataset, showing the highest (Lake Loosdrecht), median and lowest (Kortenhoef) spectra.

The tripton concentration is approximated by the Total Suspended Matter concentration.

The TSM concentration is determined by filtration over (pre-weighed) Whatmann GF/F 0.7 µm pore size filters and subsequent weighing of the dried filters and residue, according to the Dutch NEN protocol (NEN 6484 1982). The detailed TSM protocol is found in Appendix III. Please note that this dry weight also includes the phytoplankton pigments, but a correction is not performed because the phytoplankton pigment mass is on average about 100 times less than the tripton mass (see chapter 8). The tripton scattering could not be determined separately but is the largest contributor to the seston scattering described in the previous section.

5.3.6 Phytoplankton pigment absorption and concentration

Phytoplankton varies in size from sub-microsized (i.e. < than 1 µm) particles to particles with a diameter of 200 µm, depending on the species. It contains chlorophyll-α, β and related pigments (e.g. β-carotene and cyanophycocyanin), often dominating the spectral absorption of natural water in eutrophic lakes, because they absorb strongly in the blue and red wavelengths. As a result, algal-rich waters are characterised by a green water colour.

The true absorption spectrum of the algae present in a water sample (and their concentration) could not be measured in this research, because the algae and other particulate residue on the filters could not be separated. Instead the algal absorption is approximated by the difference between seston and tripton (bleached seston) absorption according to the filterpad method introduced by Trüper and Yentsch (Trüper and Yentsch 1967) and modified by Gilijamse (Gilijamse 1994) and Roesler (Roesler 1998). This because during the filter bleaching step the phytopigments are removed with hot ethanol (see protocol in Appendix III). By extracting with 80% ethanol at 75° not only the chlorophyll α and phaeopigments are released, but also the cyanophycocyanin pigments (from cyanobacteria). By bleaching the seston the pigments were removed, but not the cell material. The absorption of the non-pigmented phytoplankton cell material, however, is regarded to be part of the tripton absorption (see section on tripton).

The characterising blue and red *in vivo* chlorophyll-ɑ peaks centred at 438 and 676 nm can be seen in the specific phytoplankton absorption spectra shown in Figure 5.5. Another visible peak is the cyanophycocyanin absorption maximum at around 624 nm. Cyanophycocyanin is only present in blue-green algae (hence the name) and provides cyanobacteria a head start over their competitors as this pigment is able to carry out photosynthesis under nitrogen-limited conditions. The differences in the specific phytoplankton absorption spectra shown in Figure 5.5 are mainly caused by the abundance of different species at the sample locations (please note for instance the absence of a cyanophycocyanin shoulder in the low a^*_{ph} example of the Vecht River).

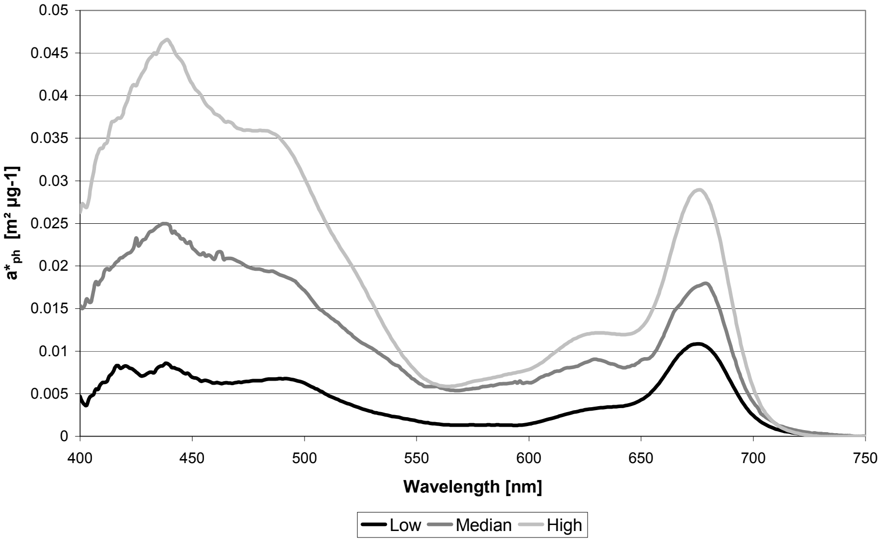

Figure 5.5: Specific phytoplankton absorption examples from the dataset, showing examples of high (Lake Loosdrecht) and low (Vecht River) absorption spectra and the median specific phytoplankton absorption spectrum of the dataset.

The absorption of the phytoplankton pigments (chlorophyll-ɑ and phaeopigments, or Total Chlorophyll) is determined photometrically by measuring the extinction coefficients at 665 and 750 [nm] before and after acidification of the residue of the filtered sample in accordance with the Dutch NEN protocol (NEN 6520 1981) (see appendix III). Please note that other pigments that can be present inside algae, such as chlorophyll-β, cyanophycocyanin and β-carotene for instance, are also included in the Total Chlorophyll absorption as a result of the bleaching process. No correction for this is applied.

The phytoplankton pigment scattering could not be determined separately in this research and is part of the seston scattering (see §5.3.4). However, since the phytoplankton concentration measured in this research only comprises of pigments, the contribution of phytoplankton scattering is expected to be small relative to the tripton scattering. The non-pigmented algal biomass is regarded as part of the tripton.

It is important to note the interdependence of some of the parameters: e.g. an underestimation of the total absorption will lead to an overestimation of the total scattering. An underestimation of the bleached absorption will lead to an overestimation of the phytoplankton pigments absorption. These effects may compensate when the coupled SIOPs are used to calculate spectral reflectance.

5.4 Discussion and conclusions

In this chapter the inherent optical characteristics of the optically active water constituents were introduced. These IOP serve as input for the Gordon-walker optical model selected in chapter 4. A total of four optical active constituents were identified: Pure water, CDOM, phytoplankton, and tripton. The absorption and scattering characteristics (IOP) of these four constituents were subsequently discussed. Although not an IOP, the concentrations of CDOM, phytoplankton, and tripton were also treated because they are required in order to obtain the Specific Inherent Optical Properties.

Due to restrictions posed by the measurement possibilities of this research some adjustments had to be made to the identified IOP. The concentration of CDOM could not be measured directly, so the C_{CDOM} is determined by taking the value of the CDOM absorption spectrum at 440 nm. As a consequence, CDOM has a normalised rather than a specific absorption spectrum. Furthermore, as it was not possible to separate the algae from the other particulate matter, the true phytoplankton absorption spectrum and concentration could not be determined. As a substitute, only the phytoplankton pigments were separated and analysed. The term ‘phytoplankton’ in this research therefore only applies to the chlorophyll ɑ and phaeopigments and not the total algal biomass. The non-pigmented algal biomass is included in the tripton absorption spectrum and concentration. Only the scattering of the complete sample could be determined in this research. Although the tripton is the largest contributor to the total scattering, influence from phytoplankton pigments and even CDOM may be present, hence the descriptor ‘seston scattering’.

A result of this chapter is that the IOP model as advocated by e.g. (Dekker, Brando, Anstee, Pinnel, Kutser, Hoogenboom, Peters, Pasterkamp, Vos, Olbert, and Malthus 2001) is confirmed based on the available instrumentation and the focus on CDOM.

Before the Gordon-Walker optical model can be applied, the measurement of the subsurface irradiance reflectance ($R(0-)$) will be elaborated in the next chapter.

6. The above water measurement of the subsurface irradiance reflectance

6.1 Introduction

In this chapter the transformation of the remotely sensed signal into the subsurface irradiance reflectance is explained. Many interactions between sunlight and optically active substances in the water and the atmosphere influence the remotely sensed signal over a water body. Most of these interactions involve scattering and absorption processes, although fluorescence and reflectance (by macrophytes or the substrate) may play a role. An overview of the path of light emitted from the sun, through the water body and to the remote sensing detector, as well as the possible interactions along the way, is given in Figure 6.1.

The interactions depicted in Figure 6.1 include:

1. Absorption and scattering by substances in the water
2. Reflection by the air-water interface
3. Reflection by the lake bottom
4. Absorption and scattering by substances in the atmosphere

The signal as recorded by the remote sensing instrument may have been influenced by all of the processes listed above. However, with regard to water quality applications for remote sensing, the processes of interest are the absorption and scattering by substances in the water, assuming there is no bottom reflection.

In the next section (6.2) the theory of obtaining the $R(0-)$ will be explained. First an overview of the necessary corrections for interactions 3 and 4 will be given, followed by the principles for measuring the subsurface irradiance reflection (correcting for interaction number 2). The protocol used for above-water reflectance measurements with a hand-held spectrometer is discussed in §6.3, leading to the $R(0-)$ spectra in the research dataset. At the end of this chapter an example of forward and inverse modelling is presented (§6.3.2) in order to illustrate the problems in achieving possible closure between observed and modelled $R(0-)$ with respect to CDOM.

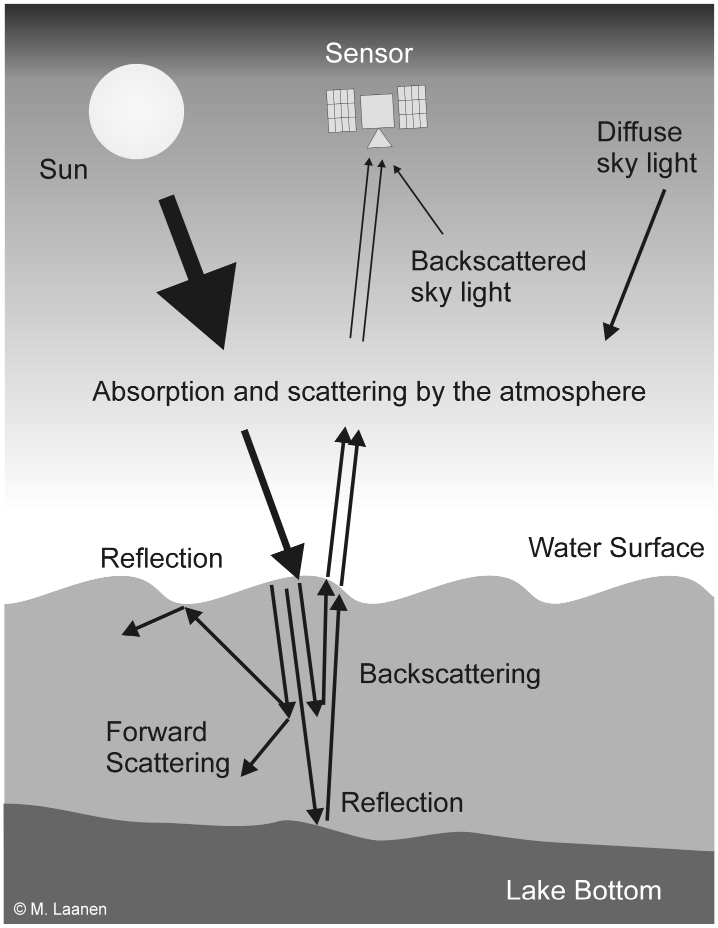

Figure 6.1: The path covered by light from the sun through the water body to the remote sensing sensor. The possible interactions are absorption and scattering by the water constituents, reflection and absorption by the lake bottom, reflection and refraction at the water/air interface and absorption and scattering by the atmosphere.

6.2 Measuring the subsurface irradiance reflectance

6.2.1 Correcting the remotely sensed signal

Absorption and scattering processes by the atmosphere

The underwater light field provides information about the water quality. However, the remote sensing instrument that is used to obtain this information is usually situated several kilometres above the water surface in the case of airborne remote sensing. When using satellites the distance is several hundreds of kilometres, as most environmental imaging satellites usually are in a polar orbit (300-1000 km altitude). The water leaving radiance thus travels large distances through the atmosphere before being recorded. Due to its relatively high particle density the bottom 2 km of the atmosphere is of greatest importance. During this voyage the photons may interact with the atmosphere. About 80% of the signal recorded by the instrument originates from light interactions in the atmosphere (Kirk 1994a), called path radiance, some 10% by interactions with the water surface and the remaining 10% is the result of interactions with the water column. Corrections must therefore be applied for the attenuation of the upwelling radiance between the surface and the sensor by the atmosphere and to subtract path radiance. In order to do so, an atmospheric correction model is applied, preferably assimilating information about the atmospheric conditions at the time of flight or overpass.

Atmospheric correction models are extensively discussed in literature {refs}. For this research however most of the remotely sensed data was gathered using a hand-held spectrometer just some 1.5 meters above the water surface. No atmospheric correction was performed on the data, as the atmospheric effects were considered negligible over this distance.

Reflection by the lake bottom

Whether or not bottom reflection has to be taken into account is determined by the vertical attenuation of light in the water column, the lake depth and the brightness (albedo) of the lake bottom material. An attenuation of the downward irradiance to 10% has to be reached throughout the water column in order to exclude bottom reflection influence. Of the 10% of the incident light that reaches the lake bottom, only a small fraction will be reflected. The lake substrates found in the study area typically consist of peat that has a low albedo, so only a small amount of light will be reflected. In turn, the water column attenuates most of this reflected light. An attenuation of 90% is achieved at an optical depth of 2.3 (Kirk 1994a). The optical depth ζ [-] is defined as a depth with a certain diminution of irradiance:

$$\zeta = K_d z \tag{6.1}$$

Optical depth is a non-dimensional entity and it can correspond to different physical depths. During the *in situ* spectrometric measurements the Secchi Disk was used to approximate the optical depth. The bottom depth was determined by gently lowering the Secchi Disk until the bottom was reached. The Secchi Disk Depth SD [cm] (see e.g. Boulton and Brock 1999) is related to the K_d by means of the empirical relation found by Dekker *et al.* (Dekker, Malthus, and Hoogenboom 1994):

$$K_d = 1.44SD \tag{6.2}$$

Although the relationship between K_d and SD should incorporate the beam attenuation according to Kirk (Kirk 1983), especially in turbid inland waters. An alternative was however not at hand, as simulations with for instance the Hydrolight program (Sequoia Scientific Inc., USA, http://www.sequoiasci.com/products/Hydrolight.aspx) (Mobley 1998) fell beyond the scope of this research.

All of the sample stations used for this research meet the requirements for optically deep waters as the ζ value calculated using equation 6.1 exceeded the value of 2.3. Corrections for reflection by the lake bottom were therefore not required.

6.2.2 Principles of above-water reflection measurements

In chapter 4 it was defined that the reflectance R is the ratio between the upwelling irradiance E_u and downwelling irradiance E_d at a given point. Directly above the water surface, the surface reflectance is the ratio between the upwelling irradiance in the water and the downwelling irradiance in the sky:

$$R(0) = \frac{E_{au}}{E_{ad}} \tag{6.3}$$

The subsurface irradiance reflectance $R(0-)$ is the desired descriptor of the underwater light field. It is the reflectance at an infinitesimal distance below the water surface. Similar to equation 6.3 the $R(0-)$ is thus the ratio between the upwelling and downwelling subsurface irradiances (E_{wu} and E_{wd}) immediately below the water surface:

$$R(0-) = \frac{E_{wu}}{E_{wd}} \tag{6.4}$$

The upwelling subsurface radiance

Because direct measurements of the water leaving irradiance are complicated, E_{wu} is approximated instead by measuring the upwelling subsurface radiance L_{wu} [W m^{-2} sr^{-1}]:

$$E_{wu} = Q(\theta,\varphi)\, L_{wu}(\theta,\varphi) \tag{6.5}$$

where Q is a geometrical conversion factor, depending on the solar zenith angle θ and the azimuthal angle φ. It is often assumed for simplicity that the water surface layer is a perfect Lambertian reflector, resulting in completely diffuse and unpolarised upwelling radiance. In this case E_{wu} would be equal to πL_{wu}. The radiance distribution however is not Lambertian (Kirk 1983), and several studies have found that Q is significantly larger than 3.14. Literature values for Q in turbid inland waters are given in Table 6.1.

Table 6.1: Literature values of Q for different inland lakes under varying scattering and absorption ratios and sun zenith angle conditions (azimuthal angles unknown)

	Q-value	Lakes	Conditions
Kirk 1983	4.9	unknown	b/a ~1.0-5.0 θ ~ 45°
Bukata, Jerome, and Bruton 1988	4.80	Great lakes, USA	b_b/b ~0.013 θ ~ 60°
Gons 1999	3.2	Vecht Area	θ ~ 35 - 78°
Vos and Pasterkamp 2001	4.6	Lake IJsselmeer	b/a ~ 1.0 θ ~ 60°

The azimuthal angle for all above-surface reflectance measurements taken in this study is 135º (see §6.3.1). Although Kirk (Kirk 1983) states that the value of Q does not vary significantly with solar altitudes, the Hydrolight simulations of Vos and Pasterkamp (Vos and Pasterkamp 2001) showed that this is only the case under diffuse light conditions. Next to a variation with the θ and φ, there is evidence that Q also has a wavelength dependency. This wavelength dependency was predicted by Gordon and Morel (Gordon and Morel 1983) and quantified by Berthon and Zibordi (Berthon and Zibordi 2000). For turbid inland waters however, the influence of this variation in Q is considered to be small (Dekker and

Peters 1993; Vos and Pasterkamp 2001). It was therefore decided to include the variation with the solar zenith angle but not the wavelength dependency of Q in the calculations made in this research. The empirical relationship by Gons (Gons 1999), established for measurements under a water surface zenith and nadir angle of 42º, was chosen to determine Q [-]:

$$Q = \frac{m}{\mu_{ad}} \qquad 6.6$$

with m a linear regression factor (2,38 as found by Gons) and μ_{ad} the average cosine of light just above the water surface [-], calculated from the sun zenith angle at the time and geographical location of the measurement and the fraction of diffuse downwelling light above the water calculated from the reflection measurements.

Taking above-water reflection measurements is more practical than underwater measurements. Instead of L_{wu} therefore the above water upwelling irradiance L_{au} is obtained by the remote sensing instrument. The L_{wu} [W m^{-2} sr^{-1}] can be calculated by using the following relationship (Dekker 1993):

$$L_{wu} = (\frac{n^2}{1-r^0}) L_{au} = g\, L_{au} \qquad 6.7$$

with the refractive index n of freshwater (1.333) and the Fresnel coefficient for loss of radiance r^0 when light passes the air-water interface with a 0° angle of incidence (0.021), abbreviated with g as the conversion constant with a value of 1.84 for freshwater.

The radiance L_{water} [W m^{-2} sr^{-1}] measured by a spectrometer pointed towards the water surface however is not only the L_{au} but also any incident sky radiance that has been reflected by the water surface (L_s [W m^{-2} sr^{-1}]) into the direction of the detector:

$$L_{water} = L_{au} + L_s \qquad 6.8$$

In order to obtain L_{au}, an accurate estimation of L_s is therefore needed. The L_s is a portion of the total incident sky radiance L_{sky} [W m^{-2} sr^{-1}] at zenith angle:

$$L_s = \rho_{sky} L_{sky} \qquad 6.9$$

with ρ_{sky} the Fresnel reflection of sky radiance reflected by the water surface into the detector [-]. The ρ_{sky} actually depends on the direction, wavelength, wind speed, the detector FOV and the sky radiance distribution and is only equal to the Fresnel reflection in case of level sea surface and a uniform sky radiance distribution (Mobley 1999e). Often the value of 0.028 for ρ_{sky} derived by Austin (Austin 1974) is used. An ρ_{sky} of 0.0256 is applied to adjust the measured spectra to correct for the 42° angle of observation in case of a smooth water surface, while an ρ_{sky} of 0.0289 is applied in case of waves exceeding a height of 0.1 m. These ρ_{sky} values have been empirically derived by Gons based on data from 42 sample locations in Lake IJsselmeer (Gons 1999). The ρ_{sky} not only depends on the sea surface, but is also influenced by clouds. Using Hydrolight simulations, Mobley derived a ρ_{sky} of 0.0337 for clear sky conditions, decreasing to 0.0248 in case of a complete overcast sky (Mobley 1999d). Because of the good performance of the ρ_{sky} derived by Gons for Lake IJsselmeer, which is reasonable similar to the Vecht Wetland lakes, it was decided to use them for this research (0.0256 for a smooth surface and 0.0289 in case of waves).

Now the parameters required by equation 6.5 are sufficiently approximated and the upwelling subsurface radiance can be determined. The actual values of Q, g and ρ_{sky} however remain subject of discussion (Vos, Peters, and Rijkeboer 1999).

The downwelling subsurface radiance

The divisor in equation 6.4, the downwelling subsurface irradiance E_{wd} is defined as the part of the E_{ad} that has penetrated the water (Gons 1999):

$$E_{wd} = (1-\rho_{\Theta}(1-F))E_{ad} + (1-r_{dif})FE_{ad} + \rho_w E_{wu} \qquad 6.10$$

with ρ_{Θ} the reflectance of the direct solar beam of the water surface, r_{dif} the average reflectance of the water surface for diffuse skylight, F the fraction of diffuse to total downwelling irradiance and ρ_w downward reflectance of the diffuse upwelling irradiance against the water air interface. Equation 6.10 shows that the E_{wd} is comprised of three components:

1. Downwelling irradiance that has penetrated the water surface originating directly from the sun, which is the largest contributor to E_{wd} under sunny and partly cloudy sky conditions.
2. Diffuse downwelling irradiance that has penetrated the water surface composed of light that is scattered in the atmosphere. Under completely overcast conditions where there is no direct sunlight the diffuse light is the sole component of E_{wd}
3. Upwelling light within the water which did not penetrate the surface but was reflected back into the water is the smallest contributor to E_{wd}

The ρ_{Θ}, the reflectance of a direct beam of a perfectly smooth water surface, is calculated by the Fresnel coefficient of sunlight (Jerlov 1968) on a water surface, which can be obtained using the Julian date, time of day and geographical position:

$$\rho_{\Theta} = 0.5\frac{\sin(\theta-\theta_w)}{\sin(\theta+\theta_w)^2} + 0.5\frac{\tan(\theta-\theta_w)}{\tan(\theta+\theta_w)^2} \qquad 6.11$$

with θ the sun zenith angle and θ_w the sun zenith angle underwater, defined as:

$$\theta_w = \arcsin\left(\frac{1}{n\theta}\right) \qquad 6.12$$

For r_{dif} a value of 0.06 is advocated in literature (Kirk 1994a; Baker and Smith 1990; Preisendorfer 1976). The range of ρ_w is between 0.485 and 0.463 as determined by Austin (Austin 1974) for wind speeds increasing from 0 to 16 m s^{-1}. During the field campaigns an average wind speed of 3 – 4 m s^{-1} was experienced, resulting in an ρ_w equal to 0.48 (Austin 1974). The $\rho_w E_{wu}$ term covers the upwelling light with zenith angles greater than 48º, which will not penetrate the surface but will be reflected back into the water instead (see Figure 6.1).

The downwelling irradiance E_{ad} can be measured directly by using a cosine-corrected hemispherical diffuser or as is the case for this research the E_{ad} is derived from the L_{rs}, the radiance reflected from a highly diffuse and highly reflecting Lambertian panel using the following equation:

$$E_{ad} = \pi L_{rs} \qquad 6.13$$

As mentioned above, the downwelling irradiance consists of a direct and a diffuse component:

$$E_{ad} = E_{sun} + E_{dif} \qquad 6.14$$

The fraction of diffuse to total downwelling irradiance is given by:

$$F = \frac{E_{ad} - E_{sun}}{E_{ad}} \qquad 6.15$$

In the field it is however more convenient to determine the E_{dif}, or rather the L_{dif}:

$$F = \frac{E_{dif}}{E_{ad}} = \frac{L_{dif}}{L_{rs}} \qquad 6.16$$

Now all the parameters to determine E_{wu} using equation 6.10 are known, concluding the theoretical principles of obtaining the $R(0-)$. In the next section the field-based above-water reflection measurements using a hand-held spectrometer that were carried out in this research will be discussed.

6.3 Above-water reflection measurements using a hand-held spectrometer

6.3.1 Measurement protocol

In the previous section it was shown that the subsurface irradiance reflectance, can be determined by combining four radiance measurements: the total water leaving radiance L_{water}, the part of L_{water} that originates from reflected sky radiance at the water surface L_{sky}, the total downwelling radiance L_{rs} and the diffuse part of L_{rs}, L_{dif}. A complicating factor is that these radiances have to be measured under an angle because perpendicular measurements of the water surface and the sky will produce erroneous results. The water surface can act as a mirror (called 'sun glint') in this case and under sunny and partly cloudy sky conditions in summer a perpendicular sky radiance measurement will be influenced by direct solar radiation. A thorough treatise on the best measurement angles is given by Mobley (Mobley 1999c). The optimal angles identified by Mobley are discussed in the section on measurement geometry below. All measurements were taken following the protocol for obtaining the subsurface reflectance $R(0-)$ published by Gons (Gons 1999). In this protocol, the $R(0-)$ is expressed as follows, with the parameters used listed in Table 6.2:

$$R(0-) = \frac{Qg(L_{au} - \rho_{sky} L_{sky})}{[E_{ad}\{1 - \rho_{\Theta}(1 - F) - r_{dif} F\} + (0.48 E_{wu})]} \tag{6.17}$$

Table 6.2: The parameters used in equation 6.17 for obtaining the subsurface irradiance reflectance

Parameter	Definition and source	Units
E_{wu}	Upward irradiance just below the water surface, from equation 6.5	W m^{-2}
Q	Conversion coefficient for L_{wu} to E_{wu}, from equation 6.6	-
g	Conversion constant of L_{au} to L_{wu}, from equation 6.7 (g =1.84)	-
L_{au}	Upward radiance above the water at nadir angle (42º), from direct measurement	W m^{-2} sr^{-1}
L_{sky}	Radiance of skylight at zenith angle (42º), from direct measurement	W m^{-2} sr^{-1}
ρ_{sky}	Fresnel reflectance coefficient of sky radiance at the water surface at zenith angle (42º), from lookup table	-
ρ_{Θ}	Fresnel reflectance coefficient for sunlight, from equation 6.11	-
E_{ad}	Downward irradiance just above the water surface, from equation 6.13	W m^{-2}
r_{dif}	Average reflectance coefficient for diffuse light, from literature (0.06)	-
F	Fraction diffuse light of E_{ad}, from equation 6.16	-

Spectrometer

During the field campaign *in situ* spectrometric measurements were taken with a PR650 hand-held spectrometer (Photo Research, Chatsworth CA, USA), scanning with a 1º-viewing angle from 380 to 780 nm with an 8 nm Full-Width Half-Maximum bandwidth. The PR650 subtracts dark measurements and selects the integration times automatically. Maximum integration times, typically occurring at the L_{au} measurements, are in the region of 1 - 2 s. The reference panel was a ~99% reflecting Spectralon® plaque (of Labsphere Inc., New Hampshire, USA) which was manually shaded for the L_{dif} measurements.

The PR650 recorded the average of 10 consecutive spectra, minimising the influence of anomalies in the water or the sky that are accidentally targeted by the instrument's 1º-FOV. PR650 measurements were stored on a RAM card while in the field and processed on a laptop computer afterwards.

Measurement sequence and geometry

The (Gons 1999) protocol calls for a series of consecutive measurements, beginning with the water-leaving radiance L_{water}, then the downward skylight radiance L_{sky}, both at an angle of 42º (respectively at nadir and zenith viewing direction), followed by measurements on a calibrated Lambertian reflectance panel, first sunlight-exposed (L_{rs}) and then shaded (L_{dif}). The consecutive measurements of the Gons protocol are shown in Figure 6.2.

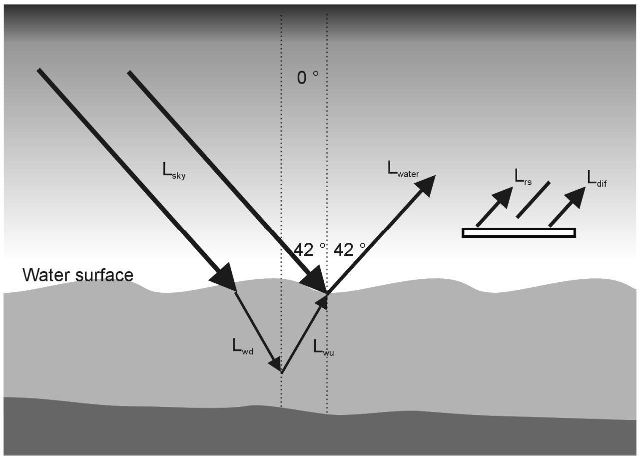

Figure 6.2: A schematic overview of the Gons protocol measurements. The $R(0-)$ is determined by four separate measurements of L_{water}, L_{sky}, L_{rs} and L_{dif}

The ratio of the two panel measurements makes up the E_{ad}. If there is no direct sunlight due to a completely overcast sky only one panel measurement was taken to obtain E_{ad}, as L_{rs} can be put on a par with L_{dif} under those circumstances. Usually three series of measurements are taken at each sample location and the average of the three measurements is taken as the $R(0-)$ spectrum of the sample location.

The spectral measurements were taken from a small boat or a jetty, at about 1.5 m above the water surface. The instrument was pointed in a direction of 135º out of the vertical plane of the sun to avoid sun glint, as is shown in Figure 6.3. When possible, measurements were performed at the side of the boat facing the sun preventing self-shading.

Although Gons prescribes an azimuthal angle of 90º, Hydrolight simulations carried out by Mobley showed that the optimum angle is 135º, a compromise between minimising shadowing problems and minimising the wind effects on the water surface (Mobley 1999b). In the field, the azimuthal angle of 135º was approximated by the PR650 operator.

The Gons protocol also calls for a polar angle of 42º, both in nadir and zenith viewing direction, as L_{water} is nearly constant in that region (Gons 1999). Although an angle between 30º and 40º would theoretically yield better results (Kirk 1983; Gons 1999 and Mobley 1999a) it is not implemented as this brings the danger of measuring in the shade or the reflection of the boat. In practice, a polar angle closer to 45º was attained, because it also had to be approximated by the PR650 operator.

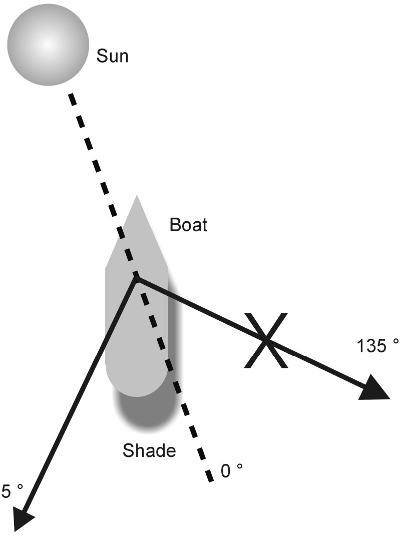

Figure 6.3: In order to avoid sun glint the spectral measurements (L_{au} and L_{sky}) were taken in a direction 135º out of the plane of the sun (0º). Of the two possibilities shown the port side measurement is recommended as there is no danger of self-shading or reflection contamination by the boat in this position.

6.3.2 Examples of measured radiance spectra

Upward radiance above the water at nadir angle

Two examples of measured upward radiance above the water at nadir angle (42º) L_{water} spectra are given in Figure 6.4. The turbid water measurement is taken in Lake Loosdrecht (C_{TCHL} = 104 µg l^{-1}, C_{TSM} = 16 mg l^{-1}, C_{CDOM} = 2.6 m^{-1}), the clear water spectrum originates from the Spiegelplas (C_{TCHL} = 6 µg l^{-1}, C_{TSM} = 2 mg l^{-1}, C_{CDOM} = 0.9 m^{-1}). Most spectral features are caused by scattering and absorption characteristics of the water body and will also be present in the $R(0-)$ spectrum calculated using the L_{water} spectra (see §6.3.3). The L_{water} of turbid waters is higher than that of clear waters, as suspended sediments are strong scatterers. Note however that the comparison between the two L_{water} spectra in Figure 6.4 is only allowed because the measurements were taken under conditions of comparable incident solar radiance.

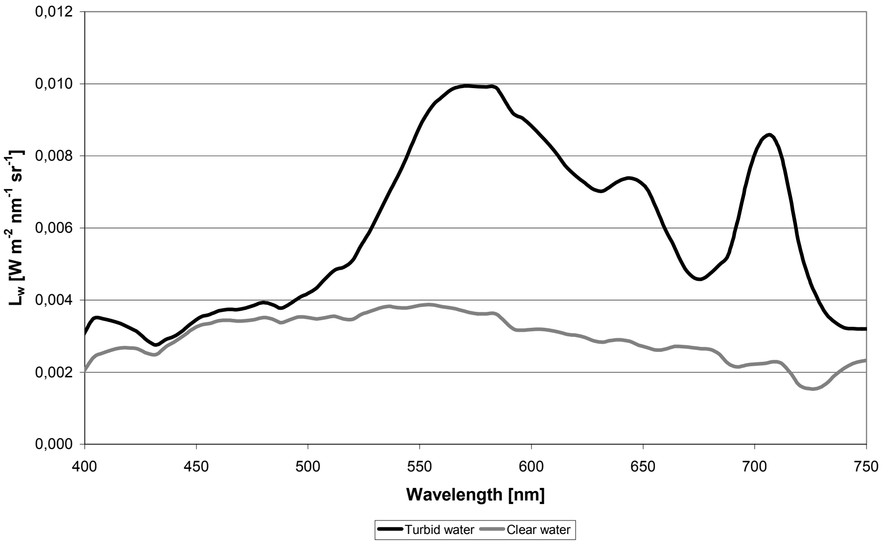

Figure 6.4: The L_{water} upward radiance above the water at nadir angle for a turbid water measurement (black line, Lake Oost Loenderveen) and a clear water measurement (grey line, Spiegelplas)

The total downwelling radiance and diffuse downwelling radiance

In Figure 6.5 some examples of total downwelling radiance and diffuse downwelling radiance spectra just above the water surface are given. The L_{rs} and L_{dif} spectra for sunny (taken at the Lake Loosdrecht station) and overcast sky (taken at the Spiegelplas station) conditions are shown. Note that under overcast sky conditions the L_{rs} is comprised completely of the L_{dif}, so $L_{rs} = L_{dif}$.

The downwelling radiance spectra share a number of spectral features that are caused by the shape of the extraterrestrial solar irradiance spectrum and the atmospheric absorption spectrum dominated by water vapour, ozone and oxygen. These features include:

- ➔ Low irradiance values at wavelengths below 400 nm as a result of the absorption by ozone layer in the atmosphere. In this research however only the wavelength region 400 – 750 nm is considered.
- ➔ A maximum irradiance at 480 nm for clear sky measurements. The maximum irradiance for more cloudy conditions shifts towards the shorter wavelengths.
- ➔ A gradual decrease in irradiance between 480 and 600, most prominent for clear sky measurements.
- ➔ A number of minima in irradiance caused by absorption bands of water vapour and oxygen in the atmosphere from 600 nm onwards.

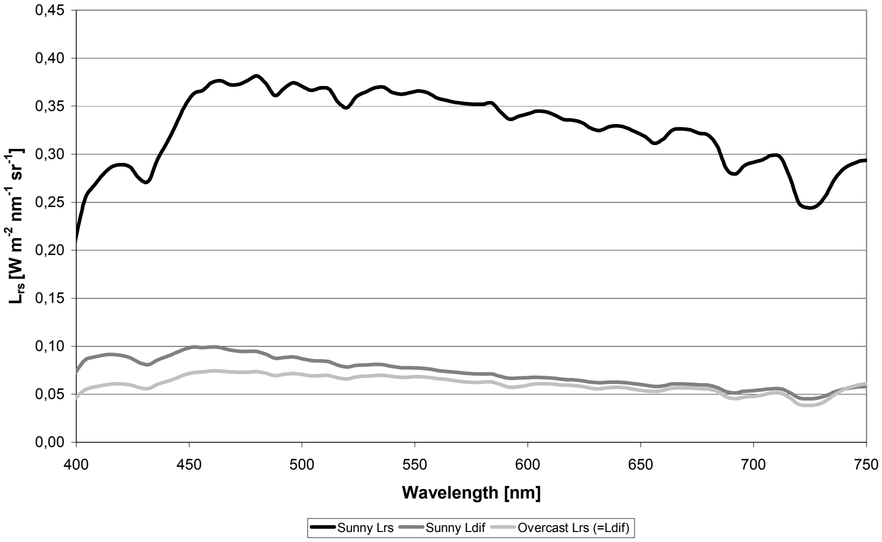

Figure 6.5: The panel and shaded panel radiance for a sunny sky measurement (black and dark grey line) and a completely overcast sky (light grey line only, as $L_{rs} = L_{dif}$ under overcast conditions) collected in Lake Oost Loenderveen.

Skylight radiance at zenith angle

Examples of the downwelling sky radiance are shown in Figure 6.6, one spectrum recorded under sunny conditions (taken at the Loosdrecht Lakes station) and one under overcast conditions (taken at the Spiegelplas station). The overcast L_{sky} is higher than the sunny sky L_{sky}, which can be explained by the fact that clouds are generally brighter than background sky, and the measurement is taken in a direction 135° out of the plane of the sun and a 42° zenith angle, minimising the influence of direct solar radiation.

Note the similarities between L_{sky} and L_{dif} spectra. The shape of the L_{sky} spectrum is also influenced by the extraterrestrial solar irradiance and the atmospheric absorption; clearly showing the water absorption bands around 700 nm. The L_{sky} and L_{dif} however are not equal, as the L_{sky} is measured at a 42° zenith angle (the same as the L_{water}) and the L_{dif} is measured using a Lambertian reflectance panel, averaging diffuse radiance from all directions.

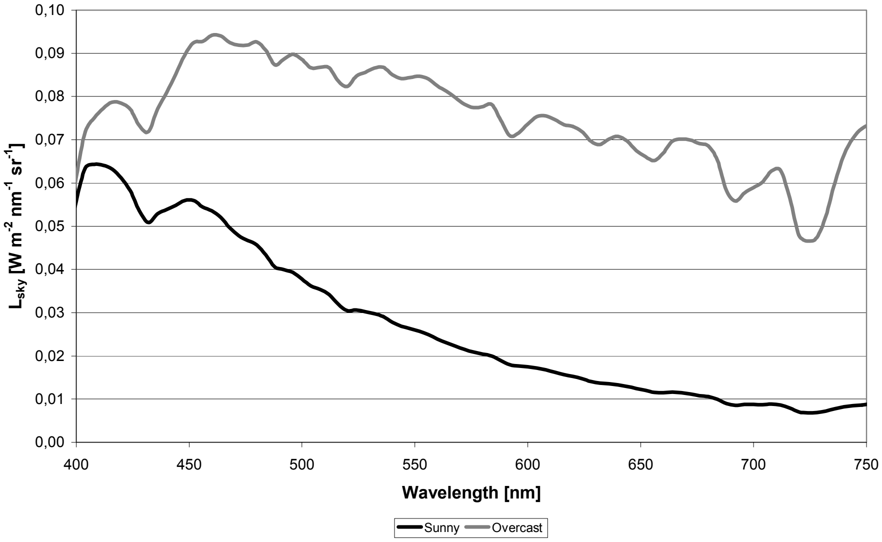

Figure 6.6: The skylight radiance at nadir angle for a sunny and cloudless sky measurement (black line) and a completely overcast sky measurement (grey line)

An ρ_{sky} of 0.026 is applied to adjust the measured spectra to correct for the 42° zenith angle of observation, and the standard freshwater value for g (1.84, Dekker 1993) was used.

6.3.3 The subsurface irradiance reflectance

In this section the resulting subsurface irradiance reflectance is discussed. Examples of $R(0-)$ spectra are shown in Figure 6.7, showing the average $R(0-)$ spectrum of the dataset (described in detail in chapter 8) and a turbid shallow lake and a clear deep lake type $R(0-)$ spectrum. The turbid shallow lake and a clear deep lake type $R(0-)$ spectrum correspond with the Optical Water Types 4 (“Large eutrophic peat excavations ”) and type 6 (“Deep clear lakes and tidal waters”) identified by Rijkeboer, studying the optical properties of over 100 Dutch inland waters (Rijkeboer 2000).

The turbid shallow lake $R(0-)$ spectrum (taken at the Lake Loosdrecht station) shows reflection peaks in the yellow-green part and the red part of the spectrum, indicating strong absorption in the blue and in the wavelength region between 600 and 700 nm. The absorption in the blue wavelengths is caused by CDOM, phytoplankton and tripton (in order of decreasing influence), while the absorption between 600 and 700 nm is caused predominantly by algal pigments. The overall height of the reflection spectrum is determined mainly by the TSM concentration. The height and shape of the Lake Loosdrecht $R(0-)$ spectrum can thus be explained by the measured relatively high concentrations of chlorophyll, TSM and CDOM (C_{TCHL} = 104 µg l^{-1}, C_{TSM} = 16 mg l^{-1}, C_{CDOM} = 2.6 m^{-1}).

The clear deep lake type $R(0-)$ spectrum (taken at the Spiegelplas station) shows only a peak in the yellow-green part of the spectrum, which is caused by relatively low concentrations of phytoplankton and CDOM. Analogous to the Loosdrecht Lakes spectrum, the shape of the Spiegelplas $R(0-)$ spectrum is explained by the measured relatively low concentrations of chlorophyll, TSM and CDOM (C_{TCHL} = 6 µg l^{-1}, C_{TSM} = 2 mg l^{-1}, C_{CDOM} = 0.9 m^{-1}).

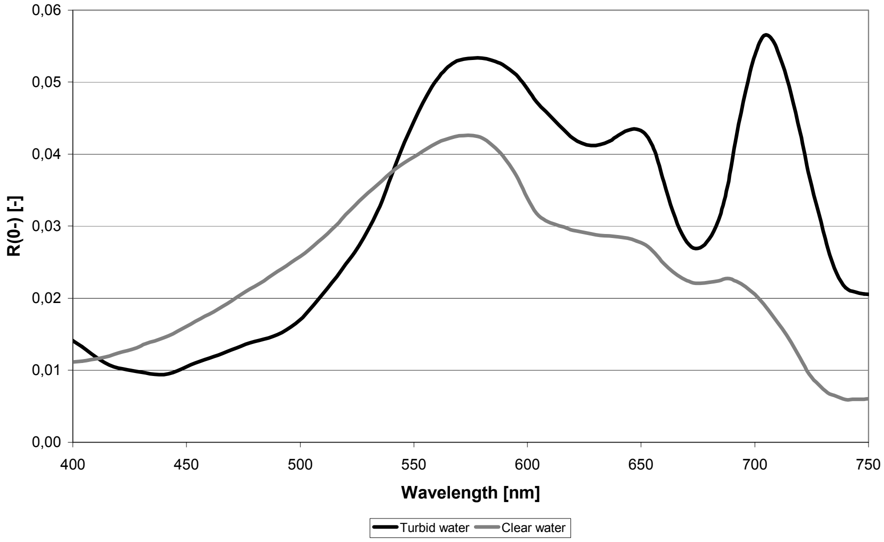

Figure 6.7: Examples of $R(0-)$ spectra, showing the $R(0-)$ spectrum of a turbid shallow lake (Lake Loosdrecht) and a clear deep lake type $R(0-)$ spectrum (Spiegelplas).

The resulting $R(0-)$ spectra is thus a complicated balance between the concentrations of TCHL, TSM and CDOM and their absorption and scattering characteristics, a reason why simple empirical methods (discussed in chapter 3) for water quality retrieval often fail.

6.4 Discussion and conclusions

In this chapter the parameterisation of the Gordon-Walker optical model was completed. The optical model was selected and described in chapters 3 and 4, while the SIOP model input was already identified and discussed in the previous chapter.

The Gordon-Walker optical model operates on the subsurface irradiance reflectance $R(0-)$. Because the measurements were taken just above the water surface, no atmospheric correction was applied. A correction for the bottom reflection was not required as calculations proved the sampled water bodies to be optically deep.

It was shown how the required $R(0-)$ is derived theoretically from above-water radiance measurements. The Gons method for above-water reflectance measurements, which is applied in this research, was also discussed. The measurement geometry was explained, as well as the air-water interface correction. Examples of the separate radiance measurements that make up the subsurface irradiance reflectances and the resulting $R(0-)$ spectra were given from the dataset collected for this research.

7. Sensitivity analysis of inversion of the bio-optical model using a simulated dataset

7.1 Introduction

In the previous chapters the theoretical framework of this research was laid out. A large number of implicit and explicit choices were made to, ultimately, allow the optical determination of CDOM. The following central problem now arises (see section 4.3.4):

$$R(0-)_{remote sensing} = R(0-)_{optical\,model}\begin{bmatrix} TCHL \\ TSM \\ CDOM \end{bmatrix} + e \tag{7.1}$$

whereby the challenge is to solve this equation for CDOM. Please note that in all equations in this chapter the spectral dependency is important but not shown to clarify the notation. On the right hand side of this equation we have the following system:

$$R(0-)_{optical\ model} = \frac{1}{1+\frac{\bar{\mu}_d}{\bar{\mu}_u}}\frac{b_b}{a+b_b} \tag{7.2}$$

with the total absorption and total backscattering coefficients

$$a = a_w + \bar{a}_{CDOM}C_{CDOM} + a^*_{ph}C_{TCHL} + a^*_{tr}C_{TSM} \tag{7.3}$$

$$b_b = B_w b_w + B\,b^*_{ses}C_{TSM}$$

and the $\bar{\mu}_d$ derived from the solar time using the latitude, date and time metadata that is recorded for every *in situ* reflection measurement and the $\bar{\mu}_u$ assumed to be a constant with the value of 0.5.

On the left hand of the equation we have another system:

$$R(0-) = \frac{Qg(L_{au} - \rho_{sky}L_{sky})}{[E_{ad}\{1-\rho_{\Theta}(1-F) - r_{dif}F\} + (0.48E_{wu})]} \tag{7.4}$$

with the following parameters (see section 6.2.2):

$$\rho_{\Theta} = 0.5\frac{\sin(\theta-\theta_w)}{\sin(\theta+\theta_w)^2} + 0.5\frac{\tan(\theta-\theta_w)}{\tan(\theta+\theta_w)^2} \tag{7.5}$$

$$\theta_w = \arcsin\left(\frac{1}{n\theta}\right)$$

$$E_{ad} = \pi L_{rs}$$

$$E_{ad} = E_{sun} + E_{dif}$$

$$F = \frac{E_{dif}}{E_{ad}} = \frac{L_{dif}}{L_{rs}}$$

It is important to realize that, to solve this complete system of equations for CDOM no further simplifications can be made. Optical CDOM determination requires hyperspectral observations of the spectrum between at least 440 and 750 nm of very high quality. It also requires a high quality parameterisation of the optical model. The approach to solve CDOM from equation 7.2 can be seen as an approach whereby CDOM is solved as rest term. The success of this approach is largely dependent on the following boundary conditions:

1. The system of equations provides sufficient closure (no parameters missed)
2. All parameters except CDOM concentration are sufficiently known

It is expected that both conditions will not be completely fulfilled because the optical model is a simplification and because e.g. the heterogeneity of optical properties can be very large. Therefore it is important to test the system of equations, by means of sensitivity studies to see under which uncertainty regimes CDOM still can be determined with sufficient accuracy. For this dissertation it was also important to identify those parameters that need improved measurement techniques or protocols in order to improve the accuracy of the optical determination of CDOM. Some of these improvements were already identified in the previous chapters (mainly related to the improved measurement of the optical characteristics of CDOM).

7.2 Inherent errors of parameters

There are a number of scalar parameters that influence the scaling of the measured or the modelled $R(0-)$. These parameters are: Q, g, ρ_{sky}, ρ_{Θ}, ρ_{Θ}, r_{dif}, ρ_w in the measured reflectance and B, $\bar{\mu}_d$ and $\bar{\mu}_u$ for the modelled reflectance. For scaling parameters such as Q and g, $\bar{\mu}_d$ and $\bar{\mu}_u$ the effect of errors would be a scaling error in the whole of the spectrum. Ignoring the spectral shape of Q introduces an unknown spectral error as well (Vos, Peters, and Rijkeboer 1999).

Errors in the ρ_{sky} cause insufficient compensation for skylight, which would typically result in over- or underestimation in the blue range of the observed spectrum.

The radiance measurements that make up the $R(0-)$ spectrum are all done with the same instrument in the same spectral resolution. This has as advantage that instrument noise is compensated for. The largest error that usually is made with these measurements is caused by sky-heterogeneity which causes the separately measured L_{sky} to differ from the L_{sky} as is seen in water leaving radiance measurement (which is contaminated with an at the surface reflected L_{sky} component). This error typically causes offsets over the entire wavelength range of the measured spectrum. Normally this error is prevented by filtering out $R(0-)$ measurements that have variable triplets.

The $\bar{\mu}_d$ and $\bar{\mu}_u$ parameters will cause a scaling error over the entire wavelength range of the modelled $R(0-)$ spectrum.

Errors in the SIOPs are also to be expected because of the inherent difficulties to make accurate observations of these parameters and because they can be very variable over space and depth (see Bricaud, Morel, and Prieur 1981; Babin, Stramski, Ferrari, Claustre, Bricaud, Obolensky, and Hoepffner 2003) for oceanic waters and Dekker 1993 and chapter 8 of this study for inland waters).

Errors in the concentrations of TCHL and in a^*_{ph} will introduce typical spectral errors caused by the shape of the specific phytoplankton absorption. Errors in the concentration of TSM (very likely in phytoplankton dominated waters and in salt water) will cause a combined effect: through the scattering term the scaling of the modelled spectrum will be affected; through the tripton absorption term an effect that is strongest in the blue region will occur. Errors in the tripton absorption or the seston scattering will cause similar affects on the spectrum. Errors in the CDOM absorption will also cause a deviation in the modelled spectrum that is strongest in the blue region similar to an error in the specific tripton absorption.

The last error term to be discussed is caused by B. This parameter is very difficult to measure (see section 4.4). Therefore it is often determined from sets of modelled and measured spectra together. By doing this, all scaling errors present are included in B which may cause a general compensation for these scaling errors. As long as B is optimised in this way for the water type under study, this compensation is effective. When literature values for B are chosen the compensation does not take place and additional scaling errors can be introduced. Ignoring the spectral shape of B also introduces an unknown spectral error in the modelled spectrum.

For the sensitivity study further on in this chapter one may conclude that it is important to study the following potential types of errors in the system of equations:

1. Errors in scaling factors
2. Offset errors in the spectrum
3. Spectral errors that increase towards the blue wavelength region
4. Spectral errors caused by not knowing the exact spectral shape of some parameters (including the a^*_{ph} and a^*_{tr})

7.3 Examples of forward and inverse modelling

To give an insightful example of the potential combined effect of all errors in this study, an analysis will be presented here in which the measured $R(0-)$ spectrum of a sample location (114_THN_2_C, see Appendix I and II) will be compared to the forward modelled $R(0-)$ spectrum. This simulated spectrum is based on measured concentrations and IOP data in order to obtain the best possible similarity with the *in situ* measured $R(0-)$ spectra.

The values for the anisotropy of downwelling irradiance correction factor f (from equation 7.2) and the (optimised) scatter to backscatter ratio B used for these simulations are 0.38 and 0.015 respectively. These values are discussed further in chapter 8. The results of the simulation are shown in Figure 7.1.

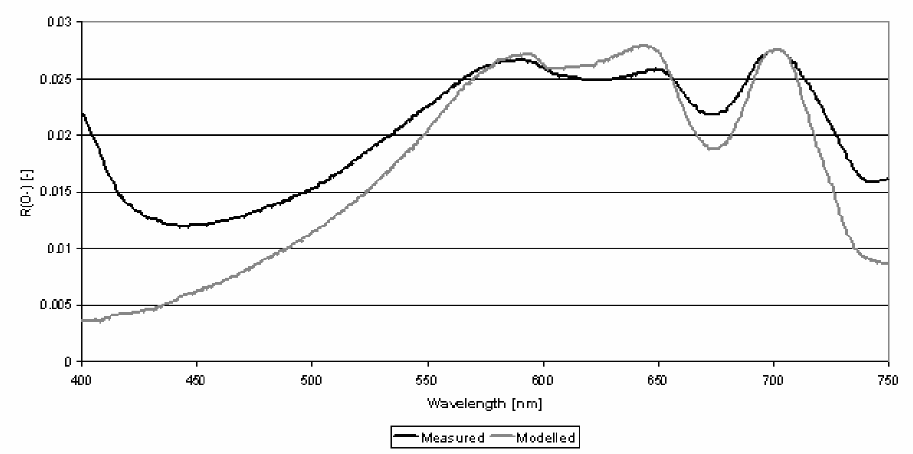

Figure 7.1: The measured $R(0-)$ spectrum (black line) and modelled $R(0-)$ spectrum (grey line) of sample location 114TNH_2_C

Various errors are present in the measured $R(0-)$ spectrum (offset, scaling and blue error) while it is unknown if and what errors there are in the SIOP set of the sample station.

An inversion of the optical model using the Levenberg-Marquardt technique (see §4.5.2) was also performed on the measured $R(0-)$ spectrum of sample station 114 TNH_2_C and its accompanying SIOP data. Using the same values for f and B as above, the measured $R(0-)$ spectrum was inverted. The measured SIOP concentrations and the retrieved concentrations for 114_TNH_2_C are shown in Table 7.1.

Table 7.1: The SIOP and retrieved concentrations of sample station 114TNH_2_C

	SIOP concentrations	Retrieved concentrations
C_{TCHL} [µg l^{-1}]	27.5	23.5
C_{TSM} [mg l^{-1}]	7.1	6.6
C_{CDOM} [m^{-1}]	4.33	2.93

Despite the notable errors in the $R(0-)$ spectrum, the retrieval accuracy of TCHL and TSM is still within a 15 and 6.5% difference with the reference concentration. For CDOM however the difference between retrieved and measured concentrations is 32%. The limited accuracy of CDOM retrieval is likely the result of the relatively large discrepancy between measured and modelled $R(0-)$ spectrum in the blue wavelength region (see Figure 7.1). In this case it is likely that the errors in the measured $R(0-)$ spectrum have accumulated in the CDOM retrieval.

7.4 The sensitivity of the Gordon-Walker model and its parameterisation

In the previous chapters of the optical modelling part a number of choices have been made regarding the choice of type and parameterisation of the optical model. Now the sensitivity of the optical model and its parameterisations will be determined. Such a sensitivity analysis serves two purposes:

1. To provide feedback on the consequences of the choices made with the parameterisation
2. To help identify areas in the optical model and its parameterisation which are important for CDOM and are suitable for improvement

With the sensitivity analysis a deliberate error is introduced in the subsurface irradiance reflectance data. These spectra are subsequently inverted and the resulting retrieved concentrations are then compared to the original concentrations. The sensitivity to two types of errors will be investigated: errors that directly influence the $R(0-)$ spectrum to be inverted and errors in the SIOP set used by the optical model during the inversion.

As a means to control the sensitivity analysis a simulated dataset will be used consisting of randomly generated concentrations. These concentrations are based on the concentration distribution of the samples collected in the Vecht Wetlands research area during this study. The accompanying $R(0-)$ spectra of the random concentrations have been generated by performing forward modelling.

7.4.1 Description of the simulated dataset using random concentrations

The sensitivity of the Gordon-Walker optical model is determined by the inversion of simulated subsurface irradiance data. After all, when no error is introduced, the retrieved concentrations should match exactly with the concentrations used to generate the $R(0-)$ spectra, because the very same optical model is applied in the forward and inverse operation. In this controlled environment the effect of a particular error (e.g. a scaling error in the $R(0-)$ spectrum) can be ascertained. This sensitivity analysis itself is performed in section 7.4.5, but the simulated dataset required is constructed in this section, as it is based on the measured dataset.

Simulated TCHL, TSM and CDOM concentrations and the measured median SIOP dataset of this research constructed and described in chapter 8 were used to generate a total of 1,000 subsurface irradiance reflectance spectra (based on the GW-model). These modelled $R(0-)$ spectra are used for the testing of CDOM retrieval algorithms.

7.4.2 Concentration distribution characteristics

Random concentrations of TSM, TCHL and CDOM were generated based on the average values and the covariance of the measured concentrations. It was decided to use concentration data from all 52 sample stations (see Appendices I & II), expanding the range of possible concentrations. The random number generation relies on a normal distribution. The distributions of the concentrations are given in Figure 7.2. Based on Figure 7.2 it was assumed that TCHL and TSM are distributed lognormal, and therefore the log values of the TCHL and TSM concentrations should be used for calculating the covariance. CDOM concentrations were assumed to be normally distributed and were therefore used as is.

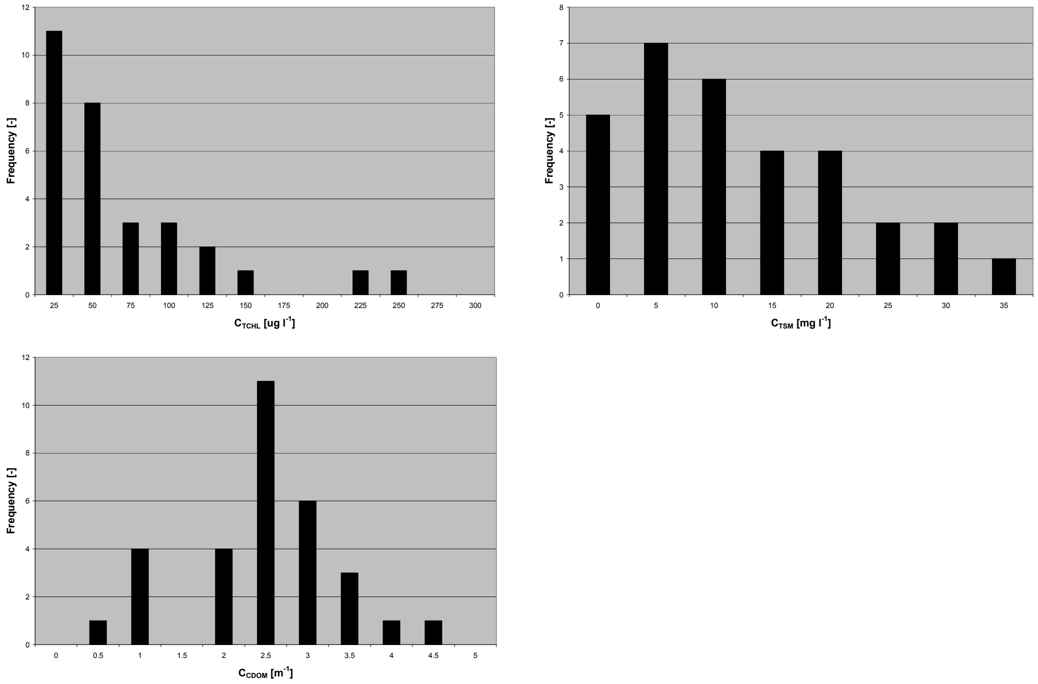

Figure 7.2: Histograms of the measured concentrations showing the type of distribution for TCHL (upper left), TSM (upper right) and CDOM (lower left). Values on the abscissa are concentrations; values on the ordinate are frequencies.

The covariance of concentrations of the complete dataset is given in Table 7.2. The covariance matrix provides two types of information:

1. The values on the diagonal are the variances of the concentrations; so the square roots of these values are the standard deviations (σ) of the log TCHL, log TSM and CDOM concentrations (1.3, 1.1 and 0.9 respectively). Please note that only sample locations with complete concentrations could be used for the covariance computation.
2. The other values in the table are a measure of the correlations between the concentrations. Table 7.2 shows that log chlorophyll and log suspended matter concentrations in the dataset are highly correlated (R^2 0.94). The correlation coefficient can be calculated using equation 7.6 below. There is also a low correlation between log chlorophyll and CDOM and log suspended matter and CDOM (0.43 and 0.32 respectively).

Table 7.2: Covariance matrix of the concentrations of the complete dataset (N =52) values in brackets on the diagonal are standard deviations, others are R^2 values

	Log TCHL	Log TSM	CDOM
Log TCHL	1.6 (1.3)	1.3 (0.94)	0.5 (0.43)
Log TSM	1.3 (0.94)	1.1 (1.1)	0.3 (0.32)
CDOM	0.5 (0.43)	0.3 (0.32)	0.8 (0.9)

$$R^2 = \frac{Covariance_{1,2}}{\sigma_1 \sigma_2} \qquad 7.6$$

7.4.3 Construction of the simulated dataset

Applying the distribution characteristics discussed above, a random number generator was used to generate 1,000 concentration sets of TCHL, TSM and CDOM. The average values of the simulated concentrations are 47.5 µg l^{-1}, 10.1 mg $l^{-1}$and 2.42 m^{-1} for TCHL, TSM and CDOM. These compare well with the measured average values of all 52 sample stations of 56.9 µg l^{-1}, 12.0 mg $l^{-1}$and 2.40 m^{-1} respectively (see chapter 8). The standard deviations of the generated concentrations are 27.1, 5.0 and 0.91 for TCHL, TSM and CDOM. The standard deviations of all 52 measured concentrations were 53.6, 8.4 and 0.84 m^{-1} respectively. As a result of the log-transformation the standard deviations of TCHL and TSM for the generated concentrations (see Table 7.2) are lower by a factor 2 compared to the standard deviations of the measured concentrations. The generated random concentrations are comparable in distribution, correlation, average and standard deviation to the measured concentrations of TCHL, TSM and CDOM.

7.4.4 Inversion techniques

Based on previous modelling experience the following three semi-analytical inversion methods are to be tested in this chapter:

1. Matrix Inversion Methods (MIM)
2. Levenberg-Marquardt optimisation (LM)
3. Ratio Levenberg-Marquardt optimisation (RLM)

The theoretical backgrounds of MIM and LM are already explained in chapter 4. MIM is a true mathematical technique where the optical model is linearised first and subsequently inverted, while Levenberg-Marquardt is an optimisation technique that uses non-linear least squares fitting in order to minimise the difference between the measured and forward modelled $R(0-)$ spectrum by adjusting the concentrations in several iteration steps. Note that the first two methods, MIM and LM, are performed on the actual bands, and that the only difference between the LM and RLM method is the use of band ratios with the latter. These band ratios were obtained by dividing two original bands, for each possible combination of bands, resulting in $N!$ number of ratios (N is the number of bands). In order to reduce the amount of data (without losing information), each combination of bands was only used once (i.e. Band1/Band2 was included, Band2/Band1 was not), and the diagonal in the band ratio matrix (Band1/Band1 etc.) was also excluded.

The band settings of three instruments were included in the sensitivity analysis: a hand-held spectrometer configuration, the band settings of the MERIS instrument and the band settings of the CASI instrument.

Hand-held, MERIS and CASI band settings

The original spectral data was acquired using a Photo Research PR650 spectroradiometer. This instrument measures over the range of 380 to 780 nm with a spectral resolution (expressed in FWHM) of 4 nm (see chapter 6). The spectral data was splined to per nanometre resolution and the section before 400 nm was discarded in order to make it compatible to the SIOP data (measured with the Ocean Optics SD2000, see chapter 9 and Appendix III). This data is referred to as the 'hand-held' band setting in this research.

Because this kind of hyperspectral remote sensing data is generally unavailable (in the case of airborne and spaceborne remote sensing data) the measured and simulated $R(0-)$ spectra were resampled to the multispectral band settings of two widely used imaging instruments: MERIS and CASI. The MEdium Resolution Imaging Spectrometer Instrument (MERIS), launched in 2002 by the European Space Agency, is designed to measure ocean colour, cloud top height, water vapour total column, and aerosol load over land. It is one of the most important satellite instruments for remote sensing of water quality at this moment. The Compact Airborne Spectrographic Imager (CASI) is an airborne scanner that has been used in 1993 and 1995 to collect remote sensing data of the Vecht Wetlands study area. The CASI instrument can be configured to a wide variety of band settings; the band settings used in this research correspond to the CASI Inland Water Mode used for the 1995 campaign (Hoogenboom, Dekker, and van Zetten 1996). Both instruments have 15 spectral bands, the location of the centre wavelengths of these bands is given in Table 7.3.

Table 7.3: The MERIS and CASI95 IWM band settings

Band	MERIS Centre wavelength (nm) [Band width (nm)]	CASI 95 Centre wavelength (nm) [Band width (nm)]
1	412 [10]	413 [19]
2	442 [10]	438 [19]
3	490 [10]	490 [19]
4	510 [10]	511 [17]
5	559 [10]	544 [19]
6	619 [10]	564 [9]
7	664 [10]	586 [9]
8	681 [7.5]	600 [9]
9	708 [10]	624 [9]
10	753 [7.5]	648 [9]
11	760 [3.8]	676 [9]
12	779 [15]	691 [9]
13	865 [20]	706 [9]
14	885 [10]	763 [9]
15	900 [10]	820 [11]

The conversion of the per-nanometre spectra to the MERIS and CASI band settings was performed using a spline function and the sensitivity curves of both instruments. Only the first 9 bands of MERIS were used for these algorithms because there was no original hand-held data available beyond 780 nm and the data beyond 750 nm is affected by noise. Analogous to the limitation of MERIS bands, the CASI band setting used was limited to bands 1 - 13 (see Table 7.3).

Two types of sensitivity analyses were performed: first the sensitivity of the inversion method with respect to errors in the measured subsurface irradiance reflectance spectra was tested in § 7.4.5, second the sensitivity of the inversion method with respect to errors in the SIOP data was tested in section 7.4.6.

7.4.5 Measured reflectance sensitivity analysis

In order to perform a sensitivity analysis a deliberate error is introduced in the simulated $R(0-)$ spectra. The subsequently retrieved concentrations after inversion are then compared to the original simulated concentrations. The correlations between the retrieved and simulated concentrations can be taken as a measure of sensitivity of the inversion method to the different error types. For optical models, such as the semi-analytical algorithms used, this correlation should be near perfect (R^2 around 1.00), because the $R(0-)$ spectra that are inverted are calculated using the simulated concentrations and the same optical model.
The following types of errors were introduced, based on error sources that have been identified in measured spectra (see Peters, Pasterkamp, and van der Woerd 2002:

1. Scaling error
2. White error (offset error)
3. Blue error
4. Cumulative error (implemented as the combination of errors 1-3 listed above)

Scaling error

A scaling error can occur e.g. during the transformation of measured above water reflectance to subsurface irradiance reflection, affecting the amplitude of the spectrum. The scaling error in this analysis is implemented by using either a 10% lower or higher value for the pre-factor f than the average calculated f (see chapter 8). The calculated average of f is 0.38, so the first 500 random generated spectra were inverted using a f value of 0.34 while the remaining 500 random generated spectra were inverted using a f value of 0.42. The effect of such a scaling error is demonstrated in Figure 7.3.

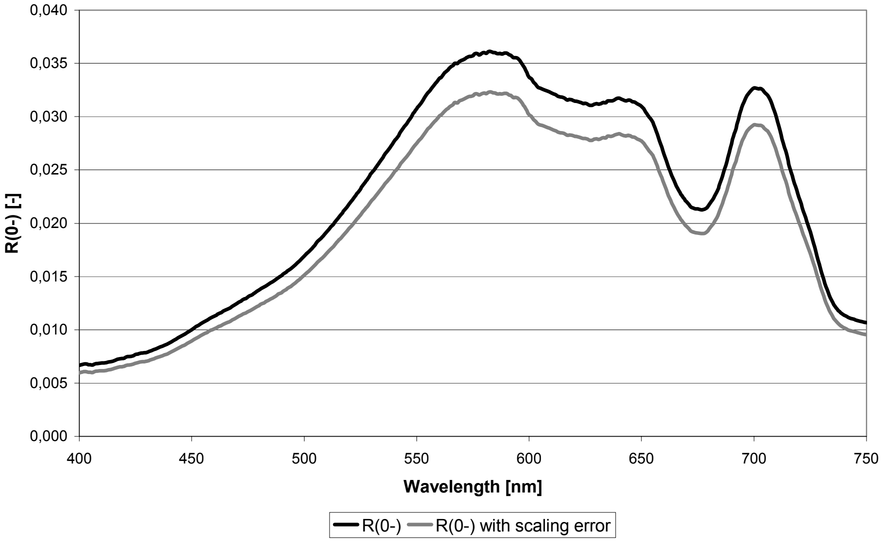

Figure 7.3: An example of the scaling error. The unaffected $R(0-)$ spectrum is shown in black (f value of 0.38), the $R(0-)$ spectrum with the scaling error is represented as a grey line (f value of 0.34).

White error

Here the entire spectrum has shifted, resulting in a higher reflectance compared to the 'true' reflectance. A negative shift was not implemented as it brings the danger of (partly) negative $R(0-)$ spectra, which cannot be inverted successfully (as negative concentrations are impossible). The source of this kind of error lies usually in the atmospheric correction. The white error is implemented by adding 10% of the value of the individual $R(0-)$ spectrum around the maximum height at 550 nm to the complete $R(0-)$ spectrum. This is graphically displayed in Figure 7.4, using one of the random spectra as an example.

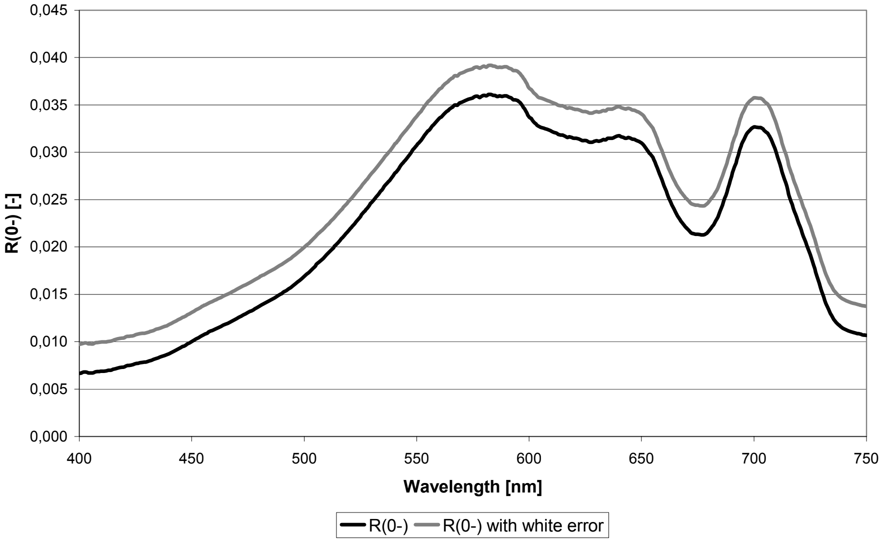

Figure 7.4: An example of the white error (10% reflectance error at 550 nm). The unaffected $R(0-)$ spectrum is shown in black, the $R(0-)$ spectrum with the white error is shown in grey.

Blue error

The signal-to-noise in the shorter wavelength part of the spectrum is generally lower as instrument sensitivity is limited and therefore the blue part is relatively more affected by for instance atmospheric processes, high diffuse light conditions and measurement noise. The blue error is implemented as by multiplying the $R(0-)$ spectrum with an exponential function. This exponential function is chosen in such a way that the $R(0-)$ value at the shortest wavelength (400 nm) will decrease by about 10%, while wavelengths beyond 500 nm are not affected. Equation 7.7 shows the blue error in mathematical form:

$$R(0-)' = R(0-)\frac{1}{0.1\exp(0.04(440-\lambda))} \qquad 7.7$$

with $R(0-)'$ the affected subsurface irradiance reflectance spectrum and λ the wavelength. The exponential function is graphically displayed in Figure 7.5, while the effect of the blue error is shown on one of the random spectra in Figure 7.6.

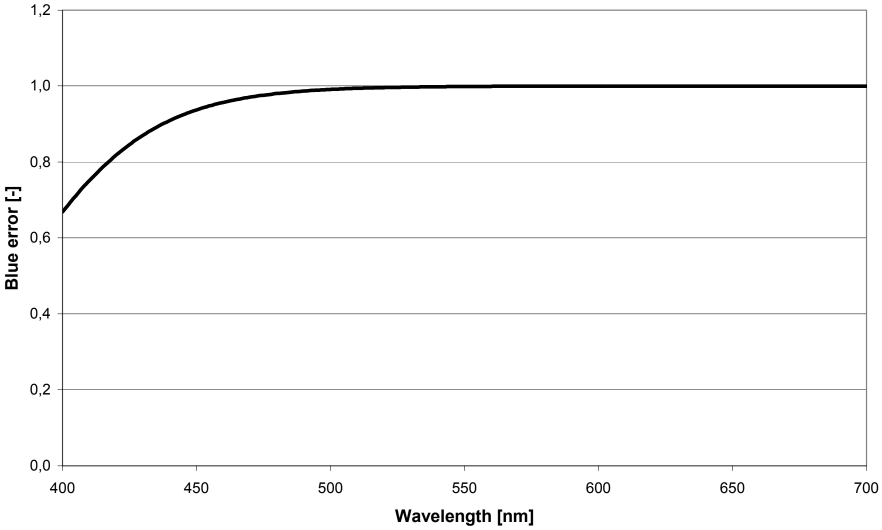

Figure 7.5: The blue error exponential function, resulting in a 10% lower $R(0-)$ value at 440 nm.

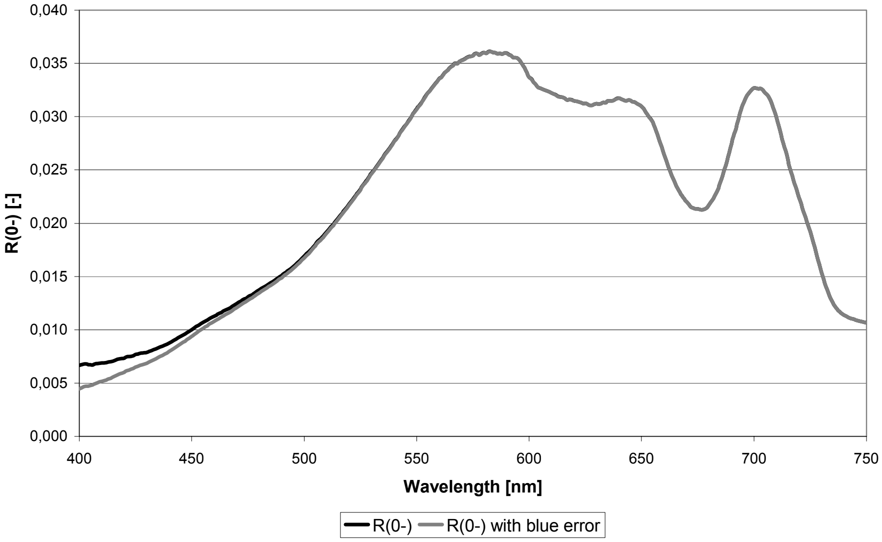

Figure 7.6: An example of the blue error (10% at 440 nm). The unaffected $R(0-)$ spectrum is shown in black, the $R(0-)$ spectrum with the blue error is shown in grey.

Results of the sensitivity analysis

The R^2 correlations between the 1,000 simulated concentrations and their retrieved counterparts using the different inversion techniques are shown in Table 7.4. The resulting correlations for the introduced scaling, white, blue and cumulative errors are also displayed in the same table. The R^2 values for the introduced errors are taken as a measure of the sensitivity of an inversion method to a particular error.

When no error is implemented all three inversion methods are capable of (near) perfect retrieval of TCHL, TSM and CDOM concentrations from spectral data in all three band settings (Hand-held, MERIS and CASI). The MERIS and CASI instrument band settings are therefore well chosen for water quality applications. All correlation coefficients are equal to 1.00, and the regression coefficients do not significantly differ from the y = x line.

The accuracy of the CDOM retrieval is the most affected in case of a scaling error (half of the spectra 10% too high, the other 10% too low value for f). The RLM method is not affected by the scaling error, because such a multiplicative error is cancelled out when using band ratios.

However, the RLM method is very sensitive to the white error (10% at 550 nm) for the retrieval of TSM and especially for CDOM, as this error is additive in nature, changing the ratios between bands. The R^2 value drops dramatically when a shift of the $R(0-)$ spectrum has occurred. Such a shift can be the result of poor atmospheric correction of an image, a common problem. This spectral shift will influence the band ratios that are used for RLM. The MIM performs slightly better than LM in case of a white error. As with the white error, the RLM method is most sensitive to the blue error (see above for details), and MIM the least. The applied blue error has the least effect on the inversions, relative to the scaling and white errors used. The sensitivity analysis showed that for all techniques and band settings the implemented white error was most influential.

When all errors are combined, the R^2 values for MIM and LM generally decrease, especially for CDOM (from 0.99 to 0.75). This is not the case for the RLM method.

Table 7.4: Matrix showing the R^2 and slope and offset values for each of the inversion techniques at the different errors introduced. Both the inversion techniques and the implemented errors are described in the text above.

			Handheld		MERIS			CASI		
			MIM	LM	MIM	LM	RLM	MIM	LM	RLM
No error	TCHL	R^2	1,00	1,00	1,00	1,00	1,00	1,00	1,00	1,00
		regression	y = 1.00x	y = 1.00x	y = 0.99x + 0.34	y = 0.99x + 0.32	y = 0.99x + 0.29	y = 0.99x + 0.26	y = 0.99x + 0.40	y = 0.99x + 0.15
	TSM	R^2	1,00	1,00	1,00	1,00	1,00	1,00	1,00	1,00
		regression	y = 1.00x	y = 1.00x	y = 1.00x + 0.04	y = 1.00x + 0.04	y = 1.00x + 0.04	y = 1.00x - 0.01	y = 1.00x + 0.01	y = 1.01x - 0.02
	CDOM	R^2	1,00	1,00	1,00	1,00	1,00	1,00	1,00	1,00
		regression	y = 1.00x	y = 1.00x	y = 1.00x	y = 1.00x	y = 1.00x	y = 1.01x - 0.01	y = 1.01x - 0.01	y = 0.99x - 0.01
Scaling error	TCHL	R^2	1,00	1,00	1,00	1,00	1,00	1,00	1,00	1,00
		regression	y = 0.99x + 0.14	y = 1.00x - 0.02	y = 0.99x + 0.36	y = 0.99x + 0.26	y = 0.99x + 0.29	y = 0.98x + 0.43	y = 0.99x + 0.37	y = 0.99x + 0.15
	TSM	R^2	0,92	0,92	0,91	0,91	1,00	0,91	0,91	1,00
		regression	y = 1.01x + 0.02	y = 1.02x - 0.03	y = 1.02x + 0.02	y = 1.02 - 0.01	y = 1.00x + 0.04	y = 1.02x + 0.01	y = 1.02x - 0.03	y = 1.01x - 0.02
	CDOM	R^2	0,87	0,86	0,88	0,87	1,00	0,85	0,85	1,00
		regression	y = 0.99x - 0.03	y = 1.00x - 0.03	y = 1.00x - 0.03	y = 1.00x - 0.03	y = 1.00x	y = 1.00x - 0.04	y = 1.00x - 0.04	y = 0.99x - 0.01
White error	TCHL	R^2	1,00	1,00	1,00	0,99	1,00	1,00	0,98	0,99
		regression	y = 0.84x +3.32	y = 0.90x + 2.26	y = 0.82x + 3.31	y = 0.85x + 2.91	y = 0.89x + 1.84	y = 0.82x + 3.40	y = 0.86x + 2.62	y = 0.88x + 2.44
	TSM	R^2	1,00	1,00	1,00	1,00	0,94	1,00	0,99	0,94
		regression	y = 0.98x + 0.83	y = 1.03x + 0.60	y = 0.98x + 0.86	y = 1.00x + 0.77	y = 1.21x + 3.29	y = 0.97x + 0.85	y = 1.01x + 0.69	y = 1.19x + 3.23
	CDOM	R^2	0,92	0,92	0,92	0,92	0,60	0,94	0,93	0,61
		regression	y = 0.81x - 0.06	y = 0.85x - 0.13	y = 0.79x - 0.05	y = 0.92x + 0.83	y = 0.44x - 0.22	y = 0.82x - 0.05	y = 0.87x - 0.12	y = 0.44x - 0.22
Blue error	TCHL	R^2	1,00	1,00	1,00	1,00	1,00	1,00	1,00	1,00
		regression	y = 0.99x - 0.03	y = 1.00x - 0.06	y = 0.99x + 0.26	y = 0.99x + 0.21	y = 0.93x + 1.62	y = 0.98x + 0.28	y = 0.98x + 0.30	y = 0.93x + 0.79
	TSM	R^2	1,00	1,00	1,00	1,00	0,99	1,00	1,00	0,99
		regression	y = 1.00x + 0.01	y = 1.00x	y = 1.00x + 0.04	y = 1.02x + 0.02	y = 0.78x - 0.31	y = 1.00x + 0.02	y = 1.00x + 0.01	y = 0.79x - 0.46
	CDOM	R^2	1,00	1,00	1,00	1,00	0,97	1,00	1,00	0,96
		regression	y = 1.02x + 0.04	y = 1.01x + 0.05	y = 1.02x + 0.05	y = 1.02x + 0.06	y = 1.16x + 0.33	y = 1.02x + 0.03	y = 1.01x + 0.05	y = 1.16x + 0.35
Cumulative error	TCHL	R^2	1,00	1,00	1,00	1,00	1,00	0,99	1,00	1,00
		regression	y = 0.84x + 3.35	y = 0.89x + 2.24	y = 0.83x + 3.26	y = 0.84x + 2.97	y = 0.86x + 2.01	y = 0.82x + 3.33	y = 0.73x + 2.53	y = 0.85 + 1.67
	TSM	R^2	0,89	0,91	0,89	0,90	0,98	0,89	0,90	0,98
		regression	y = 1.00x + 0.88	y = 1.04x + 0.65	y = 1.01x + 0.87	y = 1.02x + 0.78	y = 1.07x + 2.21	y = 1.00x + 0.89	y = 1.02x + 0.73	y = 1.05x + 2.09
	CDOM	R^2	0,77	0,76	0,78	0,77	0,92	0,75	0,75	0,94
		regression	y = 0.83x - 0.05	y = 0.85x - 0.09	y = 0.82x - 0.03	y = 0.84x - 0.06	y = 0.63x + 0.01	y = 0.84x - 0.04	y = 0.87x - 0.07	y = 0.63x + 0.04

Although the correlation coefficient is high, the CDOM concentration is underestimated by almost a factor 2 by the Ratio Levenberg-Marquardt method. The MIM and LM methods also have the tendency to underestimate CDOM (and TCHL) in this case, but less significant as RLM.

For all band setting combinations (hand-held, MERIS and CASI) there is no significant difference in the performance of the MIM and LM methods. The LM methods yields slightly better regression coefficients, probably due to the fact that this method optimises its solution rather than MIM, which has a 'fixed' solution. The per-nanometre hand-held bands give slightly but probably insignificantly better results than the MERIS or CASI bands.

In conclusion, the best inversion results are achieved by using the hand-held spectral information and the MIM or Levenberg-Marquardt algorithm. The hyperspectral information provided by the hand-held instrument therefore does contribute to CDOM retrieval accuracy. For the resampled band settings, the simulated MERIS bands are preferred, especially for CDOM retrieval. The RLM algorithm gives the best results for TCHL and TSM concentration retrieval.

7.4.6 SIOP sensitivity analysis

The most important error source with inverse optical modelling is introduced by the SIOP dataset used (Peters, Pasterkamp, and van der Woerd 2002). The effect of errors in the SIOP dataset was tested by replacing the median Vecht Wetlands SIOP set (as described in chapter 8) with another eutrophic inland water SIOP set, collected in Lake IJsselmeer, a large artificial lagoon located in the centre of the Netherlands. The Lake IJsselmeer SIOP are extensively described in Vos and Pasterkamp (Vos and Pasterkamp 2001), but for comparison purposes with the Vecht Wetlands SIOP set (see chapter 8) they are also graphically presented in Figure 7.7. The main differences with the Vecht Wetlands SIOP set are the specific phytoplankton absorption that is about three times lower and the specific tripton absorption and specific seston scattering that are about 3 - 4 times lower. The normalised CDOM absorption is similar for both SIOP sets. Because of time restraints a separate sensitivity analysis for errors in the phytoplankton absorption, the tripton absorption and the seston scattering was not performed. Instead, only the cumulative effect of SIOP errors was considered.

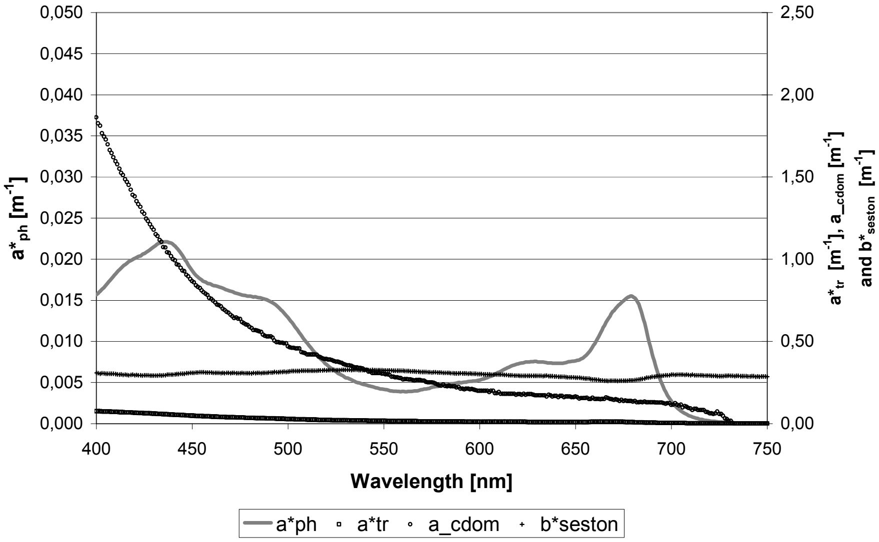

Figure 7.7: The specific absorption and seston scattering characteristics of the IJsselmeer SIOP dataset that is used to implement the SIOP error. The main differences with the Vecht Wetlands SIOP set are the specific phytoplankton absorption that is about three times lower and the specific tripton absorption and specific seston scattering which are about 3-4 times lower (see chapter 8). The normalised CDOM absorption is similar for both SIOP sets.

The sensitivity of the inversion methods to errors in the SIOP set

The results of the sensitivity analysis for errors in the SIOP set are given in table 7.5. As with the $R(0-)$ sensitivity analysis the Ratio Levenberg-Marquardt method scores high R^2 values, but suffers from a 1.5 to 3-fold overestimation (for both TCHL plus CDOM and TSM respectively). The LM method has weak correlation coefficients for CDOM, but the best slope parameters. The MIM results for TSM and CDOM are comparable to those for LM, but the SIOP error inhibits a successful TCHL estimation.

In conclusion, it is found that the MIM and LM inversion methods applied in this research are most sensitive to an error in the SIOP with respect to CDOM retrieval. The sensitivity to the imposed SIOP errors for TCHL and TSM retrieval however is small. The Ratio Levenberg-Marquardt technique is the least sensitive to the imposed SIOP errors with respect to CDOM retrieval. With RLM however it is the TSM retrieval that suffers most, a consequence of working with band ratios.

Regarding the results of the $R(0-)$ spectra and SIOP sensitivity analysis with respect to CDOM it was decided to discard the RLM method for inversion of the measured spectra in order to make the results more orderly. For the same reason the retrieved concentrations for the hand-held band settings are omitted in the following analyses.

Table 7.5: Matrix showing the R^2 and relationships for each of the inversion techniques per water quality parameter for the SIOP error analysis. Both the inversion techniques and implemented SIOP error are described in the text above.

		TCHL		TSM		CDOM	
		R^2	Slope + offset	R^2	Slope + offset	R^2	Slope + offset
Hand-held	MIM	0.99	y = 1.18 – 8.83	0.99	y = 0.99x + 0.45	0.58	y = 0.97x + 0.97
	LM	1.00	y = 1.24x – 7.71	0.99	y = 1.05x + 0.34	0.61	y = 1.08x + 0.88
MERIS	MIM	1.00	y = 1.36x - 10.30	0.99	y = 1.10x - 0.13	0.60	y = 1.11x + 0.77
	LM	0.98	y = 1.26x - 4.90	0.98	y = 1.02x + 0.59	0.67	y = 1.10x + 0.78
	RLM	0.99	y = 1.50x - 12.42	0.71	y = 2.70x - 12.64	0.96	y = 1.59x - 0.32
CASI	MIM	1.00	y = 1.29x - 9.45	0.99	y = 1.07x + 0.06	0.57	y = 1.01x + 0.87
	LM	1.00	y = 1.42x – 10.06	0.99	y = 1.17x – 0.33	0.58	y = 1.16x + 0.74
	RLM	0.99	y = 1.50x - 8.43	0.72	y = 2.67x - 12.19	0.97	y = 1.66x - 0.46

7.5 Discussion and conclusions

In this chapter the knowledge gap inhibiting the accurate retrieval of CDOM concentrations from remote sensing data has been identified, based on the optical model and its parameterisation that followed from the choices made in the theoretical chapters 3 – 6.

Because of its spectral shape and its relatively low abundance the influence of CDOM on the $R(0-)$ spectrum is small in comparison to the dominating TCHL and TSM spectral properties. As a consequence, the retrieval of CDOM is

1. Possible when using the Gordon-Walker optical model and its parameterisation as described in §7.1. Simpler models will not suffice.
2. Only possible while simultaneously retrieving TCHL and TSM
3. Performed as a rest term, affected by the cumulative effect of most of the errors in the $R(0-)$ spectrum and the SIOP set used

This was illustrated by forward and inverse modelling of a measured $R(0-)$ spectrum collected for this research that is affected by scaling and offset errors, while the errors in the measured SIOP set are unknown. Here, the forward modelled $R(0-)$ spectrum significantly differs from the measured $R(0-)$ spectrum (especially in the blue region). The error in CDOM retrieval of this $R(0-)$ spectrum is 2 to 4 times larger than in the retrieval of TCHL and TSM respectively.

Next two sensitivity analyses were performed in this study in order to establish the sensitivity of the model to errors in $R(0-)$ spectra and errors in SIOP data. To use a controlled dataset, a simulated dataset of 1,000 TCHL, TSM and CDOM concentrations was created, based on the median SIOP values and the covariance of the concentrations of the measured dataset for this research (see chapter 8).

Deliberate errors were added to the simulated $R(0-)$ spectra in order to perform sensitivity analysis. These errors include scaling, white and blue errors and a 'worst case scenario' where all errors are combined, the cumulative error. The magnitude of these errors was in the same order as observed errors in actual measurements (generally around 10% of the simulated spectrum at certain wavelengths). Robustness was expressed as the correlation coefficient value R^2 between the retrieved and simulated concentration values and the slope and offset parameters of the regression. The MIM method was least sensitive to errors in the $R(0-)$ spectra.

Next to the errors in the $R(0-)$ spectra, also a sensitivity analysis was performed introducing errors in the SIOP set used. Instead of the median SIOP set constructed in chapter 8, the Lake IJsselmeer SIOP set was put into the model. Its specific phytoplankton and tripton absorptions, as well as the seston scattering of this SIOP set are 3-5 times lower, although Lake IJsselmeer is also a turbid inland water system. The results of this analysis showed that the sensitivity for CDOM retrieval using the MIM and LM inversion methods to errors in the SIOP set is larger than to errors in the $R(0-)$ spectra, as was expected. For TSM retrieval the use of the Lake IJsselmeer SIOP set even results in better R^2 and regression parameter values. The slope and offset values for the TCHL retrieval however are significantly affected by the SIOP error. The Levenberg-Marquardt method was least sensitive to the SIOP error.

With respect to the retrieval accuracy of CDOM the sensitivity analyses have shown that the parameterisation choices made in the previous chapters have been correct. Because it is found that the sensitivity to errors in the SIOP set is larger than to errors in the $R(0-)$ spectra, the improvement of CDOM retrieval accuracy should be sought in the measurement of the SIOPs. In this research the focus is on improving the CDOM concentration and the shape of the CDOM absorption spectrum.

Part C: Improving CDOM retrieval accuracy analyses

8. Improving retrieved CDOM concentrations by state-of-art inversion of quality controlled measurement data

8.1 Introduction

In the previous chapter a sensitivity analysis was performed using representative settings for all model parameters. The objective of that sensitivity study was to test the performance of the optical model and inversion algorithms under different probable error conditions. Being a controlled exercise, its results are only valid within the framework of the chosen optical model and the SIOP dataset that was used to calibrate the model. The most important conclusions of this sensitivity study are that an accurate retrieval of CDOM is possible under controlled conditions and that the retrieval of CDOM is more sensitive to variations in the SIOP dataset than errors in the measured $R(0-)$ spectrum.

In this chapter the optical model and inversion algorithm performances will be further tested using actual data in the following steps:

1. Discussion of and selection of suitable measurement stations: a suitable sample station has a complete dataset of quality controlled Concentrations, IOPs and Spectra (CSI dataset). Description of the quality control procedures and rejection criteria (§ 8.2)
2. Determination of the optimized B per station as a means of reducing scaling errors in the measured $R(0-)$ spectrum (section 8.3.2)
3. Selection of those stations with suitable measurements of $R(0-)$ and SIOP using an approach whereby a normalized χ^2 criterion is used to find stations where the measured $R(0-)$ is sufficiently similar to modelled $R(0-)$ using per station calibration (section 8.3.4)
4. Calculation of the median SIOP over all suitable stations required for the inversion of the optical model (§ 8.4)
5. Evaluation of the errors in CDOM as a function of actual SIOP heterogeneity and inversion methodology
6. Inversion of the calibrated optical model (by using the median SIOP dataset and by using the SIOP dataset per station): Two candidate inversion methods will be tested in this chapter: Matrix Inversion Methods (MIM) and Levenberg-Marquardt optimisation (LM). It will be determined what inversion methods yields the best CDOM retrieval results (§8.5)
7. Identification of further improvements of CDOM retrieval under field conditions (improving the CDOM absorption spectrum shape and amplitude) (section 8.6).

8.2 Discussion of and selection of suitable measurement stations

From the field measurements data on Concentrations, Spectra and IOP (CSI-data) are available from 52 sample locations (See appendix I & II). Control procedures were set-up to identify and discard data of insufficient quality caused by traceable errors in the laboratory or field measurements. The suitability of the CSI data was in for instance determined by comparing measured concentration and SIOP data to literature values (this section).

Complementing this quality control, the bio-optical will be calibrated using the selected single station and averaged stations data on Concentrations and IOPS after which a comparison of measured and modelled data will be used to establish the quality of the measured subsurface irradiance reflectance spectra (Section 7.3).

A station wise approach was adopted for the data quality control procedures. Only stations that had good quality observations for all parameters were allowed for further analysis.

First measurements at sample stations were screened for values lying significantly outside the range of literature values. These stations were excluded. For brevity, a table of the concentration and SIOP data of all 52 sample locations is not given in this chapter but it is included as an appendix (Appendix II). Three published datasets were used as references: the dataset used by Dekker for his dissertation (Dekker and Peters 1993), the dataset in the SPECtral LIBrary project SPECLIB (Rijkeboer, Hoogenboom, and Dekker 1997) and the dataset gathered in the SAtellite remote sensing for Lake MONitoring project SALMON (Lindell, Pierson, Premazzi, Zillioli, and et.al. 1999).

Care was taken to copy sampling, storage and instrumental procedures from earlier studies. Residual differences in the results will probably be caused mainly by using different laboratory spectrometers. A test however, comparing results from the NIOO spectrometer and the Ocean Optics spectrometer used for this research indicated that the overall results for the filterpad method were not affected by an offset (pers. comm. M. Rijkeboer Msc.).

8.2.1 Comparison of measured to literature concentration ranges

The concentration range of chlorophyll- ɑ found in the study area in earlier research is 4 – 219 µg l^{-1} (Dekker 1993). In the study area the chlorophyll-a usually makes up 70 – 80% of the total chlorophyll (TCHL; chlorophyll-ɑ plus phaeopigments). The C_{TCHL} range found for Dutch inland waters is 1 – 1006 µg l^{-1} (Rijkeboer, Hoogenboom, and Dekker 1997). The range of C_{TCHL} for this dataset was 1 – 291 µg l^{-1}, which is well comparable to the literature chlorophyll values found in the same area.

The concentration range of total suspended matter (TSM) found in the study area in earlier research is 1 – 37 mg l^{-1} (Dekker 1993). Literature values for total suspended matter in Dutch natural freshwaters range from 1 to 174 mg l^{-1} (Rijkeboer, Hoogenboom, and Dekker 1997). The range of C_{TSM} for this dataset was 1 – 37 mg l^{-1}, which is exactly the same as found by Dekker in the study area.

The range of CDOM concentration values found in earlier research by Dekker was 0.78 – 3.51 m^{-1} (Dekker 1993). For Dutch inland waters C_{CDOM} (often called g_{440}) values range from 0.094 – 22.6 m^{-1} (Krijgsman 1994 and Rijkeboer, Hoogenboom, and Dekker 1997). The C_{CDOM} for this dataset was found to be 0.4 – 4.5 m^{-1}, which again is in good agreement with the range found by Dekker in the same area.

8.2.2 Comparison of measured SIOP to literature SIOP ranges

The literature range of specific phytoplankton absorption at 676 nm is 0.006 – 0.034 m^2 mg^{-1} (Dekker and Peters 1993; Bricaud, Bedhomme and Morel 1988; Davies-Colley and Vant 1987; Morel and Bricaud 1981 and Kirk 1975). These include a^*_{ph} values from oceanic to inland waters, even including the Vecht Wetlands study area. All of the specific phytoplankton absorption values in the dataset fall within this range.

The literature range of specific tripton absorption at 550 nm is 0.11 – 0.139 m^{-1} (at 550 nm) (Rijkeboer, Hoogenboom, and Dekker 1997). The tripton specific absorption range of the dataset was 0.04 – 0.255 m^{-1}. Some sample stations (14) in the dataset have lower specific tripton values, but these values were not discarded because the literature range is only indicative.

The literature range of Dutch inland specific seston scattering values at 550 nm is 0.15-1.10 $m^2\ g^{-1}$ (Rijkeboer, Hoogenboom, and Dekker 1997), while a smaller range for only the Vecht area is 0.23 – 0.79 $m^2\ g^{-1}$ (Dekker and Peters 1993). The specific seston scattering range found for this dataset was considerably larger: 0.15 – 7.03 $m^2\ g^{-1}$. Based on range considerations it was decided to discard b^*_{ses} values exceeding the arbitrary value of 2.00 $m^2\ g^{-1}$ because they are about two times the highest value found in literature. These include the following four sample stations: L3, L4, LEL1 and NP1, which were subsequently discarded. The very high b^*_{ses} values are most probably the result of errors in the beam attenuation measurements that also produced high values for c for these sample stations.

8.3 Forward modelling based on all-observed parameters per station in order to optimise B per station: analysis of the similarity between observed and modelled $R(0-)$ per station

In this step a further selection of good quality stations is performed by calculating the χ^2 difference between the measured $R(0-)$ spectrum and the $R(0-)$ spectrum simulated by the calibrated bio-optical model (using measured concentration and SIOP data per sample station). Here it is assumed that the SIOP data is correct so that the comparison allows for discrimination between suitable and unsuitable reflectance measurements. The similarity analysis involves also a selection of the wavelength range suitable for the comparison and estimation of the values of the pre-factor f and the forward scatter to backscatter ratio B. First the inherent quality of the spectral reflectance observations (hand-held spectrometer method by Gons as outlined in chapter 6) is discussed.

8.3.1 The stray light effect in $R(0-)$ measurements

Unfortunately, a large number of $R(0-)$ spectra collected in this research was affected by stray light effects. In the wavelength region below around 450 nm and above around 730 nm the $R(0-)$ spectra obtained during the 2001 campaign and the first field day of the GWA campaign (Julian day 114 of 2002) show a significant increase. An example of such a $R(0-)$ spectrum is given by Figure 8.1. Such an increase of reflectivity towards the edges of the $R(0-)$ spectrum cannot be explained by the optical modelling theory. Because of the shape, the feature was referred to as the 'smile'-effect.

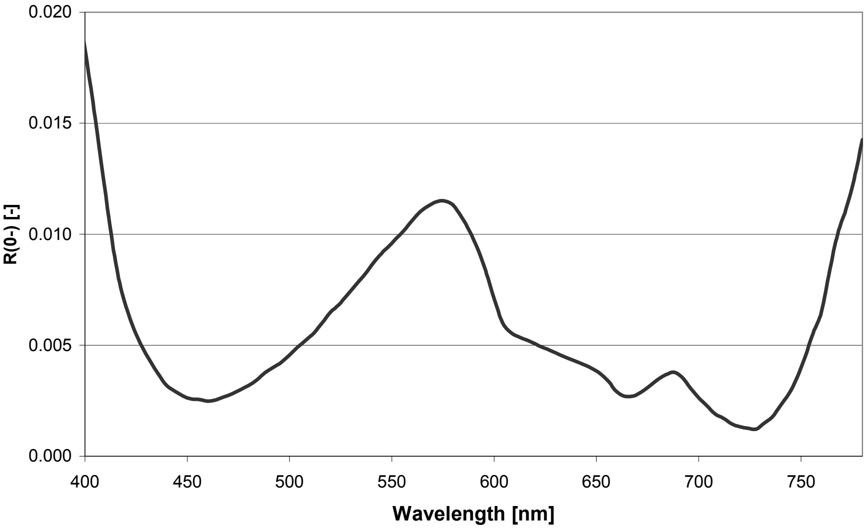

Figure 8.1: Extreme example of the 'smile'-effect (measurement series #3, sample location WL2), showing severe stray light effects in the wavelength ranges before 450 nm and after 730 nm.

After a series of methodological experiments, stray light effects in the spectrometer were identified as the source of this feature, an operational matter that was resolved for later measurements. The analysis also revealed that the $R(0-)$ spectrum was probably affected in the wavelength region 450-730 as well, although the significance of the effect at these wavelengths could not be determined. A correction method for the stray light effects was pursued, but it was found that the 'smile'-effect varied with the light conditions so the affected measurements could not be restored. Instead, it was decided to perform inverse modelling on the wavelength region 440-720 only.

As a result of the 'smile'-effect, the spectral data recorded near the water surface for this study has similar spectral errors as most airborne and spaceborne recorded remote sensing data in the blue wavelength area.

8.3.2 Optimisation of B per station from selected observations

The one parameter that was not measured at all in the field is the scatter to backscatter ratio B. This parameter is very difficult to measure. In most studies a fixed value for the scatter to backscatter ratio B is chosen for simplicity, usually in the order of 0.02 – 0.03 (Dekker 1993;Vos and Pasterkamp 2001). The theoretical range of B values lies between 0 and 0.5 (the B of pure water). In literature the range of observed B values for eutrophic inland waters lies between 0.025 and 0.046 (Dekker, Hoogenboom, Goddijn, and Malthus 1997) and between 0.005 - 0.070 (Lindell, Pierson, Premazzi, Zillioli, and et.al. 1999).

As an alternative for a fixed B (which might easily lead to rather large scaling errors) in this type of studies B is often determined by solving equation 4.24 for B. To do so it is required to have a good measurement of the surface reflectance and a calibrated bio-optical model with B as sole unknown. In this chapter we will determine for selected good stations B from $R(0-)$ observations and per station IOP and concentration measurements of all parameters.

To solve equation 4.24 for B the model scaling parameter f needs to be set as well. The value for f was calculated using equation 4.14 (see chapter 4). The average resulting f value for all 52 sample stations is 0.38, which is an average for most Dutch inland waters, as opposed to the more common value of 0.33 derived by Morel and Prieur for oceanic waters (Case I) (Morel and Prieur 1977). The average value for the pre-factor f found by Dekker in the Vecht Wetlands is 0.29, but his f values were optimised by performing regressions using equation 4.13 (Dekker 1993). Although (Whitlock, Poole, Usry, Houghton, Witte, Morris, and Gurganus 1981) and (Kirk 1991) showed that the value for f changes with water type it was decided to use a fixed f value of 0.38 for all sample stations in this research because the information to calculate f per spectrum is often not available. Thus some residual error of not knowing f exactly will be transferred to B.

The wavelength range for the simulation modelling (and the χ^2 difference calculation) was set to 440 – 720 nm, minimising the influence of the 'smile'-effect discussed in the previous section, while including as many CASI bands as possible (see table 7.3). The wavelength range 440 – 720 nm still includes most of the spectral features necessary for the optical model to discriminate between TCHL, TSM and CDOM. These include the absorption peaks of chlorophyll at 440 and 676, the area around 706 nm where scattering of TSM is most prominent and the 440-500 region where the absorption of CDOM is present (see chapter 5).

Based on the fixed average value for f, B was optimised using non-linear least squares regression (between the forward modelled and measured $R(0-)$ spectra), minimizing the root mean square error between the measured and forward modelled $R(0-)$, assuming B to be spectrally neutral (although the mentioned stray light effect may have an effect on this).

The optimised B values used for the forward modelling of the sample locations are given in table 8.1. The reader should note that any systematic and random measurement errors in the measured TCHL, TSM and CDOM concentrations and errors in the measured IOP per sample station will influence the value of B estimated from this process of optimisation. The range of B values found for this dataset is 0.002 to 0.074, which is comparable to the range of values found in the SAtellite remote sensing for Lake MONitoring project SALMON (Lindell, Pierson, Premazzi, Zillioli, and et.al. 1999). Although the optimised B values found by Dekker *et al.* are obtained from the same lakes (Vecht Wetlands) they are on average significantly higher.

The minimum B of the SALMON project (0.005) was found for Lake Vesijärvi, a relatively shallow (6 m) and hypertrophic lake in Finland (which is roughly similar to the lakes found in the Vecht study area). A relationship between very low B values and high eutrophic state is apparent. The abundance of large quantities of relatively transparent algae in these eutrophic waters possibly causes a relatively high forward scattering (and therefore low B value) as opposed to turbid waters with high sediment loads that have a relatively high backscattering.

Table 8.1: The optimised B values for all 52 sample locations (using a fixed value for f of 0.38).

Station	B	Station	B
114LEL_1_C	0.005	95163LO	0.008
114LEL_2_C	0.008	ANK3	0.034
114LEL_3_C	0.006	ANK5	0.061
114TNH_1_C	0.009	ANK7	0.081

114TNH_2_C	0.015	HIK2	0.016
114TNT_1_C	0.013	HIK5	0.006
114TNT_2_C	0.011	KORT1	0.019
210LEL_1_C	0.005	KORT4	0.014
210LEL_2_C	0.004	KORT5	0.013
210LEL_3_C	0.006	L1	0.013
210TNH_1_C	0.001	L2	0.015
210TNH_2_C	0.004	L3	0.008
210TNT_1_C	0.014	L4	0.006
210TNT_2_C	0.032	L5_sep_90	0.019
255LEL-1-C	0.013	LEL1	0.009
255LEL-2-C	0.012	NP1	0.003
255LEL-3-C	0.010	PKH10	0.031
255TNH-1-C	0.014	SP2	0.048
255TNH-2-C	0.027	V1	0.007
255TNT-1-C	0.010	V2	0.014
255TNT-2-C	0.017	WB1	0.004
95130HA	0.033	WB2	0.004
95130SA	0.030	WJB_90	0.027
95149 WL	0.059	WL_aug_90	0.028
95151WB	0.014	WL1	0.010
95151WG	0.034	WL2	0.013

The average B value of all 52 sample stations (with f = 0.38) is 0.018, while the standard deviation is 0.016 and the median value is 0.016. The use of a median value for B for the inversion when there is a large variation in B will induce scaling errors. The extent of these scaling errors however is unknown, so it is decided that none of the 52 sample stations will be excluded from inversion based on its optimised B value.

8.3.3 Results of the forward modelling using optimized B-values: comparison between measured and modelled $R(0-)$.

This chapter will show the results of forward modelling as described in the previous chapter. For this exercise the Gordon-Walker model was used (equation 4.13) which was, for each sample location, parameterised with its own measured concentrations and IOPs, a fixed value for f (0.38) and its own optimised value for B.

The modelled and measured subsurface irradiance reflectance spectra are shown in figure 8.2. On average, the modelled $R(0-)$ spectra of the sample locations are similar in shape and height to the measured subsurface irradiance reflectance spectra. Note that stations ANK5 and PKH10 experienced algal floating layers and therefore have very high subsurface irradiance reflectance values (706 nm peak value of almost 15%).

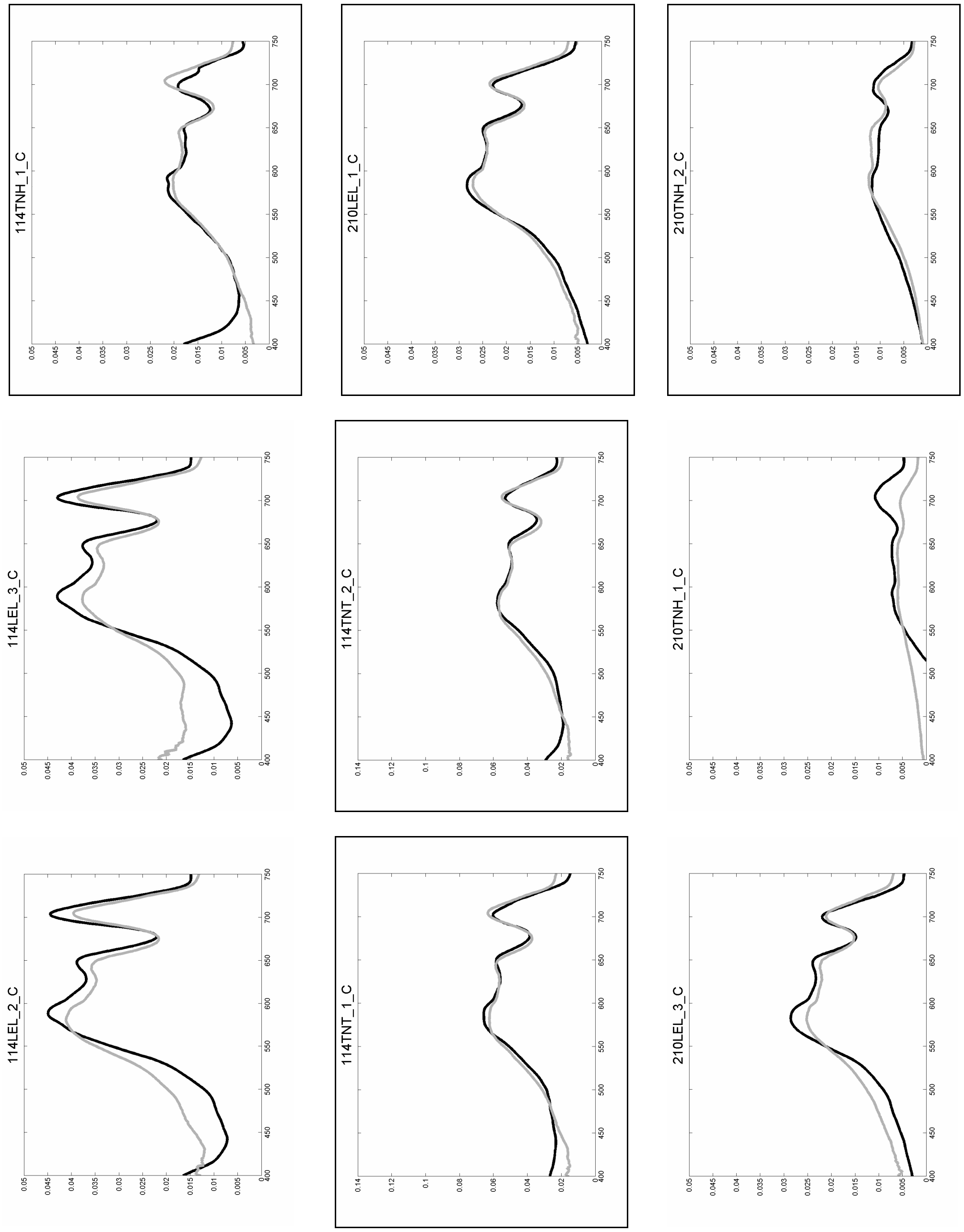

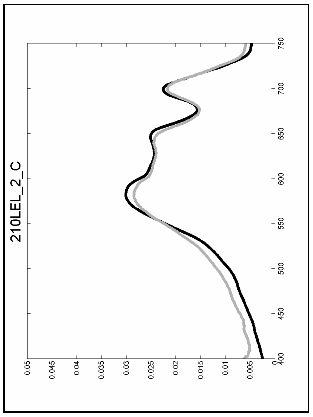
210LEL_2_C
0
0.005
0.01
0.015
0.02
0.025
0.03
0.035
0.04
0.045
0.05
400
450
500
550
600
650
700
750

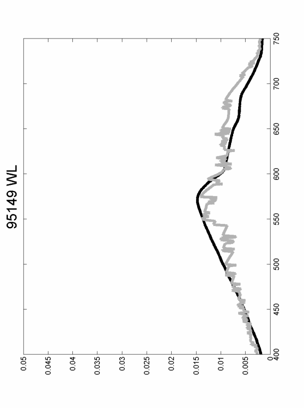
95149 WL
0
0.005
0.01
0.015
0.02
0.025
0.03
0.035
0.04
0.045
0.05
400
450
500
550
600
650
700
750

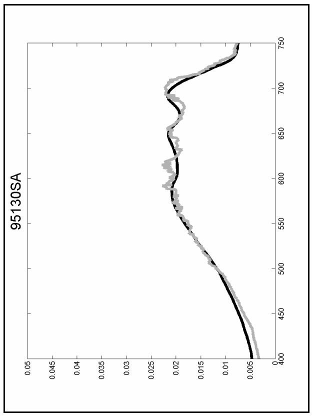
95130SA
0
0.005
0.01
0.015
0.02
0.025
0.03
0.035
0.04
0.045
0.05
400
450
500
550
600
650
700
750

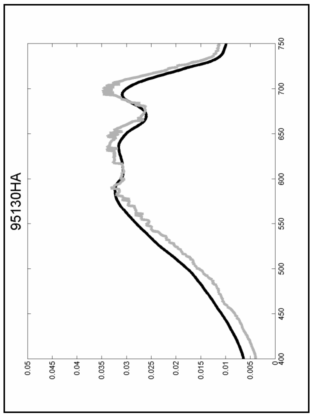
95130HA
0
0.005
0.01
0.015
0.02
0.025
0.03
0.035
0.04
0.045
0.05
400
450
500
550
600
650
700
750

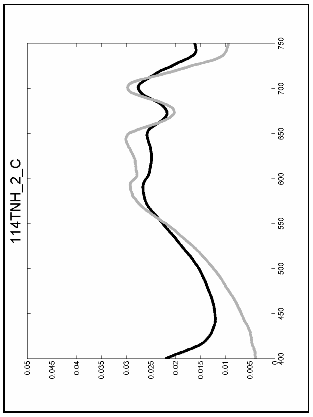
114TNH_2_C
0
0.005
0.01
0.015
0.02
0.025
0.03
0.035
0.04
0.045
0.05
400
450
500
550
600
650
700
750

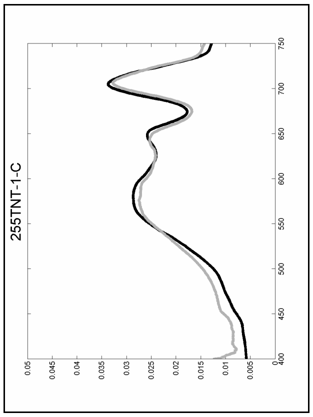
255TNT-1-C
0
0.005
0.01
0.015
0.02
0.025
0.03
0.035
0.04
0.045
0.05
400
450
500
550
600
650
700
750

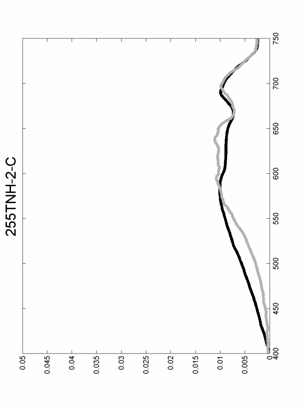
255TNH-2-C
0
0.005
0.01
0.015
0.02
0.025
0.03
0.035
0.04
0.045
0.05
400
450
500
550
600
650
700
750

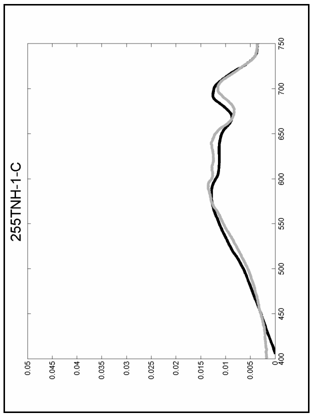
255TNH-1-C
0
0.005
0.01
0.015
0.02
0.025
0.03
0.035
0.04
0.045
0.05
400
450
500
550
600
650
700
750

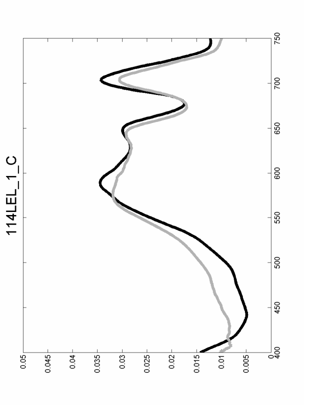
114LEL_1_C
0
0.005
0.01
0.015
0.02
0.025
0.03
0.035
0.04
0.045
0.05
400
450
500
550
600
650
700
750

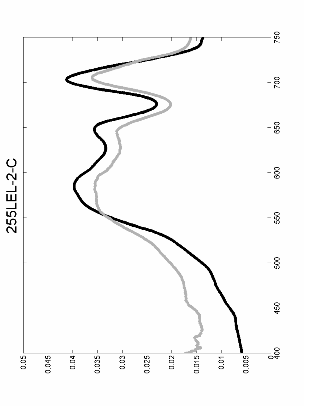
255LEL-2-C
0
0.005
0.01
0.015
0.02
0.025
0.03
0.035
0.04
0.045
0.05
400
450
500
550
600
650
700
750

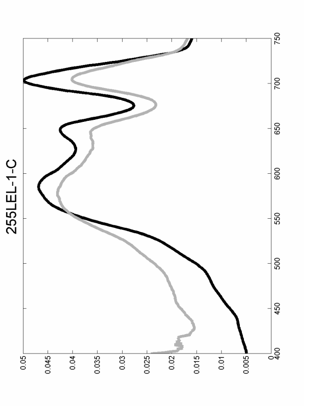
255LEL-1-C
0
0.005
0.01
0.015
0.02
0.025
0.03
0.035
0.04
0.045
0.05
400
450
500
550
600
650
700
750

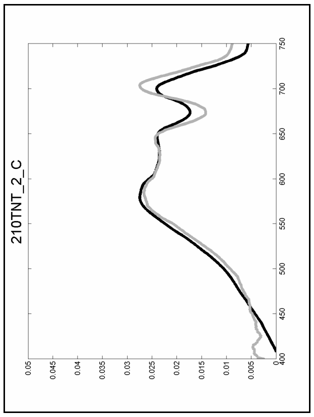
210TNT_2_C
0
0.005
0.01
0.015
0.02
0.025
0.03
0.035
0.04
0.045
0.05
400
450
500
550
600
650
700
750

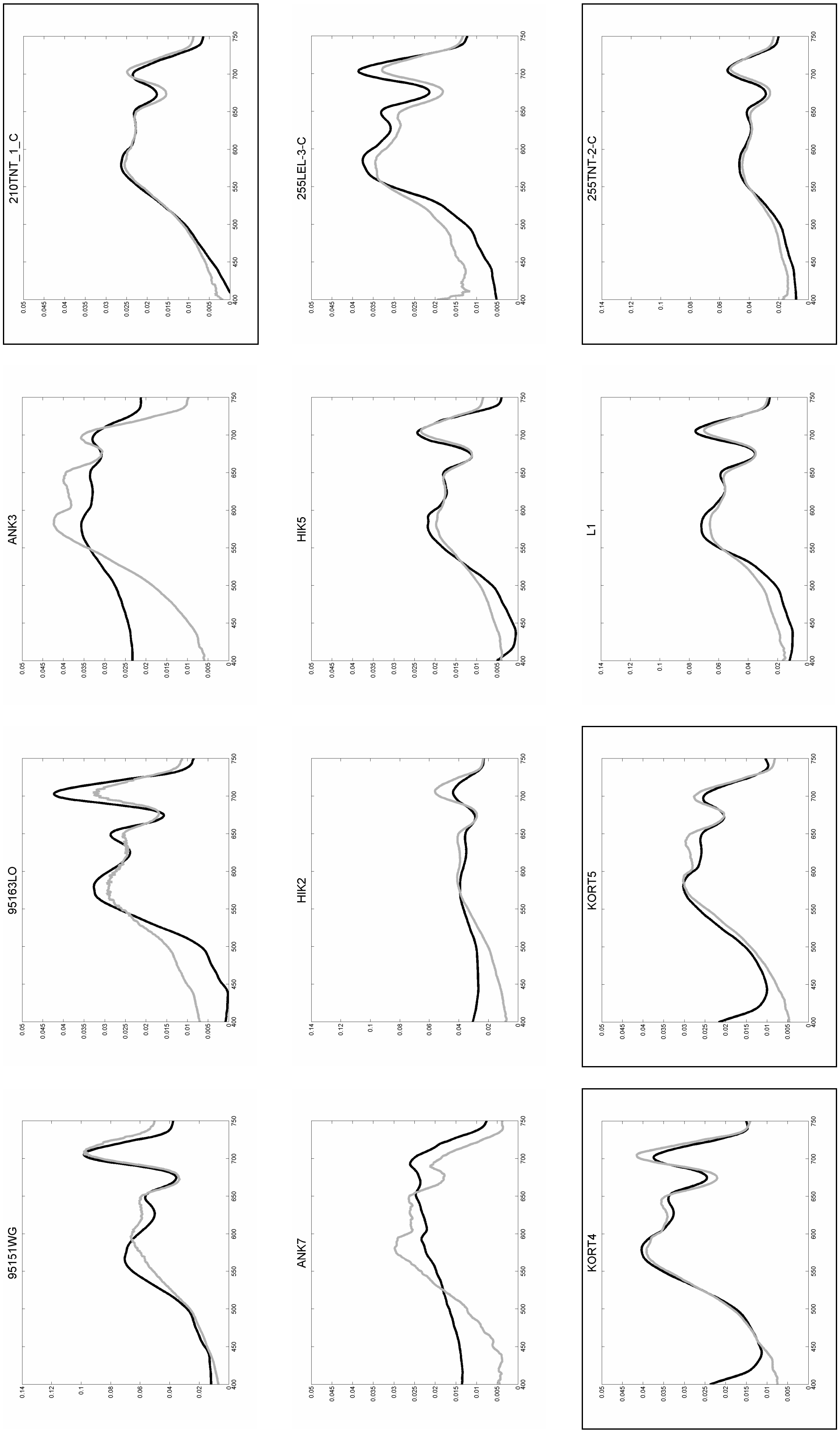
210TNT_1_C
255LEL-3-C
255TNT-2-C
ANK3
HIK5
L1
95163LO
HIK2
KORT5
95151WG
ANK7
KORT4
0
0.005
0.01
0.015
0.02
0.025
0.03
0.035
0.04
0.045
0.05
0.02
0.04
0.06
0.08
0.1
0.12
0.14
400
450
500
550
600
650
700
750

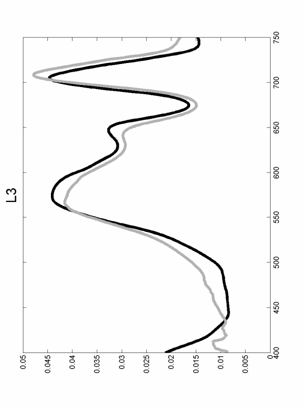
L3

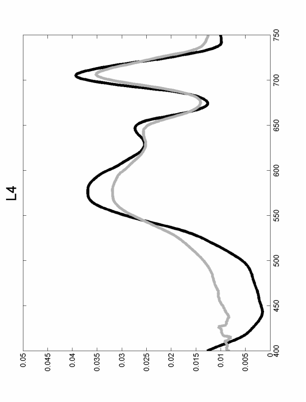
L4

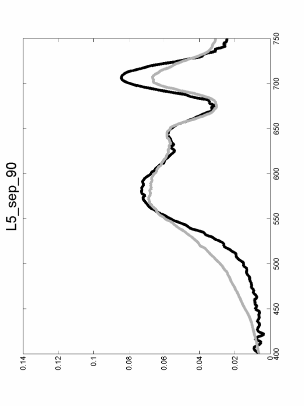
L5_sep_90

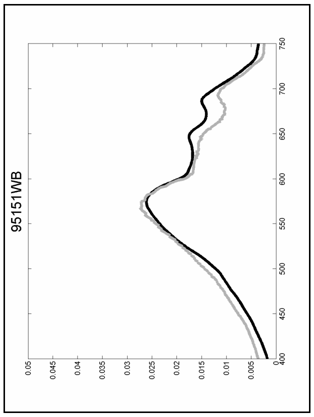
95151WB

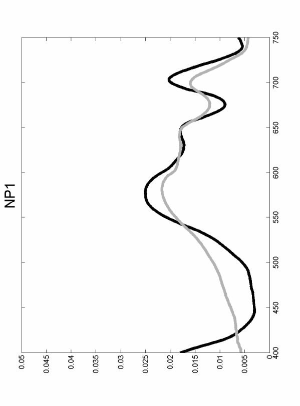
NP1

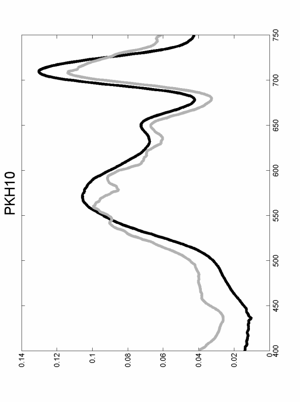
PKH10

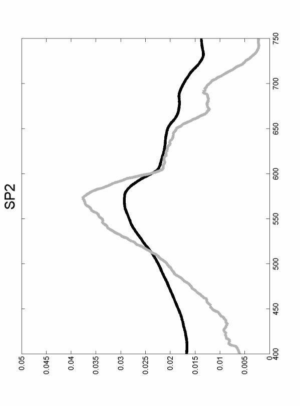
SP2

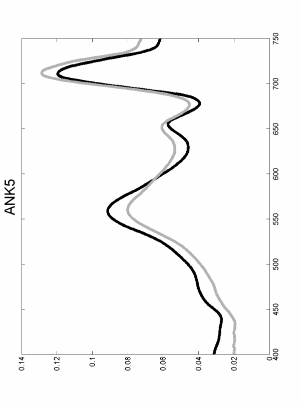
ANK5

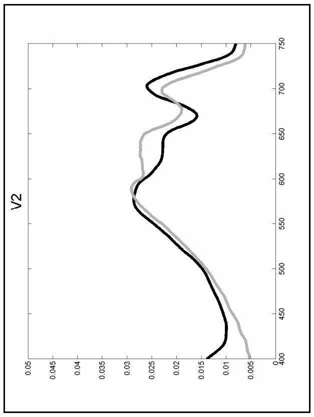
V2

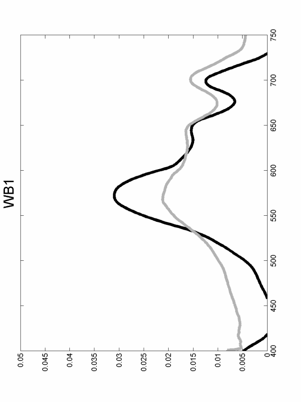
WB1

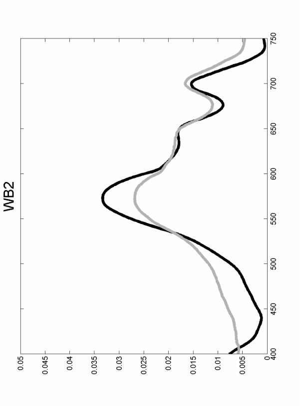
WB2

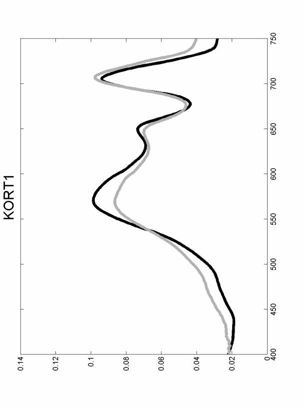
KORT1

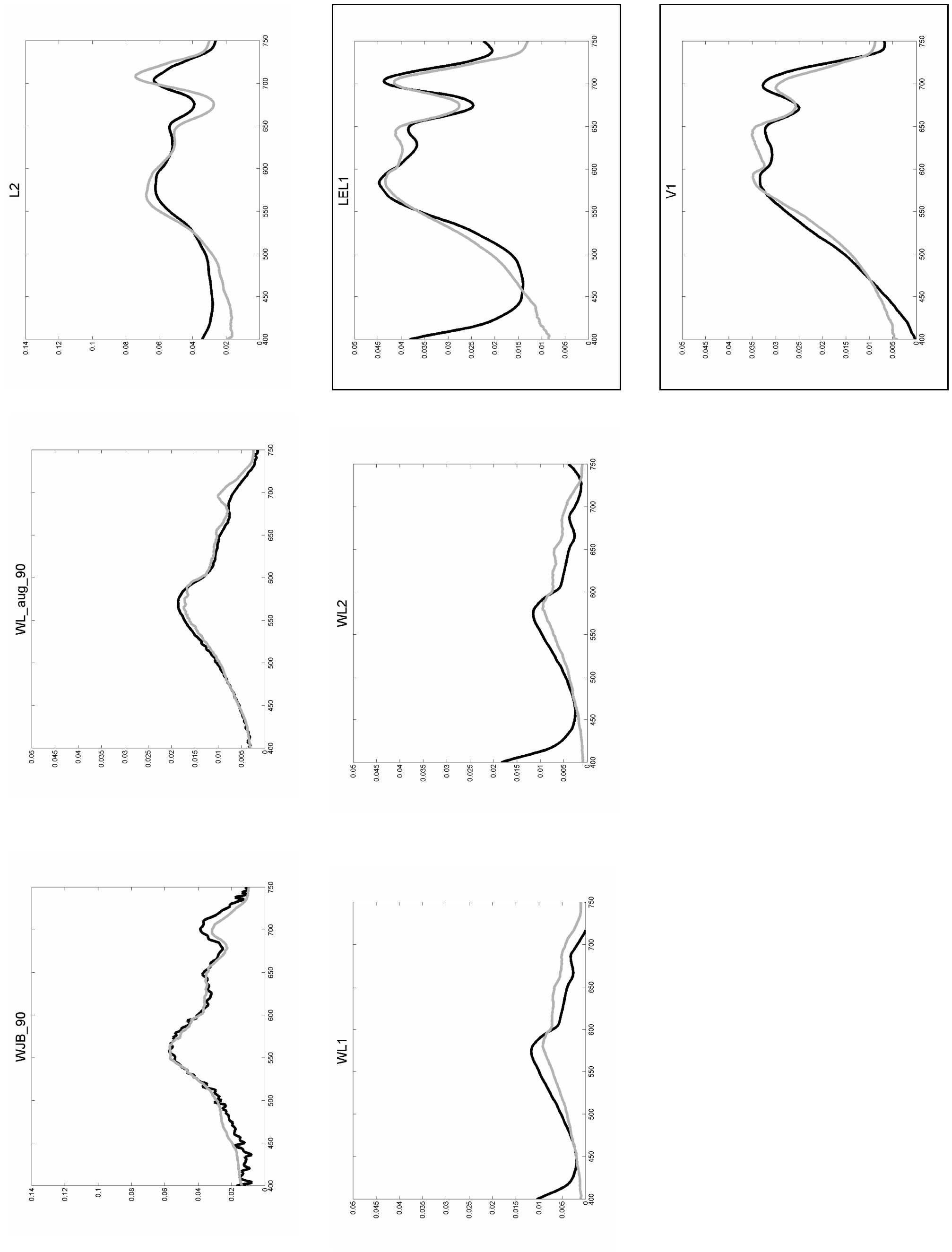

Figure 8.2: The measured and forward modelled $R(0-)$ spectra for all 52 sample locations (f = 0.38 and B is optimised per station (see table 8.1). The bordered figures are spectra from sample locations that are ultimately selected for constructing the median SIOP set and for inverse modelling.

Another noteworthy feature in both the measured and modelled $R(0-)$ spectra is the fact that for most shallow eutrophic sample locations the reflectance peaks at around 550 – 575 nm and 706 nm are almost equal in height. This is quite typical for the Vecht Wetlands water systems, as in other cases the 550 – 575 nm peak is usually significantly higher than the $R(0-)$ 706 nm peak. See for example the IJsselmeer spectra described by Vos *et al.* (Vos and Pasterkamp 2001). This phenomenon is due to the relatively high specific tripton absorption observed in the Vecht Wetlands, which in turn is caused by the relatively high abundance of algae and peat detritus.

8.3.4 Selection of sample locations based on normalised χ^2 differences between measured and forward modelled $R(0-)$ spectra

The selection of sample locations with suitable CSI data can be based on the normalised χ^2 difference between the forward modelled and measured $R(0-)$ spectra. The χ^2 difference is considered to be an objective measure of CSI data quality with low χ^2 values indicating that the concentration, SIOP and irradiance data of a sample location are all of sufficient quality to be used for further optical modelling.

The normalisation of χ^2 is necessary to correct for the total reflectivity of the sample location. Without normalising, sample locations with the same goodness of fit between the measured and modelled $R(0-)$ spectrum but with high reflectivity values ($R(0-)$ over 3%, like the ANK5 and PKH10 stations mentioned above) would also have high normalised χ^2 values compared to sample locations with low overall reflectivity. By dividing the normalised χ^2 by the measured reflectivity, the modelling error is in proportion with the total reflectivity. The normalised χ^2 value was calculated as follows:

$$\chi^2 = \sum_{440-720} \left| \frac{\left[R(0-)_{\text{modelled}} - R(0-)_{\text{measured}}\right]^2}{R(0-)_{\text{measured}}^{\;2}} \right| \qquad 8.1$$

The normalised χ^2 values for each of the 52 sample locations are shown in table 8.2. The range of χ^2 values is 0.89 (KORT4) to 3898691.28 (WL1). Very high χ^2 values ($\chi^2 > 100$) occur at 210TNH_1_C, 95163LO, HIK5, L4, NP1, WB1, WB2 and WL1. table 8.2 shows that the goodness of fit between the modelled and measured $R(0-)$ spectra for these sample locations is indeed poor. For sample location 210TNH_1_C the measured $R(0-)$ spectrum is clearly affected by some sort of measurement error, while the other ill-fitting spectra show similar characteristics: The measured $R(0-)$ spectrum is very low in the blue wavelength range, rapidly increasing towards the green wavelength range and the modelled $R(0-)$ spectrum has a more gentler slope and less difference in reflectivity between the blue and green wavelength region. This might be due to a scaling error in the measured $R(0-)$ spectra at these sample stations. Not all of the ill-fitting sample stations mentioned are part of the 2001 campaign, making it unlikely that the 'smile'-effect discussed above (§8.3.1) is the sole source of the poor fit.

Table 8.2: The normalized χ^2 differences for all 52 sample locations (normalized χ^2 differences in bold exceed the threshold value of 20)

Station	χ^2	Station	χ^2
114LEL_1_C	**42.67**	95163LO	**>1000**
114LEL_2_C	**46.83**	ANK3	**20.71**
114LEL_3_C	**86.85**	ANK5	5.56

114TNH_1_C	2.31	ANK7	**23.92**
114TNH_2_C	9.74	HIK2	16.24
114TNT_1_C	1.32	HIK5	**486.01**
114TNT_2_C	1.87	KORT1	7.03
210LEL_1_C	1.90	KORT4	0.89
210LEL_2_C	7.82	KORT5	3.24
210LEL_3_C	18.03	L1	**31.66**
210TNH_1_C	**>1000**	L2	7.63
210TNH_2_C	6.06	L3	11.85
210TNT_1_C	5.60	L4	**640.96**
210TNT_2_C	3.33	L5_sep_90	**71.36**
255LEL-1-C	**60.55**	LEL1	3.72
255LEL-2-C	**37.28**	NP1	**152.97**
255LEL-3-C	**37.11**	PKH10	**55.83**
255TNH-1-C	3.12	SP2	15.79
255TNH-2-C	**32.34**	V1	3.23
255TNT-1-C	4.70	V2	4.95
255TNT-2-C	8.93	WB1	**>1000**
95130HA	4.16	WB2	**347.15**
95130SA	1.33	WJB_90	7.37
95149 WL	19.14	WL_aug_90	5.57
95151WB	7.34	WL1	**>1000**
95151WG	4.10	WL2	**67.92**

While it is clear that the sample locations discussed above have to be excluded for optical modelling because of their poor normalised χ^2 values, it is less obvious what normalized χ^2 value is acceptable for selection of the sample locations. An arbitrary threshold value for the normalised χ^2 difference of 20 was therefore assumed in this research that is a compromise between quality and quantity. Sample locations with a normalised χ^2 smaller than 20 were selected for inverse optical modelling. From the total of 52 sample locations 30 sample stations complied and were selected (see table 8.1).

8.3.5 CDOM masking by high total chlorophyll concentrations

In the introductory chapter it was shown that under conditions of high TCHL concentrations the influence of CDOM on the reflectance spectrum is dominated by TCHL (see Figure 1.3). Under these conditions it has been found that a successful retrieval of the CDOM concentration is inhibited (Doerffer 2002a).

It was therefore decided to discard sample stations with TCHL concentrations exceeding the arbitrary threshold of 85 μg l^{-1}. A total of 10 sample stations within the dataset were discarded for this reason: ANK5, KORT1, L1, L2, L3, L4, 95151WG, PKH10, 95163LO and L5_sep_90.

8.3.6 Summary of data selection results

In section 8.2 the suitability of the measured concentration and SIOP data was determined by comparison to literature values in order to find those measurements that are too strongly dissimilar to values collected in comparable water systems and presented in literature. Until future additional studies substantiate that similar extreme values indeed occur in these waters, these values should be regarded as suspicious and may best be discarded.

Regarding the TCHL, TSM and CDOM concentrations, the measured values were within the literature range. Also with respect to the specific phytoplankton absorption, the specific tripton absorption and the normalised CDOM absorption the measured values were within the literature range. The specific seston scattering of a number of sample locations however was more than two times the maximum literature value. From the total of 52 sample stations, the sample locations, L3, L4, LEL1 and NP1 were regarded suspicious and will not be selected.

Another means of quality control was performed based on the χ^2 differences between the measured and forward modelled spectra in §8.3.4. For this, the Gordon-Walker optical model was used, with a fixed value for f while the B was optimised per sample location (and the SIOP per sample location). The χ^2 value of 30 of the total of 52 sample locations was smaller than the arbitrary threshold value 20, making them suitable for selection.

Before the final selection was made however sample locations with total chlorophyll concentrations exceeding 85 μg l^{-1} were declared unsuitable, as it is known *a priori* that very high concentrations of TCHL inhibit a successful CDOM concentration retrieval. From the total of 52 sample stations, 10 have TCHL concentrations exceeding 85 μg l^{-1}.

The final selection includes the following 24 sample stations:

114TNH_1_C, 114TNH_2_C, 114TNT_1_C, 114TNT_2_C, 210LEL_1_C, 210LEL_2_C, 210_LEL_3_C, 210TNH_2_C, 210TNT_1_C, 210TNT_2_C, 255TNH-1-C, 255TNT-1-C, 255TNT-2-C, 95130HA, 95130SA, 95149WL, 95151WB, KORT4, KORT5, SP2, V1, V2, WJB_90 and WL_aug_90.

8.4 Construction of an median SIOP set from selected stations to be used for inversion

In theory the CDOM retrieval from inversion of the optical model is most accurate when SIOP data is used that is collected at the same location and the same time as the measured $R(0-)$ spectrum. In the case of this research this is indeed possible, as the hand-held spectrometer and SIOP data were both collected *in* *situ*. In most other water remote sensing studies however the data of spaceborne and airborne imaging scanners is used, and there is usually no matching SIOP data collected at all, and if there is, it is certainly not available per spectrum (pixel). In that case one has to revert to a SIOP set that is chosen in such a way that it is representative for the SIOP conditions that are present within the image area. Instead of a SIOP set based on average values that can be strongly influenced by outliers, it was decided to use a representative SIOP set based on median values. In order to operationally apply inversions of the optical model a suitable median SIOP set will be constructed in this section based on the sample locations that were quality controlled and selected in the previous section. At the end of this section the effect of the errors introduced by using a median SIOP set on the CDOM retrieval will be discussed.

The inverse optical modelling as will be discussed in chapter XX9 requires a reference (median) set of SIOP data. The SIOP measured for this study fall roughly in two water types: shallow eutrophic and deep clear lakes. However, as data was only available of 24 suitable sample stations in total, of which only 5 could be classified as deep clear lakes, it was decided to calculate one single median SIOP set.

Statistical characteristics of the concentrations and SIOP data of the 24 selected sample stations are given in table 8.3. The average concentration of total chlorophyll, total suspended matter and C_{CDOM} in the dataset compare well to the average values reported for Dutch freshwaters (Dekker and Peters 1993; Rijkeboer, Hoogenboom, and Dekker 1997). The variation in TCHL, TSM and CDOM concentrations is considerable, according to the high standard deviations.

The average specific phytoplankton absorption value at 676 nm of 0.024 m^2 mg^{-1} is also comparable with the average values reported for Dutch freshwaters (Dekker and Peters 1993; Rijkeboer, Hoogenboom, and Dekker 1997). The average b^*_{seston} (0.72 m^2 g^{-1}) for the dataset is roughly comparable with the average values found in literature (0.62 m^2 g^{-1}, Dekker 1993).

Table 8.3: The concentration and SIOP data for the selection dataset (N =24).

N =24	Average value	Median value	Standard deviation	Minimum value	Maximum value
C_{TCHL}	31.1	32.4	20.9	1.4	81.66
C_{TSM}	9.6	8.6	5.5	0.84	21. 8
C_{CDOM}	2.38	2.43	0.96	0.45	4.33
a^*_{ph} 676 nm	0.024	0.066	0.014	0.008	0.066
a^*_{tr} 550 nm	0.057	0.049	0.033	0.016	0.129
b^*_{ses} 550 nm	0.724	0.737	0.348	0.199	1.409

The median optimised B value of the 24 sample stations was 0.014 (see §8.3.2). The 24 stations median SIOP absorption and scattering spectra are given in figure 8.3. The shapes of the spectra are comparable with literature (Dekker 1993;

Rijkeboer, Hoogenboom, and Dekker 1997). For completeness also the median $R(0-)$ spectrum is shown, although it is not used in the inverse optical model.

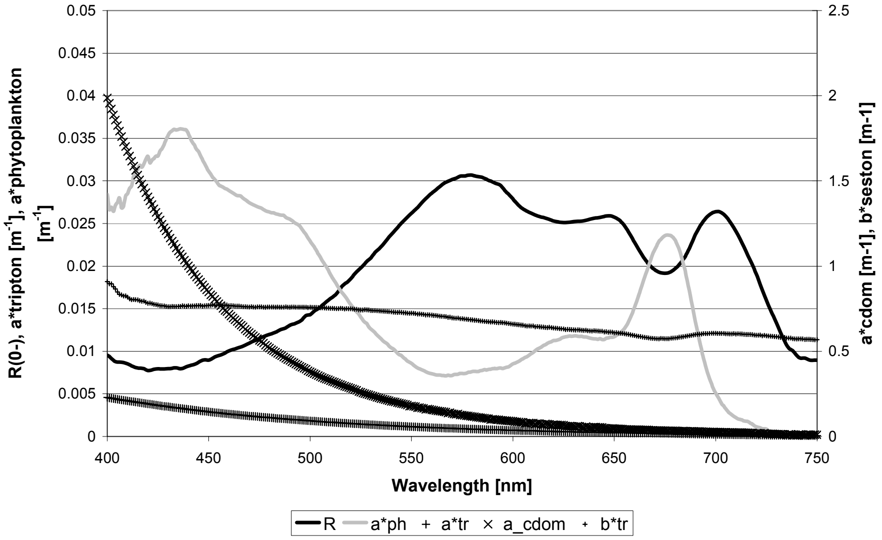

Figure 8.3: The median spectral SIOP data for the complete dataset (N=24). These SIOP are used as input for the optical modelling. Note that the median $R(0-)$ spectrum was added here for illustrative purposes only as it is not used for inverse modelling.

Effects on the CDOM retrieval of errors introduced by the use of an median SIOP set

There are four possible errors that can be introduced by the use of an median SIOP set when inverting the optical model based on hyperspectral data: errors in a^*_{ph}, a^*_{tr}, $\bar{a}_{CDOM}$, and b^*_{ses} (or B).

Because of the distinct spectral shape of the a^*_{ph} curve, the shortage or surplus in total absorption caused by an error in a^*_{ph} will only result in a respective over- and underestimation of the C_{TCHL}, without consequence for the CDOM retrieval.

Due to the similarity in spectral shape of the a^*_{tr} and $\bar{a}_{CDOM}$, the shortage or surplus in total absorption caused by an error in these absorption spectra can cause a respective over- and underestimation of both the C_{TSM} and C_{CDOM}. Because the C_{TSM} is also linked to the b^*_{ses} in the optical model, an error in a^*_{tr} is likely to result in an error in C_{CDOM}.

Likewise, an error in the b^*_{ses} spectrum (or the scatter to backscatter ratio B), causing a shortage or surplus in the total scattering coefficient, will result in a respective over- and underestimation of both the C_{TSM} *and* as a response of the model a respective under- or overestimation of the C_{CDOM}.

8.5 Retrieved CDOM concentrations from measured reflectance spectra

After the construction of a median SIOP dataset in the previous section it is now possible to retrieve CDOM concentrations from actual above-water measured subsurface reflectance spectra using state-of-art inversion techniques.

In chapter 7 a successful inversion was already performed under controlled conditions using simulated data. In this section the performance of the inversion techniques will be tested using actual measured data. First CDOM concentrations will be retrieved using measured spectra and the per-sample SIOP sets, testing inversion performance under favourable field conditions, establishing reference retrieval accuracies to be used for comparison with retrieval accuracies from other inversions. Next, CDOM concentrations will be retrieved using measured spectra and the median SIOP set, simulating standard operational water remote sensing practice.

Because of the poor performance of the Ratio Levenberg-Marquardt algorithm found at the sensitivity analysis in chapter 7, only the Matrix Inversion Methods (MIM) and Levenberg-Marquardt (LM) techniques are used for inversions in this chapter.

8.5.1 Retrieved CDOM concentrations using measured spectra and the per-sample SIOP sets

In this section CDOM was retrieved from actual measurements using the per-sample SIOP set accompanying the measured $R(0-)$ spectrum.

The resulting correlation coefficients and the slope and offset values between measured and retrieved concentrations for the MIM and LM method and MERIS and CASI band settings are given in Table 8.4, while Figure 8.4, Figure 8.5 and Figure 8.6 show the dispersion of the TSM, TCHL and CDOM concentrations of the samples (for the LM method and CASI band settings – results for MIM method and MERIS band settings are similar and thus omitted for brevity).

Table 8.4: The R^2 value and the slope and offset values of the regression equation between measured and retrieved concentrations of TCHL, TSM and CDOM after the inversion of the measured $R(0-)$ spectra (for both the MERIS and CASI band settings)

	TCHL		TSM		CDOM	
	R^2	Slope + offset	R^2	Slope + offset	R^2	Slope + offset
MERIS MIM	0.70	y= 0.73x + 1.18	0.93	y= 0.87x + 0.16	0.37	y = 0.62x + 0.80
MERIS LM	0.55	y= 0.80x + 4.81	0.91	y= 1.01x – 0.28	0.37	y = 0.66x + 0.91
CASI MIM	0.77	y= 0.70x – 0.26	0.94	y= 0.83x + 0.26	0.47	y = 0.62x + 0.66
CASI LM	0.56	y= 0.78x + 6.82	0.92	y= 0.98x - 0.03	0.49	y = 0.71x + 0.69

The correlation coefficients for TCHL are not as strong as those for TSM but still reasonable with 0.6 to 0.8. The slope and offset parameters for TCHL show a 25% underestimation. Contrary to TSM, the MIM technique yields better TCHL retrieval over LM.

Especially the retrieval of TSM is very accurate when using per-sample SIOPs. Not only is the correlation over 90%, it is even more importantly that the slope of the regression between retrieved and measured TSM concentrations is close to 1 (see Table 8.4) and the offsets are relatively small. Differences between the MIM and LM techniques are small, with a 10% better score for LM.

A likely explanation for the successful TSM retrieval when using the per-sample SIOP sets is that an optimised B value per sample station is included (which was obtained by performing forward modelling). By means of this optimised B value scaling differences between the measured SIOP and spectrum can be minimised. Because of its relatively spectrally neutral behaviour, the TSM is especially affected by such scaling problems. When a median backscatter ratio is used instead of an optimised B it is likely that scaling differences occur between the measured and forward modelled $R(0-)$ spectrum during the inversion.

The retrieval of CDOM concentrations using the per-sample SIOPs does not yield accurate results. R^2 values are down to 0.4 – 0.5, while the slope indicates a 30 – 40% underestimation. Here the results for MIM and LM are similar, but the CASI band settings produce slightly better correlations and slopes. The CDOM retrieval apparently benefits from a greater number of spectral bands, the extra information helping to discriminate between the absorption by TCHL and by CDOM in the wavelength region 400 - 600 nm.

The systematic underestimation of CDOM can be due to two reasons:

1. An error in the $\bar{a}_{CDOM}$ of the per-sample SIOP sets. An underestimation of the CDOM concentration will be caused by an erroneously steep $\bar{a}_{CDOM}$ spectrum.
2. An error in the measured reference CDOM concentrations. When the measured reference CDOM concentrations are too high, the retrieved concentrations will be underestimated.

Both of these possible problems are subject of research in the next chapters.

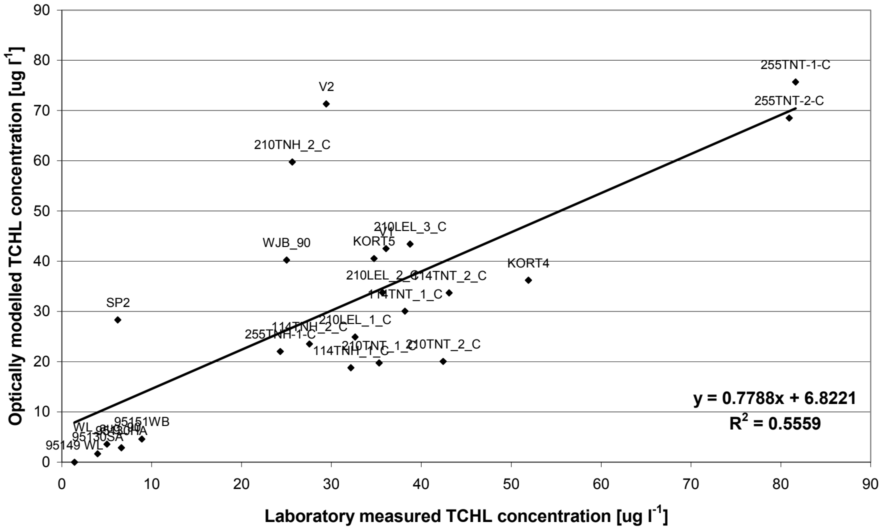

Figure 8.4: The measured and modelled TCHL concentration of the 24 selected sample locations using the per-sample SIOP set, the Levenberg-Marquardt technique and the CASI band settings (sample location codes are displayed above the data points). The thin black line shows the 1:1 relationship, while the thicker black line represents the regression relationship (regression parameters are displayed in the lower right corner).

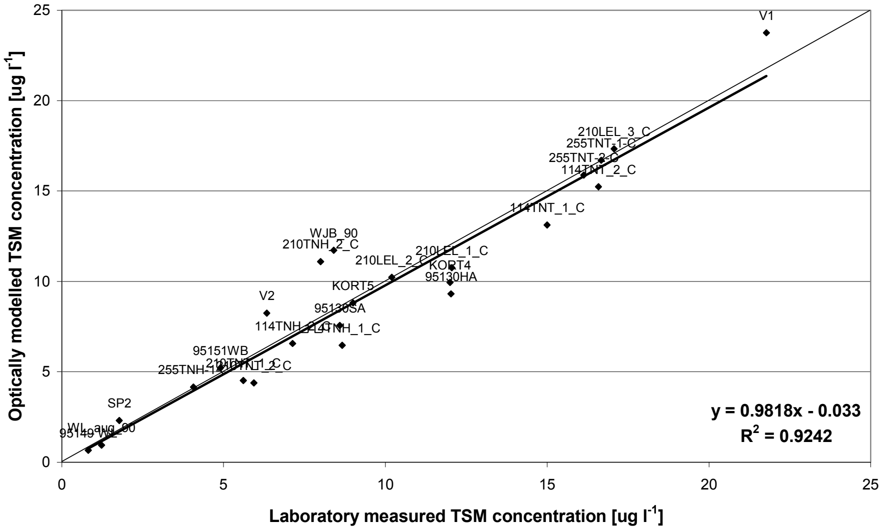

Figure 8.5: The measured and modelled TSM concentration of the 24 selected sample locations.

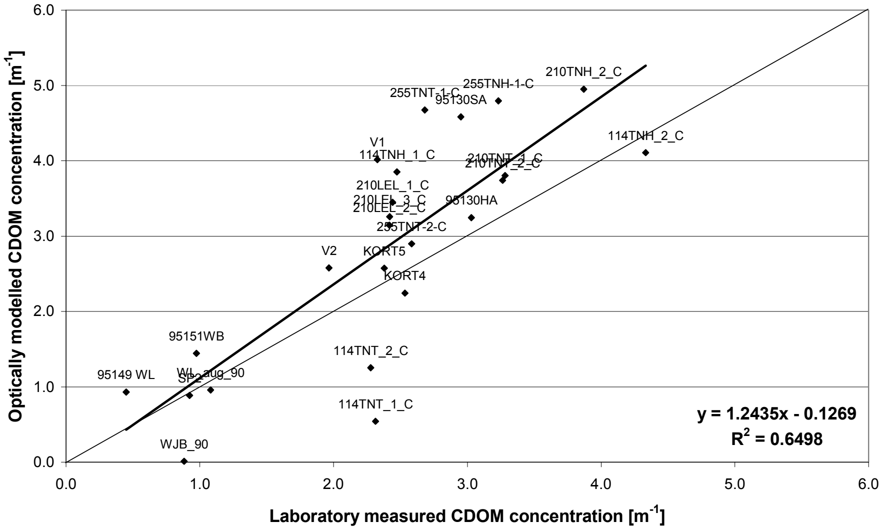

Figure 8.6: The measured and modelled CDOM concentration of the 24 selected sample locations.

8.5.2 Retrieved CDOM concentrations using measured spectra and the median SIOP set

Measured $R(0-)$ spectra from the quality-controlled 24 sample locations were inverted using the methods described earlier (Matrix Inversion Methods and Levenberg-Marquardt curve-fitting). The spectra collected by the hand-held spectrometer with per-nanometre band settings were not included in the results in order to reduce the amount of data shown, keeping the results comprehensible. It was found that the best CDOM retrieval results were obtained by discarding the wavelength bands before 440 nm and beyond 720 nm (MERIS band 1 and 10, CASI bands 1, 14 & 15, see Table 7.3). Again, the Gordon-Walker pre-factor f used was 0.38, and the backscatter to forward scatter ratio B was 0.018 (the value included in the median SIOP set calculated in §8.4). The R^2 value and the slope and offset values of the regression equation between measured and retrieved concentrations of TCHL, TSM and CDOM of 24 measured $R(0-)$ spectra are given in table 8.5.

Table 8.5: The R^2 value and the slope and offset values of the regression equation between measured and retrieved concentrations of TCHL, TSM and CDOM after the inversion (MIM and LM) of the measured $R(0-)$ spectra (for both the MERIS and CASI band settings)

	TCHL		TSM		CDOM	
	R^2	Slope + offset	R^2	Slope + offset	R^2	Slope + offset
MERIS MIM	0.88	y= 0.72x + 0.11	0.49	y= 0.71x + 0.49	0.52	y = 0.89x + 0.26
MERIS LM	0.80	y= 0.78x + 4.46	0.46	y= 0.77x + 1.35	0.61	y = 1.12x - 0.05

CASI MIM	0.84	y= 0.70x – 2.17	0.52	y= 0.66x + 0.97	0.52	y = 0.87x + 0.19
CASI LM	0.81	y= 0.80x + 5.24	0.47	y= 0.78x + 1.28	0.60	y = 1.19x – 0.28

The TCHL concentrations are retrieved with very similar correlations and slopes. The TCHL underestimation is about 30%. Also as with the inversion using per-sample SIOPs, the LM algorithm yields slightly better results (10% underestimation while MIM leads to a 20% underestimation).

As a consequence of using the median SIOP set, the accuracy of TSM retrieval decreases significantly, as scaling problems due to errors in measured spectra are not fully compensated for. The correlation coefficients decrease to 0.5, while the slope parameter shows an underestimation of about 20-30%. Figure 8.8 shows that the TSM underestimation is not systematic, and mostly due to the inversion result of station V1 (see figure 8.5 for comparison). The MIM technique yields higher R^2 values but a 10% surplus underestimation than the LM method.

The correlation coefficients for the retrieved CDOM concentrations have not changed by using the median SIOP set, while the slope parameter has improved. As shown in figure 8.9, the retrieved CDOM values in the lower concentration range appear underestimated, while the CDOM values in the higher concentration range seem overestimated (see figure 8.6 for comparison). Especially sample stations 114_TNT_1_C and 114_TNT_2_C have poor retrieval accuracy (severe CDOM underestimation and TSM overestimation), probably due to the unusually high specific seston scattering at this point (twice the value of the b^*_{ses} included in the median SIOP set). This demonstrates the limitations of using a single reference SIOP set for retrieving water quality parameters from lakes with various conditions.

For CDOM the slope parameter is underestimated by 10% when using MIM, but LM leads to an overestimation of 20%, both for the MERIS and CASI band settings.

Overall, the LM technique leads to 10-20% higher estimates, analogous to the inversion using the per-sample SIOP sets. In case of TCHL and TSM there is less underestimation while for CDOM the LM technique results in overestimations.

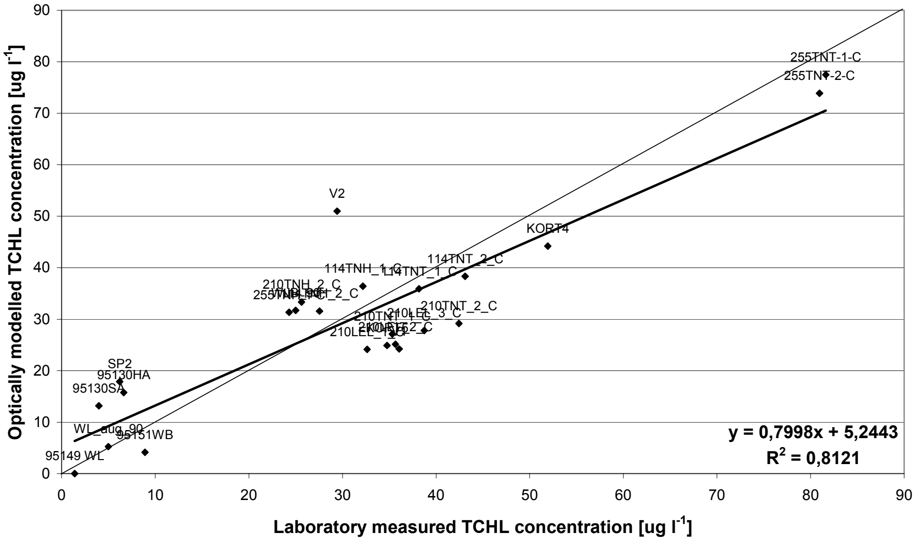

Figure 8.7: The measured and modelled TCHL concentration of the 24 selected sample locations using the median SIOP set, the Levenberg-Marquardt technique and the CASI band settings (sample location codes are displayed above the data points). The thin black line shows the 1:1 relationship, while the thick black line represents the regression relationship (regression parameters are displayed in the lower right corner).

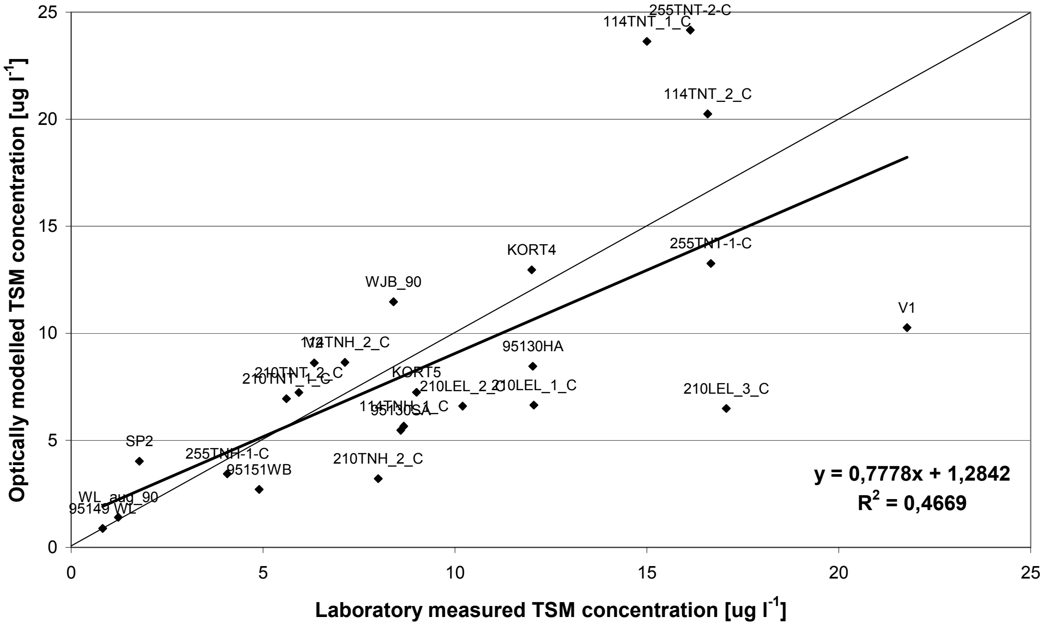

Figure 8.8: The measured and modelled TSM concentration of the 24 selected sample locations.

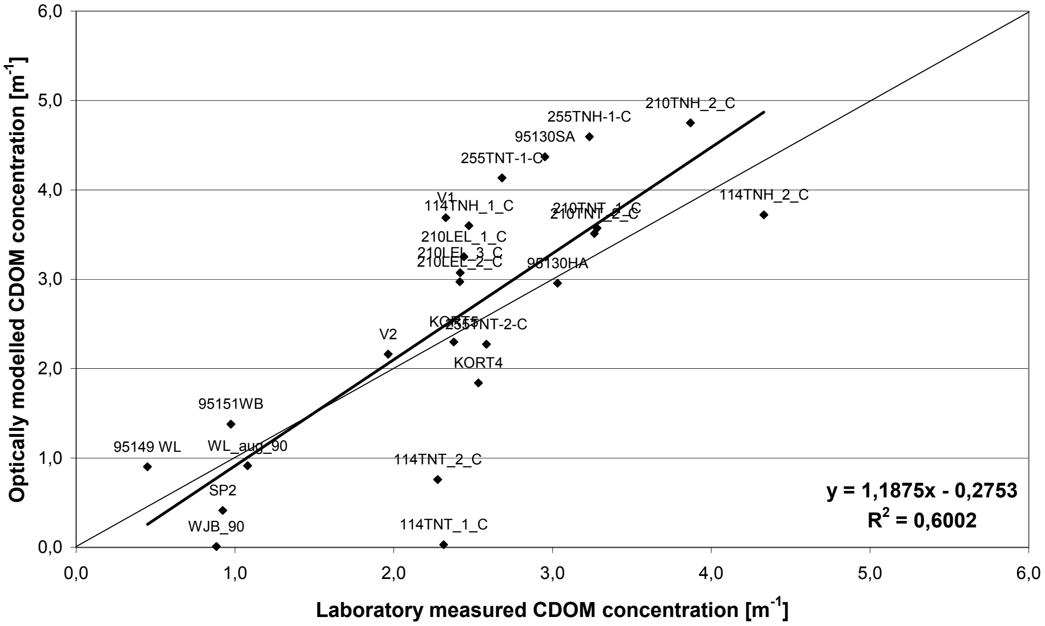

Figure 8.9: The measured and modelled CDOM concentration of the 24 selected sample locations.

8.6 CDOM retrieval discussion and conclusions

In this chapter two quality control procedures were carried out in order to select sample locations with suitable CSI data measured in this research to be used for the inversion of the optical model. The first procedure involved the comparison of measured concentration and SIOP data to values found in literature. It was found that the concentration and SIOP data of all 52 sample locations were in the same ranges as reported in publications of studies conducted in the same research area – except for the specific seston scattering of four sample stations. These stations, with b^*_{ses} exceeding 2.00 m^2 mg^{-1}, were removed from the selection. It was also observed by using a forward optical model that when the TCHL concentration at a sample location was very high, a successful retrieval of the CDOM concentration by means of inverse optical modelling is inhibited. It was therefore decided to discard all sample locations with a TCHL concentration that exceeded the arbitrary threshold value of 85 µg l^{-1}.

The final quality control procedure was based on forward modelling of the measured concentration and SIOP data and subsequent comparison of the resulting modelled $R(0-)$ spectrum with the corresponding measured $R(0-)$ spectrum. After all, when the fit of the forward simulated spectrum is poor, successful inverse optical modelling will automatically be unfeasible. The goodness of fit between the modelled and measured $R(0-)$ spectrum was determined by means of a normalised χ^2 difference. Although a poor χ^2 score can be caused by errors in the concentration, the SIOP data and the measured $R(0-)$ spectra, it is the experience within this research that usually the measured $R(0-)$

spectrum is the main error source. All sample stations were discarded with an χ^2 value that exceeded the arbitrary threshold value of 20.

The number of sample stations that passed both the quality control procedures is 24 (from 52). This means that the CSI data over half of the sample stations is of insufficient quality for analytical optical modelling. A number of 5 sample stations were discarded only because of their high TCHL concentrations. The number of suitable sample locations is therefore a poor one out of two, an observation that calls for a review of the field and laboratory protocols. A median SIOP set was constructed using data from the 24 selected sample locations to be used for the inversions of the optical model.

For the state-of-art inversions 2 semi-analytical algorithms were selected and tested for performance and robustness: Matrix Inversion Methods (MIM) and Levenberg-Marquardt (LM). The effect of available bands was also investigated by using spectra measured with a hand-held spectrometer that were transformed to MERIS and CASI band settings.

First, measured subsurface irradiance reflectance spectra from 24 sample locations were inverted using the MIM and LM inversion methods and the per-sample SIOP sets. This resulted in excellent TSM retrievals with regression slopes between measured and retrieved concentrations of near 1 and correlation coefficients exceeding 90%. The Levenberg-Marquardt optimisation scored slightly better (10%) results. The correlation coefficients for TCHL are not as strong as those for TSM but still reasonable with 0.6 to 0.8. The slope and offset parameters for TCHL show a 25% underestimation. Contrary to TSM, the MIM technique yields better TCHL retrieval over LM. The retrieval of CDOM concentrations using the per-sample SIOPs does not yield accurate results. R^2 values are down to 0.4 – 0.5, while the slope parameters show a 30 – 40% underestimation. The low performance for the retrieval of CDOM is probably due to either an error in the $\bar{a}_{CDOM}$ of the per-sample SIOP sets or an error in the measured reference CDOM concentrations.

Next the same inversion was performed, this time using the median SIOP set. The TCHL concentrations are retrieved with very similar correlations and slopes. The TCHL underestimation is about 30%. Also as with the inversion using per-sample SIOPs, the LM algorithm yields slightly better results (10% underestimation while MIM leads to a 20% underestimation).

As a consequence of using the median SIOP set, the accuracy of TSM retrieval decreases significantly, as scaling problems due to errors in measured spectra are not fully compensated for. The correlation coefficients decrease to 0.5, while the slope parameter shows an underestimation of about 20-30%. The TSM underestimation is not systematic, and mostly due to the inversion result of station V1. The MIM technique yields higher R^2 values but a 10% surplus underestimation than the LM method.

The correlation coefficients for the retrieved CDOM concentrations have not changed by using the median SIOP set, while the slope parameter has improved. The retrieved CDOM values in the lower concentration range appear underestimated, while the CDOM values in the higher concentration range seem overestimated. The slope parameter however is particularly affected by two sample stations with severe underestimation due to a large discrepancy between the local SIOP and the median SIOP set. For CDOM the slope parameter is underestimated by 10% when using MIM, but LM leads to an overestimation of 20%, both for the MERIS and CASI band settings.

Overall, the LM technique leads to 10-20% higher estimates, analogous to the inversion using the per-sample SIOP sets. In case of TCHL and TSM there is less underestimation while for CDOM the LM technique results in overestimations.

9. Improving CDOM absorption measurements by using a Point-Source Integrating-Cavity Absorption Meter

9.1 Introduction

As a result of the modelling and sensitivity studies in the previous chapters it was found that the optical determination of CDOM could possibly be improved by improving the characterisation of CDOM absorption. It was found for the 24 selected high quality measurement stations that CDOM was systematically underestimated by all inversion methods, leading to the tentative conclusion that the standard measurement of CDOM absorption leads to overestimation of the absorption curve.

An explanation for the potential overestimation of CDOM absorption by standard measurements is easily given. Usually the a is determined by measuring the light attenuation by a filtered sample (compared to a reference such as pure water) in a cuvette, assuming that the scattering coefficient of the filtrate is negligible and using the relationship between attenuation, absorption and scattering:

$$c = a + b \tag{9.1}$$

Until recently scattering was assumed to be negligible compared to absorption when measuring CDOM absorptions of natural waters using the cuvette method, but this assumption is now being questioned (Doerffer 2002a). If there is any residual scattering it will, erratically, be added to the absorption coefficient.

A crude correction for such residual scattering is to subtract the offset of the absorption spectrum at around 750 nm where it is assumed that the absorption is negligible. But this will lead to an underestimation if there is still significant absorption at that wavelength (as has been demonstrated in chapter 7). Other ways to avoid absorption overestimation caused by scattering losses in a cuvette are given by alternative measurement methods proposed in recent literature. An overview of these methods is given in Table 9.1.

Table 9.1: Various published methods to measure the absorption coefficient of optical active components in water (phytoplankton, tripton, CDOM or the total absorption)

Method	Component	Reference	Remarks
Cuvette method using a bench spectrometer (laboratory)	Phytoplankton and CDOM	NEN 6520 1981; Bricaud, Morel, and Prieur 1981	Scattering correction possible with integrating sphere
AC-9 method (in situ)	Phytoplankton and CDOM	-	
Liquid Core Waveguide / Liquid Waveguide Capillary Cell (laboratory / in	CDOM	Miller, Belz, Del Castillo, and Trzaska 2002; Kirkpatrick, Orrico, Moline, Oliver,	Some scattering correction with reflective outer layer

situ)		and Schofield 2003	
Quantitative filter technique (laboratory)	Phytoplankton and tripton	Roesler 1998	
Reflecting tube absorption meter (RTAM) (in situ)	Total absorption	Pegau, Cleveland, Doss, Kennedy, affione, ueller, Stone, Trees, Weidemann, Wells, and Zaneveld 1995	In situ, some scattering correction by design (modified AC-9)
Isotropic point source (IPS) (in situ)	Total absorption	Pegau, Cleveland, Doss, Kennedy, affione, ueller, Stone, Trees, Weidemann, Wells, and Zaneveld 1995	

Preferably, all absorption (and scattering) properties of water samples have to be measured *in situ* but such equipment was not available for this research. Also, most of these instruments (such as the AC-9) have been developed for case I waters and would not necessarily provide good results in these case II waters.

Because of these considerations it was chosen to study and apply an innovative laboratory method for the determination of CDOM absorption that may develop into an *in situ* instrument in the future: the integrating cavity concept.

Since the light field inside an integrating cavity is already totally diffuse, scattering effects will (theoretically) not affect the absorption measurement. Two types of integrating cavity devices have been proposed and developed: the cylindrical shaped Integrating-Cavity Absorption Meter (ICAM) (Fry, Kattawar, and Pope 1992) and the spherical Point-Source Integrating-Cavity Absorption Meter (Kirk 1995). The spherical shape of the PSICAM and the fact that the cavity is illuminated from a point source in the centre instead of via the cavity wall should provide a better performance of the PSICAM over the ICAM (Kirk 1995; Lerebourg, Pilgrim, Ludbrook, and Neal 2003).

A theoretical advantage of the PSICAM over cuvette measurements is that the average path length of photons that can be achieved in the cavity is much longer because of (potential) multiple collision and reflection at the cavity wall (see the PSICAM overview in Figure 9.1). Numerical modelling shows that achievable path lengths could be typically around 1 meter at an absorption coefficient of around 1 m^{-1} and can reach up to ten meters for lower absorptions (with a cavity reflectivity of 0.99) (Kirk 1995). Therefore it is expected that a PSICAM is capable to measure the absorption coefficients in the lower concentration domain (so called Case I oceanic waters but also very clear oligotrophic lakes) with higher accuracy and repeatability than a classic bench spectrometer, even when operating 200 cm cuvettes.

The ICAM was applied by Pope *et al.* (Pope, Weidemann, and Fry 2000) for measurements of dissolved organic matter in the Gulf of Mexico. Their CDOM concentrations ranged from 0.6 (Mississippi outflow) to 0.02 m-1 (out at sea). They found that absorption spectra measured with the ICAM could be accurately fitted to an exponential function (see chapter 10).

The PSICAM has been applied in practice in studies by Laanen *et al.* and Dekker *et al.*

Probably due to a poor PSICAM wall reflectivity calibration, Laanen *et al.* (Laanen, Peters, Pasterkamp, Brando, Daniel, and Dekker 2002). found that the C_{CDOM} absorption of CDOM samples collected in the Vecht Wetlands study area measured by the PSICAM was (on the average) 50% lower as compared to a conventional cuvette system. This deviation was too large to be acceptable. Dekker *et al.* found a reasonable agreement between the PSICAM and conventional cuvette system measurements only for the wavelength region between 450-550 nm (Dekker, Brando, Daniel, Anstee, and Clementson 2002). In a recent publication of Röttgers *et al.*, describing work that has been performed after the experiments carried out in this dissertation, a PSICAM was calibrated successfully and good agreement between PSICAM and laboratory spectrometer measurements of a humic acid standard (Roettgers, Schoenfeld, Kipp, and Doerffer 2005).

The PSICAM used for this research is an experimental prototype built by CSIRO (Canberra, Australia). The term PSICAM in this chapter refers to the CSIRO PSICAM, except when discussing the theoretical principles of the PSICAM. The calibration results, the residual scattering effect case study results and the conclusions and recommendations apply mainly to our version of a CSIRO PSICAM. During the course of this study it became evident that the calibration of the instrument was complicated, due to difficulties in obtaining an accurate assessment of the reflectivity of the cavity wall. Therefore the PSICAM was used in tandem with a cuvette spectrophotometric set-up using the same spectrophotometer, to be able to compare results.

In this chapter the proposed advantages of a PSICAM (a higher accuracy and a lower CDOM absorption coefficient detection limit) are investigated for the purpose of obtaining improved CDOM reference absorption coefficients to be used with inverse modelling. The chapter is organized as follows:

- ➔ Section 9.2.1 outlines the theory, concepts and instrumental specifications of the PSICAM system
- ➔ Section 9.2.2 discusses absorption measurements by a cuvette system and by the PSICAM system. The section finishes with an *a priori* comparison of cuvette and PSICAM. For both systems the signal to noise ratio is calculated using the dark current measurement and a reference measurement of pure (distilled) water
- ➔ Section 9.3, the calibration of the PSICAM, starts with a discussion on the necessity to calibrate the PSICAM by measuring directly or indirectly the cavity reflectivity
- ➔ Next in § 9.3.1 four possible calibration strategies to obtain the cavity reflectivity are listed. Evaluation criteria are given to decide between on the best possible calibration strategy. The whole calibration procedure, including preparations steps and final comparison and selection steps are outlined in a flow chart
- ➔ In §9.3.2 it is described how a concentration-absorption relationship is used as a reference for the calibration. Here dilutions series of an absorbent standard are prepared and their absorption measurements used to construct the concentration-absorption relationship.
- ➔ The results of the various methods of calibration are discussed in section 9.3.3
- ➔ Subsequently a selection of the best calibration method is performed in §9.3.4

- ➔ The discussion and conclusions of the PSICAM calibration analysis are given in §9.3.5
- ➔ In section 9.4 a case study is presented investigating the influence of scattering in the cuvette measurements by comparing PSICAM and cuvette measurements of CDOM absorption
- ➔ The possible improvement in CDOM retrieval from measured reflectance spectra by using PSICAM reference CDOM measurements is tested in section 9.5
- ➔ Finally in §9.6 the discussion and conclusions of this chapter are given

9.2 PSICAM Theory

9.2.1 PSICAM concept and specifications

A PSICAM is a device to measure light absorption in natural water samples containing scattering material. It was designed and described by Kirk (Kirk 1995 & Kirk 1997) as a spherical cavity filled with the water sample in which light is emitted by an isotropic source at the centre of the cavity. The emitted light is either absorbed by the medium or reflected by the highly reflecting cavity wall or retrieved by a diffuser leading to the spectrometer via an optical fiber (see Figure 9.1).

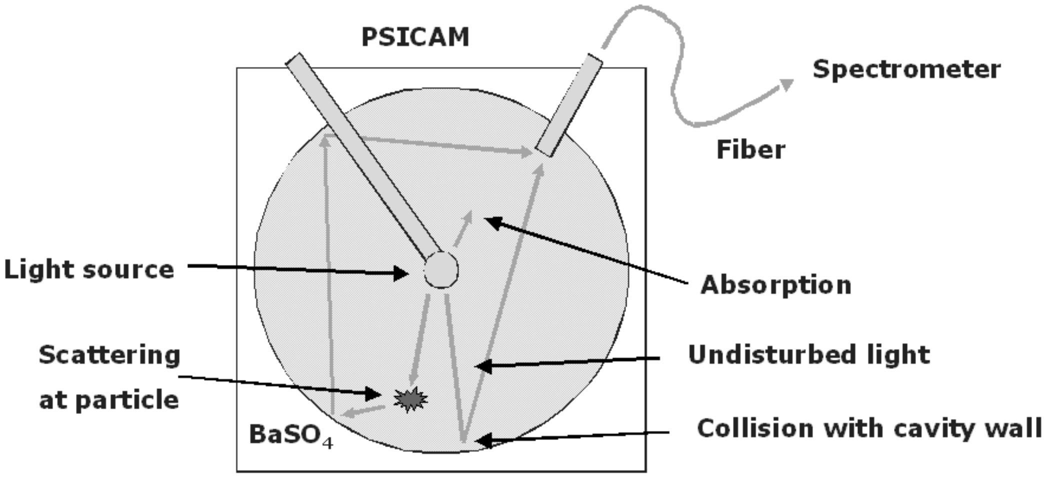

Figure 9.1: Schematic overview of the CSIRO PSICAM used for this research

Cavity

The prototype PSICAM cavity used for this research was build by CSIRO, Canberra (Australia) following the design of John Kirk. Its cavity consists of a 500 ml spherical Pyrex laboratory flask with two openings and a radius of 0.05 m. The larger opening holds the light source, while the smaller opening accepts the sampling fore-optics for irradiance measurements. In order to create a more Lambertian surface the inside of the flask was sand blasted. The flask is surrounded by tightly packed barium sulphate powder ($BaSO_4$), a highly reflective substance (~90%), and placed in a can-like metal enclosure with the flask necks protruding. Newer versions of the CSIRO PSICAM will be filled with PTFE powder with higher reflectance (~99%).

Light source

The light source is a commercial miniature 4.2 V, 0.7 A, Krypton-Halogen torch bulb that is also sand blasted, positioned at the end of a 0.004 m Ø aluminium tube. When inserted, the light bulb is located at the centre of the cavity. The tube is mounted on a glass adapter that fits into the neck of the cavity. Both are wrapped with PTFE tape in order to maintain the highest reflectance within the cavity. A constant power supply powers the light bulb, hence the designation stable light source. A stability of at least 20 ppm $°C^{-1}$ was achieved for the current-source (over a temperature range of 20 - 50°C). Both the light source and the power supply were designed and manufactured by CSIRO and are discussed by Dekker *et al.* (Dekker, Brando, Daniel, Anstee, and Clementson 2002).

Fore-optics

The sampling fore-optics consist of an CC-3-UV cosine-corrected fiber optic irradiance probe from Ocean Optics Inc. (of Florida, USA, www.oceanoptics.com) collecting irradiance from the entire cavity, coupled (with a SMA connector) with an Ocean Optics 400-2-UV-VIS 2 m single-strand silica-core optical fiber with a 400 µm diameter entering the spectrometer. When inserted, the cosine corrector aligns with the cavity wall. The cosine corrector assembly is wrapped in PTFE tape to fill the space between the glass neck of the flask and the sampling fore-optics, maintaining high cavity reflectivity.

Spectrometer

The spectrometer used is an Ocean Optics SD2000 UV-VIS-NIR Miniature Fiber Optic Spectrometer. The SD2000 has a crossed Czerny-Turner design Sony ILX511 2048-element linear CCD-array silicon detector. The grating of the instrument is optimised for UV-VIS-NIR applications, with a groove density of 300 lines mm^{-1} and a spectral range of 1700 nm. Of this spectral range however the "best efficiency" (>30% first order spectra optimisation) region is 300 – 1100 nm, which is used for measurements. In order to increase spectral resolution the SD2000 used is equipped with an internal slit of 25 µm. The Optical resolution, defined as Full Width Half Maximum ($FWHM$ [nm]), is calculated using the following equation:

$$FWHM = \frac{spectral\,range}{elements} \times resolution \qquad 9.2$$

Thus, using a spectral range of 1700 nm, a total of 2048 elements (pixels) and a pixel resolution of 4.2 pixels based on the slit size (from www.oceanoptics.com) the resulting $FWHM$ for the SD2000 used for this research is 3.5 nm. Because of the slit the $FWHM$ is independent of the diameter of the optical fibers used (as long as the fibers are larger in diameter than 25 µm).

Signal to noise ratio

In addition to the design of the PSICAM flask, the light source used plays an important role in its performance. In order to get an impression of the performance difference beforehand, the signal to noise ratios (SNR [-]) of the PSICAM and the spectrophotometric cuvette system were compared. The SNR is regarded as an indicator for measurement sensitivity and repeatability (Schaepman 1998). SNR values were computed for each of the configurations using the Ocean Optics SD2000:

- ➔ The Ocean Optics spectrometer by taking a series of reflection measurements using another halogen stable light source in a dark room enclosure at CSIRO, Canberra
- ➔ The complete PSICAM system (CSIRO stable light source, cavity and Ocean Optics) using the reference and dark readings from a series of measurements
- ➔ The spectrophotometric cuvette system (LS_1CAL Ocean Optics Tungsten-halogen lamp with a bulb temperature of 2800K), an enclosed 10 cm cuvette and the Ocean Optics SD2000) using the reference and dark readings from a series of measurements

The SNR was calculated as follows (Schaepman 1998):

$$SNR = \frac{\overline{DN_{reference}} - \overline{DN_{dark}}}{\sqrt{\left(\sigma DN_{reference}\right)^2 + \left(\sigma DN_{dark}\right)^2}} \qquad 9.3$$

With $DN_{reference}$ the digital numbers [-] recorded for the reference measurement, DN_{dark} the digital numbers [-] recorded as background or dark noise (response of the system when no light can enter the spectrometer) and σ the standard deviation [-]. The spectral SNR of the Ocean Optics, the PSICAM and the cuvette system, calculated using equation 9.3 is given in Figure 9.2.

There is a significant increase in the SNR when a stable light source is used instead of the LS-1CAL lamp.

The PSICAM system has a SNR that is about four times higher than the SNR of the spectrophotometric cuvette system in the blue wavelength region that is of most importance for CDOM absorption measurements. Thus the PSICAM is more sensitive, and the average path length of the photons is significantly longer. These two factors combined make the PSICAM more accurate for CDOM measurements.

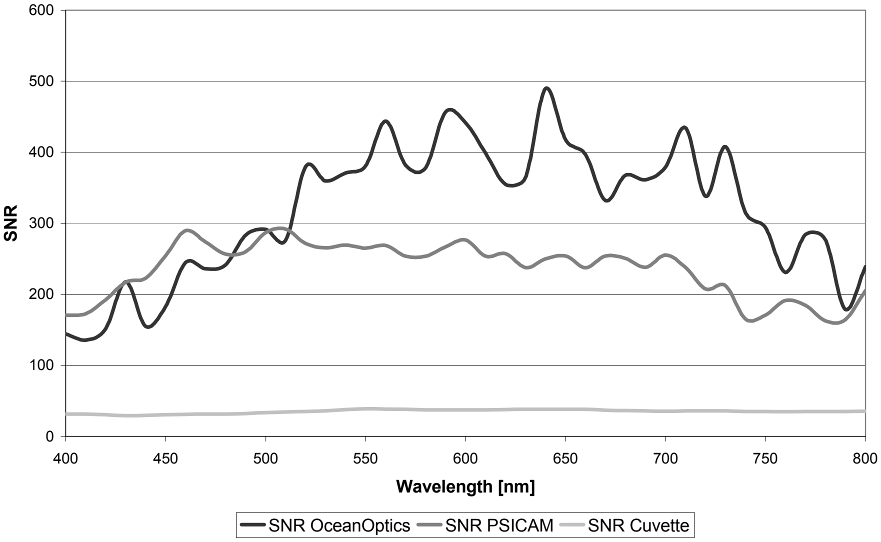

Figure 9.2: The SNR of the Ocean Optics spectrometer, the PSICAM system and the Ocean Optics cuvette system.

9.2.2 Absorption measurements: the cuvette method and the PSICAM method

Absorption measurement using the standard cuvette method

In a standard laboratory bench cuvette system the absorption coefficient of a sample is obtained by measuring the signal of the sample against the signal of a reference solution (in most cases the reference is a pure form of water, for this research distilled water was used). For more information about absorption measurements see the cuvette and PSICAM CDOM measurement protocols in Appendix III and e.g. the following publications: Tilstone, Moore, Sørensen, Doerffer, Pasterkamp, and Jørgensen (2002) for the MERIS instrument, and Mueller and Austin (2000) for the MODIS instrument.

The absorbance A of a sample is expressed as the ratio of these signals, corrected for the background signal:

$$A = \frac{DN_{sample} - DN_{dark}}{DN_{reference} - DN_{dark}} \qquad 9.4$$

with DN_{sample} the digital numbers recorded by the spectrometer measuring the sample. The absorption coefficient *a* [m^{-1}], which is dependent of the path length, is calculated as follows:

$$a = \ln(10)\frac{A}{l} \qquad 9.5$$

with l [m] the length of the cuvette used in the spectrometer. The cuvette based CDOM absorption coefficients used for comparison with the PSICAM in this study were obtained using this method (see Appendix III).

Absorption determination using a PSICAM

Unlike the cuvette, the photons reaching the sampling fore-optics of the spectrometer in a PSICAM have travelled varying distances. As they may have collided with the cavity wall a number of times their path length varies considerably. Kirk (Kirk 1995) showed that, by considering a spherical cavity, explicit expressions for the probability of photon survival in transit across the cavity P_s, the average number of photon collisions with the wall C_f and the average photon path length l_f [m] could be derived as a function of the absorption coefficient a [m^{-1}], the cavity radius r [m] and the reflectivity of the cavity wall ρ [-] (Kirk 1997):

$$P_s = \frac{1}{2a^2r^2}\left[1-(2ar+1)\exp(-ar)\right] \qquad 9.6$$

$$C_f = \frac{\exp(-ar)}{1-\rho P_s} \qquad 9.7$$

$$l_f = \frac{1}{a}\left\{1-\exp(-ar)\left[2-\rho\left(\frac{1-P_s}{1-\rho P_s}\right)\right]+(2ar+1)\exp(-2ar)\right\} \qquad 9.8$$

The absorption in a PSICAM is not calculated using the average path length. The PSICAM absorption is based on the transmittance, the ratio of the intensity of the light measured in the PSICAM containing the sample to that of the PSICAM containing pure water as a reference. The transmittance T is related to the absorbance A (see equation 9.4), which is measured by the spectrometer:

$$T = 10^{-A} \qquad 9.9$$

Kirk (Kirk 1997) states that for the PSICAM the T is also the ratio of the outwardly directed irradiance at the surface of the cavity filled with the sample (F_0 [W m^{-2}]) and the cavity filled with pure water ($F_0^{\,w}$ [W m^{-2}]):

$$T = \frac{F_0}{F_0^{\,w}} \qquad 9.10$$

The irradiance on the cavity wall is proportional to the average number of photon collisions with the wall, for a given radiant power from the point source (Kirk 1997), i.e. $F_0 \propto C_f$. Combining equations 9.7 and 9.10 then gives:

$$T = \frac{\exp(-ar)(1-\rho P_s^{\,w})}{\exp(-a_w r)(1-\rho P_s)} \qquad 9.11$$

with a_w [m^{-1}] is the absorption coefficient of pure water. It is however not possible to solve equation 9.11 for a. Only after assuming that the radiance distribution is both isotropic and homogeneous throughout the cavity, an approximate expression for the absorption can be derived. Fry *et al* (Fry, Kattawar, and Pope 1992) demonstrated that under such a homogeneous energy distribution assumption, the power P [W] absorbed by the sample is given by:

$$P = 4aVF_0 \qquad 9.12$$

with V the volume of the cavity [m^3]. The total power emitted in the cavity (P_{in} [W]) can be either be absorbed by the sample or by the cavity wall, so

$$P_{in} = P_{water} + P_{cavity} \qquad 9.13$$

The power loss trough the cavity wall in equation 9.13 can be expressed as:

$$P_{cavity} = F_0 SA(1-\rho) \qquad 9.14$$

with SA the surface area [m^2] of the cavity wall. When combining equations 9.12, 9.13 and 9.14, the absorbed power can be calculated for the sample and the reference:

$$P_{in,s} = 4a_s VF_0 + F_0 SA(1-\rho) \qquad 9.15$$

$$P_{in,w} = 4a_w VF_0^{\,w} + F_0^{\,w} SA(1-\rho) \qquad 9.16$$

The power emitted by the light source in the cavity is independent on the type of contents: a sample or the reference, so equations 9.15 and 9.16 are in fact equal to each other. Furthermore, by dividing both equations by $F_0^{\,w}$, substituting $F_0 / F_0^{\,w}$ with T and some rearranging, we get

$$T = \frac{4a_w V + SA(1-\rho)}{4aV + SA(1-\rho)} \qquad 9.17$$

From equation 9.17, with further rearranging and by expressing SA and V in terms of r, the absorption a can finally be calculated as follows (Kirk 1997):

$$a = \left[\frac{\frac{4}{3} a_w r + (1-\rho)}{\frac{4}{3} r} \right] \frac{1}{T} - \frac{3(1-\rho)}{4r} \qquad 9.18$$

Note that a in equation 9.18 is the absorption of the medium, $a_w + a_{sample}$. The absorption coefficient of water can be found in literature (Pope and Fry 1997 completed to 800 nm with Buiteveld, Hakvoort, and Donze 1994), while the radius of the cavity used was 0.0505 m. The cavity reflectivity ρ is a property dependent on the materials used inside the PSICAM. The ρ may be retrieved through several calibration approaches to be discussed further in §9.3.

Sensitivity

Two Monte Carlo simulation studies, by Kirk (Kirk 1995) and Leathers *et al* (Leathers, Downes, and Davis 2000), have been carried out to establish the sensitivity of parameters used for PSICAM calculations. The sensitivity coefficient of a with respect to ρ is given by:

$$\frac{\partial a}{\partial \rho} = -\frac{\partial T / \partial \rho}{\partial T / \partial a} \qquad 9.19$$

with ∂ the partial differential. Sensitivity coefficients for a_{ref} and r can be computed likewise. The sensitivity of the calibration can be computed as:

$$\Delta a = \left[\left(\frac{\partial a}{\partial a_{ref}} \right)^2 \left(\Delta a_{ref} \right)^2 + \left(T \frac{\partial a}{\partial T} \right)^2 \left(\frac{\Delta T}{T} \right)^2 + \left(\frac{\partial a}{\partial a_A} \right)^2 \left(\Delta a_A \right)^2 + \left(T_{AB} \frac{\partial a}{\partial T_{AB}} \right)^2 \left(\frac{\Delta T_{AB}}{T_{AB}} \right)^2 \right] \qquad 9.20$$

With a_A the absorption coefficient of solution A and T_{AB} the relative transmittance between solution A and B. It was found that the uncertainty of a depends primarily on the uncertainties of the measured absorptions of the two reference solutions A and B by calculating a with equation 9.18 with and without a small error. The high sensitivity of a to ρ is compensated for by the very low sensitivities of ρ to a_A and a_B (or a_{ref}).

Leathers *et al.* found that, when ρ is known, i.e. after calibration or by direct measurement, the uncertainty in a is primarily due to the uncertainties in ρ and a_{ref}. The sensitivities to T and r are negligible. The total uncertainty can be computed as:

$$\Delta a = \left[\left(\frac{\partial a}{\partial a_{ref}} \right)^2 \left(\Delta a_{ref} \right)^2 + \left(\frac{\partial a}{\partial \rho} \right)^2 (\Delta \rho)^2 + \left(\frac{\partial a}{\partial r} \right)^2 (\Delta r)^2 + \left(\frac{\partial a}{\partial T} \right)^2 (\Delta T)^2 \right] \qquad 9.21$$

According to Leathers *et al* (Leathers, Downes, and Davis 2000) it is not critical to have a perfectly isotropic light source, as resulting errors in T will affect both the sample as the reference measurement and cancel out to a great extent. If the anisotropy is different between the sample and reference measurements however, this will have an effect on the transmittance. In practice, this means that the light source and fiber need to be positioned exactly the same for each set of measurements in order to avoid differences in anisotropy.

9.3 Calibration of the PSICAM

9.3.1 Introduction

According to Leathers *et al.,* the PSICAM absorption values are very sensitive to uncertainties in the cavity reflectivity: a 1% error in ρ leads to a 10% error in a, considering sea water with an absorption range of 0.1 - 1.0 m^{-1} (Leathers, Downes, and Davis 2000). The value of ρ therefore has to be determined to a precise level.

As a result of the usage of a cosine corrector for irradiance measurements, the PSICAM cannot be calibrated against air as described with the calibration of the ICAM (Fry, Kattawar, and Pope 1992). Instead a number of other calibration approaches are proposed:

1. By measuring the relative transmittance T_{AB} of two dye solutions (A and B) with known absorption coefficients. The advantage of this method is that it tends to eliminate errors associated with the measurements of ρ, r and a (Leathers, Downes, and Davis 2000). Leathers et al also recommend using solutions with similar absorption coefficients ($aA \approx aB$) (Leathers, Downes, and Davis 2000) in order to achieve the highest precision.
2. By measuring the known absorption of a solution and deriving the ρ from equation 9.18. This method is simpler than the first, as it requires only one PSICAM measurement of a sample with a known absorption. This known absorption however has to be obtained with a minimal error, requiring a very accurate reference spectrometer (and a solution without scattering particles).
3. By measuring the reflective characteristics of the cavity materials directly. In this way the material reflectivity can be easily measured with considerable accuracy. The reflectivity of the foreoptics and the light source inside the cavity however are not taken into account. This measurement is only possible in air and thus less representative of actual use with a cavity filled with a water sample.
4. Dekker *et al.* (Dekker, Brando, Daniel, Anstee, and Clementson 2002) and Lerebourg *et al.* (Lerebourg, Pilgrim, Ludbrook, and Neal 2003) bypass the PSICAM calibration by assuming a spectrally neutral cavity reflectivity, with a value based on the best agreement between absorption measurements made in a PSICAM and a bench spectrometer. In these PSICAM studies the value of ρ could not be established with sufficient precision using one or more of the calibration methods described above. Such a spectrally neutral ρ is considered as an alternative for this research as well.

A calibration experiment was set up for the prototype (CSIRO) PSICAM specifically targeted at calibrating the instrument for CDOM determinations using and comparing all 4 mentioned methods. In this way, the most relevant cavity reflectivity was obtained. The calibration experiment is discussed next.

Optimisation for CDOM absorption measurement means that specific demands will be put on the absorbent that is used for calibration and that only the relevant part of the (spectral and radiometric) operating range of the PSICAM will be investigated. The calibration experiment is also set up to give insight into the detection limits and operating range of the cuvette and PSICAM methods for measuring CDOM in natural inland waters.

PSICAM calibration experiments were previously described by Laanen *et al.*, 2002 (Laanen, Peters, Pasterkamp, Brando, Daniel, and Dekker 2002), Dekker *et al.*, (Dekker, Brando, Daniel, Anstee, and Clementson 2002), Lerebourg *et al.* (Lerebourg, Pilgrim, Ludbrook, and Neal 2003) and Röttgers *et al.* (Roettgers, Schoenfeld, Kipp, and Doerffer 2005). Some characteristics of the different PSICAM devices used for these studies are given in Table 9.2 for comparison.

Table 9.2: Characteristics of PSICAM devices used in previous studies

Study	Laanen *et al.*	Dekker *et al.*	Lerebourg *et al.*	Röttgers *et al.*
Type	CSIRO prototype	CSIRO prototype	ONR Prototype	GKSS prototype
Cavity material	$BaSO_4$	PTFE	$BaSO_4$	PTFE
Cavity radius	0.00505 m	0.00505 m	0.00525 m	0.00475 m
Light source	Krypton-halogen bulb powered by a stable power supply	Krypton-halogen bulb powered by a stable power supply	Halogen generator lamp	Halogen lamp
Fore-Optics	Cosine corrector	Cosine corrector	Collimated lens, 10° FOV, not directed at the light source	Radiance collector, not directed at the light source
Fiber	400 μm	400 μm	1000 μm	N/A
Spectrometer	Ocean Optics SD2000 spectrometer	PP systems Unispec spectrometer	Ocean Optics SD1000 spectrometer	TriOS Ramses ACC UV-VIS

A summary of the findings of these experiments is:

- ➔ The calibration based on relative transmittance between two solutions with a known absorption is theoretically the best choice but in practise it appears to be very sensitive to small errors in the cavity wall reflectivity. Dekker *et al.* and Lerebourg *et al.* both report problems with respect to this method. Dekker *et al.* and Röttgers *et al.*used a commercial dye called Nigrosine as absorbing agent, while Lerebourg *et al.* used a commercial black food dye.
- ➔ Both Dekker *et al.* and Lerebourg *et al.* propose to use a spectrally neutral cavity reflectivity because of problems with the calibration (97.5% and 96% cavity reflectivity respectively).
- ➔ Dekker *et al.*, Laanen *et al.* and Lerebourg *et al.* report water absorption artefacts in the PSICAM absorption spectra at longer wavelength regions (beyond 600 nm). For this case study the wavelength range was therefore limited to 400 - 600 nm to avoid these water absorption effects. These water absorption effects have recently been attributed to temperature or salinity differences between reference and sample solutions (Brando, Kirk, Daniel, Oubelkheir, Clementson, and Dekker 2004). Röttgers *et al.* do not report on

water absorption features and have found the temperature influence to be weak.

- ➔ Dekker *et al.* propose to use a different absorbing agent than Nigrosine, and preferably a yellowish dye that has low absorption values in the longer wavelength region to keep the absorption in these wavelengths as low as possible.
- ➔ From previous experience and from work by Dekker *et al.* it was learned that dilutions series to be used for PSICAM calibration should be made with great accuracy, and that taking the reference absorption values in a bench spectrometer requires a very sensitive and accurate set up. Taking reference absorptions in a 1 cm cuvette proved to be too inaccurate. The alternative that was adopted was to measure absorption at high concentrations of dye and extrapolate to the concentration of dilutions used in the PSICAM. This technique however is also sensitive to (small) errors.
- ➔ Dekker *et al.* note that the PSICAM is highly sensitive to small perturbations in the system set up and use.

In this section a calibration experiment will be described that is performed for the four different methods mentioned above. The results of the calibration experiments for each method will be compared in order to establish the best calibration method for the CSIRO PSICAM. Two evaluation criteria were defined to establish the best calibration method for the PSICAM:

1. First a CDOM concentration-absorption relationship will be established using a bench spectrometer. Then, PSICAM absorption measurements at 440 nm of samples with known CDOM concentrations will be performed. All four calibration methods will be applied on those measurements, and subsequently the results will be compared to the concentration-absorption relationship. The calibration method that replicates the concentration-absorption relationship best is regarded as the most method of choice for this research.
2. Successful calibration of the PSICAM for CDOM should theoretically lead to absorption spectra that have a shape resembling the theoretical exponential curve of CDOM. The calibration method yielding absorption spectra with the best exponential shape is preferred, because the slope of the modelled CDOM absorption spectrum is of interest for optical modelling.

The resulting most valid and accurate cavity reflectivity was used for all PSICAM CDOM absorption measurements in this dissertation. The calibration experiments focus on the best use of the PSICAM for CDOM absorption measurements and involve the steps given in Figure 9.3.

First a suitable absorbing substance is chosen as absorption standard. Three independent dilution series of predetermined concentrations are made with this absorption standard. The absorption spectra of these dilution series are then measured in triplicate in a cuvette set up. Next the concentration-absorption relationship for measurements in the cuvette is established. Absorption measurements in a cuvette system calculated with this relationship are used as reference absorptions for the 4 different PSICAM calibration methods.

The next step is to measure the transmittance spectra of these dilution series in the PSICAM, in triplicate. This allows the calculation of the PSICAM cavity reflectivity curves. Using these ρ curves the shapes of the absorption spectra and the concentration-absorption relationships for the 4 different PSICAM calibration methods are determined. Based on the criteria addressed above (the best C_{CDOM} /

absorption at 440 nm relationship and the best exponential shape of the CDOM absorption spectrum), the best cavity reflectivity is then identified.

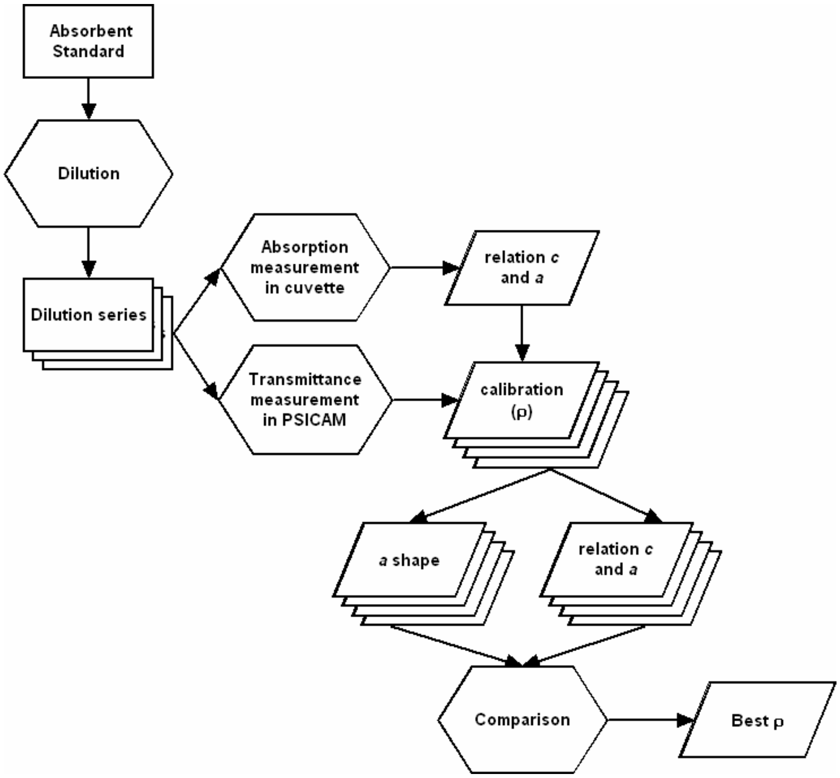

Figure 9.3: The steps of the calibration experiment. Three independent dilution series are measured both in a cuvette and in the PSICAM. Cuvette absorptions are needed as reference absorptions for the PSICAM calibrations. The results of the 4 different PSICAM calibration methods are compared and the best cavity reflectivity selected (with C the concentration, a the absorption (at 440 nm), ρ the cavity reflectivity) and $a\,shape$ the shape of the absorption spectrum).

The different steps of the calibration experiment are reflected in the structure of the remainder of this section:

- ➔ Selection of a suitable absorbent as the calibration standard and the preparation of the dilution series (§9.3.2)
- ➔ Establishing the concentration-absorption relationship for the cuvette based dilution series measurements (§9.3.2)
- ➔ Determining the cavity reflectivity of the PSICAM following each of the 4 methods (§9.3.3)
- ➔ Establishing the concentration-absorption relationship for the PSICAM dilution series measurements for each the four different methods (§9.3.3)
- ➔ Modelling of exponential curves to the absorption spectra for the PSICAM for each the four different methods (§9.3.3)
- ➔ Comparison of the four PSICAM dilution series measurements concentration-absorption relationships and the shapes of the modelled PSICAM absorption spectra for all four calibration methods, in order to determine the best cavity reflectivity (§9.3.4)

Earlier the absorption values of the dilutions measured with the cuvette and the PSICAM will be compared to investigate differences between both methods.

9.3.2 The calibration reference absorption measurements

Using a concentration-absorption relationship as the PSICAM calibration reference

Instead of using individual CDOM absorption measurements as calibration references for the PSICAM a more robust approach was applied by using a concentration-absorption relationship. The theoretical relationship between absorbance and concentration (of a substance dissolved in a liquid or gas) is given by the Lambert-Beer law. This law states the linear correlation between the spectral absorbance A [-], the path length l [cm] traversed, and the concentration of the absorbing substance in the medium:

$$A_\lambda = \kappa_\lambda \cdot C \cdot l \qquad 9.22$$

with C [mol l^{-1}] as the concentration and the proportionality constant or relative spectral absorption coefficient κ [l mol^{-1} cm^{-1}] a substance-specific function of the wavelength. Laboratory spectrometers are commonly calibrated based on such concentration-absorbance relationships, called calibration curves.

For a laboratory set-up with a fixed cuvette length (and therefore a constant path length) and the same absorbent (and thus a constant relative spectral absorption coefficient) there is a positive linear relationship between the absorption a and the concentration C. This relationship is based on equation 9.22 and modified with an offset to correct for systematic errors:

$$C = \frac{1}{\kappa \cdot \log(10) \cdot l^2} \cdot a + offset \qquad 9.23$$

The standard error of the linear regression is regarded as a measure of the correlation between the concentration and absorption. Before the concentration-absorption relationship for the PSICAM calibration can be constructed, a number of steps need to be taken first:

1. Finding an absorbent standard with absorption characteristics that resemble CDOM
2. Creating dilution series of that standard
3. Measuring the absorption coefficients of the dilution series

These steps are discussed in the next sections, concluded by the construction of the concentration-absorption relationship.

Absorbent standard

The calibration of a PSICAM calls for a number of transmittance measurements of samples with a known absorption. In order to obtain such reference absorptions, cuvette absorption measurements are made of samples with various concentrations of an absorbing substance. This absorbent is called a standard. For the PSICAM calibration carries out in this research it was decided to use a standard with similar absorption characteristics as the CDOM samples that the PSICAM will be measuring operationally instead of a strongly absorbing dye such as Nigrosine used by Kirk, Dekker *et al.* and Röttgers *et al.*.In this way the PSICAM is calibrated specifically for its intended task.

A suitable standard was found to be industrial humic acid (CAS 68131-04-4: humic acid, potassium salt, an inert ingredient in pesticide formulations increasing pesticide effectiveness) manufactured by Aldrich (currently Sigma-Aldrich Inc.). This standard was expected to have similar spectral characteristics as CDOM, which was tested prior to the main calibration experiment by measuring the absorption of the humic acid with the Ocean Optics cuvette set up. The test solution was made by dissolving 1.0 mg humic acid in 1000.0 g of distilled water (1 mg l^{-1}) at room temperature (18°C) and neutral pH. Directly afterwards the absorption of the solution was measured in the Ocean Optics cuvette set up. The triplicate of measurements was averaged, and to this average absorption spectrum an exponential function was fitted using the following equation:

$$a_{CDOM}(\lambda) = offset + a_{CDOM}(\lambda_{\circ})e^{(S(\lambda_0 - \lambda))} \tag{9.24}$$

with $a_{CDOM}(\lambda)$ [m^{-1}] the CDOM absorption at wavelength λ, $a_{CDOM}(\lambda_0)$ [m^{-1}] the CDOM absorption at the reference wavelength λ_0, usually at 440 nm for coastal and inland waters. The $a_{CDOM}(\lambda_0)$ is often taken as the concentration of CDOM, C_{CDOM}. The S [m^{-1}] is the slope of the function, while $offset$ is a correction for background scattering and refraction errors (Stedmon, Markager, and Kaas 2000). The exponential CDOM absorption modelling will be extensively discussed in the next chapter.

The average measured and modelled absorption spectra are given in Figure 9.4. Note the exponential shape of the measured humic acid absorption spectrum.

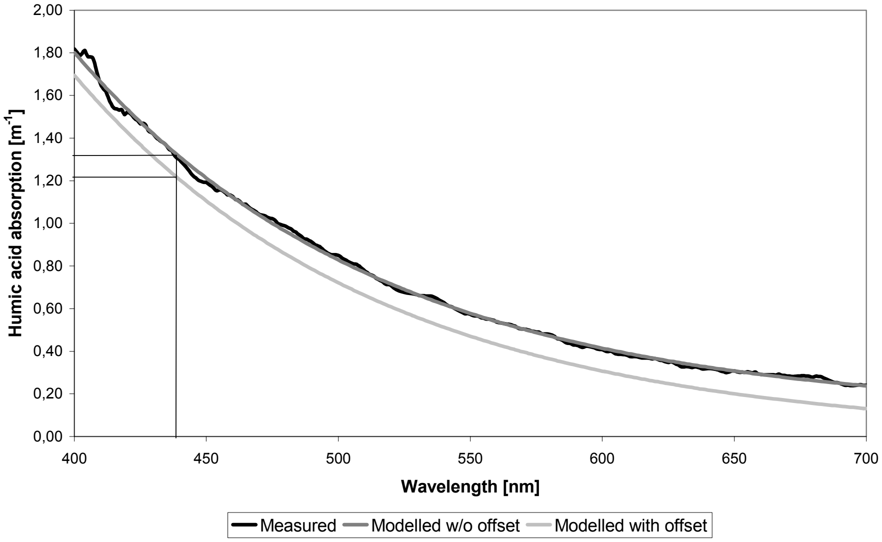

Figure 9.4: Measured absorption spectra of Aldrich humic acid (1 mg l^{-1} concentration) (black line) using a cuvette, the accompanying modelled absorption spectra (dark grey line) and the accompanying modelled absorption with the offset subtracted (light grey line). The difference in absorption coefficients at 440 nm (lower when modelling using an offset) is shown by the annotated lines.

The slope of the exponential modelled function of the measured humic acid sample is 0.0086 m^{-1} (see Figure 9.4), which is roughly in the same range with literature values for humic acids found in natural waters; 0.0104 m^{-1} for riverine humic acid (Zepp and Schlotzhauer 1981) and 0.0111 m^{-1} measured in the Gulf of Mexico (Carder, Steward, Harvey, and Ortner 1989). The slope of the Aldrich humic acid therefore is sufficiently comparable to that of natural CDOM (see next chapter), making it a suitable absorbent standard for the PSICAM calibration.

The average molecular weight for humic acids is in the 20,000 - 50,000 daltons range (see chapter 2), making the compound well soluble in water (at natural pH values). As a rule of thumb the size range for these molecules is 0.03 – 0.06 μm (see Figure 2.1 and Kracht 2001). As it is assumed that dissolved matter has a negligible contribution to the scattering of a solution (Kirk 1983), the absorption measurements of the humic acid standard can be regarded as true absorptions and used for calibration of the PSICAM.

Dilution series

In order to establish the operating range of both the PSICAM and the cuvette set up three independent replicate dilution series comprising of 7 concentrations in the range from 0.01 to 10 mg l^{-1} humic acid were produced, with the following target concentrations: 0.010, 0.033, 0.100, 0.333, 1.000, 3.333 and 10.000 mg l^{-1} humic acid.

Figure 9.4 shows that the concentration of 1 mg l^{-1} humic acid has an absorption coefficient at 440 nm of about 1.2 m^{-1}. This relationship was used for the choice of concentrations of the dilution series. Although the range of natural CDOM absorptions (at 440 nm) is smaller (about 0.5 to 5 m^{-1} in the study area), the range of 0.01 to 10 mg l^{-1} was chosen to investigate the operational applicability of the cuvette and the PSICAM methods. Dekker *et al.* (2002) found that their PSICAM (with a cavity radius of 0.0505 m) has an upper absorption limit of around 2.5 m^{-1} (Dekker, Brando, Daniel, Anstee, and Clementson 2002) and that standard cuvette spectrometers (10 cm cuvette) display a poor performance under 0.1 m^{-1}. The key concentrations that can be measured accurately in both the cuvette and the PSICAM are thus 0.0333 and 1.000 mg l^{-1}.

The target concentrations are not always achieved; it is cumbersome to weigh the precise amounts of distilled water required even using an accurate mass balance. This is however not important as long as the weighed amounts are used to calculate the actual concentration, which is then used instead of the target concentrations. The resulting concentrations of the three dilution series are therefore slightly different. This too is not important because it has no influence on the calculation of the concentration-absorption relationship.

The reason for using three independent dilution series is to reduce the effect of possible dilution errors. After all, if only one dilution series was used and one of the key concentrations was erroneous, the whole PSICAM calibration would be jeopardised. With three dilution series an erroneous concentration in one of the series may be discarded. Triplicate measurements were taken to safeguard against individual measurement errors and in order to enable the quantification of the variation in the absorption measurements.

This exponentially declining concentration range was chosen especially to determine the (lower) detection limit of both the cuvette and the PSICAM methods. The dilution series were made by first creating one 10.000 mg l^{-1} parent solution for each of the three series (to ensure independent dilution series). Each of the child solutions of a series was created from this parent solution. In this way a possible dilution error can only affect one child solution, not the rest of the series. The amount of distilled water added with each dilution was determined by weight rather than volume because a mass balance is more accurate. The mass balance used has an accuracy of 0.02 mg, while the accuracy of the laboratory glassware is 0.1 ml (if read correctly). Assuming the sample has the density of pure water for simplicity, 0.1 ml of sample has a weight of 100.0 mg. The use of the mass balance is thus roughly 5000 times more sensitive and therefore more accurate.

Cuvette absorption measurements

Absorption measurements were performed both in the cuvette and the PSICAM directly after the creation of the dilution series in order to reduce the risks of storage-induced alteration of the solutions (e.g. temperature variations, photo degradation, coagulation or precipitation). A total of 21 measurements were made, with both the samples and the reference (distilled water, from the same source as the water used for creating the dilutions) at room temperature and neutral pH. The results of these absorption measurements were modelled to an exponential function according to equation 9.24. The wavelength range for the exponential modelling was 400-600 nm, similar to the range that could be used for the PSICAM measurements (due to increased pure water absorption effects beyond 600 nm). The modelled C_{CDOM} values, together with the actual humic acid concentrations of the dilution series are given in Table 9.3.

Table 9.3: The C_{CDOM} values of the absorption measurements of the three Aldrich Humic acid standard dilution series in the 10 cm cuvette, with the average, the standard deviation and the relative standard deviation values ($(stdev / average) * 100$) of the triplicates. Absorption values in bold are erroneous and discarded for the calculation of the average and standard deviation. † this measurement was not stored due to human error.

Concentration [mg l^{-1}]	Absorption [m^{-1}] of triplicate			Average absorption [m^{-1}]	Standard deviation [m^{-1}]	Relative Standard deviation [%]
Series 1	1	2	3			
0.010	0.273	0.068	0.089	0.143	0.113	79
0.034	0.177	0.420	0.043	0.213	0.191	90
0.100	0.147	**6.026**	0.133	0.140	0.010	7
0.332	0.428	0.979	0.422	0.610	0.320	52
0.997	1.261	1.234	1.227	1.241	0.018	1
3.289	3.801	3.701	3.825	3.776	0.065	2
9.935	11.971	12.139	12.174	12.095	0.109	1
Series 2	1	2	3			
0.011	6.124	6.106	6.113	n/a	n/a	n/a
0.033	0.150	0.181	0.067	0.133	0.059	44
0.126	0.242	0.218	0.325	0.262	0.056	22
0.332	0.450	0.589	0.524	0.521	0.069	13
1.004	1.231	1.170	1.260	1.220	0.046	4
3.315	3.842	3.873	3.965	3.893	0.064	2

10.009	12.156	12.139	12.344	12.213	0.114	1
Series 3	1	2	3			
0.010	0.072	**6.154**	0.003	0.038	0.049	130
0.034	†	0.121	0.156	0.138	0.025	18
0.102	0.212	0.166	0.158	0.179	0.029	16
0.334	0.507	0.397	0.429	0.444	0.056	13
1.017	1.171	1.183	1.229	1.194	0.031	3
3.356	3.993	3.932	4.082	4.002	0.075	2
10.134	12.103	12.288	12.370	12.254	0.137	1

A number of measurement errors occur in Table 9.3. Five measurements have C_{CDOM} values of around 6 m^{-1}, most of them in the lower concentration samples. In each of these cases the absorbance measurement contained no signal. This might be due to the fact that the measurement was below the detection limit. The series 3, 0.034 mg l^{-1}, triplicate 1 measurement was not stored at all, probably due to human error.

Most of the PSICAM calibration methods require reference absorptions (see §9.3.2). PSICAM calibrations are highly sensitive to the accuracy of the reference absorptions used (Leathers, Downes, and Davis 2000). Therefore, instead of using the individual measured absorption values (see Table 9.3) these measurements are used to calculate reference absorptions based on a concentration-absorption relationship. In this way the absorption values used for the PSICAM calibration are less influenced by individual measurements (and their variations).

Determining the concentration-absorption relationship

The concentration-absorbance relationship for the cuvette can now be calculated by performing a linear regression on the concentration and the C_{CDOM} values found. However, not all C_{CDOM} values might be suited to include in this regression. Measurements that are taken outside the detection limit or that are otherwise erroneous (e.g. outliers) should be excluded from the regression in order to obtain the best relationship. So the detection limit of the cuvette method was calculated first.

The detection limit is regarded as the concentration at which the relative standard deviation ($(stdev/average)*100$) exceeds 100%. The relative standard deviations of the triplicates for each of the nominal concentrations were calculated (neglecting the small differences in concentrations). The relative standard deviation for all of the cuvette measurements is given in Figure 9.5. An outlier (0.333 mg l^{-1}), the result of a single deviating measurement (series 1, triplicate 2, see Table 9.3) was removed. The detection limit, theoretically a logarithmic curve, can be determined by drawing a straight line trough the data points in Figure 9.5 as both axes have a logarithmic scale. The detection limit is reached just before the lowest concentration, 0.01 mg l^{-1} humic acid. Although the 0.01 mg l^{-1} humic acid absorption measurements are just below the detection limit, their influence on the regression will be insignificant. It was therefore decided to use all cuvette absorption measurements to determine the concentration-absorption relationship.

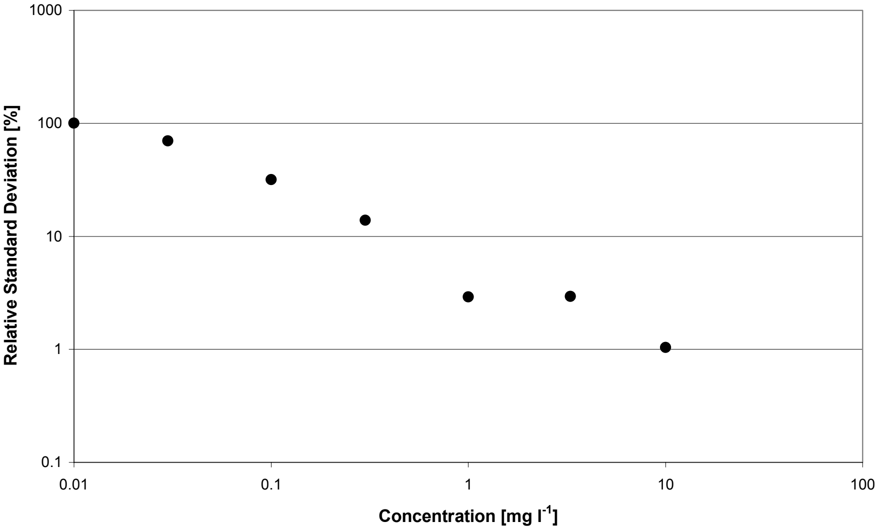

Figure 9.5: The relative standard error per concentration for the cuvette on a logarithmic scale, just reaching the detection limit (> 100%) at the lowest concentration.

In Figure 9.6 the concentration-absorption relationship for the cuvette absorption measurements is shown. In order to obtain the most valid relationship the regression was performed on the data of all three series combined. Only the outlier, series 1 triplicate 2 0.333 mg l^{-1} (see Table 9.3) was excluded from the regression.

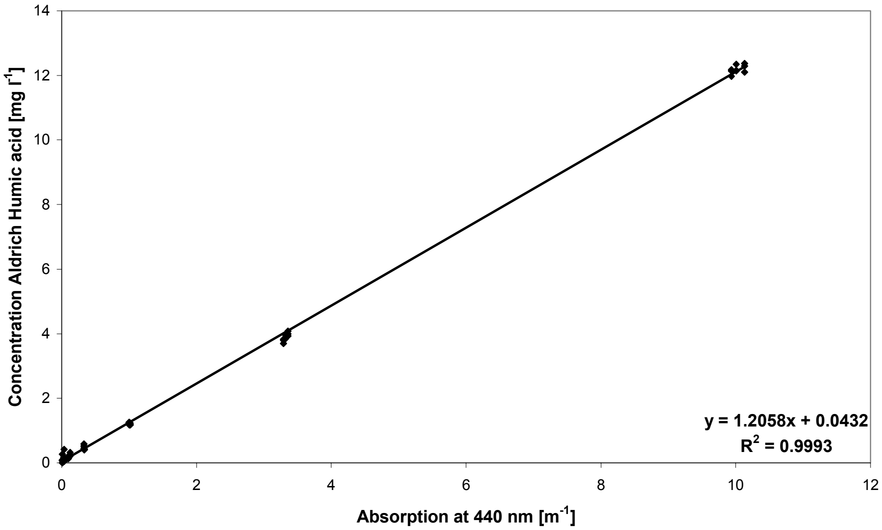

Figure 9.6: The concentration-absorption relation of Aldrich humic acid in the cuvette

An overview of the regression coefficients derived from the concentration-absorption relationship is given in Table 9.4.

Table 9.4: The cuvette linear regression coefficients and standard errors

	Slope	Standard error slope	Offset	Standard error offset
Dilution series 1-3	1.21	0.00	0.04	0.02

The standard error of the slope of the concentration-absorption relation is small (0.00), while the R^2 is very high (0.99), indicating a strong (and therefore accurate) relationship. The influence of systematic errors on the cuvette absorption measurements remaining after absorption modelling with an offset (see equation 9.24) is small based on the small value and standard error of the offset of the concentration-absorption relation. Using the slope of the concentration-absorption relation and equation, the relative spectral absorption coefficient κ can be calculated:

$$C = \frac{1}{\kappa \cdot \log(10) \cdot l^2} \cdot a + offset = \frac{1}{0.008 \cdot \log(10) \cdot 100} \cdot a + 0.04 \qquad 9.25$$

The κ of Aldrich humic acid is 0.008 l mol^{-1} cm^{-1}.

Now the reference absorptions that are required for the PSICAM calibrations can be calculated using the concentration-absorption relation given in Table 9.4 based on the dilution series. It was decided from previous experiments to use the 0.333 and 1.000 mg l^{-1} humic acid concentrations. Using the reference absorption the PSICAM calibrations were performed. In the following sections the four calibration methods are discussed:

- Measuring the relative transmittance T_{AB} of two solutions (A and B) with known absorption coefficients
- Measuring one known absorption of a solution and deriving the ρ from equation 9.18
- Measuring the reflective characteristics of the cavity materials directly
- Assuming a spectrally neutral cavity reflectivity

9.3.3 Results of the PSICAM calibration of all four methods

Calibration using relative transmittance

The original calibration of the PSICAM as proposed by Kirk involves the calculation of the ρ by using the relative transmittance of two solutions A and B with known absorption coefficients. The cavity reflectivity is then calculated as follows (Kirk 1997):

$$\rho = \frac{T_{AB}\exp(-a_B r) - \exp(-a_A r)}{T_{AB}\exp(-a_B r) P_s^{\,A} - \exp(-a_A r) P_s^{\,B}} \qquad 9.26$$

with T_{AB} as the relative transmittance [-]. See §9.2.2 for other PSICAM parameters and their symbols and for the equations. To obtain the best estimate for T_{AB} it was decided to use the transmittance measurements of the 0.333 and 1.000 mg l^{-1} humic acid solutions for this calibration, because the absorptions of these concentrations can be accurately measured in the cuvette (for obtaining the reference absorption coefficients) and in the PSICAM. According to Leathers *et al.* the difference in concentrations between the solutions A and B should be small in order to achieve the best estimate for ρ (Leathers, Downes, and Davis 2000).

For robustness, the transmittance per concentration was determined by averaging the transmittance measurement triplets for each of the dilution series. Thus, from the total of 63 transmittance measurements 21 averaged transmittance spectra were calculated, 7 for each of the dilutions series. To obtain the transmittance ratio using equation 9.26, the transmittance spectra of the 0.333 mg l^{-1} humic acid solutions were divided by the transmittance spectra of the 1.000 mg l^{-1} humic acid solutions.

By using equation 9.26 the cavity reflectivity ρ was then calculated for each of the dilution series. The three ρ curves are illustrated in Figure 9.7.

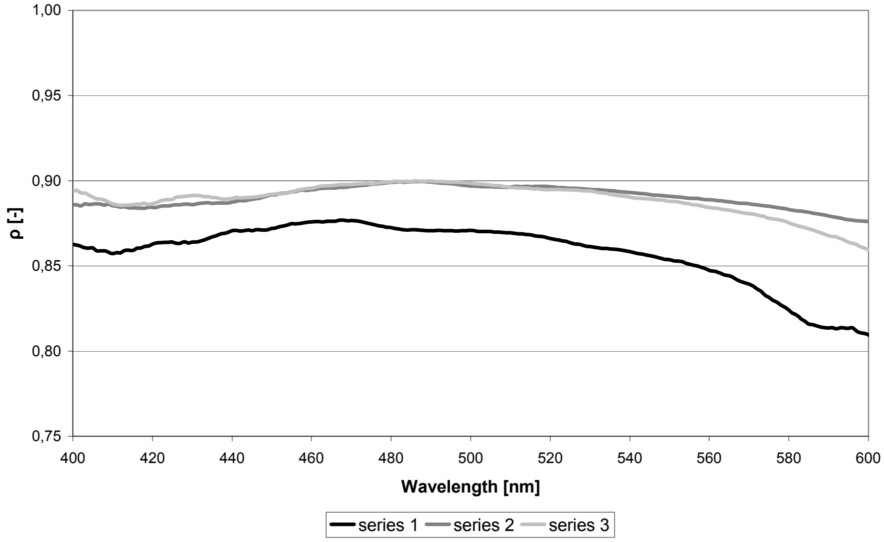

Figure 9.7: PSICAM cavity reflectivity from transmittance ratio (0.333 / 1.000 mg l^{-1} humic acid solution) for the three dilution series

The difference in the cavity reflectivities is due to the different transmittance ratios used. Figure 9.7 shows that the ρ curves of the second and third series are virtually the same and that the ρ of the first series is significantly lower. This can be traced back to the 1.000 mg l^{-1} transmittance measurement for the first series (see Table 9.3). Although the ρ of series 1 deviates in the order of just 1-5 % this is important because an error in ρ of 1% can lead to an error in absorption values of 10% according to Leathers *et al.* (Leathers, Downes, and Davis 2000). Therefore it is decided to discard series 1. The cavity reflectivities of series 2 and 3 are very similar and were averaged to enable comparison to the ρ curves of the other calibration methods.

Calibration using the inverted absorption equation

This calibration is also performed using the humic acid dilution series concentration-absorption relationship. In order to obtain the cavity reflectivity the PSICAM absorption equation 9.18 can be rewritten as follows (Kirk 1997):

$$\rho = 1 - \frac{4r(aT - a_w)}{3(1-T)} \qquad 9.27$$

In this way the ρ can be obtained using a single known absorption measurement from the cuvette and a single transmittance measurement in the PSICAM. Again only the 0.333 and 1.000 mg l^{-1} humic acid solutions were used. The reference absorption values were calculated using the regression coefficients given in Table 9.4. Similar to §0, the transmittance per concentration was determined by averaging the transmittance measurement triplets for each of the dilution series for robustness. In the end, six cavity reflectivity curves (0.333 and 1.000 mg l^{-1} humic acid for each of the 3 series) were calculated in total as can be seen in Figure 9.8.

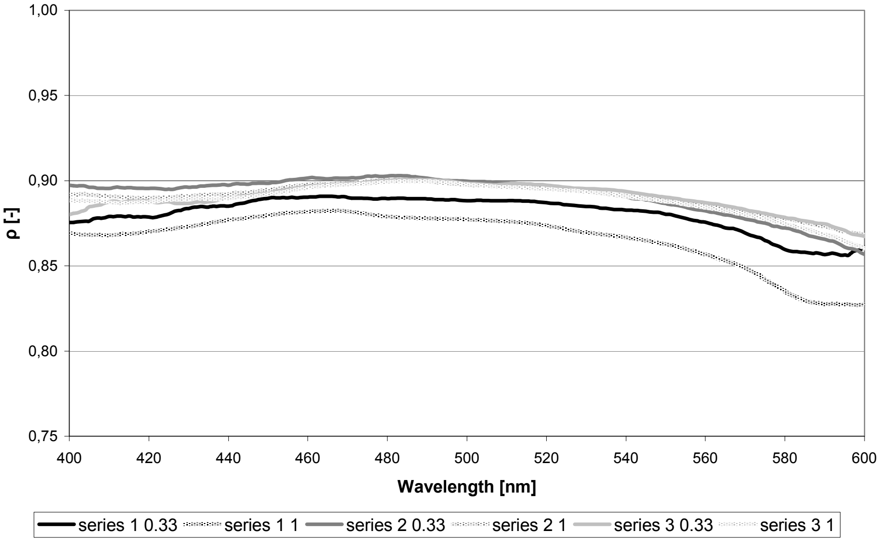

Figure 9.8: Cavity reflectivity from inverted equation for the three dilution series and the 0.3333 and 1.000 mg l^{-1} solution

Apart from the 0.333 mg l^{-1} solution from series 1 and the 1.000 mg l^{-1} solution from series 1, the ρ curve are within 1% deviation from each other. The 0.333 and 1.000 mg l^{-1} solutions from series 1 have a 2 and 3% lower ρ curve. Because the calibration of the PSICAM is very sensitive to ρ, it was decided to average the ρ curves from the second and third series only for comparison to the ρ curves with the other three calibration methods.

Calibration using material reflectivity

Another approach of obtaining the ρ is to determine the reflectivity of the cavity material directly, as described earlier by Dekker *et al.* (Dekker, Brando, Daniel, Anstee, and Clementson 2002).This was done by taking spectral measurements of the materials of which the cavity consists: Barium sulphate ($BaSO_4$, a ± 90% reflecting substance) and sand-blasted Schott Duran glass (laboratory glass surrounding the barium sulphate). By measuring pressed barium sulphate inside a (not sand-blasted) laboratory beaker of the same thickness of the cavity flask the combined reflectivity was obtained, comparable to the reflectivity of the PSICAM wall. As reflectivity is a relative measurement a highly reflective (~99%) Spectralon SRM-990 (Labsphere Inc., New Hampshire, USA) reference panel was used as the reference. Note that this method measures the reflectivity through air as opposed to the other PSICAM calibrations where the measurements are done through water, in order to avoid any water absorption or reflection influence on the cavity reflectivity.

In the CSIRO dark room (at Canberra, Australia) the only light reaching the fiber was reflected by the sample (or the reference panel). Additionally the position of the fiber and the stable light sources in the set up was chosen in such a way that light emitted by the lamp could not enter the fiber directly and that stray light was minimized.

The spectral reflectivity was calculated against the Spectralon panel using the following relation:

$$\frac{DN_{reference}}{\rho_{reference}} = \frac{DN_{BaSO_4}}{\rho_{BaSO_4}} \qquad 9.28$$

with DN the reflectance signal in digital numbers per wavelength (of the reference and the $BaSO_4$) and ρ the reflectivity (of the Spectralon panel and the $BaSO_4$). The reflectivity curve of the cavity material is shown in Figure 9.9. It must be realised that the PSICAM set-up consists of more than just glass and Barium sulphate powder: is also contains the light source positioned on a rod in the centre of the cavity and the cosine detector. The difference between the directly measured glass and Barium sulphate and the PSICAM could be attributed to these differences.

Calibration assuming a spectrally neutral reflectivity

The resulting cavity reflectivity curves of the previous three calibration methods are shown in Figure 9.9. The ρ curve derived directly from the material is about 1% higher than the two very similar ρ curves from the humic acid based calibrations in the wavelength region up to 500 nm. Based on 9 absorption measurements in a regular spectrometer and 9 transmittance values measured in the PSICAM for two concentrations the cavity reflectivity obtained by the transmittance ratio method and the inverted equation method is the same (about 89%). The spectrally neutral alternative was determined by taking the average of the three cavity reflectivity curves at 440 nm. This wavelength was chosen because it is the CDOM concentration, the property of interest for this study, is determined at 440 nm. The value of the neutral ρ is therefore set at 0.893.

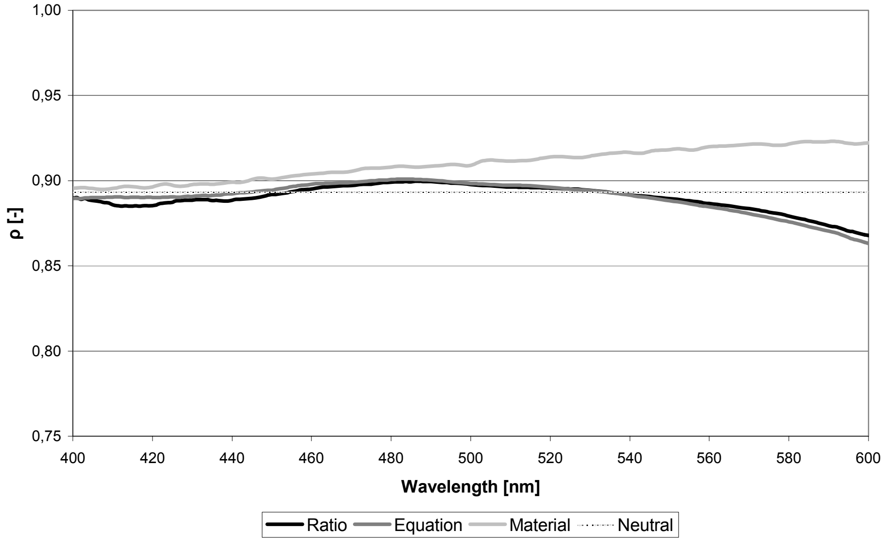

Figure 9.9: The ρ spectra as obtained by the three calibration methods: the transmittance ratio, the inverted equation and the material reflectivity

9.3.4 Selection of the best PSICAM calibration method

Cavity reflectivity

The cavity reflectivities of the different calibration methods as displayed in Figure 9.9 are just 1% apart at 440 nm, the wavelength of interest for CDOM. The material based ρ is slightly higher, which will result in slightly lower C_{CDOM} values. More variation can be seen in the shape of the different ρ curves. The transmittance ratio and inverted equation ρ curves decrease after 550 nm, while the material ρ curve increases from the beginning of the spectrum. The water absorption may have an influence on the transmittance ratio and inverted equation ρ curves, causing an overall decrease in reflectivity from 500 nm onwards. These differences in shape will be important for the agreement of the resulting absorption spectra and the theoretical exponential function of humic acid.

Detection limit and operating range

Before the PSICAM concentration-absorption relationships for each of the different cavity reflectivities could be calculated and compared, the detection limit of the PSICAM had to be established, analogous to the procedure for the cuvette based measurements (see §0.5.2293760). Figure 9.10 shows that the detection limit at 440 nm, the concentration where the relative standard deviation exceeds 100%, was not reached with the 0.010 mg l^{-1} solution and lies somewhere around 0.005 mg l^{-1}.

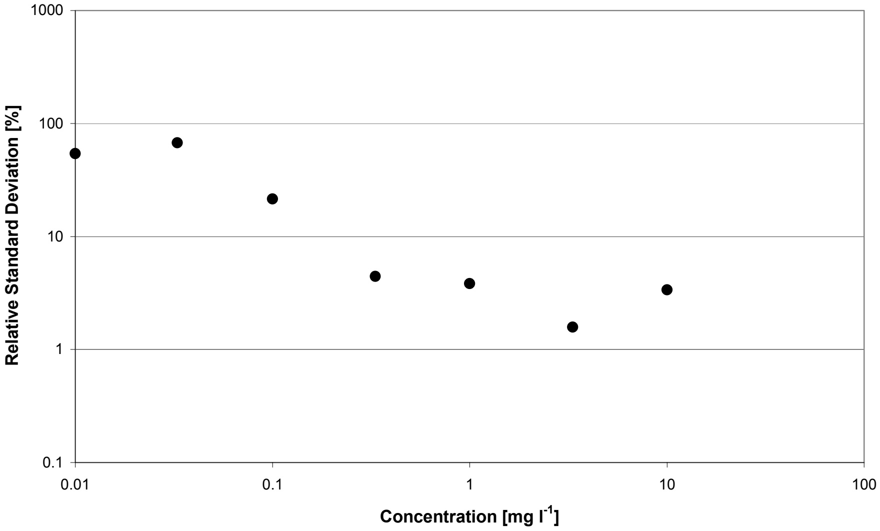

Figure 9.10: The log relative standard error per log concentration for the PSICAM, reaching the detection limit (> 100%) after the lowest concentration (at around 0.005 mg l^{-1} humic acid), which is superior to that for a 10 cm cuvette method (see Figure 9.5).

The detection limit of the PSICAM is thus significantly lower than that of the cuvette system (0.01 mg l^{-1}), as was expected based on the *SNR* calculated in §9.2.1. Another interesting feature is the increase of the relative standard deviation from the 3.333 mg l^{-1} humic acid solution onwards. This shows that the PSICAM also has an upper measurement limit. Dekker *et al.* (Dekker, Brando, Daniel, Anstee, and Clementson 2002) also reported an upper absorption measurement limit for their CSIRO PSICAM with reflective PTFE material and a radius of 0.0505 m of 1.5 m^{-1} (resulting in a 2% error in absorption). The upper absorption measurement limit of the PSICAM used for this research will be determined below. The operating range of the PSICAM in terms of the absorption was determined from Figure 9.11. With the absorption exceeding 3 m^{-1} the number of collisions with the wall drops to a level that the PSICAM principle no longer holds. The PSICAM then starts to function like a cuvette, with an average path length of 5 cm (the radius of the cavity). The PSICAM measurements of the 3.333 and 10.000 mg l^{-1} solutions were therefore not used for determining the calibration curve and the calibration method. This effect is also present and equally strong at other wavelengths (e.g. 500 nm, see Figure 9.11). In practical terms this means that samples with an (expected) absorption coefficient exceeding 3 m^{-1} need to be diluted prior to measurement in this type of PSICAM.

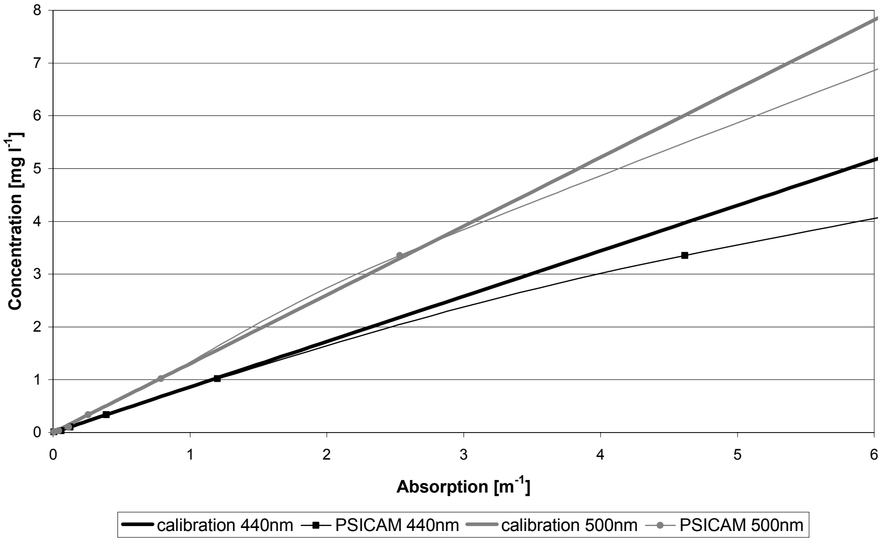

Figure 9.11: The PSICAM concentration-absorption relationships at 440 and 500 nm. The PSICAM operating range is reached at an absorption of around 3 m^{-1}, where the PSICAM absorption starts to deviate from the straight line.

PSICAM concentration-absorption relationships

With the different ρ curves found for the calibration methods, the PSICAM absorption spectra of the dilution series measurements could be calculated. The results of these absorption measurements were modelled to an exponential function according to equation 9.24. The wavelength range for the exponential modelling was 400-550 nm in order to avoid the pure water absorption effects that occur in the PSICAM beyond 600 nm.

The concentration-absorption relationships for the PSICAM were established by performing linear regressions on the modelled CDOM absorption values and the concentrations of humic acid used. From Figure 9.10 it was decided to exclude the 3.333 and 10.000 mg l^{-1} humic acid measurements from the regressions. The results of the linear regressions on the different PSICAM calibration method absorptions are given in Table 9.5. There is little difference between the calibration methods, although the neutral and material based cavity reflectivities have a slightly lower slope, resulting in higher absorption values at the same concentrations. The slope value for the transmittance ratio based ρ curve is most similar to the slope found for the cuvette (0.83). The lowest standard error in the slope is found for the transmittance ratio based ρ curve.

Table 9.5: The linear regression coefficients and accompanying standard errors of the PSICAM concentration-absorption relationships of the three dilution series for the different calibration methods.

		Slope	Standard error slope	Offset	Standard error offset
Transmittance Ratio	Series 1	0.86	0.005	-0.010	0.003
	Series 2	0.84	0.006	-0.025	0.004
	Series 3	0.84	0.006	-0.007	0.004
Inverted Equation	Series 1	0.91	0.007	-0.014	0.004
	Series 2	0.89	0.008	-0.022	0.005
	Series 3	0.91	0.006	-0.009	0.003
Material	Series 1	0.79	0.016	-0.002	0.011
	Series 2	0.75	0.007	-0.010	0.005
	Series 3	0.75	0.010	0.006	0.006
Spectrally neutral	Series 1	0.75	0.004	-0.001	0.003
	Series 2	0.74	0.007	-0.012	0.005
	Series 3	0.62	0.036	0.028	0.027

Exponential shape

The sums of squared differences between the measured and modelled PSICAM absorptions for the different calibration methods are given in Table 9.6. Here, the sums of squared differences of all triplicate measurements per dilution series were calculated and then averaged over the dilution series, resulting in a single value per calibration method. The offset was included in the modelled absorptions (see equation 9.24) so the difference is only caused by the shape of the spectra. The calibration method with the best agreement between the measured and modelled absorption (exponential function) is preferred. Based on Table 9.6 the best calibration method would be the inverted equation, followed by the transmittance ratio calibration. The material and especially the spectrally neutral ρ curves do not provide absorption spectra that resemble an exponential function.

Table 9.6: The sums of squared differences between the measured and modelled PSICAM absorptions (averaged over all dilutions series) for the different calibration methods

	Sum of squared differences
Transmittance Ratio	0.07
Inverted Equation	0.04
Material	0.11
Spectrally neutral	0.26

Best cavity reflectivity

From Table 9.5 and Table 9.6 it is clear that the best cavity reflectivity either is the result of the transmittance ratio or the inverted formula calibration method. The material and spectrally neutral ρ have less strong concentration-absorption relationships and their absorption spectra have less agreement with the theoretical exponential function. The performance differences between the transmittance ratio and the inverted formula calibration method are small. Based on the theoretical advantage of the transmittance ratio calibration method that it is least sensitive to error (Dekker, Brando, Daniel, Anstee, and Clementson 2002), it is decided to use the transmittance ratio ρ for calculating PSICAM absorption measurements.

Comparing PSICAM and cuvette absorption values

The differences between the absorptions from the cuvette and the PSICAM (using the transmittance ratio ρ) for humic acid dilutions in the range 0.1 – 1 mg l^{-1} are shown in Figure 9.12. When comparing the overall agreement in C_{CDOM} values for both devices the differences are insignificant (R^2 of 0.99). This research also demonstrates that using the concentration-absorption relationship for calculating the reference absorptions needed for the PSICAM calibration is the best method developed so far.

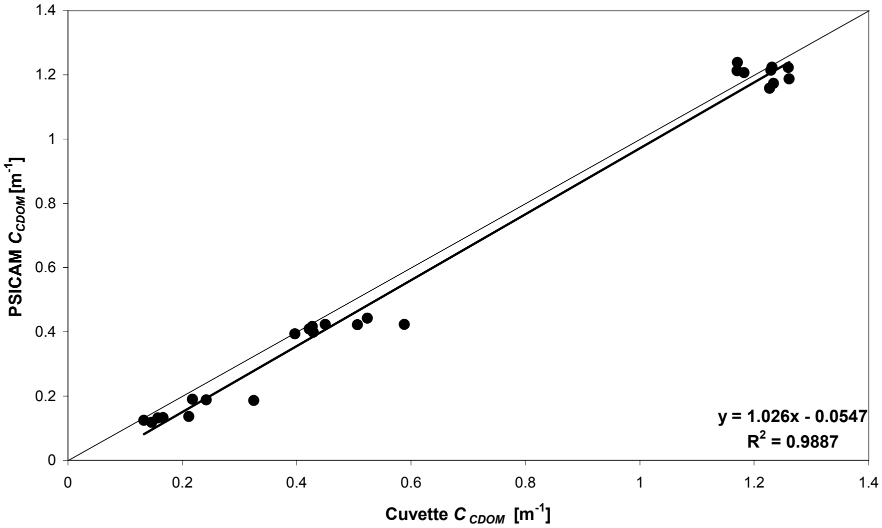

Figure 9.12: The relation between the C_{CDOM} of the cuvette and the PSICAM (using the ratio ρ).

9.3.5 Calibration discussion and conclusion

For the most accurate a_{CDOM} measurements it was necessary to calibrate the PSICAM system, especially with regards to its cavity reflectivity ρ. The calibration of the CSIRO PSICAM was performed in a number of ways. We used two criteria for selecting the preferred calibration method: the most valid relationship between the concentration and absorption and the best agreement between the absorption spectra and the theoretical exponential shape of humic acid. Dilution series of commercially available Aldrich humic acid were used to establish a concentration-absorption relationship for the reference absorption measurements in a cuvette. From these measurements the detection limit of the cuvette could be calculated, which was just over 0.010 mg l^{-1}. Using this concentration-absorption relation, reference absorption values required for the PSICAM calibrations were calculated.

Next the PSICAM calibrations were performed, resulting in 4 cavity reflectivity ρ curves. With these ρ curves, the absorption spectra of the dilution series measured in the PSICAM could be calculated. The detection limit and range of the PSICAM was also established (for the transmittance ratio ρ) at around 0.005 mg l^{-1}, making the PSICAM 2 times as accurate than the cuvette at lower concentrations. The relative standard deviation of the PSICAM is also lower (<10 % in the range 0.1 – 1 m^{-1}) than the RSD of the cuvette (>10% in the range 0.1 – 1 m^{-1}), suggesting that PSICAM measurements are more repeatable. There is also an upper limit for the PSICAM: at higher concentrations the relationship with the measured absorption in the PSICAM is no longer linear. This happens at absorptions exceeding about 3 m^{-1}. The detection limit results were used to determine which measurements were included for the PSICAM concentration-absorption relationships.

The measured absorption values in the PSICAM were used to establish PSICAM concentration-absorption relationships for each of the calibration methods. The linear regression coefficients of these concentration-absorption relationships were compared in order to identify the best PSICAM calibration method. Regarding the concentration-absorption relationships and the exponential shapes of the absorption spectra calculated there is little difference between the four cavity reflectivities applied (see Table 9.5 & Table 9.6), except for the spectrally neutral ρ that has a poor exponential fit. The material based ρ results in slightly lower absorption values. The choice would therefore be between the transmittance ratio ρ and the inverted equation ρ, which have a similar calibration curve and exponential fit error. Based on the theoretical advantage of the transmittance ratio calibration method that it is least sensitive to error (Dekker, Brando, Daniel, Anstee, and Clementson 2002), it is decided to use the transmittance ratio ρ for calculating PSICAM absorption measurements.

The cavity reflectivity found in this calibration experiment is on average 0.88 (between 400 and 600 nm) and thus about 10% lower than the ρ values reported by Dekker *et al.* and Röttgers *et al.* (both about 0.97).

This difference may be due to a number of differences between their calibration and and the one carried out in this research:

- The cavities of the Dekker *et al.* and Röttgers *et al.* PSICAMs are made of PTFE material instead of $BaSO_4$. This will be the main reason for the lower ρ values
- The PSICAM used for this research is 1-3 years older than those used by Dekker *et al.* and Röttgers *et al.*. It may be possible that the flask and / or $BaSO_4$. filling properties have deteriorated.
- Dekker *et al.* and Röttgers *et al.* used Nigrosine dye for their calibrations, which has a more spectrally neutral absorption spectrum than the Aldrich humic acid standard used for this calibration
- The absorption coefficients of the Nigrosine solutions used by Dekker *et al.* and Röttgers *et al.* are much higher than the absorption coefficients of the Aldrich humic acid

9.4 Case study: PSICAM and cuvette measurements

9.4.1 Introduction

The absorption measurement in a cuvette system is based on the additional attenuation of light that passes through a cuvette filled with filtered sample relative to the light attenuation of light travelling through a cuvette filled with a reference (mostly distilled water). The extra attenuation measured in the sample is then regarded as the absorption of the sample (see CDOM measurement protocols in Appendix III). A portion of this attenuation however is caused by the scattering of light out of the light path by (dissolved) particles in the sample, which is wrongly attributed to the absorption in this method. Such light loss due to scattering effects, as mentioned in the first paragraph of this chapter, will cause overestimation of the amount of CDOM absorption measured in a cuvette, as shown in equation 9.29:

$$a_{cuvette}' = a_{cuvette} + b_{residual} \quad 9.29$$

with $a_{cuvette}'$ the apparent absorption measured in the cuvette, $a_{cuvette}$ the true absorption of the sample in the cuvette and $b_{residual}$ the residual scattering of particles in the cuvette. The main theoretical advantage of a PSICAM over a bench spectrometer is that the PSICAM absorption measurements are not influenced by scattering light loss effects, so the absorption measured by the PSICAM is assumed to be the true absorption. A case study was performed in order to test this advantage of the PSICAM and to establish the best method for CDOM absorption measurements in eutrophic Dutch inland waters.

On filters

In water remote sensing the dissolved fraction of a water sample is defined as the filtrate after filtration over a certain filter. Filters can vary in pore size and material. Two main types of filters are used: Glass-fiber and cellulose-acetate filters. Glass-fiber filters are relatively cheap, but are only available with relatively large pore sizes. It is also important to know that the given pore size of a glass-fiber filter is the nominal pore size. It is inherent to the material used that the pore sizes of a glass-fiber filter are not uniform; the distance between strings of glass-fiber can vary between very small to the nominal given size. For instance, the Whatman GF/F filters used for this research have a nominal pore size of 0.7 µm, while the effective pore size is closer to about 0.45 µm (www.whatman.com). Glass-fiber filters with smaller pore sizes than 0.7 µm are not available.

Please note that in a number of publications this effective pore size of glass-fiber filters (0.45 µm) is erroneously given as 'the pore size' (e.g. in Krijgsman 1994; Rijkeboer, Dekker, and Hoogenboom 1998). Although it has been shown by Chavez *et al.* that tiny organisms such as prochlorophyte algae (with a diameter slightly above 0.5 µm) are quantitatively retained on GF/F filters (Chavez 1995), another research by Ferrari and Tassan (Ferrari, Dowell, Grossi, and Targa 1996) shows that there can be considerable amounts of detritus and picoplankton present in the filtrate after filtration over GF/F filters. The use of (only) GF/F filters should therefore be considered depending on the nature of the water system of interest and the types of water quality retrieval algorithms used.

Another type of filters is composed of cellulose-acetate. Contrary to the glass-fiber filters, the pore size of these kinds of filters is exact and uniform. It is possible to manufacture cellulose-acetate filters with pore sizes from 5 to 0.2 µm (www.schleicher-schuell.com). Filters with very small pore sizes are also referred to as 'membranes'. The disadvantage of using very small pore size filters is the filtration time, if filtration is possible at all. Untreated water samples will immediately clog such a cellulose-acetate filter, and a continuation of the filtration will only result in ruptured filters. Samples with particulate matter need to be pre-filtered first (e.g. using a glass-fiber filter).

Until recently in water remote sensing the particulate and dissolved matter was separated by filtration over a 0.7 µm glass-fiber filter (Doerffer 2002a). The disadvantage of this methodology is the presence of relatively large particles in the filtrate, which behaviour is more similar to the particulate matter (such as clay and picoplankton). Current satellite sensor related (CDOM) protocols for oceans or for inland waters therefore prescribe the filtration over a 0.2 µm filter (Tilstone, Moore, Sørensen, Doerffer, Pasterkamp, and Jørgensen 2002; Mueller and Austin 2000). This practice however introduces a size gap in the water constituents analysed (particles between 0.7 µm and 0.2 µm in size), which invariably inhibits optical closure and leads to sub optimal retrieval results.

An experiment was conducted to compare absorption measurements made in a cuvette and in a PSICAM. Both types of measurements were performed on samples that were filtrated over two filter types. The first filtration was over a 0.7 µm pore size filter Whatman GF/F, applied for most historic CDOM absorption measurements. The second filtration step was made over a 0.2 µm pore size filter (Schleicher & Schuell OE66). Please note that the 0.7 µm pore size is a nominal pore size while the 0.2 µm pore size is a true pore size (see 9.2.2).

Smaller particles, smaller than 2 µm, have a lower scattering efficiency in water and their scattering is mostly in the forward direction (Kirk 1983). In most bio-optical modelling literature the dissolved matter therefore is assumed to have a negligible contribution to the scattering of a water sample in relation to the absorption (Aas 2003). The threshold value for dissolved matter is set at 0.45 µm in literature (Steinberg 2003), although in operational water remote sensing studies the dissolved matter is defined as the filtrate after filtration over an GF/F glassfiber filter (with a nominal pore size of 0.7 µm). With these definitions in mind it is clear that after the 0.7 µm filtration there may be suspended and thus scattering particles in the samples. The measurement protocols for TCHL and TSM however call for a filtration over a 0.7 µm filter (a filtration over smaller pore size filters is not feasible for particulate matter). To avoid a gap in the SIOP determination, the dissolved matter is therefore defined as the filtrate after the 0.7 µm filtration. After filtration over 0.2 µm filters the filtrate only contains dissolved matter with negligible scattering in the visible light wavelength region.

Note that removed particles account for a part of the total absorption. The difference between absorption measurements at 0.7 and 0.2 µm (both in the PSICAM and in the cuvette) is (partly) due to the absorption of the fraction between 0.7 and 0.2 µm.

The results of the case study are used to determine the best method for measuring CDOM absorption coefficients from *in situ* collected water samples.

9.4.2 Data collection

A total of 19 water samples were collected on three occasions during the summer of 2002 in the lakes Loenderveen and Terra Nova (located in the study area, see §1.2 for a description of the lakes). The dates of the field days were May 6th, July 29th and September 12th. The water samples were taken just below the water surface using 1 l Polyethylene bottles. They were temporally stored in a cooler containing cooling elements until arriving in the laboratory, where the samples were immediately processed or transferred to a refrigerator.

The structure of this experiment is given in Figure 9.13. The water samples were first filtered over Whatman GF/F (45 mm ∅, 0.7 µm pore size) glass fiber filters. A fresh filter was used for each sample. The filtrate was kept at room temperature. The absorption of the filtrate was first measured in the cuvette. Prior to measurement in the PSICAM the filtrate was diluted two times with distilled water, because the absorption coefficients of the samples were too high to be accurately measured by the PSICAM directly (see §9.3). The dilutions were carried out based on weight, using a laboratory balance. For the next step the filtrate was filtered again, this time over Schleicher & Schuell OE66 (47 mm ∅, 0.2 µm pore size) cellulose-acetate membrane filters. Again, the absorption of the filtrate was both measured in a cuvette and, once diluted, in the PSICAM. The exact protocols for cuvette and PSICAM measurements performed in this research are given in Appendix III. Absorption coefficients given in the results paragraph are fitted absorption coefficients at 440 nm (C_{CDOM}). The absorption of the yellowish residue on some of the 0.2 µm filters was indicative of the presence of an optically active group of particles in this size range. However, their mass could not be determined as the cellulose-acetate filters were not pre-weighted (and the available mass-balances were not accurately enough to detect the residue) and their absorption spectrum could not be measured because the filterpad method (Trüper and Yentsch 1967) is designed for glass fiber filters (the effect of using cellulose acetate filters with a residue containing much smaller particles is unknown).

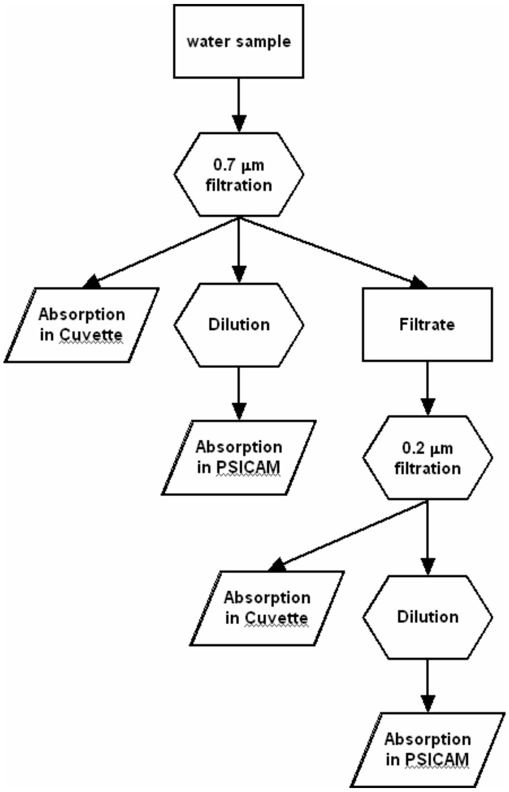

Figure 9.13: Schematic overview of the experiment showing the different steps of the case study aimed to determine residual scattering effects at CDOM absorption measurements using a cuvette

9.4.3 Results

The results of the absorption measurements by the cuvette and the PSICAM for the two filtration steps are given in Table 9.7.

Table 9.7: The absorption coefficients at 440 nm (C_{CDOM} [m^{-1}]) for the cuvette and the PSICAM after 0.7 µm and 0.2 µm filtration. The normalised differences are calculated by subtracting the PSICAM C_{CDOM} from the cuvette C_{CDOM} and dividing by the PSICAM C_{CDOM}.

Date	Station	C_{CDOM} Cuvette 0.7 µm	C_{CDOM} PSICAM 0.7 µm	Normalised difference 0.7 µm	C_{CDOM} Cuvette 0.2 µm	C_{CDOM} PSICAM 0.2 µm	Normalised difference 0.2 µm
6-May	LEL-1-C	2.55	2.36	0.08	1.98	2.19	-0.10
	LEL-2-C	2.58	2.27	0.14	2.22	2.14	0.04
	TNT-3-S	4.27	3.56	0.20	2.88	2.98	-0.03
	TNH-1-C	3.37	3.08	0.09	2.73	2.77	-0.01
	TNH-6-S	4.51	4.58	-0.02	3.92	4.00	-0.02
29-Jul	LEL-1-C	2.38	2.39	0.00	2.29	2.33	-0.02
	LEL-2-C	2.38	2.35	0.01	2.20	2.26	-0.03
	LEL-3-C	2.34	2.33	0.00	2.28	2.34	-0.03
	TNT-2-C	3.18	3.14	0.01	2.83	3.00	-0.06
	TNH-1-C	4.19	3.83	0.09	3.83	3.67	0.04
	TNH-2-C	3.86	3.78	0.02	3.45	3.69	-0.07
12-Sep	LEL-1-C	2.26	2.37	-0.05	2.33	2.08	0.12
	LEL-2-C	2.19	1.11	0.97	2.19	1.05	1.09
	LEL-3-C	2.32	1.09	1.13	2.34	1.12	1.09
	TNT-1-C	2.87	1.31	1.19	2.48	1.28	0.94
	TNT-2-C	2.71	1.28	1.12	2.46	1.31	0.88
	TNH-1-C	3.36	3.31	0.02	2.68	3.06	-0.12
	TNH-2-C	4.20	4.33	-0.03	3.21	4.11	-0.22

A number of relationships between the measurements given in Table 9.7 were investigated in order to establish the difference between the cuvette and the PSICAM at two different filtration steps:

- The cuvette 0.7 and 0.2 µm filtered water absorption measurements
- The PSICAM 0.7 and 0.2 µm filtered water absorption measurements
- The PSICAM and cuvette water sample absorption measurements after the 0.7 µm filtration
- The PSICAM and cuvette water sample absorption measurements after the 0.2 µm filtration

First paired t-tests were performed to determine significant differences between the measured values (2-sided, α = 0.05) (Blalock 1985). Secondly the strength of the relationships was given by the coefficient of determination of the regression, R^2.

The cuvette 0.7 and 0.2 µm absorption measurements

From a paired t-test (with α =0.05) it followed that there is a significant difference between the cuvette 0.7 and 0.2 µm filtered water sample absorption measurements. This can be explained a certain amount of absorbing and scattering particles being removed with the 0.2 µm filtration. By assuming that the size distribution of particles at the sample locations is the same a linear relationship is expected between the C_{CDOM} of the samples after 0.7 and 0.2 µm filtration. The offset of the linear function is forced to zero because the same set-up is used so if an absorption of zero was measured in a sample after the 0.7 µm filtration also an absorption of 0 for the same solution should be found after the 0.2 µm filtration step. The linear relationship for the 0.7 and 0.2 µm cuvette measurements is reasonably strong with a R^2 of 0.75, as shown in Figure 9.14. The average absorption loss due to the removal of matter within the size range 0.7 and 0.2 µm is given by C_{CDOM} 0.2 µm = 0.87 * C_{CDOM} 0.7 µm for the cuvette system, a difference of 13%.

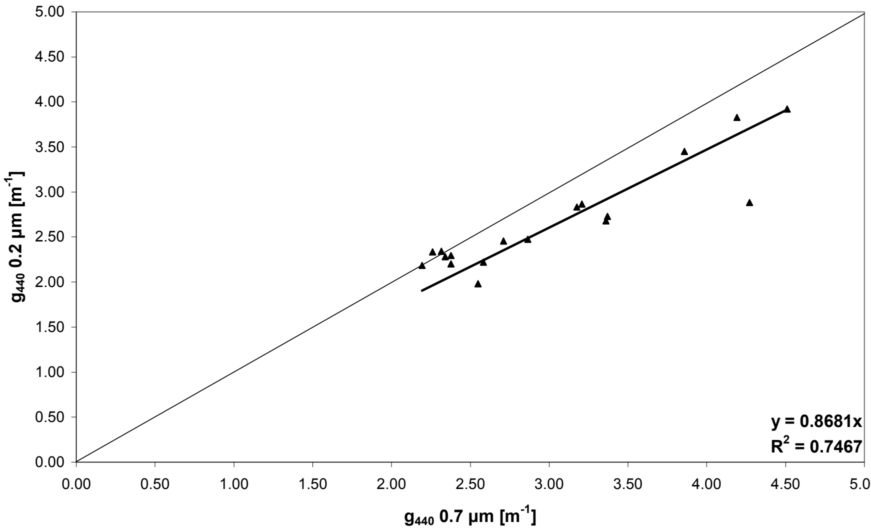

Figure 9.14: The linear relation between cuvette absorption measurements at 440 nm after 0.7 and 0.2 µm filtration.

The PSICAM 0.7 and 0.2 µm absorption measurements

There is a significant difference between the PSICAM 0.7 and 0.2 µm absorption measurements according to the t-test results. This can be explained by the removal of absorbing particles in the size range between 0.7 and 0.2 µm with the 0.2 µm filtration. The PSICAM measurements at 0.7 and 0.2 µm have a strong linear correlation with a R^2 of 0.93 as can be seen in Figure 9.15. The absorption loss due to the removal of matter is given by C_{CDOM} 0.2 µm = 0.94 * C_{CDOM} 0.7 µm as measured in a PSICAM. When combining this relationship with the relationship derived in the previous section, the scattering contribution to the absorptions measured in a cuvette system can be quantified. The average absorption loss due to the removal of matter within the size range 0.7 and 0.2 µm for the cuvette system was 13%, and some 6% is the result of the actual removal of matter

(PSICAM result). The remaining 7% absorption extra absorption in the cuvette (after 0.7 μm filtration) is thus due to the scattering effects. The CDOM absorption measured according to the MERIS protocols is therefore some 7% too high on average.

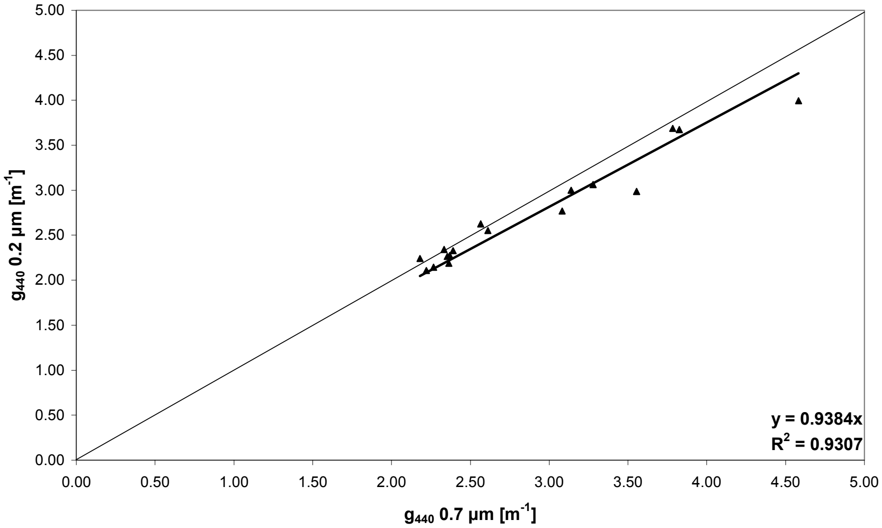

Figure 9.15: The linear relation between PSICAM absorption measurements at 440 nm after 0.7 and 0.2 μm filtration

The PSICAM and cuvette absorption measurements after the 0.7 μm filtration

There is a significant difference between the PSICAM and cuvette absorption measurements after the 0.7 μm filtration, established after the paired t-test. This can be explained with the assumption that scattering light loss effects occur in the cuvette but not in the PSICAM. A linear relationship is assumed between the cuvette and PSICAM absorption at 440 nm, with the offset forced to zero because if no absorption is measured in the cuvette, also no absorption can be measured in the PSICAM of the same sample with concentrations exceeding the detection limits. Figure 9.16 shows that the PSICAM and cuvette measurements at 0.7 μm have a strong linear correlation of c_{CDOM} cuvette = 0.95 * c_{CDOM} PSICAM with a R^2 of 0.93. This difference in absorption of about 5% is very similar to the 7% absorption overestimation that is caused by scattering in the cuvette system as derived in the previous section.

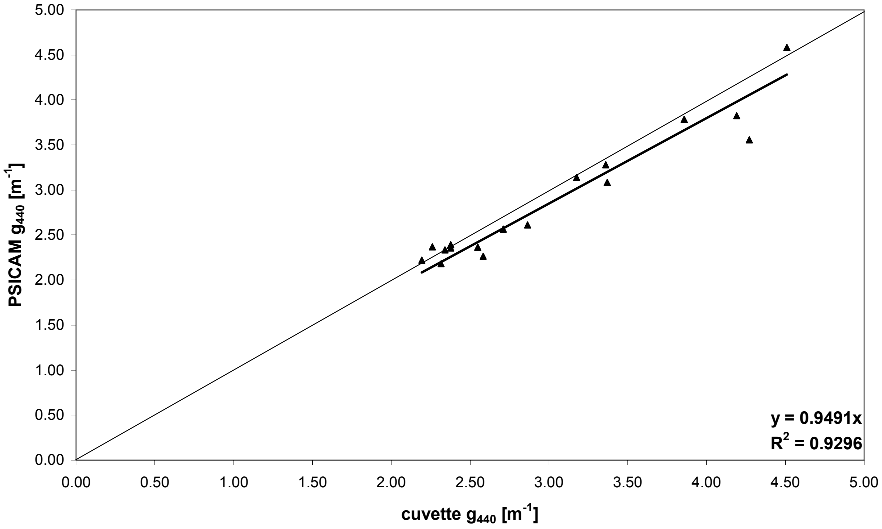

Figure 9.16: The relation between the PSICAM and the cuvette absorption measurements after the 0.7 µm filtration

The PSICAM and cuvette absorption measurements after the 0.2 µm filtration

There is no significant difference between the cuvette and the PSICAM 0.2 µm absorption measurements according to the results of the t-test. This could be explained by the fact that there is negligible scattering light loss in de cuvette after 0.2 µm filtration, so the cuvette and the PSICAM both give the true absorption value. The PSICAM and cuvette measurements at 0.2 µm have a strong linear relationship of c_{CDOM} cuvette = 1.02 * c_{CDOM} PSICAM with a R^2 of 0.95 as can be seen in Figure 9.17.

This last result completes the calculations. The 2% difference in absorption measured after 0.2 µm filtration between the PSICAM and the cuvette system is probably caused by differences in the instruments and methods themselves. In the previous section it was shown that the difference between cuvette and PSICAM CDOM measurements after 0.7µm filtration was 5%. Combining the 2% difference in instruments with this 5% absorption difference gives the 7% extra absorption in the cuvette as a result of scattering effects derived earlier.

The use of 0.7 filters in combination with a cuvette system is therefore unwanted for CDOM absorption measurements.

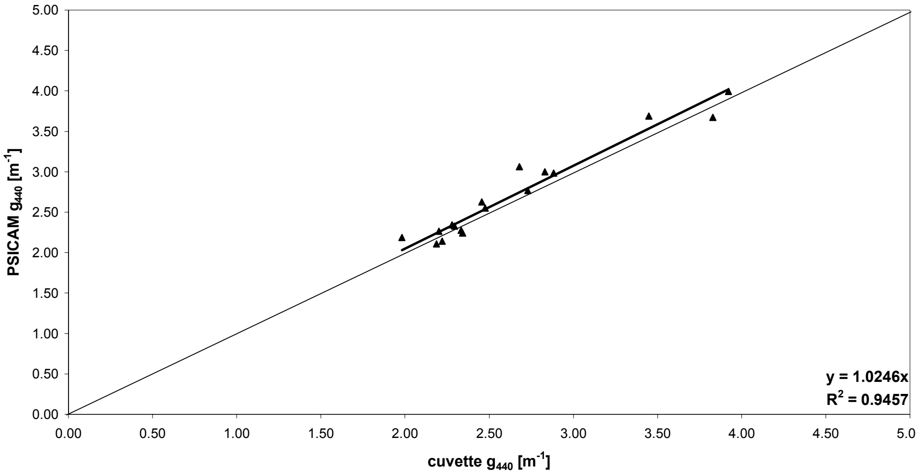

Figure 9.17: The relation between the PSICAM and the cuvette absorption measurements after the 0.2 µm filtration

9.4.4 Case study discussion and conclusions

In this case study CDOM absorption coefficients were measured in a cuvette spectrometer and a PSICAM device and subsequently compared in order to investigate the occurrence of residual scattering effects in a cuvette spectrometer set up. It was assumed in this case study that there are no residual scattering effects in a PSICAM (by design) and that the particles causing such scattering are present in the CDOM filtrate after passing a 0.7 µm GF/F glassfiber filter but are removed after filtration over an 0.2 µm cellulose-acetate filter. The absorption spectra measured in this case study were also fitted to an exponential model including an offset correction prior to comparing the resulting absorption coefficients according to standard practice in CDOM absorption measurements (see the next chapter and the protocols in Appendix III).

The offsets used to correct the absorption spectra were on average some 25% larger for the cuvette measurements (after 0.7 µm filtration), indicating that 75% of the offset corrects for instrumental and methodological errors.

There is no significant difference between the cuvette and PSICAM natural lake water samples absorption measurements after the 0.2 µm filtration. There are significant differences between the cuvette and PSICAM absorption measurements after the 0.7 µm filtration and between the 0.7 and 0.2 µm filtrations for both the cuvette and the PSICAM.

After the second filtration step an amount of particles between 0.7 and 0.2 µm is removed from the solution, which logically should result in lower absorption values. This reduction in absorption should be (relatively) the same for both the cuvette and the PSICAM, because the same fraction is removed. The difference between the PSICAM 0.7 and 0.2 µm filtrations, expressed as C_{CDOM} 0.2 µm = 0.94 * C_{CDOM} 0.7 µm, is however smaller than the difference between the cuvette 0.7 and 0.2 µm filtrations: C_{CDOM} 0.2 µm = 0.87 * C_{CDOM} 0.7 µm. In other words, by removing the same fraction in the samples, the absorption values measured in a cuvette decrease more than those of the PSICAM. There is no relation between the absorption difference between the two filtrations and the amount of absorption present in the sample, ruling out calibration problems for the cuvette. The only remaining explanation therefore is that after the 0.7 µm filtration the calculation of the absorption by measurement in the cuvette is affected by scattering, and therefore erroneously high, whilst the absorption measurement performed in the PSICAM is scatter-free. The magnitude of the scattering induced difference is on average 7% (at 440 nm).

From the PSICAM measurements it is determined that the difference in absorption between the 0.7 and 0.2 μm filtrations is 6% (on average). This means that some 7% of the CDOM absorption of a water sample filtered over a Whatmann GF/F filter that is measured in a cuvette is actually due to scattering effects. About the same percentage (5%) is also found as the difference between the PSICAM and cuvette measurements after the 0.7 μm filtration. The remaining 2% is probably introduced by the difference in instruments and methods. The cuvette is thus not able to measure true absorption coefficients after filtration over 0.7 μm filters. For instance, instead of the average C_{CDOM} of 2.40 m^{-1} recorded by the PSICAM in this case study the cuvette would measure 2.57 m^{-1}.

The scattering effect in the cuvette is lost after a filtration over 0.2 μm filters. The 0.2 μm filtration step however can be very labour intensive. Furthermore, a CDOM filtration over 0.2 μm introduces a gap in the determination of the Inherent Optical Properties for optical modelling. The other IOP, the chlorophyll and total suspended matter, are namely determined by filtration over 0.7 μm in a number of studies (Tilstone, Moore, Sørensen, Doerffer, Pasterkamp, and Jørgensen 2002).

For eutrophic inland freshwaters such as found in the case study area, the fraction between 0.7 and 0.2 μm has a significant contribution to the total absorption of a sample. Thus by applying a 0.2 μm filtration step in order to measure the CDOM absorption in a cuvette without significant scattering effects, the same 0.2 μm filtration step also has to be applied for the determination of the IOP of the particulate fractions chlorophyll and suspended matter.

The PSICAM can measure true absorption after both 0.7 and 0.2 μm filtrations. Absorption measurements with a PSICAM are comparable in complexity, speed and costs to cuvette measurements. No extra 0.2 μm filtrations for the chlorophyll and suspended matter measurements would be necessary when using a PSICAM assuming that there are relatively few detritus and plankton particles smaller than 0.7 μm present in the sample.

When there are significant amounts of small particles such as picoplankton, which could very well be the case in the Vecht Wetlands study area, a two-stage filtration protocol might be necessary. This would involve a second set of filtration (over 0.2 μm), filter pad phytoplankton and tripton absorption measurements and CDOM (filtrate) absorption measurements. Such an extra filtration step however falls beyond the scope of this research.

Within this research the conclusion of this case study therefore is that true absorption coefficients of dissolved matter can most easily be obtained by filtration over 0.7 μm and subsequent measurement in a PSICAM.

9.5 CDOM retrieval improvement by using PSICAM instead of cuvette reference measurements

In chapter 8 it was found that the retrieved CDOM concentrations from inversion of the optical model were systematically underestimated when using the per-sample SIOPs. Possible explanations of this result were errors in the measured CDOM concentrations that were used as the reference concentrations or an error in the normalised CDOM absorption spectrum included in the SIOP set used by the optical model.

In this section it will be tested whether the use of CDOM reference concentrations measured in a PSICAM show better correlation with the retrieved CDOM concentrations, and thus improving the CDOM retrieval accuracy.

In this analysis a similar inversion was performed as discussed in section 8.5. Again the per-sample SIOP sets were used, together with the same fixed value of f (0.38). Also the performance of both the Matrix Inversion Methods (MIM) and the Levenberg-Marquardt algorithm was tested, based on reflectance measured with a hand-held spectrometer and resampled to the MERIS and CASI instrument band settings. This time however the retrieved concentrations were validated using reference CDOM absorption measurements collected using a PSICAM and a cuvette system.

Obviously, only sample stations where the CDOM concentration was measured both in the cuvette and in the PSICAM (in total 14 stations from the 2001 and GWA campaign – see Appendix II) are included in this analysis in order to allow meaningful comparison. The correlation coefficients and regression parameters are thus slightly different than the ones given in section 8.5. The CDOM retrieval correlation coefficients and the slope and offset parameters of the regression between retrieved and measured concentrations are given in Table 9.8.

Table 9.8: The differences between the PSICAM and the cuvette

N =14	CDOM	Cuvette	CDOM	PSICAM
	R^2	Slope + offset	R^2	Slope + offset
MERIS MIM	0.33	y= 0.74x + 0.71	0.44	y= 0.77 x + 0.74
MERIS LM	0.24	y= 0.69x + 1.07	0.37	y= 0.78 x + 0.98
CASI MIM	0.42	y= 0.73x + 0.55	0.58	y= 0.78x + 0.54
CASI LM	0.33	y= 0.74x + 0.77	0.52	y= 0.84x - 0.68

The CDOM retrieval correlation coefficients for the PSICAM is between 11 and 19% higher while the overestimation of CDOM is 3 - 10% higher when using PSICAM references (see Table 9.8). Because of the generally lower CDOM absorption reference measurements by the PSICAM, the underestimation of CDOM concentrations is reduced. The generally low R^2 values are probably due to the low number of sample stations in this case. Despite the low number of sample stations however, the underestimation of CDOM is systematically, just as with the inversion performed in section 8.5.2. The underestimation in that case was 30 – 40%, similar to that of the retrieved concentrations compared to the cuvette measurements in Table 9.8, while the underestimation of retrieved concentrations compared to the PSICAM references is improved to about 20%.

A notable feature in the regression parameters is that the CASI band settings have higher correlation coefficients than those of MERIS, regardless of the algorithm or the CDOM reference measurements used, probably due to the larger number of spectral bands for CASI. As for the algorithms, the matrix inversions score slightly higher correlations.

Figure 9.18 shows the dispersion of the retrieved C_{CDOM} values versus the C_{CDOM} values measured in the cuvette and the PSICAM per sample station for the LM method and the CASI band settings (results are similar for MIM inversions and MERIS band settings and thus omitted for brevity).

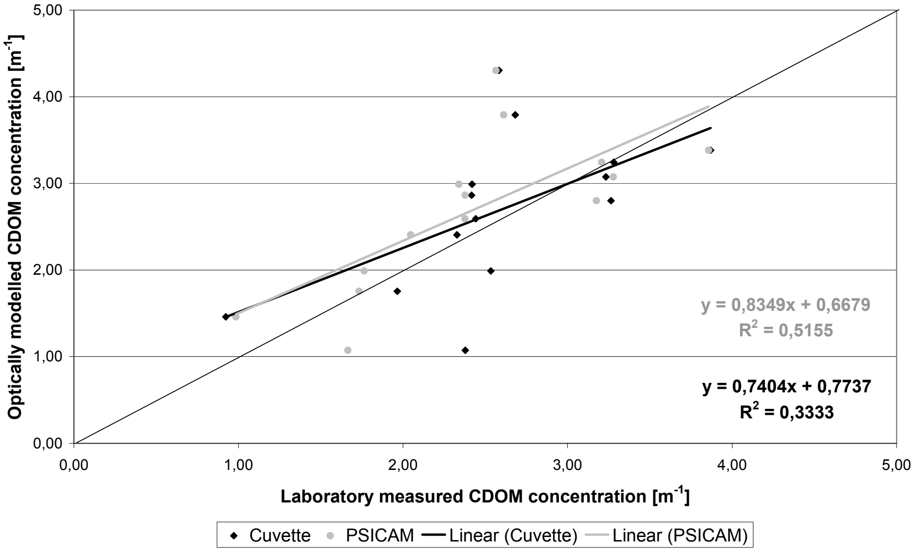

Figure 9.18: The retrieved C_{CDOM} values using the Levenberg-Marquardt inversion on the CASI band settings versus the C_{CDOM} values measured in the cuvette (in black) and the PSICAM (in grey)

9.6 PSICAM Discussion and conclusions

9.6.1 Applicability of the PSICAM

Although this research only involves CDOM absorptions, the PSICAM is also capable of performing another type of optical water property measurement: the total absorption. Currently in spectrophotometry the total absorption cannot be measured directly, as this would also include the scattering of the sample, but it is calculated by summing up the separately measured seston absorption measured using the filter pad technique and the CDOM absorption measured in a cuvette system. For the total absorption the wavelength region up to at least around 700 nm is important (chlorophyll absorption maximum at 676 nm). The present calibration however was performed using a humic acid standard with little absorption in the range beyond 550 nm. The cavity reflectivity found in the calibration section of this chapter decreases significantly in the region 500 - 600 nm, while the ρ was not determined beyond 600 nm. Before the PSICAM can be applied for total absorption measurements it will thus be necessary to recalibrate it and check the behaviour of ρ beyond 600 nm. Another issue is the reported water absorption residuals noticeable in the PSICAM absorption measurements beyond 600 nm, although these are thought to be due to temperature differences between the reference and sample measurements (Dekker, Brando, Daniel, Anstee, and Clementson 2002). Further research should thus be conducted to establish the applicability of the PSICAM for total absorption measurements. The operational range of the PSICAM with respect to absorption coefficients has been established during the calibration experiment. It was found that above an absorption coefficient of around 3 m^{-1} the PSICAM starts to overestimate absorption values progressively. It is therefore advised to dilute absorption samples that exceed the value of 3 m^{-1} (at 440 nm) prior to measurement in the PSICAM.

The results of the PSICAM calibration further showed that the PSICAM detection limit and standard deviation were lower than for the bench spectrometer. Next to this, the case study proved that after filtration of a water sample over a 0.7 µm filter a scattering effect could be observed in the bench spectrometer, but not in the PSICAM. This effect is negligible after filtration over a 0.2 µm filter, but then a fraction of the optically active water constituents is discarded because the measurement protocols used for this research for the TCHL and TSM call for use of residue material on 0.7 µm filters.

9.6.2 PSICAM recommendations

The performance of the PSICAM system is determined by three factors:

1. The signal to noise ratio (of the complete system: spectrometer, cavity and light source)
2. The characteristics of the spectrometer (wavelength range and scan speed)
3. The average path length of the photons/light that passes through the sample and interacts with the cavity wall.

The exact spectral characteristics the CSIRO stable light source with Krypton-halogen torch globe (see §9.2.1) were not determined in this research. In combination with the Ocean optics SD2000 spectrometer and the PSICAM however a sufficient average SNR was reached (of about 300:1). Halogen lamps have relatively low output in the blue part of the spectrum, increasing towards the red and infrared part of the spectrum. But no alternative to the halogen lamp is yet available. Other light sources, such as Deuterium lamps, Xenon lamps and Light-Emitting Diodes are either too weak or impossible to mount inside the PSICAM. An advantage of the Krypton-Halogen bulb is that it responds quickly after being turned on or off, avoiding warming of the sample and enabling relatively quick measurements.

The characteristics of the spectrometer are already mentioned in section 9.2.1. The Ocean Optics SD2000 has a spectral resolution of 3.5 nm, a range of 400 - 900 nm and a quick scan time (average of 10 readings that last 40 ms each, avoiding warming of the sample), making it a suitable device for PSICAM measurements. The Ocean Optics scans all wavelengths instantaneously, reducing the effect of temporal changes in the light source or the sample. A test series in the CSIRO dark room enclosure showed that the Ocean Optics is consistent within a 5-minute time interval. It is possible to fill the PSICAM with pure water, perform a reference and a dark signal measurement, empty and refill the cavity with sample and perform a sample measurement within 5 minutes.

The CSIRO PSICAM used for this research had a cavity reflectivity of around 0.89 and a cavity radius of 0.0505 m. Using equation 9.7 the average path length can be calculated, assuming an absorption of the sample of 1 m^{-1}. The average path length of the CSIRO PSICAM was around 0.40 m with an average of less than 6 collisions with the cavity wall (calculated using equation 9.8).

We limit discussion on the sensitivity of the CSIRO PSICAM to the influence of the cavity reflectivity and the cavity radius, the factors influencing the path length. Modelling work by Leathers *et al* (Leathers, Downes, and Davis 2000) showed that high cavity reflectivities are considered desirable for low sample concentrations since they reduce the transmittance (relative to pure water, see equation9.30) to a level that can be measured by the spectrometer with acceptable accuracy (under 90%). By adjusting the ρ, the difference between pure water and the sample is thus enhanced. A PSICAM with a ρ of around 0.99 is therefore the most suited for absorption measurements in clear oceanic (Case I) waters. For coastal and inland (Case II) waters it is the other way around: here the sample concentrations are high, resulting in lower transmittances. By using a low ρ (e.g. 0.90), the difference between pure water and the sample is reduced and the transmittances are thus increased to a level that can be measured with acceptable accuracy (over 10%).

The PSICAM cavity used for this research has a relatively low cavity reflectivity, mainly due to the fact that barium sulphate is the reflective medium in the cavity as PTFE powder was not available at the time of manufacturing. For this dissertation Dutch natural inland waters were studied, which high absorption coefficients (1 to 4 m^{-1}). As mentioned in the previous section however, transmittance measurements in a PSICAM with a high cavity reflectivity using pure water as the reference and strong absorbing samples result in very low values. The use of a $BaSO_4$ filled PSICAM therefore probably has turned out beneficial for this study.

Instead of altering the cavity material it is also possible to change the cavity radius of the PSICAM. Kirk (Kirk 1995) already proposed using different sizes of cavities dependent on the absorption range of the water type of interest. In the case of inland waters with strong absorbing samples a smaller cavity radius (<0.05 m) would also increase the transmittance to suitable levels. Because the size of the cavity is easier to adjust than the reflectivity of the wall, the use of different cavities for different absorption ranges is recommended.

In order to avoid errors introduced by any anisotropy of the light source inside the cavity it is recommended that after each re-insertion the light source and the fiber need to be aligned properly, by using a set of markers, although some quick test runs did not show significant differences between aligned and misaligned readings.

Finally it was found crucial to avoid air between the detector and the sample when filling the cavity because the measured absorption will decrease, and the reference and sample measurement are no longer related in this way. In some quick test runs the effect of air between the sample and the detector was significant.

9.6.3 Conclusions

CDOM absorption measurements made in a bench spectrometer with a cuvette are influenced by scattering effects depending on the pore size of the filters used to collect the dissolved matter. A new instrument, a Point-Source Integrating-Cavity Absorption Meter, is not affected by scattering. Scattered light is reflected by a highly reflective cavity wall until the light is either absorbed by the sample or it has reached the detector. Another advantage of the PSICAM is its ability to measure low absorption values as it has a very long effective path length. The calibration of a CSIRO built PSICAM was performed in this chapter. Using a dilution series the cavity reflectivity of the PSICAM was determined by the best of three different calculation methods. In this chapter also a case study was conducted, comparing PSICAM and cuvette CDOM measurements of natural water samples. In this case study the scattering effect in the cuvette was observed and quantified. No scattering effect was noticed in the PSICAM.

A successful PSICAM calibration was achieved through the use of three independent dilution series of Aldrich humic acid standard in the absorption range around 1 m^{-1}. The absorption spectra of the dilution series were measured in a bench spectrometer with a 10 cm cuvette, and because there were three independent series, the calculation of an accurate concentration-absorption relation was possible. With this concentration-absorption relation reference absorptions needed for the PSICAM calibration could be derived. The best cavity reflectivity of the PSICAM, which best approached the concentration-absorption relation, was obtained by applying the transmittance ratio calibration method. After calibration, absorption measurements of the dilution series made with the PSICAM and a bench spectrometer are within 1% of each other (over the absorption range 0.1 – 2 m^{-1})

The calibration experiment brought to light one limitation of the PSICAM: The accuracy of absorption measurements with the PSICAM rapidly declines when the absorption coefficient of the sample exceeds 3 m^{-1}, due to the size of the cavity and the cavity reflectivity. As Kirk (Kirk 1995) already suggested, different cavities dependent on the absorption range of the water type of interest can be used. Another possibility is the dilution of samples prior to measurement in the PSICAM.

The case study showed that absorption measurements in a cuvette are likely to be affected with scattering effects when a 0.7 µm filter is used, as CDOM absorption coefficients at 440 nm values between the PSICAM and cuvette differ significantly. After filtration over a 0.2 µm filter there is no significant difference in C_{CDOM} between both methods. The differences of PSICAM absorption values between the two filtration steps are also significant. Therefore, the fraction between 0.7 and 0.2 µm does significantly contribute to the absorption and scattering of a sample and should not be discarded.

Because there is evidence that there is still particulate matter (clay, picoplankton) present in the filtrate after filtration over 0.7 μm, a two-staged filtration is proposed. If possible, the filter pad phytoplankton and tripton absorption measurements and the CDOM absorption should be measured both after 0.7 μm and 0.2 μm filtration. Such extra measurements could however not be performed in this research. It was therefore decided to measure CDOM absorption after 0.7 μm filtration in a PSICAM device.

The final conclusion is that the theoretical advantages of a PSICAM over a bench spectrometer (absorption measurement not affected by scattering and capable of measuring lower concentrations due to a longer path length) is supported by actual measurements. This means that by using a PSICAM more accurate CDOM absorption spectra can be measured, improving the SIOP that are required for optical modelling.

Finally, when validating retrieved CDOM concentrations after inversions of the optical model with PSICAM reference absorption measurements rather than cuvette references, the structural underestimation of CDOM was reduced by 10 – 15%, while the correlations increased by 10 – 20 %. This is another clue indicating PSICAM CDOM absorptions are more accurate than cuvette CDOM absorptions.

10. Improving CDOM concentration retrieval by using two-component CDOM absorption spectrum modelling

10.1 Introduction

When performing state-of-art inversions of the optical model using measured data the CDOM concentration is underestimated (see chapter 8). Excluding errors in the measured spectra, probable causes are 1) errors in the normalised CDOM absorption spectrum (slope of the spectrum too steep or flat) and 2) errors in the CDOM reference concentrations. In the previous chapter it was already demonstrated that the reference CDOM measurements performed in a cuvette are indeed affected by scattering processes, resulting in apparent CDOM concentrations that are higher than the CDOM concentrations measured in the scattering independent environment of the Point-Source Integrating-Cavity Absorption Meter (PSICAM). This chapter focuses on the shape of the $\bar{a}_{CDOM}$ spectrum by investigating current and possibly improved modelling techniques.

The practice of fitting measured CDOM absorption spectra to an exponential function prior to the determination of the CDOM absorption coefficient is generally accepted. By performing CDOM absorption modelling the measurement noise is reduced and the CDOM absorption spectrum can be extrapolated to the wavelength range and resolution that is required for bio-optical modelling (usually 400-750 nm).

Current CDOM absorption modelling consists of a single exponential function as was already applied in the previous chapter. Various forms are proposed in literature (Bricaud, Morel, and Prieur 1981; Davies-Colley and Vant 1987; Stedmon, Markager, and Kaas 2000), even improving model fit by performing additional operations such as a baseline or offset correction. These models, however, are developed for oceanic or coastal waters with relatively low CDOM concentrations. CDOM absorption spectra of inland waters, typically with higher CDOM concentrations, sometimes show a combination of a steep slope below 450 nm and a gentle slope beyond 450 nm. For more complex CDOM absorption spectra therefore the use of absorption models based on two components has been proposed (Hansell and Carlson 2002).

Two-component absorption modelling was first performed by Carder *et al.* Based on direct measurements, they found that 2 components with different spectral characteristics were responsible for almost all of the absorption of CDOM (Carder, Steward, Harvey, and Ortner 1989). In order to improve the goodness of fit, they proposed to model the absorption spectrum of CDOM by a function that is the sum of *two* exponentials. The two main components of CDOM identified by Carder *et al.* associated with these two spectral components are humic and fulvic acids (HA and FA, see also chapter 2).

Carder *et al.* used a chemical separation of CDOM into humic and fulvic acids. The International Humic Substances Society (IHSS, www.ihss.gatech.edu) provides a protocol for such a separation, which is adapted from earlier work by Aiken *et al.* (Aiken, McKnight, Wershaw, and MacCarthy 1985). This chemical separation is based on the fact that humic acid precipitates by a pH less than 2, while fulvic acids remain soluble at the same level of acidity. It was not possible to perform such a chemical separation in this research.

The separate absorption spectra of HA and FA in this research were obtained by carrying out spectral decomposition on the measured CDOM absorption spectra. Spectral decomposition was performed by fitting the sum of two exponential functions to a measured CDOM absorption spectrum using both a linear and a non-linear approach. A linear solution can be found when fixed values, so-called end-members, are assumed for the HA and FA absorption slopes and only the absorption coefficients are fitted. By using a non-linear approach both the slope values and the absorption coefficients are fitted.

A study was conducted to validate the improvement of goodness of fit as a result of the application of a two-component absorption model on measured absorption spectra instead of the single exponential model. Several end-member combinations for the linear approach were tested, and the non-linear approach was tested.

The retrieval of HA and FA concentration data from CDOM absorption measurements also might provide valuable additional water quality information for water quality management. The ratio between humic and fulvic acids is related to the origin of CDOM material, as relatively high HA content indicates terrestrial origin and relatively high FA content is attributed to in situ production (see chapter 2) (Imai, Fukushima, Matsushige, and Kim 2001 and McKnight, Boyer, Westerhof, Doran, Kulbe, and Andersen 2001).

In §10.2 the principles of CDOM absorption modelling are explained. In §10.3 the proposed spectral decomposition is discussed, including both the linear method involving fixed end-members and the non-linear approach with dynamic end-members. In the case study (§10.4) 40 CDOM measured absorption spectra of samples taken in the Vecht wetlands study area are decomposed using a number of two-component CDOM absorption modelling. Based on the goodness of fit between the measured and modelled CDOM absorption spectrum, the best decomposition method is chosen. The resulting CDOM concentrations are compared to the CDOM concentrations found with a single component CDOM modelling technique, quantifying the improvement in CDOM absorption accuracy. The final paragraph contains conclusions, discussion and recommendations.

10.2 Theory of CDOM absorption modelling

Early studies of CDOM absorption showed a negative linear relationship between the absorption and wavelength when the absorption values are log-transformed (Jerlov 1968). The CDOM absorption spectrum could be determined by measuring the absorption at two wavelengths and subsequently fitting a straight line between the absorption measurements plotted at a logarithmic scale. When the slope of the exponential was fixed even a single absorption measurement would suffice. Widely used fixed values for the slope of the exponential function include the value of 0.014 found by Zepp and Schlotzhauer for freshwater aquatic humus (Zepp and Schlotzhauer 1981) or the value of 0.015 found by Morel and Prieur for seawater in the upwelling regions off Mauritania (Morel and Prieur 1976). The practice of fitting of the CDOM absorption spectrum was common before the 1970’s as most available spectrometers were equipped with a limited number of monochromatic light sources. Nowadays it is possible to measure CDOM absorption over a broad range of wavelengths with high spectral resolution, but the need for fitting an exponential function to the measured absorption spectrum remains, for a number of reasons:

1. The CDOM absorption spectrum still has to be extrapolated because data is needed that lies outside of the measured or measurable wavelength range, or data is needed at another spectral resolution. Extrapolation is performed in two directions: In the case for marine water samples with very low CDOM

concentrations the CDOM absorption is sometimes determined in the UV wavelength range using a standard bench spectrometer with standard cuvette cell sizes, and the CDOM absorption spectrum is extrapolated towards the visible and near-infrared wavelengths When the light source and detector of the spectrometer used for CDOM absorption measurements are limited to the visible wavelengths, an extrapolation in the UV wavelengths is performed as the signal to noise ratio in this region is usually low.

2. A large source of error in bench spectrometer CDOM absorption measurements is scattering. Scattering of small particles that are still present in the sample after filtration affects the absorption measurements using a cuvette set-up (Bricaud, Morel, and Prieur 1981). After all, the amount of scattered light that has not reached the detector is erroneously added to the amount of absorption of a sample. This effect, which is more extensively discussed in chapter 4 can also be reduced by extra filtration over filters with smaller pore sizes (thus reducing the amount of scattering particles) and by using a Point-Source Integrating-Cavity Absorption Meter (PSICAM, see chapter 4). Smaller systematic errors in the absorption measurement can also be caused by differences in refractive indices of the reference and the sample (Green and Blough 1994), or in temperature differences between the reference and sample measurements (Kishino 2002), leading to a slight shift of the absorption spectrum. This systematic error can be corrected for by performing a baseline correction or by fitting the measured CDOM absorption spectrum using an offset.
3. At low CDOM concentrations the noise in the measured absorption spectrum is more pronounced. In this case the accuracy of the absorption value at the reference wavelength (usually 440 nm for inland waters) is increased by fitting an exponential function.
4. Depending on the size of the filters used to obtain CDOM, it is possible that algal pigments are still present in the filtrate. In this case CDOM absorption spectra show an absorption peak around 676 nm. This chlorophyll relict can be removed by exponential CDOM absorption fitting. Because the CDOM absorption at the shorter wavelengths is about an order of magnitude higher than the absorption of the chlorophyll, the influence of this peak on the shape and height of the fitted absorption curve is insignificant. It may however cause erroneous TCHL concentration estimates from inverse modelling.
5. By reducing measurement noise and systematic errors in the modelling of the CDOM absorption spectrum the accuracy of optical modelling is enlarged. Errors in the normalised CDOM absorption (part of the Specific Inherent Optical Properties) will lead to errors in the forward simulated subsurface irradiance reflectance and to errors in the retrieved CDOM, TCHL and TSM concentrations with inverse optical modelling.

The theoretical exponential model for the absorption of CODM has recently been challenged by Gege (Gege 2000). Instead of an exponential function, three symmetrical peaks with Gaussian line shapes are fitted to the measured CDOM absorption spectrum. The centre wavelengths of these Gaussian peaks are 205, 233 and 251 nm. Gege reports that the Gaussian model has a better fit in the complete wavelength range 190 - 820 nm, but the exponential model explains the measured CDOM absorption better in the wavelength range 340 – 540 (Gege 2000). Because in this dissertation the focus is on the visible wavelengths (400 – 700 nm), and no absorption could be measured at wavelengths smaller than 400 nm due to restrictions of the spectrometer system used, it was decided to proceed with the exponential model.

In the next sections the different CDOM absorption exponential fit models will be discussed within the context of their suitability for producing CDOM absorption spectra that can serve as input for the Gordon-Walker optical model.

10.2.1 Single component CDOM absorption models

The absorption of CDOM decreases with increasing wavelength. In a first approximation the shape of the CDOM absorption spectrum can be described by an exponential function. The original exponential model, first derived for marine CDOM, is given below (after (Jerlov 1968)):

$$a_{CDOM}(\lambda) = C_{CDOM}\exp^{(-0.015\lambda)} \qquad 10.1$$

with $a_{CDOM}(\lambda)$ the CDOM absorption at wavelength λ and C_{CDOM} the concentration of CDOM. Equation 10.1 was later modified to its well-known form by Bricaud (Bricaud, Morel, and Prieur 1981):

$$a_{CDOM}(\lambda) = a_{CDOM}(\lambda_0)\exp^{(S(\lambda_0-\lambda))} \qquad 10.2$$

with S the slope of the exponential function and λ_0 the reference wavelength (440 nm in this study). The CDOM absorption value at 440 nm is regarded as the concentration of CDOM (see chapter 2), so in this research the $a_{CDOM}(\lambda_0)$ in equation 10.5 is referred to as C_{CDOM}, similar to the concentrations of Total Chlorophyll C_{TCHL} and Total Suspended Matter and C_{TSM}.

The reference wavelength of 440 nm was originally chosen because it corresponds approximately to the mid-point of the blue-green chlorophyll absorption maximum (Kirk 1983) (Mobley 1994). This chlorophyll-ɑ peak is often used for chlorophyll-ɑ determination of Case I waters, and by determining the CDOM absorption at the same wavelength it allows for easier comparison. Because the CDOM absorption has an exponentially declining shape without distinctive peaks, any wavelength can be used as a reference although it is preferable to use a wavelength in the blue-green region where the CDOM absorption is the highest. Other reference wavelengths found in literature are around 355 nm (Hansell and Carlson 2002) or around 380 nm (Bricaud, Morel, and Prieur 1981). These shorter reference wavelengths were chosen to enable CDOM absorption measurements at lower concentrations typically found in Case I waters or very clear lakes. Due to the exponential characteristics of the CDOM absorption spectrum the amount of CDOM absorption could be accurately measured at the shorter wavelengths, while at longer wavelengths the absorption fell below the detection limit of most systems. For this research, the 440 nm reference wavelength has been adopted because it has also been used in comparable inland water CDOM studies by (Dekker and Peters 1993; Krijgsman 1994; Rijkeboer, Dekker, and Hoogenboom 1998).

Equation 10.1 is widely used in literature to describe CDOM absorption (e.g. Zepp and Schlotzhauer 1981; Kirk 1983; Mobley 1994; Hayase and Tsubota 1985; Dekker 1993; Krijgsman 1994; Hansell and Carlson 2002 and Dekker, Brando, Anstee, Pinnel, Kutser, Hoogenboom, Peters, Pasterkamp, Vos, Olbert, and Malthus 2001). The fitting procedure was often simplified by calculating a linear least squares regression of the log-transformed absorption data instead of calculating a non-linear least squares fitting to an exponential function (Bricaud, Morel, and Prieur 1981; Green and Blough 1994). The linear least squares regression technique favours the relative weights of the low absorption values at the longer wavelengths, resulting in lower absorption slope values compared to the non-linear least squares fitting where the emphasis is on the higher absorption values in the shorter wavelength region. Non-linear least squares fitting generally produces better model fits. In this study all the exponential CDOM absorption fit calculations are performed using non-linear least squares fitting.

10.2.2 Correcting for baseline shifts: the offset

An underlying assumption for the original exponential CDOM absorption model given by equation 10.1 is that the CDOM absorption beyond 700 nm is negligible, largely based on oceanic CDOM studies. Actual CDOM absorption measurements, however, show a residual attenuation at the longer wavelengths, especially with inland water samples. This residual attenuation was assumed to be scattering of particles in the medium (Bricaud, Morel, and Prieur 1981). In order to correct for these scattering effects after filtrations over 0.2 µm filters, Bricaud *et al.* proposed to transform the apparent absorption measurements (a'_{CDOM}) of oceanic CDOM samples through the following relationship (Bricaud, Morel, and Prieur 1981):

$$a_{CDOM}(\lambda) = a'_{CDOM}(\lambda) - a'_{CDOM}(700)\left(\frac{\lambda}{700}\right) \qquad 10.3$$

A similar relationship was used by Davies-Colley and Vant for their research of CDOM absorption in freshwater lakes (Davies and Charlton 1987):

$$a_{CDOM}(\lambda) = a'_{CDOM}(\lambda) - a'_{CDOM}(740)\left(\frac{740}{\lambda}\right) \qquad 10.4$$

Please note that except for a different reference wavelength Davies-Colley and Vant also multiply the apparent absorption at the reference wavelength by inverse of the wavelength term used by Bricaud *et al.*. The scattering correction of Davies-Colley and Vant (equation 10.4) therefore has a better shape agreement with the measured absorption spectrum, as the slope parameter of the absorption spectrum corrected with equation 10.3 becomes steeper as a result of the correction.

Others advise a simpler baseline correction for scattering effects by subtracting the absorption value of CDOM at 750 nm from the whole CDOM spectrum (Green and Blough 1994), or even at 600 nm (Sasaki, Tanaka, Ishizaka, and Saitoh 2002). In the previous chapter on the PSICAM however it was shown that the CDOM attenuation at 750 nm is not caused by scattering and therefore the CDOM absorption is not negligible for the inland waters studied. In this research the correction by Bricaud *et al.* or a baseline correction is therefore not performed.

Recent work by Stedmon *et al.* shows that by also fitting an offset in the exponential model the standard deviation in the slope parameter is substantially reduced by as much as 72% (Stedmon, Markager, and Kaas 2000). Such an offset is designed to reduce systematic errors in the CDOM absorption measurement, caused by any baseline shift or attenuation not due to CDOM. In the previous chapter it was shown that some 25% of the offset can be caused by residual scattering in the cuvette. Extending equation 10.1 with an $Offset$ results in:

$$a_{CDOM}(\lambda) = Offset + a_{CDOM}(\lambda_0)\exp^{(S(\lambda_0-\lambda))} \qquad 10.5$$

Equation 10.5 can for instance be solved by performing a non-linear least squares optimisation. When the $a_{CDOM}(\lambda_0)$, S and $Offset$ parameters are obtained, the CDOM absorption spectrum SIOP required for optical modelling is calculated using only the $a_{CDOM}(\lambda_0)$ and S (similar to equation10.2). The $Offset$ parameter is discarded because it is essentially a correction parameter required to obtain the true CDOM absorption and the true values for $a_{CDOM}(\lambda_0)$ and S. The C_{CDOM} is equal to the fitted $a_{CDOM}(\lambda_0)$ and can thus be significantly different than the measured CDOM absorption at 440 nm (which is approximated by $a_{CDOM}(\lambda_0) + Offset$). By using equation 10.5, fitting an offset, the slope of the exponential CDOM absorption function generally will become steeper, because the offset has a relatively larger effect on the exponential fit at the longer wavelengths. The larger the CDOM attenuation in the red wavelength interval, the larger the modelled $Offset$ and S. In some cases, when the measured CDOM absorption spectrum does approach zero at the longer wavelengths, the fitted $Offset$ is negative, causing a decrease in the S value compared to the CDOM absorption fit using equation 10.2. This means that CDOM absorption fit parameters collected by using equation 10.1, without offset, are not necessarily comparable with C_{CDOM} and S values resulting from equation 10.5.

The effect of the offset in CDOM exponential fitting is illustrated by Figure 10.1. On the basis of the absorption spectra of commercially available Aldrich humic acid, the difference between the original measurement and the fitted spectra with and without offset is shown.

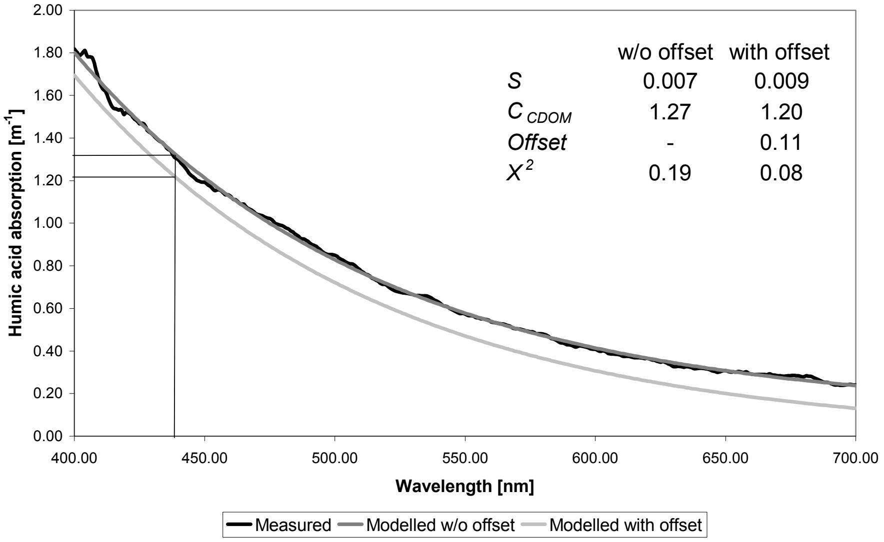

Figure 10.1: The difference between the measured Aldrich Humic Acid absorption spectrum (black line) and the modelled spectra fitted without offset (dark grey line) and with offset (light grey line, with the offset subtracted). The inset shows the S, C_{CDOM}, $Offset$ and χ^2 fit values of the two CDOM absorption models. The CDOM absorption modelling with offset parameter results in a steeper (higher S) exponential function, with a lower CDOM concentration (a_{CDOM} at 440 nm) and a better fit with the measured spectrum (lower χ^2 error) compared with the CDOM modelling without offset.

Please note that the modelled absorption spectrum with $Offset$ parameter has the $Offset$ already subtracted in Figure 10.1, correcting the CDOM absorption for baseline shifts. The shape of the modelled CDOM absorption spectra resulting from equation 10.5 has better agreement with the original measurement (lower χ^2 error).

In section 10.2.2 it was already mentioned that the value of the offset (as defined in equation 10.5) can largely be explained by systematic errors that are the result of scattering effects or baseline shifts. Evidence that the CDOM absorption spectrum is shifted as a result of scattering effects is given by the comparison between offset fit parameters found for CDOM absorption spectra measured using a cuvette set-up and offset fit parameters found for CDOM absorption spectra measured using a PSICAM (see chapter 9). The average $Offset$ for cuvette measurements of 19 samples was 0.35 (± 0.25) while the average $Offset$ for PSICAM CDOM absorption measurements of the same samples was 0.13 (± 0.15). In other words, scattering effects cause two thirds of the systematic errors encountered at cuvette CDOM absorption measurements of these Dutch shallow inland eutrophic freshwaters. The result of the scattering effects is an overestimation of the CDOM concentration, as was also demonstrated in the previous chapter, where PSICAM C_{CDOM} values were on average 5% lower than those measured in a cuvette. Finally, the scattering in the cuvette has an effect on the slope parameter as PSICAM S values were on average 10% higher than those of the cuvette in the experiment discussed above.

10.2.3 Proposed two-component CDOM absorption model for this study

Carder *et al.* found that marine humic and fulvic acid accounted for most of the CDOM absorption in the offshore regions of the Gulf of Mexico (Carder, Steward, Harvey, and Ortner 1989). In order to give a better description of the CDOM absorption spectrum, they proposed a two component exponential fit model for CDOM:

$$a_{CDOM}(\lambda) = a_{HA}(\lambda_0)\exp^{(S_{HA}(\lambda_0-\lambda))} + a_{FA}(\lambda_0)\exp^{(S_{FA}(\lambda_0-\lambda))} \qquad 10.6$$

using two combined exponential functions similar to equation 10.2 with different slopes, one for the (marine) humic acid plus the residual dissolved material (the S_{HA}, with absorption a_{HA}) and one for the (marine) fulvic acid component (the S_{FA}, with absorption a_{FA}). Carder *et al.* used fixed values for the humic and fulvic acid slopes, S_{HA} and S_{FA}. These fixed slope values can be regarded as end-members. Please note that the original equation from Carder *et al.* does not include an offset (see previous section) and that the model was explicitly developed for marine CDOM.

Combining the offset and two-component approach

So far, two ways of improving the agreement between the measured and modelled CDOM have been discussed. The first method is by using an offset, as proposed by Stedmon *et al.* (Stedmon, Markager, and Kaas 2000), the second method is by using a two component model with humic and fulvic acids as end-members as proposed by Carder *et al.* (Carder, Steward, Harvey, and Ortner 1989). Combining these two approaches should conceivably lead to the best agreement between measured and modelled CDOM absorption. In this study therefore it is proposed to combine equation 10.5 and 10.6 into the following fit model:

$$a_{CDOM}(\lambda) = Offset + a_{HA}\exp^{(S_{HA}(\lambda_0-\lambda))} + a_{FA}\exp^{(S_{FA}(\lambda_0-\lambda))} \qquad 10.7$$

The exponential CDOM absorption fit model given by equation 10.7 is used as the CDOM absorption spectral decomposition model in this research.

In conclusion, it is expected that by using a PSICAM and the two-component CDOM absorption model including an offset parameter systematic errors in the absorption measurements and estimation will be significantly reduced. The value of the offset parameter included in equation 10.7 for the proposed two component CDOM absorption model, is therefore expected to be small for PSICAM based measurements of CDOM

10.3 Linear and non-linear CDOM decomposition techniques

There are two types of two-component CDOM absorption modelling: linear and non-linear decomposition techniques. The theoretical background of these types will be discussed in this section.

The absorption model that will be used for the spectral decomposition of CDOM, equation 10.7, has five parameters: the humic acid slope (S_{HA} [nm^{-1}]) the humic acid concentration (C_{HA} [m^{-1}]) the fulvic acid slope (S_{FA} [nm^{-1}]) the fulvic acid concentration (C_{FA} [m^{-1}]) and the $Offset$. The complete parameter set in the two-component model can be calculated by using a non-linear least squares optimisation technique, while linear least squares regression can be used when fixed values for the slope parameters are assigned.

10.3.1 Linear least squares regression and its end-member slopes

For the linear least squares regression the humic and fulvic acid slope end-members used should be chosen as valid and accurate as possible. Below are a number of possible end-member candidates that will be discussed:

1. The slope values for (marine) humic and fulvic acid found by Carder *et al.*(Carder, Steward, Harvey, and Ortner 1989)
2. The minimum (as S_{FA}) and maximum (as S_{HA}) CDOM absorption slope value found in the study area (Vecht area).
3. The literature values for Suwannee River humic and fulvic acid, humic substances that are regarded as standards by the International Humic Substances Society (IHSS, www.ihss.gatech.edu)
4. The slope of Aldrich humic acid standard as measured in the laboratory and the S_{FA} set equal to the highest CDOM absorption slope parameter found in the study area (see number 2), further referred to as the hybrid approach.

Carder end-members

The (marine) humic and fulvic acid absorption slope values found by Carder *et al.* are 0.0111 and 0.0189 nm^{-1} respectively. Krijgsman already studied the CDOM absorption and slope for 40 Dutch surface water samples (Krijgsman 1994). Target factor analysis was used in conjunction with the Carder *et al.* mass-specific absorption coefficients and slopes for (marine) humic and fulvic acid (Carder, Steward, Harvey, and Ortner 1989). In conclusion Krijgsman found that the two-component model based on marine humic and fulvic acids from Carder *et al.* did not accurately describe the CDOM absorption of his dataset. In his dissertation, Krijgsman argues that the spectral shapes of humic and fulvic acids vary in nature, and that chemical and optical determination of both components should be repeated for every application. It is therefore expected that by using the end-members from Carder *et al.* an unsatisfactory goodness of fit between the measured and modelled CDOM absorption will be achieved. Furthermore the slope values used by Carder *et al.* were determined by using equation 10.1 without the use of an offset and are therefore presumed to be higher than the actual values.

Vecht Wetlands water body end-members

For this study the assumption is made that the minimum CDOM absorption slope value found in the Vecht area dataset (see §8.2) corresponds to a sample containing only humic acid, and that the maximum CDOM absorption slope value corresponds to a sample containing only fulvic acid. The minimum and maximum CDOM absorption slope values found for these lakes both in literature and in the dataset collected for this research are 0.011 and 0.021 nm^{-1} respectively (Dekker and Peters 1993). Under natural conditions however it seems unlikely that only one of the two groups is present. The slope values found both fall in the fulvic acid range so it could even mean that there is little humic acid present in the study area. It is therefore more probable that the end-members in this case are not pure humic and fulvic acid but 'humic dominated' and 'fulvic dominated'. This would also mean that the ratio between the absorptions of the two groups is only qualitative, not quantitative.

Suwannee River end-members

The literature slope values for Suwannee River humic and fulvic acid, 0.0137 and 0.0172 nm^{-1} (Hansell and Carlson 2002), are used by the International Humic Substances Society as standards. The Suwannee River is a black water river in Georgia and Florida, USA. Its origin lies in the Okefenokee wetland area (Averett, Leenheer, McKnight, and Thorn 2003), which is incomparable with the Vecht area as it has a sub-tropical climate, a limestone substrate and is flooded by salt seawater occasionally, while the Vecht Wetlands lie in a temperate climate, in a thick peat layer and are fed by fresh groundwater or rivers. Furthermore, the Suwannee River humic and fulvic acid slopes are probably calculated by using equation 10.1 without the use of an offset and are therefore higher than the actual values. It is noted that the Suwannee River fulvic acid slope is lower than the maximum CDOM absorption slope found in the Dutch study area, indicating that the Suwannee River end-members are not applicable for use in Dutch shallow eutrophic natural freshwaters. Krijgsman already warned against using end-members found at different locations (Krijgsman 1994).

Hybrid end-members

As one international standard is available: Aldrich humic acid, it is proposed to combine this value with the best achievable value for fulvic acid. This is a hybrid approach. The absorption spectrum slope of Aldrich humic acid was measured in the laboratory (0.0089 m^{-1}). As no fulvic acid standard was available, the fulvic acid absorption slope was set equal to the maximum CDOM absorption slope found in the study area. The highest slope found was 0.021 nm^{-1} (Dekker and Peters 1993).

10.3.2 Non-linear least squares optimisation

The advantage of the non-linear least squares optimisation method is that the slope values are allowed to change (within a certain range if required). The slope parameters of humic and fulvic acid are likely to vary as a result of changes in the chemical composition of humic and fulvic acid (Krijgsman 1994), (Hansell and Carlson 2002). The disadvantage of using non-linear least squares optimisation is that the parameter space of valid solutions may be considerable, leading to non-unique solutions.

By assuming fixed values (end-members) for the slopes of the humic and fulvic acid absorptions (S_{HA} and S_{FA}) the model can also be solved by applying linear least squares regression, which is less computationally demanding and leads to an unique solution. The disadvantage of this method is that, in nature, the humic and fulvic acid slope values may not be constant.

Another consideration is the expected goodness of fit for both the linear and non-linear approach. From a mathematical point of view the more parameters that are used for fitting, the better the solution will be. However, the best measure for the goodness of fit is given by the normalised goodness of fit χ^2/v, with v the degrees of freedom (Blalock 1985). By fitting more parameters (S_{HA} and S_{FA}), the number of degrees of freedom will decrease (by 2). It is therefore less straightforward to predict whether the linear or non-linear approach will have the best *normalised* goodness of fit.

In order to evaluate the modelling performance of the two-component CDOM absorption decomposition, a case study is performed. Using natural samples taken in the study area the humic and fulvic acid absorptions were estimated using the linear least squares regression technique with different end-member combinations and the non-linear least squares optimisation technique described above.

10.4 Case study: Decomposing measured CDOM absorption spectra of inland waters

10.4.1 Introduction

The decomposition of CDOM absorption spectra methods described in the previous section were tested on absorption spectra collected from Dutch shallow eutrophic inland freshwaters. Both linear and non-linear approaches are used and the *normalised* goodness of fit values of the results are compared to the fit of the widely used single exponential model with offset by Stedmon *et al.* All of the exponential fit models were performed over the range 400-700 nm. A test using humic acid standard was also conducted to investigate the ability of the non-linear approach to produce a unique solution. See Figure 10.2 for the outline of the case study.

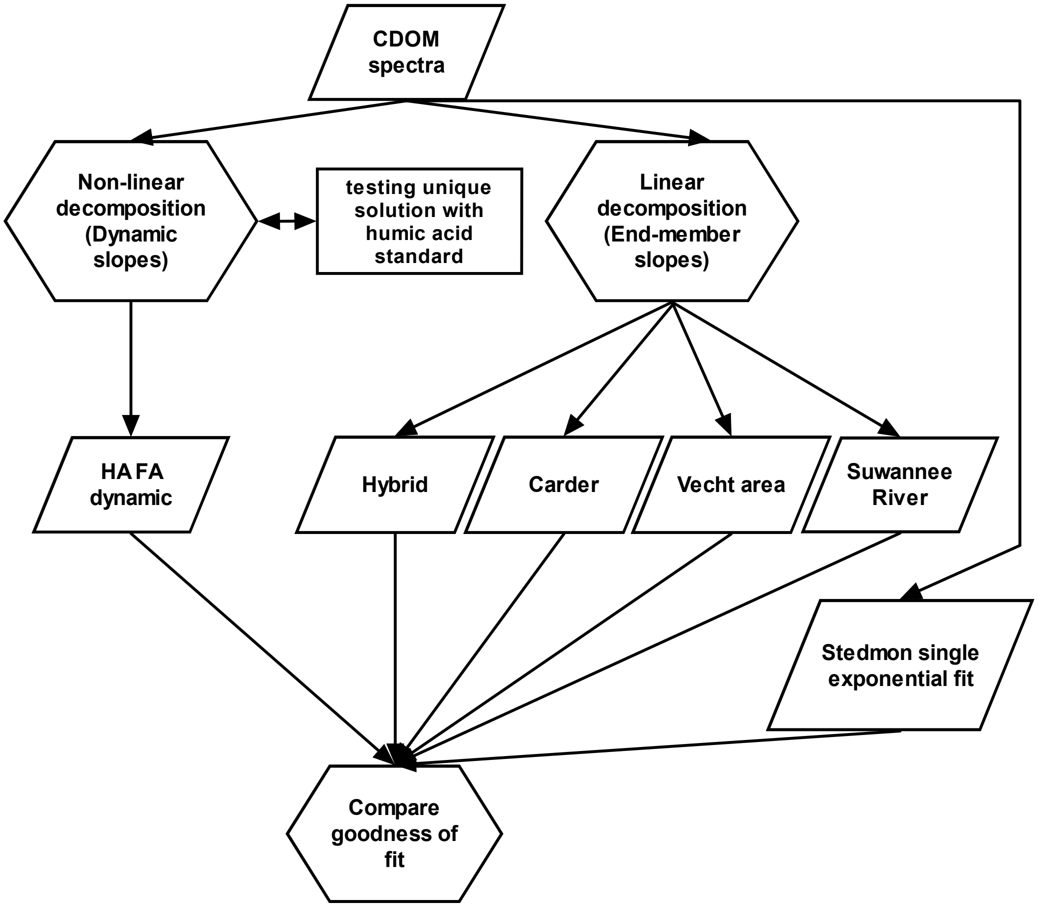

Figure 10.2: The outline of the case study showing all necessary steps. CDOM spectra are decomposed using the linear and non-linear models and the resulting goodness of fit is compared.

10.4.2 Methods

40 water samples were collected during field campaigns in 2001 and 2002 in the study area, which is described in §1.2. A total of 21 samples were taken in August 2001 from locations covering almost all water bodies in the Vecht study area. From the remaining 19 samples, 6 were taken on May 6, 2002, 6 on July 29, 2002 and 7 on September 12, 2002. The 2002 campaign only involved locations in Lake Loenderveen and Terra Nova (see Appendix II). Sampling, storage and measurement was performed according to the protocols in Appendix III. All CDOM absorption measurements were performed using a Point-Source Integrating-Cavity Absorption Meter device (see chapter 9 for the PSICAM), reducing influences of scattering on the absorption measurement (and on the *Offset* value).

Non-linear decomposition techniques

From the large number of non-linear optimisation methods two methods that were readily available were tested for calculating the decomposition models based on equation 10.7: non-linear least squares regression (LSQNONLIN in Matlab®, the Mathworks Inc.) and the Generalized Reduced Gradient optimiser (GRG2, in Microsoft® Excel Solver, Microsoft Corporation). Background knowledge on non-linear least squares regression can be found in many textbooks such as the one by Press *et al.* (Press, Flannery, Teukolsky, and Vetterling 1992), the theory behind the Generalized Reduced Gradient optimiser in Excel is explained in Lasdon *et al.* (Lasdon, Waren, Jain, and Ratner 1978).

Linear decomposition techniques using fixed end-members

The linear calculation method for the fixed end-member approach is less complicated than the non-linear method, as the parameters can be determined by simple linear regression on equation 10.7, thus including an offset for all end-member combinations, including the Carder *et al.* end-members. Four different sets of end-members were tested and compared (see also §10.3.1), these are given in Table 10.1.

Table 10.1: The end-members sets and their humic and fulvic acid slopes

	End-member set	Humic and fulvic acid slopes
1	Carder *et al.*	0.0111 and 0.0189 nm^{-1}
2	The Vecht area dataset	0.011 and 0.021 nm^{-1}
3	The Suwannee River humic and fulvic acid	0.0137 and 0.0172 nm^{-1}
4	The slope Aldrich humic acid standard and the average S_{FA} from the Vecht area dataset	0.0089 and 0.021 nm^{-1}

10.4.3 Results

Testing non-linear decomposition techniques for unique solutions

The drawback of non-linear optimisation is the fact that the solution found may not be unique. Depending on the size of the parameter space and the constraints given and the starting value, multiple solutions can be possible within the same degree of accuracy. A test was conducted in order to establish the ability of the two non-linear optimisation methods of reaching (near) unique solutions. The measured absorption spectrum of Aldrich humic acid standard, thus containing *only* humic acid, was spectrally decomposed using the two non-linear optimisation methods. The unique solution in this case should then be similar to the fit parameters found ($Offset$, S_{HA} and a_{HA}) when applying the Stedmon *et al.* single exponential CDOM absorption fit model (see equation 10.5). After all, the value for a_{FA} retrieved should be equal to zero.

For this test the following different exponential CDOM absorption fit models were used (see §10.2):

1. Bricaud (see equation 10.1).
2. Stedmon *et al* (see equation 10.5).
3. Carder *et al.* (see equation 10.6).
4. This study (see equation 10.7).

The models by Bricaud and Carder *et al.,* were included to demonstrate the effect of not using an offset. The model by Stedmon *et al.,* was included as a reference. The goodness of fit (χ^2/v, the Chi-square divided by the degrees of freedom) was calculated as a measure of performance. The maximum precision settings used for both methods are shown in Table 10.2, these settings determine the maximum number of iterations allowed and the level of precision at which the solution is calculated. Both the number of iterations and the precision settings for the GRG2 and LSQNONLIN method are set at a very high level for this analysis.

Table 10.2: Modelling method settings

	GRG2	LSQNONLIN
Max. Iterations	1000	1000
Precision	0.000001	-
Convergence	0.000001	-
Tolerance Fun	-	0.00000001
Tolerance X	-	0.000001

The results of the exponential modelling of the absorption of Aldrich humic acid standard for the different models and methods are given in Table 10.3.

Table 10.3: Aldrich humic acid standard S, a, offset and χ^2/v values for the four different CDOM decomposition models and the two optimisation methods.

	GRG2				LSQNONLIN			
	Bricaud	Stedmon	Carder	This study	Bricaud	Stedmon	Carder	This study
S_{HA} [nm^{-1}]	0.008	0.008	0.011	0.008	0.008	0.008	0.011	0.008
a_{HA} [m^{-1}]	1.37	1.33	1.44	1.33	1.36	1.34	1.40	1.28
S_{FA} [nm^{-1}]	-	-	0.019	0.014	-	-	0.019	0.014
a_{FA} [m^{-1}]	-	-	0.00	0.00	-	-	0.00	0.06
Offset	-	0.03	-	0.03	-	0.02	-	0.02
χ^2/v	0.084	0.080	2.011	0.084	0.089	0.081	2.107	0.084

Table 10.3 shows that the methods with an offset (Stedmon and this study) have better performance than the methods without an offset (Bricaud and Carder). The high normalised χ^2/v values (>1) for the Carder method indicate that the model assumptions, that is the slope values used by Carder et al, are not valid for this sample. This is no surprise because the sample consisted solely of Aldrich humic acid standard, apparently with different spectral characteristics than marine humic acid found in the Gulf of Mexico. The normalized χ^2 values for all models are equal or slightly lower for the GRG2 technique than for the non-linear least-squares regression, but the difference is not significant.

The GRG2 technique based solutions finds no a_{FA} in the sample, while the least-squares non-linear regression yields a fulvic acid absorption of 0.06 m^{-1}. Also the GRG2 technique found S_{HA} and a_{HA} values that are exactly the same as the slope and C_{CDOM} absorption found by the Stedmon *et al.* single exponential model with offset and by the Bricaud *et al.* model without offset. This means that GRG2 was capable of finding the unique solution in this case. It was therefore decided to use the GRG2 technique embedded in the Microsoft® Excel Solver for the non-linear modelling in the case study.

Another method was used to verify the ability of GRG2 technique to reach unique CDOM decomposition solutions. The equation used for optimisation, equation 10.7 requires positive slope parameters. By rearranging equation 10.7 into the following equation negative slope factors are needed as input:

$$a_{CDOM}(\lambda) = Offset + a_{HA}\exp^{(-S_{HA}(\lambda-\lambda_0))} + a_{FA}\exp^{(-S_{FA}(\lambda-\lambda_0))} \qquad 10.8$$

The optimisation results of GRG2 technique for both methods should be the same when a unique solution was found. When both methods were applied on the CDOM absorption spectra in the dataset (under the restrictions listed in the previous paragraph), significantly different solutions were found. Apparently by using different starting points, the GRG2 technique reaches different solutions.

The non-linear GRG2 optimisation of the two-component CDOM absorption model given by equation 10.7 was also applied on the measured CDOM absorption spectra in the Vecht Wetlands dataset. In order to reduce the solution space for the GRG2 optimisation technique, lower and upper boundaries were given for the slope parameters to be fitted. Values for S_{HA} should lie between 0.005 and 0.014 and the S_{FA} should be larger than 0.014. The range of values for a_{HA} and a_{FA} was equal or greater than zero (no negative concentrations allowed). When applied to the CDOM absorptions of the dataset, roughly two-thirds of the resulting S_{HA} values in this case appeared equal to either the upper or lower boundary, with high χ^2 errors indicating that the GRG2 optimisation performed poorly.

Thus with non-linear fitting of all five parameters on measured natural absorption spectra the parameter space is too large and a unique solution is not found. The non-linear exponential fit method was therefore discarded for spectral CDOM absorption decomposition.

Results of the linear decomposition

The results of the linear decompositions of the 40 water samples using a two component model were compared in order to determine the best decomposition method. The results of end-members that produced the best decomposition were also compared to the results of the single exponential CDOM absorption fit technique to asses the accuracy improvement gained by using a two-component exponential CDOM absorption fit model. The comparison was done on the basis of the goodness of fit, the values of the offset parameters and the C_{CDOM} values.

In section 10.2.3 it was assumed that by performing the best spectral decomposition the offset value, which are regarded as a correction for systematic errors other than the scattering effects, would decrease. Therefore the average offset parameters for the different decomposition methods are also compared. The method with the lowest average offset is considered the best. The C_{CDOM} values were also compared in order to assess the influence on C_{CDOM} using a two-component exponential CDOM absorption fit model.

In Table 10.4 the sum of the squared differences and the resulting offset parameters of the linear methods are shown, together with the values for the single exponential model used by Stedmon *et al.* as a reference. The hybrid end-members give the best goodness of fit between the measured and modelled CDOM spectra, closely followed by the Carder end-members. The average offset value of the hybrid end-members is also the lowest. The hybrid end-members thus lead to the best results for the linear decomposition method. The average C_{CDOM} value of the hybrid end-members is slightly higher than the C_{CDOM} value of the Stedmon *et al.* single exponential model. The sum of the C_{CDOM} value and the $Offset$ however is equal to the measured CDOM absorption at 440 nm (2.83 and 2.80 m^{-1} for Stedmon and Hybrid methods). The low $Offset$ value for the two-component linear CDOM decomposition using Hybrid end-member shows that the systematic errors in the absorption measurement may actually be quite small.

Table 10.4: The average goodness of fit of 40 samples between the measured and modelled CDOM absorptions, the average offset parameters and the average C_{CDOM} values for the single exponential model used by Stedmon *et al.* as a reference and the different end-member sets of the linear decomposition method. The Hybrid end-members give the smallest χ^2 error and $Offset$ values and thus the best representation of the measured absorption spectrum.

	Stedmon	Carder	Vecht	Suwannee	Hybrid
χ^2	0.58	0.54	0.57	0.57	0.53
$Offset$	0.19	0.16	0.18	0.19	0.06
C_{CDOM}	2.64	2.68	2.65	2.65	2.74

10.4.4 Case study discussion and conclusions

The CDOM spectra of 40 natural water samples were decomposed into absorptions of humic and fulvic acids. Spectral CDOM decomposition was carried out using both linear and non-linear regression techniques. The linear regression model requires fixed humic and fulvic acid absorption slopes, referred to as end-members. A number of end-member combinations were tested: The humic and fulvic acid slope parameters found by Carder *et al.* (Carder, Steward, Harvey, and Ortner 1989), the minimum and maximum slope parameters found for CDOM absorption spectra measured in the Vecht Wetlands study area, the Suwannee River humic and fulvic acid slope parameters used by the International Humic Substances Society as standards and a hybrid combination consisting of the slope parameter of the Aldrich Humic Acid standard and the maximum slope parameter measured in the Vecht Wetlands.

The non-linear regression model did not use end-members, instead the humic and fulvic acid slope parameters were also optimised (so called ‘dynamic’ slopes). Because there was concern that the fitting of two extra parameters with a non-linear model would not lead to unique solutions, tests were performed by feeding it with an absorption spectrum of a humic acid standard. A unique solution was found for the humic acid standard using the generalised reduced gradient optimiser.

The GRG2 however was not capable of retrieving unique solutions for the measured CDOM absorption spectra of the case study, as subsequent modelling revealed. The use of non-linear two-component exponential CDOM absorption fitting of five parameters is therefore not recommended because the parameter space is too large, even when restrictions are imposed on the range of slope parameters allowed.

The linear CDOM absorption spectrum decomposition showed that the hybrid end-members yielded the best results. By applying a two-component exponential CDOM absorption fit model with an offset and the hybrid end-members, the accuracy of the CDOM absorption spectrum fit was improved by 7% on average compared to the accuracy of the fit using a single exponential CDOM absorption model with an offset. As a result, the C_{CDOM} value of the samples that were decomposed increased with an average of 3%.

In Part B of this dissertation the principles of optical modelling for the purpose of retrieving concentrations of optically active water constituents such as CDOM were discussed. In order to retrieve concentrations of optically active water constituents by means of inverse modelling, a reference set of Specific Inherent Optical Properties is required. The normalised modelled CDOM absorption is one of those SIOP. By using a two-component exponential model with an offset and carefully selected end-members, it is possible to improve the accuracy of the normalised CDOM absorption SIOP by 7% on average over the spectrum from 400 to 700 nm ($N = 40$). Inverse modelling simulations in chapter 7 have shown that the Gordon-Walker optical model is most sensitive to errors in the SIOP set used (Peters, Pasterkamp, and van der Woerd 2002). It is therefore expected that this significant improvement in the CDOM absorption SIOP by using two-component modelling leads to a significant improvement in forward and inverse optical modelling.

10.5 Improvement of CDOM retrieval by using the two-component model for the normalised CDOM absorption spectrum SIOP

The second proposed CDOM retrieval improvement was the modelling of the measured CDOM absorption spectrum using a two-component exponential model, rather than the single component exponential fit. Measured CDOM absorption spectra are fitted to a theoretical exponential function in order to enable extrapolation of the wavelength range and also in order to reduce noise. Instead of regarding CDOM as a single component, the two main constituents of CDOM, Humic and Fulvic acid were modelled as two separate exponential functions in the two-component model.

An inversion of the optical model was performed using the normalised CDOM absorption spectrum in the SIOP set modelled with the two-component model, similar to the inversions performed in section 8.5. Again, the measured $R(0-)$ spectra collected with the hand-held spectrometer were resampled to the band settings of the frequently used MERIS and CASI instruments. Also both the Matrix Inversion Methods (MIM) and the Levenberg-Marquardt (LM) algorithms were applied. The same 24 selected and quality controlled sample locations have been used together with the same median SIOP set with the exception of the $\bar{a}_{CDOM}$ spectrum that was remodelled using the two-component approach based on the hybrid end-members. The CDOM absorption measurements used as reference were PSICAM measurements (if available).

The resulting R^2, slope and offset values are shown in Table 10.5, while Figure 10.3 gives an impression of the error contribution per sample station (for the Levenberg-Marquardt method and CASI band settings, results are similar for MIM inversion and MERIS band settings).

Table 10.5: The R^2, slope and offset value matrix for CDOM retrieval for both the single and two-component CDOM modelling applying MIM and LM techniques to the MERIS and CASI band settings.

$N = 24$	CDOM	Single component	CDOM	Two-component
	R^2	Slope + offset	R^2	Slope + offset
MERIS MIM	0.52	y = 0.89x + 0.26	0.55	y= 0.78x + 0.12
MERIS LM	0.61	y = 1.12x - 0.05	0.56	y= 0.89x + 0.07
CASI MIM	0.52	y = 0.87x + 0.19	0.52	y= 0.77x + 0.04
CASI LM	0.60	y = 1.19x – 0.28	0.56	y= 0.87x - 0.05

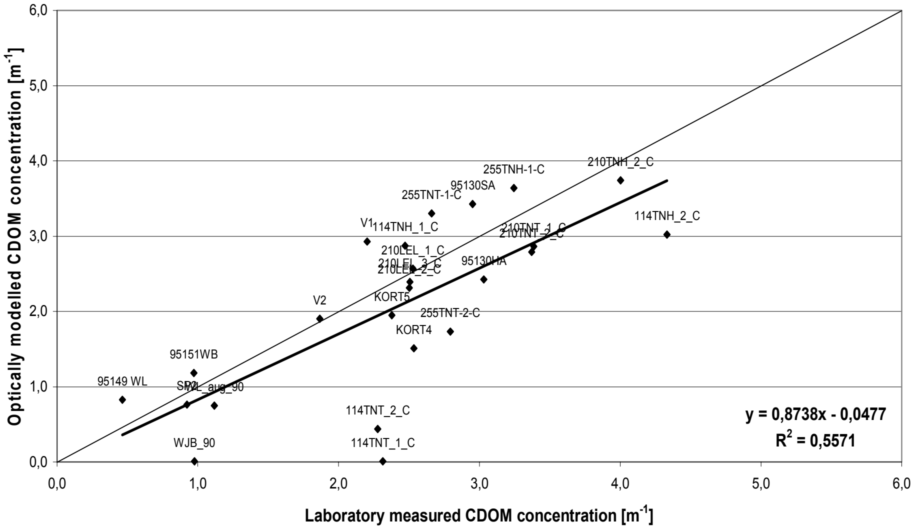

Figure 10.3: The retrieved C_{CDOM} values using the Levenberg-Marquardt inversion on the CASI band settings versus the reference C_{CDOM} values based on the single exponent (in black) and two-component CDOM absorption fit model (in grey)

It was found that the correlation coefficients of the retrieved C_{CDOM} using the single component fit were 0-5% higher than those of the retrieved C_{CDOM} using the two-component fit. The slope values of the retrieved C_{CDOM} using the first method fit were 10-30% higher than those of the latter. For LM retrieval of CASI data, the single component fit leads to a 20% overestimation while the two-component fit yields a 10% underestimation. The scatterplots reveal that the results for two-component approach may in fact have improved compared with the results of the single component fit values. Analogous to the inversion performed in section 8.5.2 with the median SIOP set, sample stations 114_TNT_1_C and 114_TNT_2_C have a poor retrieval accuracy (see §8.5.2 and Figure 10.3), but the sample stations with higher CDOM concentrations (especially the 210_ series), who are overestimated with the single component model, are now closer to the reference values. Due to the outlier stations and the very small differences it cannot be established whether the two-component model leads to CDOM retrieval improvements.

The slope values shown that the MIM method produces accurate estimates of the CDOM concentration, while the LM method overestimates C_{CDOM}.

10.6 Two component CDOM modelling discussion and conclusion

The absorption spectrum of CDOM in the visible wavelength range can be accurately described by an exponential function, with high absorption values in the blue wavelength region decreasing to very low absorption values at the longer wavelengths. Such an exponential function is often fitted to the measured CDOM absorption spectra in order to reduce measurement noise or to interpolate or extrapolate the CDOM absorption spectrum. Next to noise, the measured CDOM absorption spectrum can also be affected by systematic errors. These include mainly scattering effects by particles in the sample, but also effects of light refraction by the cuvette wall and baseline shifts due to for instance temperature differences between the reference and the sample. The systematic errors can be partly corrected for by including an offset parameter in the exponential fit model. Typical offset values found for cuvette measurements were significantly higher than those found for PSICAM CDOM absorption measurements, indicating that the offset compensates partly for scattering effects (see previous chapter). Using an offset, the goodness of fit between the measured and the modelled CDOM absorption spectrum is significantly improved.

Another way of improving the goodness of fit between the measured and modelled CDOM absorption spectrum is investigated in this chapter. Instead of regarding CDOM as a whole, the CDOM pool is divided into its two major components humic and fulvic acids. The absorption of CDOM is then the sum of the absorption of humic acid and the absorption of fulvic acid. Both humic and fulvic acids have absorption spectra that are shaped as exponential functions. So instead of fitting a single exponential function to describe the absorption, two exponential functions are used to describe the CDOM absorption. In this chapter the improvement in goodness of fit between measured and modelled CDOM absorption using such a two-component exponential fit model was investigated based on actual measured data.

Two-component exponential CDOM decomposition can be performed using linear and non-linear regression techniques. Linear regression requires the use of fixed slope parameters, called end-members. The end-members should be chosen with great care as spectral characteristics of humic and fulvic acids may vary in time and space. A number of suitable end-member pairs were proposed. Non-linear regression techniques allow the slope parameters to be modelled as well, but the disadvantage is that unique solutions may not be reached with this type of modelling and it is computationally more demanding.

A case study was performed in this research to assess the best decomposition model, using a dataset of PSICAM CDOM absorption measurements from 40 samples collected in Dutch shallow eutrophic inland waters. The case study showed that unique solutions were indeed not reached when fitting all five parameters of the non-linear model (S_{HA}, S_{FA}, a_{HA}, a_{FA} and $Offset$). The parameter space is too large in this case, so non-linear spectral CDOM absorption decomposition was discarded.

In order to investigate the possibilities of two-component modelling it is recommended to perform a true chemical separation of CDOM into humic and fulvic acid of a large number of water samples. The maximum of median slope parameter of the two fractions can then be established. In this way the true humic and fulvic acid end-members needed to perform a two-component linear exponential fit on the measured CDOM absorption spectrum are known, increasing the accuracy of the a_{HA}, a_{FA} and C_{CDOM} retrieval.

In the previous chapter it was shown that the $Offset$ parameter can be significantly decreased by correcting for scattering effects, for instance by measuring the CDOM absorption in a PSICAM. In the beginning of this chapter it was explained that the remaining $Offset$ (without scattering effects) consists primarily of systematic errors in the absorption measurement. This is contradictory with the results of the case study, where it has been shown that, with two-component CDOM absorption modelling of PSICAM CDOM measurements (which are unaffected by scattering effects) and the right end-member slopes, the $Offset$ parameter is significantly reduced (by 50%). Together with an improvement in goodness of fit between the measured and two-component modelled CDOM absorption spectra over the single component model, this decrease of the $Offset$ parameter gives evidence that the two-component CDOM absorption model is valid. The CDOM absorption spectrum is more accurately described by a double exponential function than by a single exponential function. By neutralising scattering effects using the PSICAM and by applying a two-component CDOM absorption model, the remaining $Offset$ is small, and due to true absorption of CDOM at the longer wavelengths or to refraction effects and baseline shifts between the reference and the sample caused by for instance temperature differences.

It was found in this chapter that by using a linear two-component exponential model and well-chosen end-members the goodness of fit between the measured and modelled CDOM absorption spectrum does improve, on average with some 7% over the wavelength range between 400 and 700 nm. As a reference the CDOM absorption was fitted using a single exponential fit model with an offset. The best goodness of fit was found for the linear regression technique with an offset and the hybrid end-members. Such an improvement in the accuracy of the modelled CDOM absorption is expected to lead to a significant improvement in inverse optical modelling. The normalised modelled CDOM absorption is part of the Specific Inherent Optical Properties required as input for the optical model. The average C_{CDOM} value of the samples that were decomposed increased with some 3% in the case study.

The goal of this research is the improvement of CDOM concentration retrieval from remote sensing data. An inversion of the optical model was performed using the normalised CDOM absorption spectrum in the SIOP set modelled with the two-component model. The same 24 selected and quality controlled sample locations as in chapter 8 and the same median SIOP set, with the exception of the normalised CDOM absorption spectrum that was remodelled using the two-component approach were used. The observed differences in correlation coefficients were very small, but the slope parameter may improve by some 10% using LM methods. Due to the outlier stations and the very small differences however it cannot be established whether the two-component model leads to CDOM retrieval improvements. An additional study, including a larger dataset, is advised to establish the effect of two-component CDOM modelling.

An advantage of using a two-component model, or performing actual absorption measurements of humic and fulvic acids, is the ability to provide extra water quality information given by the humic and fulvic acid absorptions. The ratio between the two fractions is expected to be related to the origin of the organic material. Humic acid has relatively larger molecules, and is associated with allochthonous or terrigenous input, while the fulvic acid with its relatively shorter and simpler molecules is generally the result of autochthonous production (see chapter 2). The information provided by the humic to fulvic acid ratio was not discussed in this chapter but is recommended to be investigated in future studies.

Part D Synthesis

11. Synthesis

11.1 Summary and conclusions

The amount and type of dissolved organic matter (DOM) that is present in natural waters is regarded as an important measure of physico-chemical water quality. This DOM has been identified as a source of organic pollution, as an energy source for microbe-based aquatic food webs, as a factor in the cycling of trace elements and also as a factor in the biological activity of phytoplankton and bacteria. Because of its large organic complexes DOM usually acts as a buffer, thereby regulating the phyto- and zooplankton ecosystem and immobilising xenobiotic compounds such as heavy metals (Kramer, Jak, Stroomberg, Hooftman, and Mayer 2002). By binding contaminants, their bioavailability is reduced. At the same time, the oceanic DOM pool is identified as a major reservoir of organic carbon for the global carbon cycle.

As DOM cannot be measured directly, the determination of the dissolved organic carbon (DOC) concentration is therefore included in many Dutch and international water monitoring programmes (Anonymus 2000). DOC measurements involve point sampling and laboratory analysis. The coloured fraction of DOM, called Coloured Dissolved Organic Matter (CDOM), is proposed as an alternative proxy for DOM. It has been postulated that CDOM may be accurately determined from remotely sensed data. In that case it would be more cost-effective than traditional in-situ methods in most cases and the remote sensing method would, in addition, provide a wealth of spatial and temporal information.

Amongst others, spatial CDOM maps may provide an insight in the extension of river water plumes in coastal waters and the spatial effects on water- and ecosystem quality. Because of the high absorption in the UV CDOM can act as a protecting agent for the ecosystem in shallow waters

The goal of this research, as stated in chapter 1, is to improve the accuracy of the concentration of coloured dissolved organic matter retrieved from remote sensing spectra in shallow eutrophic inland waters. This is pursued in three complementary ways: by deriving a more accurate CDOM algorithm using new techniques in optical modelling, by using a Point-Source Integrating-Cavity Absorption Meter (PSICAM) device for more accurate CDOM absorption measurements in the laboratory and by decomposing CDOM into its major groups of humic and fulvic acids and modelling the measured absorption spectra separately. In addition the prerequisites for accurate CDOM concentration detection using remote sensing are determined.

11.1.1 Part A: Background on Coloured Dissolved Organic Matter

Before starting with optical modelling of remotely sensed data, I first performed a literature study on the chemical and ecological background of CDOM (chapter 2). This was necessary to understand the optical properties of CDOM (that are determined by the molecular structures of CDOM) and relationships with other water quality parameters and the abundance of CDOM and variation therein that are determined by the formation and degradation processes. From the available literature I found that CDOM has spectral characteristics in the visible wavelength region that are significantly different than the spectral characteristics of chlorophyll and suspended matter. In theory it should therefore be possible to retrieve CDOM concentrations from remote sensing. Next to this, I learned that CDOM comprises roughly of two very broad groups of molecules: humic and fulvic acids (HA and FA for short). Although the naming of these groups can cause confusion because of the weak and aged definitions of HA and FA, I chose to stick to them to make my work more compatible with other publications on this subject. Because HA and FA have different absorption spectrum slopes I suspected that by modelling HA and FA separately, the accuracy of CDOM retrieval as a whole would increase. Another possible advantage of modelling HA and FA separately arising from the literature study was that the ratio between HA and FA present in a water body could provide valuable information to water managers about the origin of the organic matter of that water body, as HA are mostly of terrestrious or allochthonous origin while FA are mostly produced locally by the algae (autochthonous).

A small case study at the end of chapter 2 that I performed on CDOM data collected in the Vecht Wetlands research area during this study showed that CDOM concentrations and slope parameters varied during the summer season. Although insufficient data was available to allow solid conclusions, I found that the CDOM appears to be consumed by blooming algae populations in spring and autumn, and is released in early summer.

11.1.2 Part B: Optical modelling theory

After establishing that CDOM is indeed distinguishable from remote sensing data, I had to select a suitable optical modelling approach from literature (chapter 3). Because of optical interference with ever present chlorophyll and suspended matter in Dutch inland waters, (semi-)empiricial models would not suffice. Neural networks do not operate transparently so the insight in the relationships between the optically active parameters which I was looking for could not be gained this way. True analytical models were not feasible for my research because no operational model code was available at that time. Moreover, these models require extensive input data which could not be gathered during this study. By elimination I chose to use semi-analytical models, which are physically based but simplified, and have proven their worth in many other water remote sensing studies.

The next step was to select which simplifications, or which semi-analytical model, should be used (chapter 4). Considering the parameters that could be determined within this research, a further simplification of the optical model was needed as provided by the Gordon-Walker (GW) semi-analytical model (Gordon, Brown, and Jacobs 1975). This GW-model is known for its good performance in general; it has the least assumptions, its parameters could be obtained within this research and it can easily be linearised for inverse modelling. At the end of this chapter I selected two commonly used state-of-art inversion techniques: Matrix Inversion Methods (MIM) and Levenberg-Marquardt optimisation (LM). The reason for also selecting a non-linear method like LM is that it is less sensitive to small spectral errors, which are often present in the measured spectra.

At this stage, I knew exactly what model I would be using, so it was time to consider the exact parameterisation before running the model. The GW-model requires Inherent Optical Properties (IOP), concentrations and Apparent Optical Properties (AOP). The IOPs I selected are discussed in chapter 5:

1. The absorption and scattering of pure water
2. The absorption and (normalized) concentration of Coloured Dissolved Organic Matter, the only optically active dissolved constituent
3. The absorption and concentration of tripton
4. The scattering and concentration of seston
5. The absorption and concentration of phytoplankton pigments

These SIOPs both fulfil the requirements of the GW-model and could be measured within the framework of my research.

Besides the SIOPs I also needed matching AOP measurements during my field works. AOPs can be measured in a variety of ways (chapter 6), but because of the encouraging results reported individually by Gons (Gons 1999; Gons, Rijkeboer, and Ruddick 2002), and Rijkeboer (Rijkeboer, Dekker, and Hoogenboom 1998; Rijkeboer 2000) and the availability of the necessary instrument, I chose to use the Gons method (Gons 1999) for above water subsurface irradiance reflectance measurements. Here too a number of choices were made for its parameterisation, concerning for instance the Q-factor, the ρ_{sky} and the nadir and azimuthal angles for measurement. Consequences of these choices were analysed and discussed; it should however be noted that the scatter to backscatter ratio B was optimised for each sample station prior to inversion, largely neutralising the effects of errors in Q and ρ_{sky}.

In chapter 7 the model and its parametrisation were selected and I performed a sensitivity analysis to check whether the model was robust enough to cope with small errors in the AOP and SIOP inputs that are commonly present in measured data. I selected the following types of potential errors to be examined:

1. Errors in scaling factors (introduced by e.g. Q, g, $\bar{\mu}_d$ and $\bar{\mu}_u$)
2. Offset errors in the spectrum (introduced by e.g. L_{sky})
3. Spectral errors that increase towards the blue wavelength region (introduced by e.g. ρ_{sky})
4. Spectral errors caused by not knowing the exact spectral shape of some parameters (including the a^*_{ph} and a^*_{tr})
5. Errors in the reference SIOP set

The sensitivity analysis was performed using a simulated dataset. Simulated TCHL, TSM and CDOM concentrations (based on the distribution characteristics found in my measured data) and the measured median SIOP dataset of this research were used to generate a total of 1,000 subsurface irradiance reflectance spectra (based on the GW-model).

When no error is implemented, all three inversion methods are capable of (near) perfect retrieval of TCHL, TSM and CDOM concentrations for both MIM and LM, indicating that the parameterisation of the GW-model was correct for my research. When all spectral errors are combined, the R^2 values between the modelled and simulated concentrations generally decrease, especially for CDOM (from 0.99 to 0.75), but this performance is still acceptable. The LM method, unsurprisingly, scored slightly better agreements than MIM in this case. I further found that the GW-model was most sensitive to errors in the SIOP reference set used. This finding backed my initial goal of improving CDOM retrieval by improving CDOM reference measurements.

11.1.3 Part C: Improving CDOM retrieval accuracy analyses

After having determined the performance of the GW-model and its parameterisation I could start running the model fed with actually measured data testing the first proposed CDOM retrieval accuracy improvement by using state-of-art algorithms (chapter 8). My measured data however needed to be quality controlled first, as only sample stations of sufficient quality can be accurately inverted. The quality control procedure, always performed but often omitted in publications, consisted in this research of four checks: comparison with literature values, comparison of optimised B values, comparison of normalized χ^2 differences between measured and forward modelled $R(0-)$ spectra and the occurrence of masking TCHL concentrations. Only sample stations that passed all checks were selected for inversion (24 out of 52 stations for my research, an average score I have learned trough personal communications).

Two rounds of inversions were carried out. In the first round the per-sample SIOP sets were used as references, in the second round a constructed median SIOP was used for all stations. As a consequence of using the median SIOP set, the accuracy of TSM retrieval decreased significantly (0.9 to 0.5), as scaling problems due to errors in measured spectra are not fully compensated for. The accuracies for TCHL and CDOM decreased only slightly (10%). The LM method yielded slightly better results. For Dutch inland waters the use of a single median SIOP set has apparently only a dramatic effect on the TSM retrieval accuracy. As this study focusess on CDOM it was decided to use the median SIOP set, determining the CDOM retrieval potential in the least favourable condition, as perfectly matching SIOPs are generally not available for inversion, leaving at best regional or water type based lumped SIOP sets.

The second proposed CDOM retrieval accuracy improvement involved the use of better CDOM reference measurements. This was tested by me in chapter 9 by using a Point-Source Integrating-Cavity Absorption Meter (PSICAM), which has 2 important advantages over using a standard spectrometer with a cuvette:

1. There is no loss of light due to scattering effects in the PSICAM, so it measures the true absorption.
2. The average path lenght of the PSICAM is much higher (in the case of this research about 3 m) than in a standard 10 cm cuvette, allowing for accurate measurements of very low concentrations.

Before the PSICAM available for this research could be used, I developed a successful calibration method through the use of three independent dilution series of Aldrich humic acid standard in the absorption range around 1 m^{-1}. The absorption spectra of the dilution series were measured in a bench spectrometer with a 10 cm cuvette, and because there were three independent series, the calculation of an accurate concentration-absorption relation was possible. With this concentration-absorption relation reference absorptions needed for the PSICAM calibration could be derived. This sound approach, which is common in chemistry, has not been applied at other published PSICAM calibrations to date. The best cavity reflectivity of the PSICAM, which best approached the concentration-absorption relation, was obtained by applying the transmittance ratio calibration method. After calibration, I found that the absorption measurements of the dilution series made with the PSICAM and a bench spectrometer are within 1% of each other (over the absorption range 0.1 – 2 m^{-1})

The calibration experiment brought to light one limitation of the PSICAM: The accuracy of absorption measurements with the PSICAM rapidly declines when the absorption coefficient of the sample exceeds 3 m^{-1}, due to the size of the cavity and the cavity reflectivity. As Kirk (Kirk 1995) already suggested, different cavities dependent on the absorption range of the water type of interest can be used. Another possibility is the dilution of samples prior to measurement in the PSICAM, which was applied in this research.

In a subsequent PSICAM case study I showed that absorption measurements in a cuvette are likely to be affected with scattering effects when a 0.7 µm filter is used, as CDOM absorption coefficients at 440 nm values between the PSICAM and cuvette differ significantly. After filtration over a 0.2 µm filter there is no significant difference in C_{CDOM} between both methods. The difference of PSICAM absorption values between the two filtration steps is also significant. Therefore, the fraction between 0.7 and 0.2 µm does significantly contribute to the absorption and scattering of a sample and should not be discarded in my opinion. This finding is in contrast with the SEAWiFS and MERIS sampling protocols and the general opinion in the water remote sensing community.

My final conclusion is that the theoretical advantages of a PSICAM over a bench spectrometer (absorption measurement not affected by scattering and capable of measuring lower concentrations due to a longer path length) is supported by actual measurements performed in this study. By using a PSICAM more accurate CDOM absorption spectra can thus be measured, improving the SIOP that are required for optical modelling.

When validating retrieved CDOM concentrations after inversions of the optical model with PSICAM reference absorption measurements in this research rather than cuvette references, the structural underestimation of CDOM was reduced by 10 – 15%, while the correlations increased by 10 – 20 %. This is a significant finding indicating that PSICAM CDOM absorptions are more accurate than cuvette CDOM absorptions.

The last of the three proposed CDOM retrieval accuracy improvements is discussed in chapter 10: the decomposition of CDOM into HA and FA. First I selected the most appropriate exponential HA and FA fit model, based on the CDOM fit models of Carder *et al.* (Carder, Steward, Harvey, and Ortner 1989) and Stedmon *et al.* (Stedmon, Markager, and Kaas 2000):

$$a_{CDOM}(\lambda) = Offset + a_{HA}\exp^{(S_{HA}(\lambda_0-\lambda))} + a_{FA}\exp^{(S_{FA}(\lambda_0-\lambda))} \qquad 11.1$$

Next, two CDOM decomposition methods were tested in this research: linear and non-linear regression techniques. Linear regression requires the use of fixed slope parameters, called end-members. The end-members should be chosen with great care as spectral characteristics of humic and fulvic acids may vary in time and space. A number of suitable end-member pairs were proposed. Non-linear regression techniques allow the slope parameters to be modelled as well, but a unique solution was not be reached with this type of modelling and it was further discarded

A CDOM decomposition case study showed that the CDOM absorption spectrum modelling $Offset$ parameter is significantly reduced (by 50%). It was also found that by using a linear two-component exponential model and well-chosen end-members the goodness of fit between the measured and modelled CDOM absorption spectrum does improve, on average with some 7% over the wavelength range between 400 and 700 nm. This provides evidence that the two-component CDOM absorption model is valid.

An inversion of the optical model was performed in this research using the normalised CDOM absorption spectrum in the SIOP set modelled with the two-component model. The same 24 selected and quality controlled sample locations as in chapter 8 and the same median SIOP set, with the exception of the normalised CDOM absorption spectrum that was remodelled using the two-component approach were used. The observed differences in correlation coefficients were very small, but the slope parameter may improve by some 10% using LM methods. Due to the outlier stations and the very small changes it could, however, not be established whether the two-component model leads to CDOM retrieval accuracy improvements. An additional study, including a larger dataset, is advised to establish the effect of two-component CDOM modelling.

11.2 Recommendations

11.2.1 Recommendations for optical model development

As demonstrated in this research, the accuracy of retrieved parameters is primarily depending on the qaulity and suitability of the reference SIOP set(s) used. Applying complex true analytical optical models will not generate better results when the input data still consists of unsuitable SIOP references. A novel approach here is the use of lookup tables with SIOPs as proposed by e.g. Mobley (Mobley 1999f). The true analyticl model HYDROLIGHT can for instance be used to generate a simulated look-up table containing absorption and scattering values using series of input concentrations {pasterkamp2005}, leading to a whole range of possible SIOP reference sets from which a suitable one can be automatically selected while inverting. Such a development is encouraged.

11.2.2 Recommendations for Specific Inherent Optical Property measurements

Point-Source Integrating-Cavity Absorption Meter measurements

In chapter 9 it was shown that CDOM absorption measurements made using a cuvette system are affected by scattering effects, while those made in a PSICAM are not. It is therefore recommended to use a PSICAM for CDOM absorption spectrum measurements, at least for inland and coastal water samples.

Further testing is recommended to investigate the true scattering independency of the PSICAM absorption measurements by using a dilution series with fixed absorption and increasing scattering coefficients. This could for instance be achieved by using opaque scattering particles such as microscopic sized glass pearls. This way it can be determined if the PSICAM principle still holds even at extreme scattering conditions.

The calibration of a PSICAM for CDOM absorption measurement purposes should be performed using a dilution series of laboratory grade humic substances (such as the Aldrich Humic acid standard used in chapter 9). Each measurement in dilution series measurement should be performed in triplicate, and a total of three independent dilution series should be sampled. With these measurements, a concentration-absorption relationship can be established that forms the basis of the calibration. The PSICAM calibration technique based on the transmittance ratio between two measurements of different solutions gives the best results.

It was found that the CSIRO built PSICAM available for this research could not accurately measure absorptions exceeding 3.0 m^{-1} (at 440 nm) because the number of collisions with the cavity wall was then reduced to a level that the PSICAM starts to operate as a normal cuvette. For higher concentrations smaller cavities should be used or the sample has to be diluted (the latter was done in this research). An investigation into the relation between cavity size and operating range of the PSICAM is however recommended.

On filters used for SIOP measurements

In the PSICAM chapter (9) it was shown that CDOM measurements in a cuvette system require filtrate that has passed through 0.22 µm filters rather than 0.7 µm filters in order to avoid scattering effects. However the use of 0.22 µm filters to separate the dissolved component and the 0.7 µm filters to retain the phytoplankton and tripton introduces a gap in the SIOP measurements. It has been demonstrated in this research that the fraction between 0.22 and 0.7 µm contributes significantly to the total absorption. It is therefore necessary to include this fraction in SIOP measurements, contrary to current common practice in water remote sensing (Mueller and Austin 1992;Doerffer 2002b;Tilstone, Moore, Sørensen, Doerffer, Pasterkamp, and Jørgensen 2002).

The current measurement protocols should therefore be adjusted. This can be done in two ways:

1. Strict use of the treshold between suspended and dissolved matter by filtration of all SIOPs over over 0.22 μm filters.The filtration of suspended matter over 0.22 μm filters however is very cumbersome in turbid inland waters, as the filters will clog and rupture constantly.
2. Use e.g. a PSICAM system to measure true absorption and two filtration steps (0.22 and 0.7 μm). The absorption after the 0.22 μm filtration is then regarded as the CDOM absorption. The difference between the absorption after the 0.7 and after the 0.22 μm filtration step is then an extra seston absorption term. As this option has no operational drawbacks it is recommended at this stage.

Measuring the humic and fulvic acids instead of CDOM

The concentration of CDOM can thus far only be determined optically as it is impossible to separate the optically active fraction of DOC from the colourless fraction. The relationship between DOC and the optically derived CDOM concentration varies, most likely due to differences in the CDOM composition. The investigation of another approach however is recommended. The actual concentrations of the two main groups that make up CDOM, the humic and fulvic acids, can be measured with relative ease (with the proper equipment). It would be interesting to investigate the relationship between the combined humic and fulvic acid concentrations and the optically derived CDOM concentration. Then, instead of a normalised CDOM absorption a true specific CDOM absorption could be used in the SIOP dataset. Besides this, agreement should be sought over the best subdivision and naming of the two groups of humic substances, as the names of humic and fulvic acids are found obsolete and confusing by many, but no alternatives are presently at hand.

11.2.3 Recommendations for Apparent Optical Property measurements

The $R(0-)$ spectrum is calculated from 4 separate optical measurements: the total water leaving radiance L_{water}, the part of L_{water} that originates from reflected sky radiance at the water surface L_{sky}, the total downwelling radiance L_{rs} and the diffuse part of L_{rs}, L_{dif}. The simultaneous measurement of L_{water} and L_{sky} is intended in order to avoid errors due to instable light conditions. Field experiments with a dual channel spectrometer however revealed intercalibration problems between the two sensors. Recent experiences with three simultaneous operating autonomous sensors (a TRIOS system) show that, in principle, very reliable subsurface reflectance measurements can be done in this way (pers. comm. M. Wernand from NIOZ). The (inter-) calibration of the sensors should be done with care, though.

It is recommended that for future irradiance measurements the $R(0-)$ is instantly calculated from the individual measurements and tested for severe anomalies. At a large number of sample locations erroneous $R(0-)$ spectra were recorded, due to operational matters (see section 8.3.1 on the 'smile'-effect), instable light conditions, the occurrence of water plants, the occurrence of bottom sight and human error. With the current instrument readout and calculation software the

$R(0-)$ spectrum can be viewed after about 15 minutes, which is too long to wait for per sample location. It should be possible (with relatively small effort) to optimise the software and have the $R(0-)$ spectrum in Near Real Time, incorporating flags signalling if the calculated $R(0-)$ spectrum is valid or not. In that case it would be instantly clear whether an AOP measurement was successful or not, optimising valuable field measurement opportunities.

11.3 Outlook to the future

The reader should note that this section was completed considerable time after the other chapters in this dissertation and therefore may contain more recent literature, new insights and a number of recent comments that are not included in the other chapters.

11.3.1 Retrieving CDOM from remote sensing images

In this dissertation it has been demonstrated that accurate CDOM concentration (and composition) retrieval from remote sensing is possible (after improvements of the SIOP reference measurements), when applied to individually measured hyperspectral $R(0-)$ data obtained just above the water surface. The same algorithms can be applied to a remote sensing *image*, resulting in a map of water quality parameters. From marketing researches it has been found that water managers are very interested in such spatial information.

The acquisition of a suitable remote sensing image however poses a number of challenges, especially for successful retrieval of CDOM. The experience of this research has shown that airborne platforms can be suitable for water quality remote sensing, but only with extensive infrastructure and logistics. Because of the Dutch weather conditions (often cloudy), airspace restrictions and limited available standby time, only a few suitable images can be acquired per year. These images are very costly, yet their availability and quality cannot be assured, severely limiting the operational capability of airborne water quality monitoring solutions. The classical approach to airborne remote sensing using instruments such as e.g. the CASI scanner discussed in this dissertation are therefore not considered here. Novel approaches such as UAVs, Ultralights and all weather capability are not yet mature enough but should be considered in the future. Spaceborne data are relatively cheaper and much more frequently available. Images taken with satellites however often lack the spatial resolution required for water quality assessment of most Dutch inland waters.

Although not a goal of this study, enough insight has been gained during this research to contribute to the ongoing discussion on the requirements for accurate CDOM concentration retrieval (of turbid inland waters). The following requirements have been identified by the author (in order of importance):

1. Sufficient spectral range and resolution of radiance data
2. Sufficient spatial resolution
3. Successful atmospheric correction (especially for the blue bands)
4. Suitable SIOP reference set
5. PSICAM or otherwise true absorption CDOM reference measurements
6. No masking of CDOM by TCHL

In this section the discussion is limited to the requirements posed on the sensor and the atmospheric correction (numbers 1 – 3) as the other requirements are already discussed elsewhere.

Sufficient spectral range and resolution of radiance data

As already shown in the introductory chapter (see figure 1.3), the individual effects of the water quality parameters TCHL, TSM and CDOM on the subsurface irradiance reflectance spectrum can be demonstrated by performing model simulations with Bio-Opti (a tool developed by E. Hoogenboom at the IVM, see e.g. Hoogenboom, Dekker, and De Haan 1998). These individual effects form the basis of a sensor configuration in terms of spectral range and resolution. It should be noted that the absorption spectra of different species of phytoplankton vary with respect to the amplitude of the spectra but very little in the position of the absorption peaks (440 and 676 nm) because of the usually dominating presence of the Chlorophyll-*a* pigment, see e.g. Briceaud (1995). The shapes of the absorption and scattering spectra of CDOM and TSM of varying compositions are also comparable for different types of organic matter and sediments, thus the effects of the water quality parameters in the simulations shown above on the shape of the reflectance spectrum will be rather similar when other SIOPs are used. Although TSM scattering may have different spectral tilts and there may be other coloured substances in the water suach as hevay metals, this is a valid starting point in general. The recommendations posed in this section should however be considered within the framework of the water types, optical model and parameterisation encountered in this research and may not be directly applicable to other cases such as coastal or tropical inland waters. For convenience figure 1.3 is repeated below as figure 11.1.

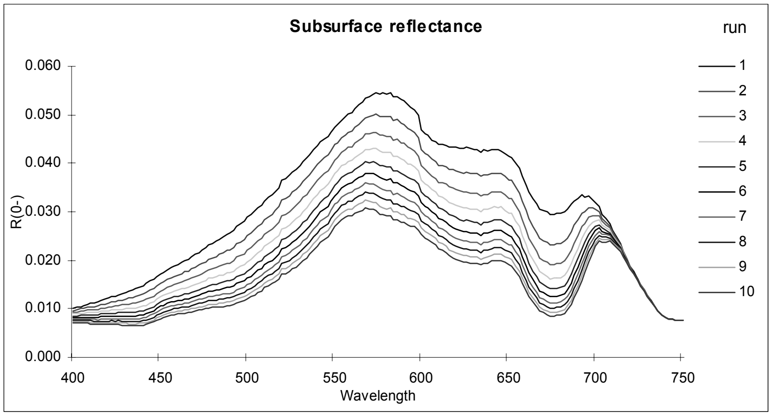

A

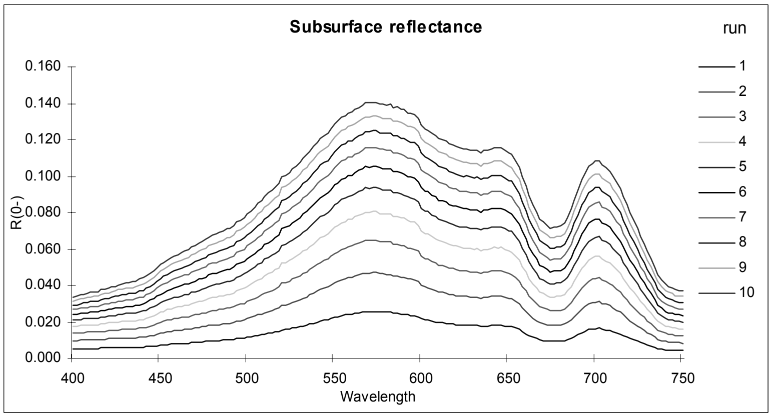

B

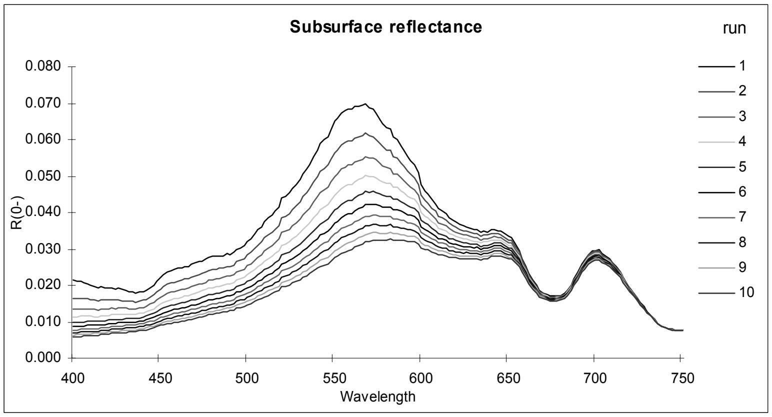

C

Figure 11.1 Simulated subsurface reflectance showing the effect of increasing concentrations (using Bio-Opti): A) increasing TCHL (10 – 100 µg l^{-1}) at fixed TSM (9 mg l^{-1}) and CDOM (2,4 m^{-1}) concentrations (top line is series 1) B) increasing TSM (5 – 50 mg l^{-1}) at fixed TCHL (40 µg l^{-1}) and CDOM (2,4 m^{-1}) concentrations (top line is series 10) and C) increasing CDOM (0.5 – 4 m^{-1}) at fixed TSM (9 mg l^{-1}) and TCHL (40 µg l^{-1}) concentrations (top line is series 1)

Ideally the sensor would be hyperspectral, e.g. similar to the PR650 field spectroradiometer used in this research or even with smaller bandwiths. The advantages of recording the complete spectrum in a continuous series of (not too) narrow spectral bands (between 2 and 5 nm wide) are for instance robustness to measurement noise and the possibility of using the sensor in the future for determining other or newly developed parameters such as e.g. the concentration of blue algae, using spectral information around 624 nm. Such spaceborne hyperspectral imaging instruments are however not yet operationally available. On the other hand, hyperspectral information is often only highly redundant, providing little extra information. This leaves the author to consider sensors with a limited number of well-chosen bands.

In the green wavelength region (500 – 600 nm) CDOM and TCHL have the same effect on the $R(0-)$ spectrum: an increase in the concentration leads to decrease in $R(0-)$. The absorption features of CDOM and TCHL fortunately differ in the red (600 - 700 nm) and blue (400 – 500 nm) regions, enabling spectral discrimination between CDOM and TCHL. It should however be noted that high concentrations of either TCHL or CDOM will mask relatively low concentrations of the other. This masking effect is not yet studied in detail, as i.e. very high concentrations of chlorophyll did not always inhibit successful CDOM retrieval in this research, and it is therefore recommended for further investigation. Perhaps the amount of seston backscattering plays a role here, as higher scattering results in a stronger $R(0-)$ signal.

Another observation by the author which was not elaborated on in this dissertation was that by fixing the TCHL and or TSM concentrations to the *in situ* measured concentrations did not result in more accurate CDOM concentrations after inversion while using the median SIOP set. A simple explanation can be given for this result: the specific phytoplankton and tripton absorptions in median SIOP set differ from the *in situ* SIOPs, and because the concentrations are fixed, this difference is accounted for in the only remaining free parameter, CDOM concentration. This observation backs the earlier made deduction that the simultaneous retrieval of TCHL, TSM and CDOM is preferred.

From experience with the inversions performed in this research, the inclusion of information from the blue wavelengths does improve the CDOM retrieval accuracy. The inclusion of blue bands however also introduces errors and noise as a result of low signal-to-noise ratios in these shorter wavelengths due to blue sensor limitations (should be better now) and artefacts and effects still present after atmospheric correction. Prior to the inclusion of spectral information in the blue wavelength region a careful consideration should thus be made whether the information is valuable or not. This trade-off between adding information or noise needs to be made for each individual image or even for each individual pixel in an image.

Instead of selecting available and suitable blue bands individually, another approach may be to combine the available blue bands into a single, broad blue band. This way the signal-to-noise ratio is improved and local effects of the atmospheric correction are reduced. Combining the available bands in the green wavelength region into a single broad green band will also improve robustness.

As opposed to the blue and green bands, two very narrow bands are required in the red wavelength region: one around 676 nm (absorption peak of TCHL) and one around 706 nm were the spectrum is dominated by TSM.

Again, this recommended band setting is made specifically for algae-rich turbid inland waters. In other cases, such as Scandinavian lakes where CDOM virtually dominates the reflectance spectrum (Koponen 2006) or Australia's subtropical Moreton Bay (Dekker, Brando, Oubelkheir, Wettle, Clementson, Peters, and van der Woerd 2005) much simpler band settings suffice. Dekker *et al.* were able to map CDOM and TSM in an almost phytoplankton free environment using the three broad bands in the visible light region of the Landsat ETM 7 satellite sensor. Discrimination between CDOM and TSM was possible because 'the tripton absorption is always associated with a (back)scattering' (Dekker, Brando, Oubelkheir, Wettle, Clementson, Peters, and Woerd 2005). Fixing the chlorophyll concentration however may introduce errors in the CDOM retrieval when the actual TCHL concentrations vary.

A study by Blondeau-Patissier et al. in Northern European coastal waters showed that high concentrations of TSM and CDOM (common in turbid inland waters) cause a decoupling of the phytoplankton absorption and the underwater light field, resulting in poor accuracy of standard MODIS and SeaWiFS TCHL, TSM and CDOM algorithms (Blondeau-Patissier, Tilstone, Martinez-Vicente, and Moore 2004).

This brings the discussion from the spectral range to the required spectral resolution. The PR650 had a band width of 8 nm. In order to discriminate between the 676 nm reflectance valley and the 706 nm peak, the band width of a suitable sensor should not exceed 10 – 15 nm.

The required signal-to-noise ratios for the proposed bands for the specific purpose of CDOM retrieval could not be found, therefore in the future a specific sensitivity analysis should de performed to determine the required SNR for CDOM retrieval, perhaps partly based on the dataset collected for this research. Attention should be given to the transport of the above water observed signal through the atmosphere using realistic atmospheric model simulation parameterisations. A very preliminary analysis is however discussed below.

At Chlorophyll-*a* (TCHL) concentrations of about 40 µg l^{-1} (and TSM 9 mg l^{-1}) the difference in $R(0-)$ is still some 0.2% between a CDOM concentration of 3.7 and 4 m^{-1} (see figure 1.3) in the green wavelength area. When the chlorophyll concentration is fixed at 85 µg l^{-1}, this $R(0-)$ difference decreases to 0.1% (these are absolute reflectance percentages).

To get a better understanding of the sensitivities of $R(0-)$ to changes in the CDOM concentration (at various TCHL concentrations) an analysis was performed determining the sensitivity of $R(0-)$ to small increments of TCHL and (separately) to CDOM using the aforementioned Bio-Opti model. This analysis is performed in very roughly the same way as the study by Hoogenboom *et al.* (Hoogenboom, Dekker, and De Haan 1998), where the sensitivity of the MERIS instrument was determined by bio-optical modelling including atmospheric effects. The input parameters for the model were the median concentrations of 40 µg l^{-1}, 9 mg l^{-1} and 2.4 m^{-1}, first varying the TCHL 10% between 36 – 44 µg l^{-1} and for the second run varying the CDOM 10% between 2.2 and 2.6 m^{-1}. The results are given in figure 11.2 below.

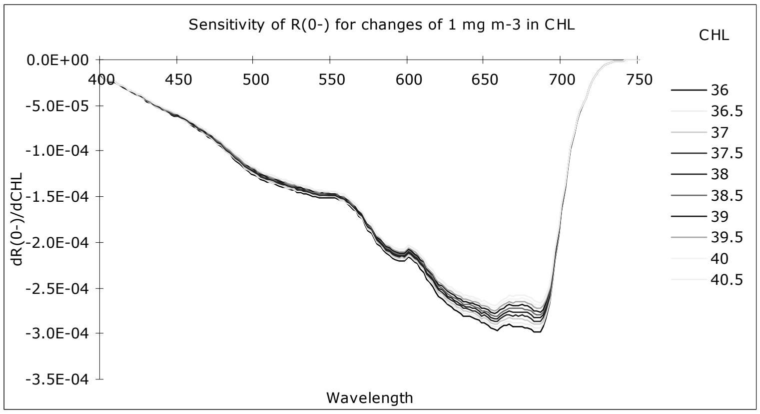

A

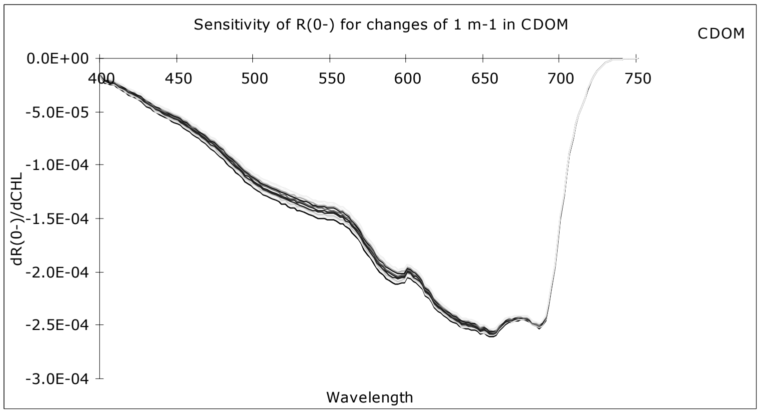

B

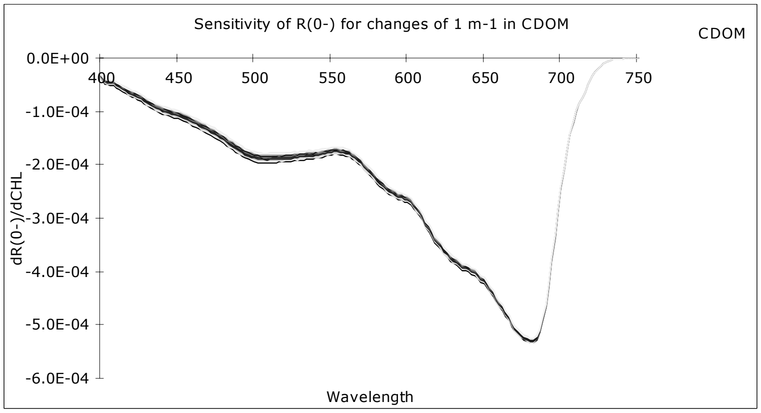

C

Figure 11.2 Simulated subsurface reflectance differences showing the effect a 10% increase of concentrations (using Bio-Opti): A) increasing TCHL (36 – 44 μg l^{-1}) at fixed TSM (9 mg l^{-1}) and CDOM (2,4 m^{-1}) concentrations (bottom line is series 1) B) increasing CDOM (2.2 – 2.6 m^{-1}) at fixed TSM (9 mg l^{-1}) and TCHL (40 μg l^{-1}) concentrations (bottom line is series 1) C) increasing CDOM (1.0 – 1.5 m^{-1}) at fixed TSM (22 mg l^{-1}) and TCHL (30 μg l^{-1}) concentrations (bottom line is series 1)

The difference in $R(0-)$ TCHL as a result of changes in shown in figure 11.2 are in the region of 0.003% (at around 650 nm), while those of CDOM are more in the order of 0.002% (at around 575 nm). Roughly speaking the sensitivity of $R(0-)$ to CDOM around its median value found in this research is thus 1.5 times less than to TCHL, meaning that a sensor that can accurately retrieve CDOM should have a SNR that is 1.5 times higher than currently required for TCHL mapping.

Another insight gained from the Bio-opti simulations shown in figure 11.2 (B and C) is that at high CDOM and low TSM concentrations the CDOM information (difference in $R(0-)$) can be found primarily in the green wavelength region, while at lower CDOM and higher TSM (scattering) levels, the CDOM information is mostly present in the blue wavelength region. In other words, the $R(0-)$ spectrum in blue wavelength region may get saturated at high CDOM concentrations, leaving CDOM retrieval up to information present in the green wavelength region. It is recommended to further investigate this CDOM saturation effect.

Sufficient spatial resolution

In order to successfully monitor Dutch inland waters that are typically only several hundredths of meters across, the spatial resolution should be around 400 m^2. Most multispectral spaceborne sensors however have spatial resolutions that are 1 to 2 orders of magnitude larger (1 km^2 to 900 m^2), so only the largest inland waters, e.g. lake IJsselmeer, can be monitored at present. A problem often associated with spatial resolution if the adjacency effect, where atmospheric path radiance from land pixels adjacent to the water cause erroneously high reflectance above the water pixels, especially in the Red-NIR wavelength regions. This adjacency effect can still be present in water pixels up to 1 km or more away from the shore (see e.g. Santer and Schmechting 2000).

Successful atmospheric correction (especially for the blue bands)

Because information in the blue wavelength region is required for discrimination between TCHL and CDOM absorption, a very good atmospheric correction is required. Huot *et al.* have recently discussed the atmospheric correction of MERIS (Huot, Belanger, Bourg, Brockmann, Kramer, and Delwart 2005). A problem regarding CDOM and atmospheric corrections is that the spectral shape of the Angström coefficient (used for correcting scattering in the atmosphere) and the aerosol absorption are similar to the absorption spectrum of CDOM: an exponentially declining function towards the longer wavelengths. The classical method of propagating the atmospheric signal measured in the infrared region to the blue wavelength region is not optimal for waters which are absorbing in the blue (e.g. by CDOM) (Huot, Belanger, Bourg, Brockmann, Kramer, and Delwart 2005). Huot *et al.* also propose to use non-absorbing aerosols for the atmospheric correction in these waters. They conclude by stating that the atmospheric correction of MERIS in coastal waters needs to be improved, for instance by neural networks trained on top-of-atmosphere reflectances.

To enhance the atmospheric correction, it is recommend to set up small networks of autonomous registering sensors at optimised locations observing the $R(0-)$ and the atmospheric transparency in relevant wavelenths bands. This will provide a much better solution to atmiospheric correction than using overall averaged atmosperic optical properties.

Now the sensor requirements for accurate CDOM retrieval have been drawn up, a quick scan can be made among existing satellites for suitable operational instruments. This yields the following three instruments: MERIS, MODIS and CHRIS/PROBA.

The ESA MEdium Resolution Imaging Spectrometer Instrument (MERIS) instrument was already discussed in §7.4.4 when resampling the measured spectra of this research. It is one of the most important satellite instruments for remote sensing of water quality at this moment. The spatial resolution of MERIS is 1 km^2 (reduced resolution) or 0.09 km^2 (full resolution, not operationally available until 2007).

The NASA MODIS (Moderate Resolution Imaging Spectroradiometer) satellites were launched in 1999 and 2002. The spatial resolution of MODIS for Ocean Colour products is 1 km^2.

Another interesting ESA instrument is the CHRIS/PROBA (Compact High Resolution Imaging Spectrometer / Project for On-board Autonomy) satellite, launched in October 2001. The CHRIS instrument has an optimized mode for water applications, which has 18 bands and a full spatial resolution of 400 m^2.

In table 11.1 the band settings of the MERIS, MODIS and CHRIS/PROBA instruments are given.

Table 11.1: The band settings of MERIS (http://earth.esa.int/pub/ESA_DOC/ENVISAT/MERIS/VT-P017-DOC-005-E-01-00_meris.faq.1_0.pdf), MODIS (mode: Ocean Colour, http://modis.gsfc.nasa.gov/about/specifications.php) and CHRIS/PROBA (mode 2: water, http://www.tisda.org/fordate/chrisproba.html)

Band	MERIS Centre wavelength (nm) [Band width (nm)]	MODIS Centre wavelength (nm) [Band width (nm)]	CHRIS Centre wavelength (nm) [Band width (nm)]
1	412 [10]	412 [15]	410 [10]
2	442 [10]	443 [10]	441 [12]
3	490 [10]	488 [10]	490 [12]
4	510 [10]	531 [10]	509 [13]
5	559 [10]	551 [10]	529 [11]
6	619 [10]	667 [10]	560 [14]
7	664 [10]	678 [10]	572 [11]
8	681 [7.5]	748 [10]	589 [16]
9	708 [10]	870 [15]	620 [13]
10	753 [7.5]	-	649 [15]
11	760 [3.8]	-	667 [11]

12	779 [15]	-	678 [11]
13	865 [20]	-	686 [6]
14	885 [10]	-	704 [18]
15	900 [10]	-	752 [14]
16	-	-	777 [22]
17	-	-	867 [27]
18	-	-	1012 [43]

Because only a handful CDOM validation studies have been performed in Case II (coastal and inland) waters the discussion below on the suitability of the mentioned instruments for CDOM retrieval remains largely theoretical. Examples of validated CDOM retrieval studies in coastal waters are Darecki & Stramsky (Darecki, Weeks, Sagan, Kowalczuk, and Kaczmarek 2003), finding a poor correlation and severe underestimation (n=8) between MODIS retrieved CDOM concentrations and *in situ* data, and Sørensen *et al.* (Sorensen, Hokedal, Aas, Doerffer, and Dahl 2003) who found that the CDOM concentration in the Norwegian Skaggerag region was underestimated 10 times in the MERIS standard CDOM product (probably as a result of poor atmospheric correction in the blue. A similar study was performed by Doerffer et al. (Doerffer 2002b), also reporting a CDOM underestimation in the German Bight using MERIS data. It should be noted that both Sørensen and Doerrfer *cs.* lump together the CDOM and tripton absorption as a single term YSBPA. In this research such an approach was not followed as the tripton absorption is not negligible and the Gordon-Walker model used couples the tripton absorption to the seston backscattering.

When comparing the characteristics of MERIS, MODIS and CHRIS/PROBA the absence of the important band around 706 nm in the MODIS instrument is noticed. This hampers the discrimination between TCHL and TSM in highly turbid waters, making the instrument less suitable for retrieving water quality by inverting a semi-analytical optical model as performed in this research. Both the MERIS and MODIS instrument lack the spatial resolution required for monitoring Dutch inland waters.

The MERIS and MODIS instruments already offer a CDOM product ('MER_RR__2P yellow substance' and 'MOD24' respectively), which are only valid for Case I oceanic waters. As reported by Huot *et al.*, the atmospheric correction of the MERIS instrument needs improvement (Huot, Belanger, Bourg, Brockmann, Kramer, and Delwart 2005), implying that CDOM retrieval may not yet be feasible with MERIS.

Ignoring any potential calibration and likely atmospheric correction problems or operational constraints that may be present, the CHRIS/PROBA instrument appears to be suitable to retrieve chlorophyll, suspended matter and CDOM from most inland waters. The disadvantage of CHRIS/PROBA is that is no operational atmospheric correction tool available. It would be a worthwhile future experiment retrieving CDOM concentrations from CHRIS/PROBA imagery, applying an atmospheric correction based on locally measured atmospheric transparencies.

As both the MERIS and the CHRIS/PROBA instrument have already outlived their expected lifespan, it is strongly recommended that they will be superseded in the near future by instruments with similar characteristics such as e.g. the ESA SENTINEL 3 mission (succeeding MERIS).

11.3.2 PSICAM total absorption

The design of the PSICAM allows for absorption measurements that are not influenced by scattering effects, a feature that was proven in chapter 9 with actual CDOM absorption measurements. Not only does this characteristic of the PSICAM lead to more accurate measurements, it also allows for the measurement of the total absorption spectrum of a (unfiltered) water sample. The total absorption is used to calculate the scattering of a water sample in the SIOP measurements methodology used for this research. Currently the total absorption is determined by adding up the separately measured seston and CDOM absorptions. Recently a promising start was made with total absorption measurements by Roettgers *et al.* (2006)

In theory it would also be possible to determine the concentrations of TCHL, TSM and CDOM from the total, the filtered and/or the bleached absorption spectrum instead of a reflectance spectrum. A significant advantage when using the PSICAM for *in situ* total absorption measurements is that there is no need for corrections regarding the light conditions, angular dependencies and air/water interface effects.

As the PSICAM used in this research was only calibrated for the wavelength range 400 – 600 nm, a re-calibration will be necessary to obtain a cavity reflectivity up to 700 or 750 nm because the total absorption in this region is important.

11.3.3 Water quality information provided by humic and fulvic acid absorption data

In chapter 2 it was already explained that organic matter plays an important role in the aquatic ecosystem. The organic matter in the water system can either be of allochthonous or autochthonous origin. Information on the origin of organic matter can be useful for water managers, as it helps in their understanding of the water system. This information can for instance be used to identify ground water flows, to monitor the eutrophication process and to monitor sewage spills.

The fluorescence index (FI) by McKnight *et al.* is an example of a method to collect information on the origin of organic matter (McKnight, Boyer, Westerhof, Doran, Kulbe, and Andersen 2001). It is based on the ratio between the emission intensity at 450 nm to the emission intensity at 500 nm (obtained with an excitation at 370 nm) of isolated fulvic acids. The fluorescence index has a value of around 1.9 for microbially (or autochthonous) produced fulvic acids and a value of around 1.4 for terrestrial (or allochthonous) produced fulvic acids. Based on the same principles as the fluorescence index, a humic and fulvic acid absorption ratio index can be developed.

When the two-component exponential CDOM absorption spectrum fit model (see chapter 10) is build into the semi-analytical model, it is possible to retrieve the concentrations (and thus the ratio) of the humic and fulvic acids in a remote sensing image. A map of the origin of organic matter can subsequently be presented. If the humic and fulvic acid concentrations or true end-members cannot be determined, the slope S of the (single) exponential function that describes the CDOM absorption curve might be taken as an indicator for the origin of the humic substances present in a water sample. A low value for S indicates a primarily terrestrial origin of the dissolved organic matter. It is recommended to further investigate the possibility of creating dissolved organic matter origin maps.

12. References

Aas, E. 2003. Spectral Slope Of Yellow Substance: Problems Caused By Small Particles. Monaco, Ocean Optics XV. Ocean Optics XV.

Aas, E. 1987. Two-stream irradiance model for deep waters. Appl.Opt. 26: 2095-2101.

Aiken, G.R., D.M. McKnight, R.L. Wershaw, and P. MacCarthy. 1985. Humic substances In Soil, Sediment, and Water. John Wiley & Sons.

Aikenhead-Peterson, J.A., W.H. McDowell, and J.C. Neff 2002. Sources, Production and Regulation of Allochthonous DOM, In [ed.], S.Findlay Aquatic Ecosystems: Interactivity of Dissolved Organic Matter. Academic Press.

Albert, A. and C.D. Mobley 2003. An analytical model for subsurface irradiance and remote sensing reflectance in deep and shallow case-2 waters. Optics Express 11: 2873-2890.

Anonymus. 2000. Establishing a framework for Community action in the field of water policy. L 327/1.

Atkins, P.W. 1989. General Chemistry. Scientific Amerrican Books.

Atkinson, P.M. and A.R.L. Tatnall 1997. Neural Networks in Remote Sensing. Int.J.Remote Sensing 18: 699-799.

Austin, R.W. 1974. The remote sensing of spectral radiance from below the ocean surface. Academic Press.

Averett, R.C., J.A. Leenheer, D.M. McKnight, and K.A. Thorn. 2003. Humic Substances in the Suwannee River, Georgia: Interactions, Properties, and Proposed Structures. 2373. US Geological Survey.

Babin, M., D. Stramski, G.M. Ferrari, H. Claustre, A. Bricaud, G. Obolensky, and N. Hoepffner 2003. Variations in the light absorption coefficients of phytoplankton, nonalgal particles, and dissolved organic matter in coastal waters around Europe. Journal of Geophysical Research-Oceans 108: 3211-3231.

Baker, K.S. and R.C. Smith. 1990. Irradiance transmittance through the air/water interface. 1302, 556-565. SPIE. Ocean Optics X.

Baruah, P.J., K. Oki, and H. Nishimura. 2000. A Neural Network Model For Estimating Surface Chlorophyll And Sediment Content At The Lake Kasumi Gaura Of Japan. (Asian Conference on Remote Sensing). Asian Association on Remote Sensing.

Bergh, J.C.M.J. v.d., A. Barendregt, A. Gilbert, M. v.Herwijnen, P. v.Horssen, P. Kandelaars, C. Lorenz, and B. Rabeling. 1999. Integrated analysis of wetlands: the Dutch Vechtstreek case study. Final report of the case study as part of the ECOWET project. -, -128 pp. Contract No. ENV4-CT96-0273.

Bergh, O., K.Y. Borsheim, G. Bratbak, and M. Heldal 1989. High abundance of viruses found in aquatic environments. Nature 340: 467-468.

Berthon, J.-F. and G. Zibordi. 2000. In situ relationships between Q-factor and seawater optical properties in the Northern Adriatic Sea. Ocean Optics XV. Monaco. 16-10-2000.

Bertilsson, S. and J.B.Jr. Jones 2002. Supply of DOM to Aquatic Ecosystems: Autochthonous Sources, In [ed.], S.Findlay Aquatic Ecosystems: Interactivity of Dissolved Organic Matter. Academic Press.

Bjørnsen, G., R.Gimbel, and H.D. Spangenberg 1998. A concept for an integrative consideration of drinking water and wastewater-sewage management. Water science and technology 37: 333-342.

Blalock, H.M. 1985. Social Statistics, 6 ed. McGraw-Hill.

Blondeau-Patissier, D., G. Tilstone, V. Martinez-Vicente, and G.F. Moore 2004. Comparison of bio-physical marine products from SeaWiFS, MODIS and a bio-optical model with in situ measurements from Northern European waters. Journal of Optics A: Pure and Applied Optics 6: 875-889.

Boulton, A.J. and M.A. Brock. 1999. Australian Freshwater Ecology. Gleneagles Publishing.

Brando, V.E. 2003. Satellite hyperspectral remote sensing for estimating estuarine and coastal water quality. IEEE Transactions on Geoscience and Remote Sensing 41: 1378-1387.

Brando, V.E. and A.G. Dekker. 2002. The flourescence term on the observed 690-7100 peak in eutrophic turbid (inland) waters: myth or reality? Ocean Optics (XVI).

Brando, V.E., J.T.O. Kirk, P.J. Daniel, K. Oubelkheir, L. Clementson, and A.G.Dekker. 2004. Measured sensitivity of the PSICAM: effects of anisotrophic light source, fluorescence, temperature and salinity. Ocean Optics (XVII).

Breebaart, L., J. Ebert, and L. van Liere. 1989. Water Quality Research Loosdrecht Lakes: Basic data 1983-1988 (in Dutch). 1989. Nieuwersluis, The Netherlands., Limnological Institute. WOL-Report.

Bricaud, A., M. Babin, A. Morel, and H. Claustre 1995. Variability in the chlorophyll-specific absorption coefficients of natural phytoplankton: Analysis and parameterization. J.Geophys.Res. 100: 13321-13332.

Bricaud, A., A.-L. Bedhomme, and A. Morel 1988. Optical properties of diverse phytoplanktonic species: experimental results and theoretical interpretation. J.Plankton Res. 10: 851-873.

Bricaud, A., A. Morel, and L. Prieur 1981. Absorption by dissolved organic matter of the sea (yellow substance) in the UV and visible domains. Limnol.Oceanogr. 26: 43-53.

Bricaud, A. and D. Stramski 1990. Spectral absorption coefficients of living phytoplankton and nonalgal biogenous matter: A comparison between the Peru upwelling area and the Sargasso Sea. Limnol.Oceanogr. 35: 562-582.

Buckton, D., E. O'Mongain, and S. Danaher 1999. The use of Neural Networks for the estimation of oceanic constituents based on the MERIS instrument. Int.J.Remote Sensing 20: 1841-1851.

Buiteveld, H., J.H.M. Hakvoort, and M. Donze. 1994. Optical properties of pure water. XII, 174-183. Bellingham, Washington, USA, SPIE. Ocean Optics XII. 1994.

Bukata, R.P., J.H. Jerome, and J.E. Bruton 1988. Particulate concentrations in Lake St. Clair as recorded by a shipborne multispectral optical monitoring system. Remote Sens.Environ. 25: 201-299.

Bukata, R.P., J.H. Jerome, D.V. Pozdnyakov, and K.Y. Kondratyev. 1995. Optical Properties and Remote Sensing of Inland and Coastal Waters. CRC Press.

Burger-Wiersma, T. 1991. Prochlorothrix hollandica; a filamentous prokaryotic species containing chlorophylls a and b. Algological Studies 64: 555-558.

Burger-Wiersma, T., M. Veenhuis, H.J. Korthals, C.C.M. van de Wiel, and L.R. Mur 1986. A new prokaryote containing chlorophylls a and b. Letters to Nature 262-264.

Buscail, R., R. Pocklington, and C. Germain 1995. Seasonal variability of the organic matter in a sedimentary coastal environment: sources, degradation and accumulation (continental shelf of the Gulf of Lions - northwestern Mediterranean Sea). Continent.Shelf Res. 15: 843-869.

Carder, K.L., F.R. Chen, J.P. Cannizzaro, J.W. Campbell, and B.G. Mitchell. 2004. Performance of the MODIS semi-analytical ocean color algorithm for chlorophyll-a. Pergamon-Elsevier Science ltd.

Carder, K.L., R.G. Steward, G.R. Harvey, and P.B. Ortner 1989. Marine humic and fulvic acids: Their effects on remote sensing of ocean chlorophyll. Limnol.Oceanogr. 34: 68-81.

Chavez, F.P. 1995. On the chlorophyll-a retention properties of glass-fiber GF/F filters. Limnology and Oceanography 40: 428-433.

Chin, Y.P. 2002. Speciation of Hydrophobic Organic Compounds, In [ed.], S.Findlay Aquatic ecosystems: interactivity of dissolved organic matter. Academic Press.

CIW. 2001. Leidraad Monitoring. Commissie Integraal Waterbeheer.

Darecki, M. and D. Stramski 2004. An evaluation of MODIS and SeaWiFS bio-optical algorithms in the Baltic Sea. Remote Sens.Environ. 89: 326-350.

Darecki, M., A. Weeks, S. Sagan, P. Kowalczuk, and S. Kaczmarek 2003. Optical characteristics of two contrasting Case 2 waters and their influence on remote sensing algorithms. Continent.Shelf Res. 23: 237-250.

Davies, P.A. and J.A. Charlton 1987. The determination of the internal structure of an effluent plume using MSS data. Int.J.Remote Sensing 8: 75-83.

Davies-Colley, R.J. 1983. Optical properties and reflectance spectra of 3 shallow lakes obtained from a spectrophotometric study. New Zealand J.Mar.& Freshw.Res. 17: 445-459.

Davies-Colley, R.J. and W.N. Vant 1987. Absorption of light by yellow substance in freshwater lakes. Limnol.Oceanogr. 32: 416-425.

De Haan, H. 1986. De invloed van de metaalvormen op de groei van algen, met speciale aandacht voor ijzer. Vakbl.Biol. 65: 26-29.

De Haan, H., T. de Boer, H.A. Kramer, and J. Voerman 1982. Applicability of light absorbance as a measure of organic carbon in humic lake water. Water Resources Research 16: 1047-1050.

Dekker, A.G. 1993. Detection of optical water quality parameters for eutrophic waters by high resolution remote sensing. 1-240. Dissertation. Vrije Universiteit, Amsterdam, The Netherlands.

Dekker, A.G., V.E. Brando, J.M. Anstee, N. Pinnel, T. Kutser, H.J. Hoogenboom, S.W.M. Peters, R. Pasterkamp, R.J. Vos, C. Olbert, and T.J.M. Malthus 2001. Imaging Spectrometry of Water, p. 307-359. In [eds.], F.D. van der Meer and S.M. de Jong Imaging Spectrometry, Basic Principles and Prospective Applications. Kluwer Academic Publishers.

Dekker, A.G., V.E. Brando, P.J. Daniel, J.M. Anstee, and L. Clementson. 2002. PSICAM - FROM MYTH TO REALITY. Miami, Veridian. Seventh International Conference on Remote sensing for Marine and Coastal Environments.

Dekker, A.G., V.E. Brando, K. Oubelkheir, M. Wettle, L. Clementson, S.W.M.Peters, and H.v.d.Woerd. 2005. When Freshwater Meets Ocean Water: How Variable SIOPS Affect Remote Sensing Products of Estuaries, Bays and Coastal Seas. ONR-NASA. Ocean Optics XVII.

Dekker, A.G., H.J. Hoogenboom, L.M. Goddijn, and T.J.M. Malthus 1997. The relationship between inherent optical properties and reflectance spectra in turbid inland waters. Remote Sens.Reviews 15: 59-74.

Dekker, A.G., T.J.M. Malthus, and H.J. Hoogenboom. 1994. Quantitative determination of chlorophyll a, cyanophycocyanin, seston dry weight, secchi depth transparency and the vertical attenuation coefficient in eutrophic surface waters by airborne imaging spectrometry. I, 141-152. Strasbourg, France. First International Airborne Remote Sensing Conference and Exhibition: Applications Technology and Science; Plenary Session 6:Environment-Water and Atmospheric Applications. 1994.

Dekker, A.G., T.J.M. Malthus, S.W.M. Peters, and E. Seyhan. 1990. The Remote Sensing Loosdrecht Lakes Project. 90, 1-99. BCRS.

Dekker, A.G., J.P. Moen, E.J. Kootwijk, G. van Rossum, H.J. Hoogenboom, A.C. Belfroid, and T.H.L. Claassen. 1999. De kwaliteit van enkele Friese binnenwateren gemeten met vliegtuig-remote sensing (augustus 1997). NRSP-2 99-22, 1-101. Delft, The Netherlands, Netherlands Remote Sensing Board, Programme Bureau, Rijkswaterstaat Survey Department.

Dekker, A.G. and S.W.M. Peters 1993. The use of the Thematic Mapper for the analysis of eutrophic lakes: A case study in The Netherlands. Int.J.Remote Sensing 14: 799-822.

Dekker, A.G. and E. Seyhan 1988. The Remote Sensing Loosdrecht Lakes Project. Int.J.Remote Sensing 10: 1761-1773.

Dekker, A.G., R.J. Vos, and S.W.M. Peters 2001. Comparison of remote sensing data, model results and in situ data for total suspended matter (TSM) in the southern Frisian lakes. The Science of The Total Environment 268: 197-214.

Dekker, A.G., Z. Zamurovic-Nenad, H.J. Hoogenboom, and S.W.M. Peters 1996. Remote sensing, ecological water quality modelling and in situ measurements: a case study in shallow lakes. Hydrol.Sci.J. 41: 531-547.

Del Castillo, C.E. and P.G. Coble 2000. Seasonal variability of the colored dissolved organic matter during the 1994-95 NE and SW Monsoons in the Arabian Sea. Deep Sea Research Part II: Topical Studies in Oceanography 47: 1563-1579.

Doerffer, R. 2002a. Protocols for the Validation of MERIS Water Products. PO-TN-MEL-GS-0043, 1-42. Noordwijk, The Netherlands, ESA Publications devision.

Doxaran, D., J.M. Froidefond, S. Lavender, and P. Castaing 2002. Spectral signature of highly turbid waters; Application with SPOT data to quantify suspended particulate matter concentrations. Remote Sensing of Environment 81: 149-161.

Ferrari, G.M., M.D. Dowell, S. Grossi, and C. Targa 1996. Relationship between the optical properties of chromophoric dissolved organic matter and the total concentration of dissolved organic carbon in the southern Baltic Sea region. Marine Chemistry 55: 299-316.

Fogg, G.E. 1966. Algal cultures and phytoplankton ecology. University of Wisconsin Press.

Flaig, W. 1968. Uptake of organic substances from soil organic matter by plant and their influence on metabolism. Pontificiae Academiae Scientarum Scripta Varia, vol 32, P 1-48

Fry, E.S., G.W. Kattawar, and R.M. Pope 1992. Integrating Cavity Absorption Meter. Appl.Opt. 31: 2055-2065.

Gao, H. and R.G. Zepp 1998. Factors Influencing Photoreactions of Dissolved Organic Matter in a Coastal River of the Southeastern United States. Environ.Sci.Technol. 32: 2940-2946.

Gavis, J., R.R.L. Guillard, and B.L. Woodward 2004. Cupric ion activity and the growth of phytoplankton clones isolated from different marine environments. Journal of Marine Research 39: 315-333.

Gege, P. 2000. Gaussian model for yellow substance absorption spectra. SPIE Ocean Optics XV. 2000.

Gege, P. 1994. Gewässeranalyse mit passiver Fernerkundung: Ein Modell zur Interpretation optischer Spektralmessungen. 1 - 170. Köln. DLR Forschungsbericht 94-15.

Gilijamse, L.I. 1994. Absorptiecoefficienten van de fytoplankton en tripton in enkele Nederlandse meren. -53. Nieuwersluis, NIOO.

Gons, H.J. 1999. Optical teledetection of chlorophyll a in turbid inland waters. Environ.Sci.Technol. 33: 1127-1132.

Gons, H.J., M. Rijkeboer, and K.G. Ruddick 2002. A chlorophyll-retrieval algorithm for satellite imagery (Medium Resolution Imaging Spectrometer) of inland and coastal waters. J.Plankton Res. 24: 947-951.

Gordon, H.R., O.B. Brown, R. Evans, J. Brown, R.C. Smith, K.S. Baker, and D.K. Clark 1988. A semianalytical Radiance model of ocean colour. J.Geophys.Res. 93(D9): 10,909-10,924.

Gordon, H.R., O.B. Brown, and M.M. Jacobs 1975. Computed relationships between the inherent and apparent optical properties of a flat homogeneous ocean. Appl.Opt. 14: 417-427.

Gordon, H.R. and A. Morel. 1983. Remote assessment of ocean color for interpretation of satellite visible imagery: a review. Springer-Verlag.

Gordon, H.R., R.C. Smith, and J.R.V. Zaneveld. 1984. Introduction to ocean optics. 489. SPIE. Ocean Optics VII.

Green, S.A. and N.V. Blough 1994. Optical absorption and fluorescence of chromophoric dissolved organic matter in natural waters. Limnol.Oceanogr. 39: 1903-1916.

Gulati, R.D. and E. v.Donk 2002. Lakes in the Netherlands, their origin, eutrophication and restoration: state-of-the-art review. Hydrobiologia 478: 73-106.

Gulati, R.D., L. van Liere, and K. Siewertsen 1991. The Loosdrecht lake system: Man's role in its creation, perturbation and rehabilitation, p. 593-606. Ellis Horwood Ltd.

Hakvoort, J.H.M., H. de Haan, R.W.L. Jordans, R.J. Vos, S.W.M. Peters, and M. Rijkeboer. 2000. Towards airborne remote sensing of water quality in the Netherlands; validation and error analysis. Second EARSEL Workshop on Imaging Spectroscopy .

Hakvoort, J.H.M. 1994. Absorption of light by surface water. Thesis. Delft University Press.

Hansell, D.A. and C.A. Carlson. 2002. Biochemistry of Marine Dissolved Organic Matter. Elsivier Science, Academic Press.

Harvey, G.R., D.A. Boran, L.A. Chesal, and J.M. Tokar 1983. The Structure Of Marine Fulvic And Humic Acids. Marine Chemistry 12: 119-132.

Hayase, K. and H. Tsubota 1985. Sedimentary humic acid and fulvic acid as fluorescent organic materials. Geochimica et Cosmochimica Acta 49: 159-163.

Henderson, I.F. 1979. Henderson's Dictionary of Biological Terms, 9 ed. Longman Science & Technology.

Higler, B. 2000. Natuurlijke leefgemeenschappen van de Nederlandse binnenwateren - Deel 7, Laagveenwateren. EC-LNV AS-07. Wageningen, EC-LNV. Natuurlijke leefgemeenschappen van de Nederlandse binnenwateren.

Hoge, F.E. and P.E. Lyon 1996. Satellite retrieval of inherent optical properties by linear matrix inversion of oceanic radiance models: An analysis of model and radiance measurement errors. Journal Of Geophysical Research 101: 16.631-16.648.

Hoge, F.E., A. Vodacek, R.N. Swift, J.K. Yungel, and N.V. Blough 1995. Inherent optical properties of the ocean: retrieval of the absorption coefficient of chromophoric dissolved organic matter from airborne laser spectral fluorescence measurements. Appl.Opt. 34: 7032-7038.

Hoogenboom, H.J., A.G. Dekker, and J.F. de Haan. 1998. InveRSion: assessment of water composition from spectral reflectance: a feasibility study to the use of the matrix inversion method. NRSP-2 98-15, -48. Delft, The Netherlands, Netherlands Remote Sensing Board, Programme Bureau, Rijkswaterstaat Survey Department.

Hoogenboom, H.J., A.G. Dekker, and J.D. van Zetten. 1996. Waterkwaliteit in waterleidingplas en omringende wateren; deel III: een analyse op basis van remote sensing beelden in 1995. E-96/, 1-52. Amsterdam, GWA.

Hoogenboom, H.J. and P.E.G. Leonards. 1997. Schatten van mobiliteit en beschikbaarheid van PCB's met behulp van remote sensing. IVM W-97/01, -29. Amsterdam, IVM.

Huot, J., S. Belanger, L. Bourg, C. Brockmann, U. Kramer, and S. Delwart. 2005. The MERIS Atmospheric Correction above Marine Surfaces:
Successes, Limitations and Perpectives. ONR-NASA. Ocean Optics XVII.

Imai, A., T. Fukushima, K. Matsushige, and Y.H. Kim 2001. Fractionation And Characterization Of Dissolved Organic Matter In A Shallow Eutrophic Lake, Its Inflowing Rivers, And Other Organic Sources. Water Resources Research 35: 4019-4028.

IOCCG. 2000. Remote Sensing of Ocean Colour in Coastal, and Other Optically-Complex, Waters. No. 3, 1-140. Dartmouth, Canada, IOCCG. Reports of the International Ocean-Colour Coordinating Group.

Jerlov, N.G. 1968. Optical Oceanography, 5 ed. Elsevier.

Kalle, K. 1966. The problem of the gelbstoff in the sea. Oceanography Marine Biology Annual Review 4: 91-104.

Keith, D.J., J.A. Yoder, and S.A. Freeman 2002. Spatial and Temporal Distribution of Coloured Dissolved Organic Matter (CDOM) in Narragansett Bay, Rhode Island: Implications for Phytoplankton in Coastal Waters. Estuarine, Coastal and Shelf Science 55: 705-717.

Keller,P.A. 2001. Comparison of two inversion techniques of a semi-analytical model for the determination of lake water constituents using imaging spectrometry data. The Science of The Total Environment 268: 189-196.

Kirk, J.T.O. 1975. A theoretical analysis of the contribution of algal cells to the attenuation of light within natural waters. I. General treatment of suspensions of living cells. New Phytol. 75: 11-20.

Kirk, J.T.O. 1980. Spectral absorption properties of natural waters: contribution of the soluble and particulate fractions to light absorption in some inland waters of South-eastern Australia. Aust.J.Mar.Freshwater Res. 31: 287-296.

Kirk, J.T.O. 1991. Volume scattering function, average cosines, and the underwater light field. Limnol.Oceanogr. 36: 455-467.

Kirk, J.T.O. 1994a. Light and photosynthesis in aquatic ecosystems, 2nd ed., 2 ed.

Kirk ,J.T.O. 1994b. Characteristics of the light field in highly turbid waters: a Monte Carlo study. Limnol.Oceanogr. 39: 702-706.

Kirk, J.T.O. 1995. Modeling the performace of an integrating-cavity absorption meter: theory and calculations for a spherical cavity. Appl.Opt. 34: 4397-4408.

Kirk, J.T.O. 1997. Point-source integrating-cavity absorption meter: theoretical principles and numerical modeling. Appl.Opt. 36: 6123-6127.

Kirkpatrick, G.J., C.Orrico, M.A.Moline, M.Oliver, and O.M.Schofield 2003. Continuous hyperspectral absorption measurements of colored dissolved organic matter in aquatic systems. Appl.Opt. 42: 6564-6568.

Kishino, M., M. Takahashi, N. Okami, and S. Ichimura 1985. Estimation of the spectral absorption coefficients of phytoplankton in the sea. Bull.Mar.Sci. 37: 634-642.

Klavins, M. and E. Apsite 2002. Sedimentary Humic Substances From Lakes in Latvia. Environmental International 23: 783-790.

Koponen, S. 2006. Remote sensing of water quality for Finnish lakes and coastal areas. HUT.

Kracht, O. 2001. Origin and genesis of dissolved organic matter: A study by Py-GC/MS-IRMS. Friedrich-Schiller-Universität.

Kracht, O. and G. Gleixner 2000. Isotope analysis of pyrolysis products from Sphagnum peat
and dissolved organic matter from bog water. Organic Geochemistry 31: 645-654.

Kramer, K.J.M., R.G. Jak, G. Stroomberg, R.N. Hooftman, and Ph. Mayer. 2003. Onderzoek naar de biologische beschikbaarheid van koper in Nederlandse oppervlaktewateren.
Fase III: Effecten op vissen en algen. MERMAYDE Rapport MM-1047. Ministerie van Volkshuisvesting, Ruimtelijke Ordening en Milieubeheer, Directoraat Generaal Milieubeheer.

Krasnapolski, V.M., W.H. Gemmil, and L.C. Breaker 2000. A Neural Network Multiparameter Algorithm for SSM/I Ocean Retrievals: Comparisons and Validations. Remote Sens.Environ. 73: 133-142.

Krijgsman, J. 1994. Optical Remote Sensing of Water Quality Parameters: Interpretation of Reflectance Spectra. 1-198. Thesis. TU Delft.

Laanen, M., G. Hopman, and H.J. van der Woerd. 2003. Verkenning van een spectroradiometrische meetmethode voor het monitoren van waterkwaliteitsparameters in Loenderveen en Terra Nova. E-03/03, 1-34. Amsterdam, IVM.

Laanen, M.L., S.W.M. Peters, R. Pasterkamp, V.E. Brando, P.J. Daniel, and A.G. Dekker. 2002. Using A Point-Source Integrating-Cavity Absorption Meter To Measure Coloured Dissolved Organic Matter Absorption Of Dutch Natural Waters. Miami, Veridian. Seventh International Conference on Remote sensing for Marine and Coastal Environments. 20-5-2002.

Lasdon, L.S., A.D. Waren, A. Jain, and M. Ratner 1978. Design and testing of a generalized reduced gradient code for nonlinear programming. ACM Transactions on Mathematical Software 4: 34-50.

Leathers, R.A., V.T. Downes, and C.O. Davis 2000. Analysis of a point-source integrating-cavity absorption meter. Appl.Opt. 39: 1-10.

Lee, L.H., B. Lustigman, and J. Maccari 1993. Effect of copper on the growth of Anacystis nidulans. Bulletin of Environmental Contamination and Toxicology 50: 600-607.

Lee, Z.P. and K.L. Carder 2004. Absorption spectrum of phytoplankton pigments derived from hyperspectral remote-sensing reflectance. Remote Sens.Environ. 89: 361-368.

Lehtonen, K., K. Hänninen, and M. Ketola 2001. Structurally bound lipids in peat humic acids. Organic Chemistry 32: 33-43.

Lerebourg, C.J.-Y., D.A. Pilgrim, G.D. Ludbrook, and R. Neal 2003. Development of a point source integrating cavity absorption meter. Journal of Optics A: Pure and Applied Optics 4: S56-S65.

Li, H.Y., J.W. Budd, and S. Green 2004. Evaluation and regional optimization of bio-optical algorithms for central Lake Superior. Journal of Great Lakes Research 30: 443-458.

Liere, L. v. and R.D. Gulati. 1991. Restoration and Recovery of Shallow Eutrophic Lake Ecosystems in the Netherlands. Springer.

Lindell, L.T., D. Pierson, G. Premazzi, E. Zillioli 1999. Manual for monitoring European lakes using remote sensing techniques. European Communities.

Malthus, T.J.M., E.P.H. Best, and A.G. Dekker 1990. An assessment of the importance of emergent and floating-leaved macrophytes to trophic status in the Loosdrecht lakes (The Netherlands). Hydrobiologia 191: 257-263.

McKnight, D.M. and G.R. Aiken 1998. Sources and age of aquatic humic substances, p. 9-39. In [ed.], D. Hessen Aquatic Humic Substances: Ecology and Biogeochemistry. Springer.

McKnight, D.M., E.W. Boyer, P.K. Westerhof, P.T. Doran, T. Kulbe, and D.T. Andersen 2001. Spectrofluorometric characterization of dissolved organic matter for indication of precursor organic material and aromaticity. Limnology and Oceanography 46: 38-48.

Mehrtens, H. and T. Martin 2002. Remote sensing of oligotrophic waters: model divergence at low chlorophyll concentrations. Appl.Opt. 41: 7058-7067.

Miller, R.L., M. Belz, C. Del Castillo, and R. Trzaska 2002. Determining CDOM absorption spectra in diverse coastal environments using a multiple pathlength, liquid core waveguide system. Continent.Shelf Res. 22: 1301-1310.

Mobley, C.D. 1999a. Estimation of the remote-sensing reflectance from above-surface measurements. Appl.Opt. 38: 7442-7455.

Mobley, C.D. 1999f. Remote Sensing - Estimation of the remote-sensing reflectance from above-surface measurements. Appl.Opt. 38: 7442-7455.

Mobley, C.D. 1994. Light and water; Radiative transfer in natural waters. Academic Press.

Mobley, C.D. 1998. Hydrolight 4.0 Users' guide. 1-106. Mercer Island, USA, Sequoia Scientific, Inc.

Mobley, C.D., L.K. Sundman, C.O. Davis, M. Montes, and W. Paul Bisset. 2002. A Look-Up-Table approach to inverting remotely sensed ocean color data. Santa Fé. Ocean Optics XVI.

Morel, A. and A. Bricaud 1981. theoretical results concerning light absorption in a discrete medium, and application to specific absorption of phytoplankton. Deep-Sea Res. 28: 1375-1393.

Morel, A. and L. Prieur 1977. Analysis of variations in ocean colour. Limnol.Oceanogr. 22: 709-722.

Morel, A. and L. Prieur. 1976. Analyse spectrale de l'absorption par les substances dissoutes (substances jaunes). CNEXO. Résultats de la campagne CINECA V.

Morris, D.P. and B.R. Hargreaves 1997. The Role of Photochemical Degradation of Dissolved Organic Carbon in Regulating the UV Transparency of Three Lakes on the Pocono Plateau. Limnology and Oceanography 42: 239-249.

Mueller, J.L. and R.W. Austin. 1992. Ocean Optics Protocols for SeaWiFS Validation. NASA Tech. Memo. 2000-104566 Vol. 25, 1-39. Greenbelt, Maryland, USA, NASA Goddard Space Flight Center.

NEN 6484. 1982. Water: Determination of the content of not dissolved material and its ignition residue. Nederlandse Norm.

NEN 6520. 1981. Water: Spectrophotometric determination of chlorophyll a content. Nederlandse Norm.

O'Reilly, J.F., S. Maritorena, B.G. Mitchell, D.A. Siegel, S.A. Garver, and M. Kahru 1998. Ocean color chlorophyll algorithms for SeaWiFS. J.Geophys.Res 103: 24891-24900.

Pasterkamp, R., Woerd, H.J. van der, Peters, S.W.M., Eleveld, M.A. & Roberti, H. 2005. Simultaneous determination of suspended sediment and chlorophyll-a: validation for the Dutch North Sea in 2003. Halifax, 8th Conference on Remote Sensing for Marine and Coastal Environments.

Pegau, W.S., J.S. Cleveland, W. Doss, C.D. Kennedy, R.A. Affione, J. Lueller, R. Stone, C.C. Trees, A.D. Weidemann, W.H. Wells, and J.R.V. Zaneveld 1995. A comparison of methods for the measurement of the absorption coefficient in natural waters (Paper 95JC00456). J.Geophys.Res. 100: 13,201-13,220.

Peters, S.W.M., A.G. Dekker, and P. Keller. 1998. From end-user requirements to sensor requirements. 215-220. Zurich, EARSEL. 1st EARSeL Workshop on Imaging Spectroscopy. 8-10-1998.

Peters, S.W.M. and H. Landa. 1998. Methods and requirements for the extraction of spatial water quality information from multisource, multiscale and multitemporal data; an exploratory research within the WAKWAGIS project. -38. Delft, RWS/MD.

Peters, S.W.M., R. Pasterkamp, and H.J. van der Woerd. 2002. A sensitivity analysis of analytical inversion methods to derive chlorophyll from MERIS spectra in Case-II waters. Ocean Optics XVI.

Petzold, T.J. 1972. Volume scattering functions for selected ocean waters. San Diego: Scripps Inst. Oceanogr. Visibility Lab.

Pfeifer, T., U. Klaus, R. Hoffman, and M. Spiteller 2001. Characterization of humic substances using atmospheric pressure chemical ionisation and electrospray ionisation mass spectrometry combined with size-exclusion chromatography. Journal of Chromatography A 926: 151-159.

Pierson, D.C. and N. Strombeck 2001. Estimation of radiance reflectance and the concentrations of optically active substances in Lake Malaren, Sweden, based on direct and inverse solutions of a simple model. The Science of The Total Environment 268: 171-188.

Pope, R.M. and E.S. Fry 1997. Absorption spectrum (380-700 nm) of pure water. II. Integrating cavity measurements. Appl.Opt. 36: 8710-8723.

Pope, R.M., A.D. Weidemann, and E.S. Fry 2000. Integrating Cavity Absorption Meter measurements of dissolved substances and suspended particles in ocean water. Dynamics of Atmospheres and Oceans 31: 307-320.

Preisendorfer, R.W. 1976. Hydrologic Optics, Vol 1. Washington, Dep. of Commerce.

Press, J.S. 1989. Bayesian Statistics; princilpes, modelsm and applications. Wiley.

Press, W.H., B.P. Flannery, S.A. Teukolsky, and W.T. Vetterling. 1992. Numerical recipes: the art of scientific computing in Fortran. Cambridge University Press.

Rijkeboer, M. 2000. Algoritmen voor het bepalen van de concentratie chloropfyl-a en zwevend stof met de Opticshe Teledetectie Methode in verschillende optische watertypen. IVM-O-00/08, -35. Amsterdam, The Netherlands, Institute for Environmental Studies.

Rijkeboer, M., A.G. Dekker, and H.J. Hoogenboom. 1998. Reflectance spectra with associated water quality parameters measured in Dutch waters (Speclib-TK-database). E98/12, -18.

Rijkeboer, M., H.J. Hoogenboom, and A.G. Dekker. 1997. Realisatie spectrale bibliotheek van Nederlandse wateren. W-97/07, 1-48.

Robinson, M.G. and L.N. Brown 1991. Copper complexation during a bloom of Gymnodinium sanguineum Hirasake (Dinophyceae) measured by ASV. Marine Chemistry 33: 105-118.

Roesler, C.S. 1998. Theoretical and experimental approaches to improve the accuracy of particulate absorption coeeficients derived from the quantitative filter technique. Limnol.Oceanogr. 43: 1649-1660.

Roettgers, R., W. Schoenfeld, P. Kipp, and R. Doerffer 2005. Practical test of a point-source integrating-cavity absorption meter (PSICAM): the performance of different collector assemblies. Appl.Opt. 44: 5549-5560.

Santer, R. and C. Schmechting 2000. Adjacency effectson water surfaces: Primary scattering approximation and sensitivity study. Appl.Opt. 39: 361-375.

Sasaki, H., A. Tanaka, J. Ishizaka, and S. Saitoh. 2002. Variations of Light Absorption by Colored Dissolved Organic Matter (CDOM) in Various Areas of the Western North Pacific. Santa Fe, New Mexico, USA, 18-22 November 2002, Proceedings of Ocean Optics XVI Conference.

Sathyendranath, S., L. Prieur, and A. Morel 1989. A three-component model of ocean colour and its application to remote sensing of phytoplankton pigments in coastal waters. Int.J.Remote Sensing 10: 1373-1394.

Schaepman, M.E. 1998. Calibration of a field spectroradiometer. Thesis. Remote Sensing Laboratories.

Schiller, H. and R. Doerffer 1997. Neural network for emulation of an inverse model - operational derivation of Case II water properties from MERIS data. Int.J.Remote Sensing 20: 1735-1746.

Schnitzer, M. and S.U. Kahn. 1972. Humic Substances in the Environment. Marcel and Dekker Inc.

Siegel, D.A., S. Maritorena, N.B. Nelson, D.A. Hansell, and M. Lorenzi-Kayser 2002. Global distribution and dynamics of colored dissolved and detrital organic materials. J.Geophys.Res 107: 21-1-21-13.

Simis, S.G., 2006 Blue-green catastrophe - remote sensing pf mass viral lysis of cyanobacteria. 1-144. Thesis. NIOO-KNAW and Vrije Universiteit, Amsterdam, The Netherlands.

Søndergaard, M., J.P. Jensen, and E. Jeppesen 1999. Internal phosphorus loading in shallow Danish lakes. Hydrobiologia 408/409: 145-152.

Sorensen, K., J. Hokedal, E. Aas, R. Doerffer, and E. Dahl. 2003. Early Results for Validation of MERIS water products in the Skagerrak. SP-531. ESA. Envisat Validation Workshop.

Stedmon, C.A., S. Markager, and H. Kaas 2000. Optical Properties and Signatures of Chromophoric Dissolved Organic Matter (CDOM) in Danish Coastal Waters. Estuarine, Coastal and Shelf Science 51: 267-278.

Steinberg, C.E.W. 2003. Ecology of Humic Substances in Freshwater, 1 ed. Springer.

Stevenson, F.J. 1982. Humus. Chemistry, Genesis, Composition, Reactions. John Wiley & Sons, Inc.

Stumm, W. and J.J. Morgan. 1981. Aquatic Chemistry, 2 ed. John Wiley & Sons.

Tilstone, G., G.F. Moore, R. Sørensen, R. Doerffer, R. Pasterkamp, and P.V. Jørgensen. 2002. REVAMP Protocols. REVAMP methodologies – EVG1 – CT – 2001 - 00049. Regional Validation of MERIS Chlorophyll products in North Sea coastal waters.

Trüper, H.G. and C.M. Yentsch 1967. Use of glass fiber filters for the rapid preparation of in vivo absorption spectra of photosynthetic bacteria. J.Bact. 94: 1255-1256.

Twardowski, M.S. and P.L. Donaghay 2002. Photobleaching of aquatic dissolved materials: Absorption removal, spectral alteration, and their relationship. J.Geophys.Res. 107.

Twardowski, M.S. and P.L. Donaghay 2001. Separating in situ and terrigenous sources of absorption by dissolved materials in coastal waters. J.Geophys.Res. 106: 2545-2560.

van der Molen, D.T. and P.C.M. Boers. 1994. Influence of internal loading on phosphorus concentration in shallow lakes befor and after reduction of the external loading. Hydrobiologia 275/276, 379-389. Silkeborg Denmark, Proceedings International Conference on Nutrient Dynamics and Biological Structure in Shakllow Freshwater and Brackish Lakes. 1992.

van Liere, L., R.M.M. Roijackers, and P.J.T. Verstraelen. 1989. Integraal waterbeheer in het Gooi/Utrechts stuwwallen- en plassengebied.

Visser, S.A. 1984. Seasonal changes in the concentration and colour of humic substances in some aquatic environments. Freshwater Biol. 14: 79-87.

Vodacek, A., N.V. Blough, M.D. DeGrandpre, E. Peltzer, and R.K. Nelson 1997. Seasonal variations of CDOM and DOC in the Middle Atlantic Bight: Terrestrial inputs and photooxidation. Limnol.Oceanogr. 42: 674-686.

Vos, R.J., P. Boderie, H.J. Gons, I. v. Splunder, H.J. Hoogenboom, H. v.d. Woerd, N. Villars, H. Hoogveld, M. Rijkeboer, R.W.L. Jordans, and J.H.M. Hakvoort. 2002. Het gebruik van remote sensing voor monitoring en modellering van algen in het IJsselmeer. BCRS 2.3 AP/-07. BCRS.

Vos, R.J. and R. Pasterkamp. 2001. Optical Closure in Case 2 Waters: Hydrolight simulations of the optical dataset of Lake IJssel in the Netherlands. W-01/24, 1-69. Amsterdam, The Netherlands, Institute for Environmental Studies.

Vos, R.J., S.W.M. Peters, and M. Rijkeboer. 1999. Validation and error analysis of retrieval of water quality parameters from field spectra for inland waters. W-99/48, 1-45. IVM\VU Amsterdam, The Netherlands.

Waksman, S.A. 1932. Principles of soil microbiology. The Williams & Wilkins Co.

Walker, R.E. 1994. Marine light field statistics. Wiley.

Wetzel, R.G. 1983. Limnology, 1 ed. Saunders College Publishing.

Wetzel, R.G. 2002. Dissolved organic carbon: Detrital energetics, metabolic regulators, and drivers of ecosystem stability of aquatic ecosystems, In [ed.], S.Findlay Aquatic Ecosystems: Interactivity of Dissolved Organic Matter. Academic Press.

Whitehead, R.F., S. de Mora, S. Demers, M. Gosselin, P. Monfort, and B. Mostajir 2000. Interactions of ultraviolet-B radiation, mixing, and biological activity on photobleaching of natural chromophoric dissolved organic matter: A mesocosm study. Limnology and Oceanography 45: 278-291.

Whitlock, C.H., L.R. Poole, J. Usry, W.M. Houghton, W.G. Witte, W.D. Morris, and E.A. Gurganus 1981. Comparison of reflectance with backscatter and absorption parameters for turbid waters. Appl.Opt. 20: 517-522.

Wirdum, G. v. 1993. An ecosystem approach to base-rich freshwater wetlands, with special reference to fenlands. Hydrobiologia 265: 129-153.

Zepp, R.G. and P.F. Schlotzhauer 1981. Comparison Of Photochemical Behaviour Of Various Humic Substances In Water: III. Spectroscopic Properties Of Humic Substances. Chemosphere 10: 479-486.

Zhang, Y., J. Pulliainen, S. Koponen, and M. Hallikainen 2002. Application of an empirical neural network to surface water quality estimation in the Gulf of Finland using combined optical data and microwave data. Remote Sens.Environ. 81: 327-336.

Appendix I. Map of the sample locations

Figure I-1: Map of the Vecht Wetlands showing all sample locations. Please note that the LELxC, TNTxC and TNHxC sample locations have been visited three times in 2001 (at Julian days 114, 210 and 255), resulting in additional 'sample stations'.

Appendix II. Description of the field campaigns

All data for this research was collected in the Vecht Wetlands study area that is shown in Figure 1.2. A dataset was created by combining CSI data collected during a number of field campaigns. These campaigns include data from 4 sample stations gathered by Dekker around 1990 (Dekker and Peters 1993), another 6 sample stations obtained within the SPECLIB project in 1995 (Rijkeboer, Hoogenboom, and Dekker 1997), 21 sample stations collected specifically for this research in 2001 by the author and the remaining 21 sample stations originate from the GWA-CDOM project, also conducted by the author *et al.* (Laanen, Hopman, and van der Woerd 2003) for the Gemeente Waterleidingen Amsterdam (GWA) in 2002. In total complete CSI data from 52 sample locations is available.

From 2001 onwards the *in situ* CDOM concentration could also be determined by using a 'Point-Source Integrating-Cavity Absorption Meter' (PSICAM), which is elaborated on in chapter 9. The hand-held spectrometers used were a Spectron SE590 (Dekker 1990 campaign) and several Photo Research PR650 units. Although these different hand-held spectrometers used different protocols, all measured spectra were eventually transformed into comparable subsurface irradiance spectra. A description of the protocols for *in situ* and laboratory measurements used in these campaigns is given in appendix I. A metadata overview of these field campaigns is given in table II-1.

Table II-2: Overview of the various field campaigns . Notes:†) All GWA sample stations were visited on the dates in 2002, while in 2003 only the K_d was measured. ‡ Lake numbers correspond to the numbers shown in table 1.1.

Campaign	Dekker	Speclib	2001	GWA
Date(s)	Summer 1990	Summer 1995	August 9, 23, 28 and 30, 2001	April 24, July 26, September 12, 2002 and August 7, 2003†
Lakes visited‡	1-18	1-18	3-8, 11, 12, 14, 15 & 18	10-12
PSICAM CDOM measurements available	No	No	Yes	Yes (except for Julian day 114 samples)
Spectrometer used	Spectron SE590	Photo Research PR650	Photo Research PR650	Photo Research PR650

The concentration (the C_{TCHL}, C_{TSM} and C_{CDOM})and SIOP data (the a^*_{ph} at 676 nm, a^*_{tr} at 550 nm and b^*_{ses} at 550 nm) for all 52 sample stations is given in table II-3 below:

Tabel II-3: The concentration and SIOP data for all sample stations

Sample station	C_{TCHL}	C_{TSM}	C_{CDOM}	a^*_{ph} 676 nm	a^*_{tr} 550 nm	b^*_{ses} 550 nm
210LEL_1_C	32,64	12,06	2,44	0,021	0,026	1,226
210LEL_2_C	35,66	10,20	2,42	0,017	0,027	1,433
210LEL_3_C	38,74	17,07	2,42	0,016	0,038	0,807
210TNH_1_C	25,46	8,43	3,89	0,014	0,079	1,657
210TNH_2_C	25,63	8,00	3,87	0,015	0,023	0,895
210TNT_1_C	35,32	5,61	3,28	0,023	0,119	1,108
210TNT_2_C	42,44	5,93	3,26	0,017	0,059	0,434
255LEL-1-C	65,05	20,93	2,42	0,021	0,078	0,863
255LEL-2-C	67,52	18,00	2,30	0,022	0,102	0,981
255LEL-3-C	65,43	13,60	2,23	0,022	0,112	1,368
255TNH-1-C	24,31	4,07	3,23	0,019	0,131	0,756
255TNH-2-C	14,82	3,67	4,49	0,016	0,102	0,401
255TNT-1-C	81,63	16,67	2,68	0,021	0,087	0,941
255TNT-2-C	80,94	16,13	2,58	0,022	0,085	0,983
114LEL_1_C	60,30	18,58	2,15	0,019	0,031	1,269
114LEL_2_C	61,88	18,17	2,01	0,019	0,035	1,132
114LEL_3_C	60,14	19,66	1,90	0,018	0,039	1,079
114TNH_1_C	32,17	8,67	2,47	0,032	0,080	0,738
114TNH_2_C	27,54	7,13	4,33	0,022	0,101	1,112
114TNT_1_C	38,18	15,00	2,31	0,029	0,046	1,233
114TNT_2_C	43,10	16,58	2,28	0,026	0,034	1,152
95149 WL	1,40	0,82	0,45	0,015	0,087	0,154
WL_aug_90	5,00	1,23	1,08	0,058	0,073	0,663
95151WG	142,52	30,10	2,67	0,025	0,030	0,450
PKH10	290,67	37,33	2,15	0,017	0,004	0,663
95151WB	8,90	4,90	0,97	0,018	0,030	0,359
WJB_90	25,00	8,40	0,88	0,021	0,016	0,402
L1	103,87	15,65	2,55	0,015	0,040	1,506
V1	36,06	21,78	2,33	0,008	0,021	0,480

V2	29,43	6,33	1,97	0,011	0,071	0,655
ANK3	20,55	6,11	3,24	0,014	0,020	0,421
ANK5	211,82	20,67	3,51	0,015	0,040	0,528
ANK7	6,20	1,83	2,78	0,021	0,034	0,319
SP2	6,20	1,78	2,03	0,017	0,040	0,343
95163LO	103,60	22,78	2,35	0,013	0,027	0,637
L5_sep_90	119,00	32,50	2,35	0,022	0,038	0,772
HIK2	115,93	14,00	2,48	0,012	0,086	0,900
HIK5	84,51	12,00	2,24	0,018	0,030	0,982
KORT1	100,90	26,00	2,94	0,018	0,031	0,842
KORT4	51,92	12,00	2,88	0,019	0,075	0,815
KORT5	34,75	9,00	2,79	0,016	0,016	0,598
WB1	32,62	8,00	1,32	0,022	0,019	1,344
WB2	29,99	8,00	1,47	0,023	0,010	1,358
L2	96,12	13,33	2,67	0,029	0,049	1,817
L3	104,68	10,67	2,54	0,030	0,052	2,350
L4	103,00	7,33	2,48	0,020	0,073	3,439
LEL1	63,30	4,00	2,82	0,011	0,151	4,181
NP1	51,43	2,00	1,27	0,009	0,255	7,033
WL1	3,57	0,75	1,12	0,010	0,114	1,157
WL2	3,89	1,00	1,18	0,014	0,116	0,674
210LEL_1_C	32,64	12,06	2,44	0,021	0,026	1,226
210LEL_2_C	35,66	10,20	2,42	0,017	0,027	1,433

Appendix III. Measurement protocols

III.1 Field Measurements

III.1.1 Ancillary measurements

Apart from the spectral measurements described in the next paragraph the following variables were determined at each sample location: Date and local daylight savings time (Mid-European Standard Time, MEST), GPS coordinates (in the Dutch Rijks Driehoeks (RD) coordinate system), Secchi Disk depth (SD) and bottom depth (where possible). The GPS device used, a Garmin e-Trex, reported accuracies averaging about 10 m. It should be kept in mind that Secchi Disk depths are only indications of the visibility, biased by the light conditions and the interpretation of the operator, and not a strict physical property. Bottom depth was determined by gently lowering the Secchi Disk until the bottom was felt.

Water samples were taken just below the water surface or from a bucket using 1 litre Polyethylene bottles. They were temporally stored in a cooler containing cooling elements and/or ice until arriving in the laboratory, where the samples were immediately processed or transferred to a refrigerator. All analyses were done within 72 hours after collection.

III.1.2 Spectral measurements of Apparent Optical Properties

In chapter 6 it is shown that the AOP of interest, the subsurface irradiance reflectance, can be determined by combining four radiance measurements: the total water leaving radiance L_{water}, the part of L_{water} that originates from reflected sky radiance at the water surface L_{sky}, the total downwelling radiance L_{rs} and the diffuse part of L_{rs}, L_{dif}. Because it is crucial for understanding the remote sensing techniques, the AOP measurement protocol is already explained at length in the text in chapter 6. For brevity the protocol will not be repeated here.

III.2 Laboratory Measurements

III.2.1 Concentration of Total Suspended Matter (TSM)

TSM is determined according to Dutch Standard Norm 6484 (NEN 6484 1982)}. The sample is filtered on a Whatman GF/F (25 mm ∅, 0.7 µm nominal pore size) glass fiber filter, dried (at 105° C for 2 hours) and weighed. All filters were first filtrated using distilled water to remove any loose particles from the filter and then pre-weighed before use.

The TSM concentration is calculated by:

$$C_{TSM} = \frac{m_1 - m_0}{V} \qquad \text{III.I}$$

Where C_{TSM} is the TSM concentration in [mg l^{-1}], m_0 is the mass of the empty (pre-weighed) filter [mg], m_1 is the mass of the filter with residue [mg], and V is the volume of filtrated sample [l]. No correction for salt was made, as the salt concentrations in the Vecht Wetlands are negligible.

III.2.2 Concentration of chlorophyll-a and phaeopigments

The method is in accordance with Dutch Standard Norm 6520 (NEN 6520 1981)}. Pigments are extracted using 80%$_{vol}$ ethanol (C_2H_6O) at 75 °C. The concentration is determined photometrically by measuring the extinction coefficients at 665 and 750 [nm] before and after acidification (with 0.40 mol/l HCl) of the sample. Again Whatman GF/F glass fiber filters with 45 mm ∅ are used. For this research all cuvette measurements were performed using a 10 cm quartz cuvette and the aforementioned Ocean Optics SD2000 spectrometer.

The extinction of the ethanol extract before acidification is calculated as

$$E(\lambda) = \frac{A(\lambda)V_{ethanol}}{lV_{sample}} \qquad \text{III.II}$$

Where A is the measured absorbance, $V_{ethanol}$ [m^3] is the volume of ethanol added to the reagent tube with residue, V_{sample} [m^3] is the volume of filtrated sample and l [m] is the cuvette length. Using equation III.II, $A_{extract}$ is converted to $E_{extract}$ and A_{acid} is converted to E_{acid}.

The corrected extinction of the ethanol extract before acidification is calculated as

$$E'_{extract}(\lambda) = E_{extract}(\lambda) - E_{extract}(750nm) \qquad \text{III.III}$$

and the corrected extinction of the extract after acidification is calculated as

$$E'_{acid}(\lambda) = E_{acid}(\lambda) - E_{acid}(750nm) \qquad \text{III.IV}$$

The chlorophyll-a concentration C_{CHL} [mg m^{-3}] is calculated as

$$C_{CHL} = 296\left[E'_{extract}(665nm) - E'_{acid}(665nm)\right] \qquad \text{III.V}$$

and the concentration of phaeopigments (C_{PHAEO}) [mg m^{-3}] is calculated as

$$C_{PHAEO} = 296\left[1.7 \cdot E'_{acid}(665nm) - E'_{extract}(665nm)\right] \qquad \text{III.VI}$$

Finally the total chlorophyll concentration C_{TCHL} [mg m^{-3}] is then defined as the concentration of chlorophyll a and the concentration of phaeopigments together.

$$C_{TCHL} = C_{CHL} + C_{PHAEO} \qquad \text{III.VII}$$

III.2.3 Absorption of Coloured Dissolved Organic Matter (CDOM) using a cuvette

The dissolved fraction of the natural water sample is obtained by filtration over a Whatman GF/F (45 mm ∅, 0.7 µm pore size) glass fiber filter.

Absorption is measured using an absorbance measurement in a 10 cm cuvette. The measurement is referenced against Milli-Q water, and a baseline correction is applied. The measured spectrum is then fitted to an exponential curve using a non-linear least squares polynomial fit in the wavelength region from 400 to 700 nm.

Absorbance A [-] is calculated from the spectrometer readings as:

$$A(\lambda) = -\log^{10}\left(\frac{DN_{sample}(\lambda) - DN_{dark}(\lambda)}{DN_{reference}(\lambda) - DN_{dark}(\lambda)}\right) \qquad \text{III.VIII}$$

Where DN_{sample} is the sample spectrum in digital numbers, $DN_{reference}$ is the reference spectrum and DN_{dark} is the dark-current spectrum. The absorption a [m^{-1}] is then calculated as:

$$a(\lambda) = \ln(10)\frac{A(\lambda)}{l} \qquad \text{III.IX}$$

Where l is the cuvette length [m]. For this research all cuvette measurements were performed using a 10 cm quartz cuvette and the Ocean Optics SD2000 spectrometer.

The optical absorption measurements are sensitive to:

- ➔ Temperature differences between the reference and the sample. If the sample has a higher temperature than the reference, the absorption values recorded will be higher. Prior to measurement it should be determined that both the reference and the sample(s) have reached room temperature.
- ➔ Another temperature related issue is the fogging up of the cuvette when inserting samples straight out of their cold storage. This effect also dramatically increases absorption measurements. Again samples should be allowed to reach room temperature before measurement.
- ➔ Air bubbles in the sample should also be avoided when filling the cuvette. Air bubbles will also increase the amount of absorption measured.

Modelling of the CDOM absorption

In literature, CDOM absorption is commonly described by an exponential function (Kalle 1966) in order to extrapolate beyond the measured data range and to correct for measurement noise (see chapter 10). To fit the exponential slope of this function, the measured absorption curve according to equation III.IX is fitted to an exponential function expressed as

$$a_{CDOM}(\lambda) = \Delta + a_{CDOM}(\lambda_0)\exp^{-S_{CDOM}(\lambda-\lambda_0)} \qquad \text{III.X}$$

Where Δ is a wavelength independent offset, $a_{CDOM}(\lambda_0)$ is the absorption at reference wavelength λ_0 (usually at 440 nm, also denoted as g_{440}), and S_{CDOM} is the exponential slope (Stedmon, Markager, and Kaas 2000). CDOM absorption spectrum fitting is discussed at length in chapter 10.

III.2.4 Absorption of Coloured Dissolved Organic Matter (CDOM) using a Point-Source Integrating-Cavity Absorption Meter (PSICAM):

Another way of measuring the CDOM absorption is by using a Point-Source Integrating-Cavity Absorption Meter (PSICAM). A PSICAM is a device to measure light absorption of water samples. The principles and operation of the PSICAM are the subject of chapter 9. The measurement protocol for the PSICAM is explained at length in section 9. For brevity the protocol will not be repeated here.

III.2.5 Seston and tripton (bleached seston) absorption

The total suspended fraction present in natural waters is denoted as seston, which can be subdivided into tripton (roughly the non-living suspended material) and phytoplankton (roughly the living suspended material) as expressed in the following equation:

$$a_{seston} = a_{tripton} + a_{phytoplankton} \qquad \text{III.XI}$$

The method for determining seston and tripton is based on the filterpad method (Trüper and Yentsch 1967), (Gilijamse 1994)). Suspended particles are concentrated on a Whatman GF/F (25 mm ∅, 0.7 µm pore size) glass fiber filters and attenuation is measured against a reference filter. Subsequently, algal pigments are extracted ('bleached') from the same filter using hot ethanol (80%$_{vol}$, 75 ºC) (Kishino, Takahashi, Okami, and Ichimura 1985)} and the attenuation is measured likewise. A drawback of the filterpad method is that after the bleaching with hot ethanol some cell material, which would be part of the phytoplankton, remains in the sample and is present in the tripton spectrum. Although the contribution of this cell material is assumed to be small, the filterpad method does not provide tripton as it is defined but a property described as bleached seston. In the calculations however we use the bleached seston as true tripton.

Absorption is calculated similar as in equation III.IX, but is corrected for

1. Small differences in the optical density of the blank filters;
2. Path length amplification. Because the light field within the filter is not a straight beam, as it is in a cuvette, but diffuse, the absorption has to be corrected by a so called path length amplification factor.

Seston absorption is thus calculated as

$$a'_{seston}(\lambda) = \ln(10)\frac{A_{seston}(\lambda) - A_{blank}(\lambda)}{\beta l'} \qquad \text{III.XII}$$

Where β is the path length amplification factor, which is a function of scattering by particles on the filter (which is in turn dependent of the particle load) and by the filterpad fibers themselves. The β can be derived empirically, but is then likely to be biased by other factors than path length amplification according to Roesler (Roesler 1998). Based on theoretical and experimental work Roesler therefore suggests to set the correction factor β to 2, which is followed for this research. The effective path length l' [m] is calculated as

$$l' = \frac{V}{\pi r^2} \qquad \text{III.XIII}$$

Where V [m^3] is the filtered volume, and r [m] is the radius of the filtered area (which is smaller than the total filter size). Finally, a baseline correction is applied, setting the absorption at the largest wavelength ($\lambda_{\max}$ > 750 nm) to zero:

$$a_{seston}(\lambda) = a'_{seston}(\lambda) - a'_{seston}(\lambda_{\max}) \qquad \text{III.XIV}$$

Likewise, the tripton absorption is calculated as

$$a'_{tripton}(\lambda) = \ln(10)\frac{A_{tripton}(\lambda) - A_{blank}(\lambda)}{\beta l'} \qquad \text{III.XV}$$

and a baseline correction is applied, setting the absorption at the largest wavelength ($\lambda_{\max}$ > 750 nm) to zero:

$$a_{tripton}(\lambda) = a'_{tripton}(\lambda) - a'_{tripton}(\lambda_{\max}) \qquad \text{III.XVI}$$

In literature, tripton absorption is commonly described by an exponential function. To asses the exponential slope of this function, the measured absorption curve according to equation III.XVI is fitted to an exponential function expressed as

$$a_{tripton}(\lambda) \approx a_{tripton}(\lambda_0)\exp^{-S_{tripton}(\lambda-\lambda_0)} \qquad \text{III.XVII}$$

Where $a_{tripton}(\lambda_0)$ is the absorption at reference wavelength λ_0 (usually 550 nm), and $S_{tripton}$ is the exponential slope of the tripton absorption spectrum.

III.2.6 Beam attenuation

Beam attenuation is measured using an absorbance measurement in a 10 cm cuvette. The measurement is referenced against distilled water.

Absorbance A [-] is calculated from the spectrometer readings as:

$$A(\lambda) = -\log^{10}\left(\frac{DN_{sample}(\lambda) - DN_{dark}(\lambda)}{DN_{reference}(\lambda) - DN_{dark}(\lambda)}\right) \qquad \text{III.XVIII}$$

Where DN_{sample} is the sample spectrum in digital numbers, $DN_{reference}$ is the reference spectrum and DN_{dark} is the dark-current spectrum. The absorption a [m^{-1}] is then calculated as:

$$a(\lambda) = \ln(10)\frac{A(\lambda)}{l} \qquad \text{III.XIX}$$

Where l is the cuvette length [m]. For this research all cuvette measurements were performed using a 10 cm quartz cuvette and the Ocean Optics SD2000 spectrometer.

III.2.7 Derived optical properties

The phytoplankton pigment absorption $a_{phytoplankton}$ can be calculated as

$$a_{phytoplankton}(\lambda) = a_{seston}(\lambda) - a_{tripton}(\lambda) \qquad \text{III.XX}$$

Seston scattering is estimated as

$$b_{seston}(\lambda) = c(\lambda) - a_{CDOM}(\lambda) - a_{seston}(\lambda) \qquad \text{III.XXI}$$

III.2.8 Specific inherent optical properties

The Specific inherent optical properties (SIOP) are calculated from the optical measurements and the concentrations. The following SIOP are required for optical modelling.

SIOP	Formula	Unit

Specific phytoplankton pigment absorption	$a^{*}_{phytoplankton}(\lambda) = \dfrac{a_{phytoplankton}(\lambda)}{C_{TCHL}}$	$m^2\ mg^{-1}$
Specific tripton absorption	$a^{*}_{tripton}(\lambda) = \dfrac{a_{tripton}(\lambda)}{C_{TSM}}$	$m^2\ g^{-1}$
Specific seston scattering	$b^{*}_{seston}(\lambda) = \dfrac{b_{seston}(\lambda)}{C_{TSM}}$	$m^2\ g^{-1}$
Normalised CDOM absorption	$\bar{a}_{CDOM}(\lambda) = \dfrac{a_{CDOM}(\lambda)}{C_{CDOM}}$	m^{-1}

Samenvatting

Deze Nederlandse samenvatting van het proefschrift is speciaal geschreven voor leken op het gebied van remote sensing en waterkwaliteit.

De hoeveelheid opgeloste organische stoffen (Dissolved Organic Matter - DOM) in oppervlaktewater, en de samenstelling ervan, is een belangrijke graadmeter van de fysisch-chemische waterkwaliteit. Dit proefschrift beschrijft een drietal mogelijkheden om de concentratie van gekleurde opgeloste organische stoffen (Coloured Dissolved Organic Matter - CDOM) in natuurlijke Nederlandse oppervlaktewateren beter te kunnen afleiden uit metingen van de kleur van het water. CDOM kleurt (verder helder) oppervlaktewater lichtgeel tot donkerbruin. De precieze kleur van het water, een spectrum van uit het water opwellend licht (reflectiespectrum), kan worden gemeten met een spectrometer. Er bestaan draagbare spectrometers om losse spectra te meten maar er zijn ook beeldvormende spectrometers die zijn gemonteerd op satellieten of onder vliegtuigen, welke digitale multi-spectrale foto's produceren. Met behulp van een fysisch optisch model is het mogelijk om uit een reflectiespectrum concentraties van de gekleurde natuurlijke bestanddelen van het oppervlaktewater te bepalen. Deze bestanddelen zijn over het algemeen beperkt tot algen, slib en CDOM.

Tot een paar jaar geleden is er vooral gewerkt aan technieken voor het afleiden van concentraties algen en slib, eerst in optisch relatief simpele omgevingen als de open oceanen, later ook in complexer kust- en binnenwateren. CDOM is lange tijd genegeerd als parameter omdat het, zeker in oceaanwater, een relatief kleine bijdrage aan het spectrum levert en omdat deze bijdrage ook nog eens voornamelijk in de korte golflengtes (UV – blauw) voorkomt die met oudere generaties (satelliet)spectrometers niet goed konden worden waargenomen of goed konden worden atmosferisch gecorrigeerd.

Tegenwoordig is de techniek echter verder gevorderd. Ook is vastgesteld dat de nauwkeurigheid van de afgeleide concentraties algen en slib uit aardobservatiedata kan worden verhoogd door CDOM mee te nemen in het optisch model. Hiervoor is het echter wel noodzakelijk dat CDOM zelf ook goed kan worden afgeleid. Het doel van dit proefschrift is dan ook het vaststellen van de nauwkeurigheid waarmee CDOM in binnenwater kan worden afgeleid uit reflectiespectra en wat het effect is van drie voor de hand liggende mogelijke verbeteringen hiervoor. Deze drie mogelijke verbeteringen omvatten:

1. Het toepassen van de geavanceerde oplossingstechnieken op een fysisch optisch model van het onderwaterlichtklimaat
2. Het gebruik van een speciale integrerende bol (Point-Source Integrating-Cavity Absorption Meter - PSICAM) voor betere CDOM absorptie referentiemetingen in het laboratorium
3. Het opsplitsen van het absorptiespectrum van CDOM in de twee grootste groepen organische stoffen (humine en fulvine zuren) en deze apart te modelleren

Gekleurde opgeloste organische stoffen in oppervlaktewater

Opgeloste organische stoffen zijn niet alleen een belangrijke voedselbron voor microben en algen, maar spelen ook een grote rol binnen het waterlichaam als een buffer, waarbij het aquatische ecosysteem wordt beschermd tegen bijvoorbeeld vervuiling (zware metalen kunnen bijvoorbeeld worden gebonden aan het organische complex) en schadelijke ultraviolette zonnestraling die door DOM wordt geabsorbeerd. In feite bestaat DOM vooral uit de afbraakproducten van ofwel de in het water aanwezige algen (autochtoon materiaal) ofwel van plantresten die door afspoeling in het water terecht zijn gekomen (allochtoon materiaal). Een andere onderverdeling van DOM is in humine en fulvine zuren (Humic and Fulvic acid - HA en FA), welke zich onderscheiden in complexiteit van de koolstofverbindingen wat weer bepalend is voor hun spectrale eigenschappen. Deze eigenschappen van opgeloste organische stoffen worden beschreven in hoofdstuk 2.

Omdat het lastig is om DOM rechtstreeks te meten, wordt voor de controle van het oppervlaktewater gekeken naar een verwante parameter, de concentratie opgelost organisch koolstof (Dissolved Organic Carbon – DOC) die wel relatief eenvoudig kan worden bepaald. DOC metingen worden routinematig uitgevoerd door waterbeheerders (waterschappen en het Rijksinstituut voor Integraal Zoetwaterbeheer en Afvalwaterbehandeling) en zijn tegenwoordig ook verplicht binnen de Europese Unie middels de Kaderrichtlijn Water (KRW).

Als een alternatief voor DOC kan de concentratie DOM ook worden benaderd door de hoeveelheid gekleurde opgeloste organische stoffen (Coloured Dissolved Organic Matter – CDOM) te bepalen. Hier zijn een aantal voordelen aan verbonden. DOC metingen bestaan uit het verzamelen van monsters op puntlocaties welke worden geanalyseerd in het laboratorium. CDOM concentraties kunnen echter worden afgeleid van optische puntmetingen zonder relatief dure en tijdrovende laboratoriumbepalingen. Verder is het mogelijk om met behulp van dezelfde technieken CDOM te bepalen uit aardobservatiedata zoals satelliet- en vliegtuigopnames zodat ook de ruimtelijke verspreiding inzichtelijk gemaakt wordt.

Waarnemingen van waterkleur

In de aardobservatie wordt gebruik gemaakt van twee verschillende rekenmethodes om informatie af te leiden uit gemeten reflectiespectra: empirische en analytische algoritmen. Empirische algoritmen maken gebruik van statistische relaties tussen de sterkte van het gemeten signaal en de aanwezige hoeveelheid van de te bestuderen grootheid. Bij analytische algoritmes is er sprake van een fysisch verband tussen deze twee.

Beide types algoritmen worden behandeld in hoofdstuk 3. Vanwege de vorm van het CDOM absorptiespectrum (vooral absorptie in de lastige korte golflengtes) en de relatief kleine invloed van CDOM op het totale reflectiespectrum is het tot op heden nog niet gelukt om goed werkende empirische CDOM algoritmes te ontwikkelen. Hierdoor is de keus voor dit onderzoek beperkt tot analytische algoritmes. Zoals gezegd zijn deze algoritmes gebaseerd op de inversie van een optisch model.

Uit de verschillende analytische algoritmes is ook weer een selectie gemaakt. Omdat neurale netwerken niet transparant zijn en dus geen inzicht verschaffen in de interactie tussen de verschillende parameters is besloten deze niet te gebruiken. Volledig analytische modellen waren helaas te veeleisend in termen van de benodigde invoerdata en vielen dus ook af. Hierdoor bleven de semi-analytische optische modellen over, welke nog steeds fysisch onderbouwd zijn maar enige versimpeling kennen.

Het modelleren van de waterkleur

Bij wijze van compromis tussen enerzijds de parameters die binnen het onderzoek gemeten konden worden en de tijd die beschikbaar was voor het opzetten van een model en anderzijds de benodigde nauwkeurigheid voor het afleiden van CDOM concentraties is ervoor gekozen om het semi-analytische optische model van Gordon-Walker te gebruiken. Als geavanceerde inversietechnieken werden de Matrix Inversie Methoden (MIM) en de Levenberg-Marquardt (LM) optimalisatietechniek geselecteerd, mede omdat deze technieken het gehele spectrum kunnen oplossen.

Het Gordon-Walker model vraagt om zogenaamde inherente optische eigenschappen (IOP) en apparente optische eigenschappen (AOP). De IOP worden alleen bepaald door de absorptie- en verstrooiingseigenschappen van de gekleurde bestanddelen van water. Als AOP worden in deze studie de gemeten reflectiespectra gebruikt.

Metingen van specifieke inherente optische eigenschappen

Nadat het optische model was gekozen werd de invulling of parameterisatie ervan bepaald (hoofdstuk 5) door middel van gemeten IOPs. IOP data bestaan uit absorptie- en verstrooiingseigenschappen die *in situ* zijn gemeten of aan watermonsters in een laboratorium. De IOP en concentratie data voor het in deze studie gehanteerde model omvatten:

1. De absorptie en verstrooiing van puur water (uit de literatuur)
2. De absorptie en concentratie van CDOM
3. De absorptie en concentratie van alle in suspensie zijnde deeltjes met uitzondering van algenpigmenten
4. De verstrooiing en concentratie van alle in suspensie zijnde deeltjes
5. De absorptie en concentratie van alle algenpigmenten

Metingen van apparente optische eigenschappen

Het licht wat uiteindelijk door een spectrometer wordt geregistreerd heeft een lange weg afgelegd. Van het invallend zonlicht op het wateroppervlak dringt slechts een deel door in het water. Eenmaal in de waterkolom kan het licht worden geabsorbeerd of verstrooid door het water zelf of aan deeltjes of opgeloste stoffen in het water. Alleen het gedeelte van het licht dat wordt terugverstrooid en uiteindelijk weer door het wateroppervlak dringt wordt gemeten door een draagbare spectrometer. Indien er gebruik wordt gemaakt van satelliet- of vliegtuigsystemen wordt nog eens een groot deel van het uit het water gereflecteerde licht door de atmosfeer geabsorbeerd of verstrooid, en zal het signaal aan de spectrometer nog zwakker zijn.

In hoofdstuk 6 wordt beschreven hoe de boven water reflectiemetingen zijn uitgevoerd die zijn gebruikt als apparente optische eigenschappen voor de optische modellering in deze studie.

Gevoeligheidsstudie van het onderwaterlichtklimaatmodel

In de voorgaande hoofdstukken zijn er een aantal keuzes gemaakt met betrekking tot het soort optisch model en de IOPs en AOPs die nodig zijn om het model te voeden. Voordat het model nu toegepast gaat worden is het van belang om eerst de gevoeligheid van het model vast te leggen. In hoofdstuk 7 is daarom gekeken naar de invloed van verschillende voor de hand liggende onzekerheden die kunnen voorkomen op de nauwkeurigheid van de afleidingen van de concentraties van waterkwaliteitsparameters. Uit de gevoeligheidsstudie, uitgevoerd met een gesimuleerde dataset, bleek dat het geselecteerde Gordon-Walker model inclusief de gekozen parameterisatie geschikt si voor de nauwkeurige afleiding van de CDOM concentratie. Verder is vastgesteld dat de bepaling van waterkwaliteitsparameters met dit model het meest gevoelig is voor fouten in de gebruikte IOP set. Verbeteringen dienen dan ook vooral in deze richting gezocht te worden, wat ook is gedaan in dit proefschrift.

Het verbeteren van de afleiding van gekleurde opgeloste organische stoffen door middel van de modernste inversietechnieken

In hoofdstuk 8 zijn er gemeten spectra gebruikt als invoer van model inversie, waar tevens gemeten IOP data gebruikt zijn voor de parameterisatie en calibratie. Hiervoor is eerst een kwaliteitscontrole uitgevoerd op de gemeten data. Van de 52 monsterpunten bleek slechts de data verzameld op 24 punten van voldoende kwaliteit om een succesvolle inversie te verwachten, een score die overigens gemiddeld kan worden genoemd. Dit vanwege het grote aantal verschillende bepalingen per monsterpunt en de gevoeligheid van het optisch model.

Uit de inversies kwam naar voren dat CDOM met een nauwkeurigheid van $R^2 = 0.6$ en een structurele onderschatting van 20% kan worden afgeleid uit gemeten spectra.

Het verbeteren van de afleiding van gekleurde opgeloste organische stoffen door middel van verbeterde referentiemetingen in een PSICAM

Omdat het model vooral gevoelig voor fouten in de gebruikte IOP data is in hoofdstuk 9 een nieuwe methode getest om betere CDOM referentiemetingen uit te voeren in het laboratorium. Daarbij is gebruik gemaakt van een zogenaamde PSICAM. Dit apparaat kent twee voordelen ten opzichte van de standaard absorptiemeting in een cuvet:

1. In een PSICAM is er geen lichtverlies als gevolg van verstrooiing, zodat de ware absorptie gemeten wordt (in plaats van absorptie plus verstrooiing)
2. De gemiddelde padlengte van het licht in een PSICAM is veel langer dan in een cuvet, waardoor er veel lagere concentraties nauwkeurig gemeten kunnen worden.

De metingen met de PSICAM werden voorbereid door eerst een calibratie uit te voeren, gebaseerd op de relatie tussen concentratie en absorptie (Lambert-Beer). Een dergelijke calibratie was nog niet eerder uitgevoerd op een PSICAM.

In een case study in dit hoofdstuk is vervolgens aangetoond met behulp van de PSICAM dat de huidige Ocean Colour labprotocollen voor IOPs moeten worden aangepast, zeker voor gebruik in binnenwater. Wanneer namelijk de CDOM referentie concentratie wordt bepaald in een cuvet na filtratie over GF/F filters met een nominale poriëngrootte van 0.7 µm zorgen verstrooiende deeltjes in het filtraat ervoor dat de absorptie zo’n 7% te hoog wordt gemeten. Indien echter over 0.2 µm membraanfilters wordt gefiltreerd is de gemeten CDOM absorptie wel juist, maar mist er een significant deel van de totale absorptie omdat de absorptie van de gesuspendeerde deeltjes (algen en slib) slechts wordt bepaald tot 0.7 µm.

Door het meten van de CDOM referentie absorptie in een PSICAM kon de nauwkeurigheid van de afgeleide CDOM concentraties uit gemeten spectra met 10 – 20% worden verhoog terwijl de structurele onderschatting met 10 – 15% werd verminderd. Het belang van betere SIOP bepalingen is hiermee aangetoond.

Het verbeteren van de afleiding van gekleurde opgeloste organische stoffen door middel van het toepassen van een twee componenten CDOM model

De derde mogelijke verbetering voor het afleiden van CDOM uit reflectiespectra wordt besproken in hoofdstuk 10: het splitsen van CDOM in twee hoofdgroepen moleculen: humine en fulvine zuren (HA en FA). Vervolgens worden de absorptiespectra en concentraties van deze twee groepen als aparte parameters meegenomen in het model.

Bij het splitsen van het CDOM absorptiespectrum in HA en FA waren er helaas teveel vrijheidsgraden om de absorptie en de hellingsparameters voor HA en FA te bepalen en moest er gewerkt worden met gefixeerde hellingsparameters.

Opvallend was dat bij het gebruik van een twee-componenten CDOM absorptie model de offset parameter met 50% kon worden verminderd, wat aangeeft dat het twee-componenten model het werkelijk gemeten absorptiespectrum veel beter kan benaderen.

Een verbetering van de nauwkeurigheid van de afgeleide CDOM concentraties uit gemeten spectra met behulp van HA en FA referentiedata kon helaas niet met zekerheid worden vastgesteld, vooral doordat de dataset erg klein was en er een aantal uitschieters voorkwamen.

Aanbevelingen

Zoal eerder genoemd dienen de gebruikte labprotocollen voor SIOP bepalingen te worden aangepast om CDOM absorptiemetingen zonder verstrooiingseffecten uit te voeren in een PSICAM. Het filtreren over 0.2 μm filters introduceert een lacune in de totale absorptie van een watermonster en is dus geen oplossing voor het verstrooiingsprobleem in een cuvet.

Het splitsen van de CDOM absorptie in HA en FA absorptie welke apart gemodelleerd worden lijkt een potentiële verbetering voor het optisch modelleren, maar kon niet worden vastgesteld in dit onderzoek. Hiernaar is nader onderzoek gewenst.

Vooruitblik

In deze studie is aangetoond dat het mogelijk is om de CDOM concentratie nauwkeurig af te leiden aan een gemeten spectrum. De gebruikte gemeten spectra voor dit onderzoek waren opgenomen met een draagbare spectrometer slechts ongeveer 1 - 2 meter boven het wateroppervlak. Of CDOM ook kan worden afgeleid van vliegtuig- of satellietdata is hiermee nog niet bewezen, aangezien het gemeten signaal in dergelijke gevallen nog significant wordt afgezwakt, vooral in het blauwe deel van het spectrum waar de informatie met betrekking tot CDOM zit. Uit een ruwe gevoeligheidsanalyse blijkt dat voor het kunnen onderscheiden van CDOM een satelliet- of vliegtuigsensor een signaal/ruis verhouding moet hebben die ongeveer 1,5 beter is dan nodig voor het onderscheiden van chlorofyl.

Verder is het wenselijk dat er vooruitgang geboekt wordt met de atmosferische correctie van bestaande satellietsensoren, niet alleen om het signaal in de blauwe golflengtes te verbeteren, maar ook om te kunnen corrigeren voor overstraling van binnenwater door het omringende vaste land in het infrarood (het zogenaamde adjacency effect).

Tenslotte zal het afleiden van CDOM uit aardobservatiebeelden niet alleen een ongeëvenaard inzicht geven in de hoeveelheid en verspreiding van de belangrijke waterkwaliteitsparameter opgeloste organische stoffen, maar zal een onderverdeling van CDOM in HA en FA tevens informatie verschaffen over de herkomst van het organische materiaal, hetgeen ook van belang is voor de waterbeheerder.

Acknowledgements

Of course, a lot of people have contributed in some way to this dissertation. In the first place these include my supervisors Steef Peters, Arnold Dekker, Pier Vellinga and Wim Salomons. With ideas and possibilities popping out with every breath, Steef always had, and still has, an answer for everything. If it wasn't for our shared endless optimism this 'mission impossible' would have never been accomplished (nor would we have started an even bolder adventure: Water Insight BV). Arnold, it took some effort to get you aboard, but then you did manage to keep me on course towards an interesting dissertation, which must have been quite a challenge.

I started in a wooden shelter called the Institute of Environmental Sciences, which later evolved into the most pleasant floor of the W&N building. During this time I worked with, or shared offices with, or just had coffee with numerous IVM staff. A proper 'thank you' would include most people who were somehow connected with the IVM during the period 1999 – 2003. As this would make a very long list, let me constrain myself to the most important people:

For starters, let me thank the 'remote senselaars': Robert Vos, Machteld Rijkeboer, Hans van der Woerd, Marieke Eleveld, Nancy Omtzigt and last but certainly not least Reinold Pasterkamp. I remember the crash course in reflectance measurements and laboratory analysis by Machteld which included joining the Belgian Navy (just for a few days thankfully). Reinold, your grasp of physics, logical reasoning and above all Matlab has undoubtedly saved me a lot of time and did prevent a lot of errors. I also enjoyed sharing an office with you, or climbing trees to get better reflectance spectra or getting seasick while holding Ocean Optics fibers overboard.

Another IVM department to which I am indebted is the chemistry department of Bert van der Horst, Kees Swart, Martin van Velzen, Petra Booij, Gerda Hopman and especially Jan-Willem Wegener who started me off in the right direction with the PSICAM calibration.

Of course a special thanks goes to the 'Wetpants' in the Randstad research programme: Leontien Bos, Hasse Goossen, Eva de Rijke, Jerry van Dijk and Alison Gilbert. The SENSE course in Apeldoorn was hilarious. Supervising student field work with Leo, Remco and Jerry was also big fun.

I would also like to express my gratitude to John Kirk, Paul Daniel, Vittorio Brando, Janet Anstee, and Nicole Pinnel for significant contributions concerning the PSICAM and for their hospitality during my 2-month stay at CSIRO (Canberra, Australia) in 2001.

And then there are the odds and ends: Margot, thanks for a multitude of coffee breaks and a very exciting photo finish at the end! Katrien, Cécil, Saskia & Babacar, thanks for letting me seek refuge in your houses for undisturbed writing. Roos and Ingeborg, thank you for extra babysitting allowing me to write.

Finally, there is still one person who deserves a truckload of gratitude: my wife Bregje. Without your support, patience and sacrifice this book would have never seen the light of day. I hereby promise never to say the phrase 'just another three months' ever again!

Curriculum Vitae Marnix L. Laanen

Marnix Leo Laanen was born on the 24th of June 1973 in Vlissingen, the Netherlands, where he also attended primary and secondary school. After graduation from RSG Scheldemond in 1991 he begun studying Geology at Utrecht University, but found after a year that his true interests lay more in Physical Geography. Marnix completed his MSc. in Physical Geography in 1996, with specializations in GIS and Remote Sensing, including an internship at Dutch TNO Physics and Electronics Laboratory.

After a number of regular jobs, including 2 years at Dutch multinational Fugro (Fugro Inpark Oil & Gas Department), he applied for a Ph.D. position at the Institute of Environmental Studies of the Vrije Universiteit Amsterdam, where he subsequently worked from November 1999 to March 2004.

It was already during his time as a Ph.D. student that the idea of starting a water remote sensing company sprung to life. Observing the huge gap between ‘completed’ water remote sensing research trees at the one hand and the requirements of water managers concerning the application of new techniques at the other hand, it seemed that there was a need for a knowledgeable but commercial entity to act as a bridge. So, after about a year of preparations, Marnix and his former supervisor Steef Peters officially started Water Insight BV in fall 2005, aimed at the awareness, acceptance and implementation of remote sensing techniques in the routine operations of water management organisations. The activities of Water Insight can be followed at www.waterinsight.nl.